Demonstration of electroluminescent TPC technology for neutrinoless double beta searches using the NEXT-DEMO detector

A DISSERTATION PRESENTED

BY

FRANCESC MONRABAL CAPILLA

TO

THE DEPARTAMENT DE FÍSICA ATÓMICA MOLECULAR I NUCLEAR

IN PARTIAL FULFILLMENT OF THE REQUIREMENTS

FOR THE DEGREE OF

DOCTOR OF PHILOSOPHY

IN THE SUBJECT OF

NEUTRINO PHYSICS

UNIVERSITAT DE VALENCIA

VALENCIA, VALENCIA

JUNE 2014

THESIS ADVISOR: JUAN J. GÓMEZ CADENAS

"Perquè hi haurà un dia que no podrem mès, i llavors ho podrem tot."
Vicent Andrés Estellés

Agraïments

Els agraïments solen ser la part que més gent llegeix en una tesi, molt més quan aquesta és en anglès i sobre una partícula que gairebé no existeix. Podria limitar-me a enumerar a la gent que ha estat al meu costat al llarg de tots aquests anys, donar les gràcies per suportar-me, per fer-me saber que podia tirar endavant sense por, per ensenyar-me on estava el camí o per a ajudar-me a crear eixe camí. Així segur que quede bé amb tothom, però aço seria injust, perquè per a mi la tesi ha sigut molt més que un treball o uns quants cursos més a la universitat. Durant aquestos anys he tingut experiències que van molt més enllà del àmbit acadèmic i hi ha persones que es mereixen molt més que un curt nomenament al principi d'aquest treball. Deixeu-me que tracti d'explicar-vos-ho amb una història:

Comença el viatge

Una de les coses més importants que cal fer molt abans de començar qualsevol viatge és entendre quina direcció volem agafar, on volem anar i on pensem que aplegarem. De vegades semblen les coses més fàcils de fer, tothom pensa que va cap a algun lloc, però decidir a quin lloc sovint no és tan fàcil. En el meu cas ho vaig tenir un poc més fàcil que molta gent gràcies a aquelles persones que m'han acompanyat al llarg de tots els meus anteriors viatges, llargs o curts. Aquestes persones són la meua família, especialment els **meus pares** que sempre han estat al meu costat per a què no em fes mal en caure, per a ajudar a alçar-me ràpidament si calia. Inclús aquests cops que no els mereixia, ells sempre estaven allí, encara no entenc com ho feien però encara ho fan. Hi ha altra persona que m'ha ajudat a obrir portes i camins, la que va fer el seu propi recorregut molt abans que jo per terrenys molt més durs (ser el primer sempre costa més), aquesta persona és la meua **germana** sense la qual m'hages perdut tantes voltes que ni tan sols sabria trobar-me ara a mi mateixa.

Gràcies a aquestes persones vaig aplegar a la facultat de física on just abans d'acabar la carrera em vaig trobar amb un home d'energia desmesurada, un home diferent de tots aquells professors que havia conegut durant els meus anys a la facultat. Aquest home no parlava d'exercicis, beques, contractes, ... Parlava de recórrer camins que desconeguts, de trobar coses que possiblement no existiren, de pujar a les muntanyes més altes. Una persona que difícilment et deixava indiferent, pot ser penses que estava boig però sempre et deixaria eixe dubte: "I si no ho està?". En el meu cas vaig decidir seguir-lo, per veure si aquelles muntanyes de les quals parlava eren tan altes com deia. Així, més o menys, és com **JJ** es va convertir en el meu supervisor, el jefe.

Vaig començar a caminar, primer amb un any més d'entrenament per al que havia

de vindre. No és que en aquest any aprengues tècniques fonamentalment noves, però si vaig dependre el que era treballar. Treballar durant hores per a donar passos molt petits, una forma nova d'avançar que fins ara no m'havia fet falta però que més endavant seria fonamental. I si aço fora poc, en aquest any també vaig conèixer a una de les persones més importants que han passat per la meva vida: **Maria**.

Pujant la muntanya

Després d'aquest any ja havia de començar a pujar aquella muntanya que m'havien promés. Com podreu imaginar, abans d'atacar un pic és fonamental conéixer-lo bé. Així que el que vàrem fer és començar a resoldre els possibles problemes que podríem trobar quan estiguérem allí dalt, calia descriure molt bé la muntanya, els seus camins, les seves pedres, de forma que després tindríem poques sorpreses. Per a fer açò, en el grup hi havia un altre estudiant amb una experiència sorprenent per a la seva edat, **Justo**, sense ell no hages pogut començar tot aquest viatge. Amb ell vaig passar els primers anys estudiant cada detall de què ens podríem trobar més endavant fins que un dia vaig tenir l'oportunitat de fer un viatge a l'altra banda del món per aprendre del que allí sabien.

Cada dia d'aquest viatge veia coses noves que em fascinaven: la gent, la forma de treballar d'aquell lloc estrany, els paisatges infinits en el temps. Era fàcil trobar-se còmode rodejat de gent com **Azriel** o **Josh**, que sempre tenien un somriure a la cara i coses interessant per a fer al laboratori. O amb gent com **Dave** amb cada dia la idea més brillant que havies escoltat, amb **Derek** que semblava capaç de fer realitat totes aquelles idees. Aquest viatge em va semblar curt, però va ser suficientment llarg per a donar-me forces en tot el que estava per vindre.

Quan vaig tornar tot havia canviat, pot ser era jo o pot ser aquella màquina estranya, una espècie de monstre incontrolable que havia aparegut al laboratori. L'interior d'aquesta màquina era meravellós i fascinant, havia sigut dissenyat amb tot detall per una de les persones que més em va ajudar en tot aquest viatge, **James**. Aquest home sempre trobava la solució a problemes que semblaven sense eixida, al seu costat l'impossible tan sols era una il·lusió. "We will do it, if that can be done", aquesta era la frase que et donava la seguretat de què tot es resoldria. De vegades semblava que **James** tenia totes les respostes però tenia una cosa més important, les preguntes correctes. **James** se'n va anar (molt) abans del que nosaltres desitjàvem, però un poc de la seva personalitat continuarà sempre amb nosaltres i això ens ajudarà a seguir sempre endavant.

James no ens va visitar sol, sempre venia acompanyat per l'incansable **Clement**,

que després d'haver navegat per les profunditats de tots els oceans ens va ajudar a tractar amb aquell animalot que teníem al laboratori. Aquell aparell estrany que havia de permetre'ns pujar muntanyes però que de moment no feia més que soroll, centellejava i treia senyals sense massa sentit.

Doncs molt bé, si aquest aparell era amb el que pujaríem fins a dalt més valia que aprenguéssim a controlar-lo. Per fer-ho, vàrem crear un grup increïble ple de gent amb capacitat per a fer que coses impossibles semblaren fàcils. Estaven **Javi** i **Vicente**, que varen donar forma a aquells senyals tan estranys que teníem al principi. També estaven **Raül** i **Curro** que varen idear tota una serie de trampes per a seleccionar exactament el tipus de senyal que ens feia falta a cada moment.

Ajudant-nos a llegir i interpretar tot el que treia el monstre ens acompanyaven **Michel**, amb una mirada de franctirador que sempre aplegava als punts més febles dels nostres raonaments, i **Luis** i **Toni** que varen ser capaços de fer que la maquina parlés el nostre idioma o **Paola** que va continuar i perfeccionar el model que ens permetria entendre molt millor tot el que estàvem fent.

Fent dissenys dins i fora d'aquell aparell ens van acompanyar **Sara** i **Alberto**, dissenys que és feien realitat gràcies al gran **Manolo** que semblava capaç de canviar el món amb les seves mans. A més teníem **Japepe** i **David** treballant en els ulls d'aquell animalot, un calibrant-li la vista per a què no es perdés res del que passava al seu interior, l'altre creant un sistema amb ulls d'última tecnologia que ens permetria vore amb molt més detall el que estava passant al seu dintre. Per últim però una de les peces més important en aquesta aventura estava amb nosaltres algú que mai deixarà de ser un misteri, **Igor** who was able to describe with all the details the structure and the behaviour of that machine.

Amb aquest equip vàrem començar un viatge ple d'incerteses, ple de matinades i nits sense dormir. Hi havia dies que tot s'enfonsava, dies que els arbres caiguts en mig del camí ens empresonaven. En aquells dies, **Pilar** sempre ens acompanyava per a fer-nos sortir d'aquella presó que en realitat no existia, per a donar-nos eixa visió del món que feia escampar qualsevol boira quan més ho necessitàvem. Altres dies el camí es convertia en un riu d'aigües clares i per moments oblidàvem que el viatge era duríssim. En aquest riu vàrem conéixer a altres companys com **Raphael**, **Andrew** que es va decidir a fer el camí amb nosaltres després de fer un gran camí per països estranys pel seu compte. També ens vàrem trobar amb el gegant **Diego**, gegant en tants sentits que no us ho podria explicar. **Diego** va decidir acompanyar-nos en el nostre viatge, si mes no, mai va sortir de l'aigua. No semblava interessat en aplegar dalt d'aquella muntanya que semblava no tenir final, més bé es pareixia que disfrutava vent com caminàvem. A més, en alguns dels moments més durs ens seiem amb ell vora el

riu i ens contava històries d'herois llegendaris amb formes increïbles i colors màgics que havien habitat aquell riu. Herois que encara es podien sentir a l'aigua, histories sense les que no haguéssim pogut trobar el final del camí.

Aquest viatge va ser increïble, però va estar molt lluny de ser senzill o fàcil. Els moments d'incertesa varen ser molts, moments molt durs on el camí era un seguit de tempestes. Ganes d'abandonar? Clar, perquè no? Però a cada pas **JJ** aconseguia convèncer-me de què estàvem més a prop, de què no ens havíem equivocat de camí, de seguir caminant. I en els pitjors dies sempre podia apartar-me una mica, sentar-me a la vora del camí que sabia que allí trobaria als meus pares, la meva germana i sempre a **Maria**. Ells varen fer el camí amb mi i gran part és tant meu com seu, o pot ser més seu.

Aplegar al cim

Per fi, en l'últim moment, quan menys ho esperàvem, ahí va aparèixer "El pico del Cesio" pel que tantes persones ens havien preguntat. El que devia ser el final del principi. Aquest si era el primer pas de tot el que estava per vindre.

Durant mesos ens vàrem dedicar a estudiar-lo amb cura, a veure'l des d'una banda, des de l'altra. Vàrem tractar de pujar a les pedres més afilades, aquelles que feien que el pic semblés més alt i prim. Vàrem conèixer allò que tant ens havia costat d'aconseguir. Quan ja pensàvem que ho teníem, que ho havíem entès, que no quedaven secrets en aquella muntanya que poguessin sorprendre'ns vàrem trobar un nou company, **Ander**, que estava allà dalt enlluernant el cim, i vaja si el va enlluernar! El pic ens va tornar a sorprendre un cop més.

Finalment, un cop allà dalt, vàrem poder alçar la vista d'aquelles pedres que tant ens va costar d'esmolar i vàrem poder veure el paisatge. El que havíem fet no era més que una curta travessia en comparació amb tot el que teníem per davant. Quan alguns ja pensàvem que estàvem a la fi del camí vàrem trobar noves sendes. Muntanyes altíssimes, boscos d'arbres desconeguts que ens oculten els camins que hem de recórrer.

Carregats dels anys i l'experiència estem construint el nou aparell que ens permetrà aplegar a tots els racons d'aquest paisatge, de travessar nous rius, noves batalles, nous camins. Però això ja són altres històries, la del primer camí que, encara que no ens agrade, s'acaba ací.

Fins aquí la història del que va ser la meva tesi, espere haver aconseguit explicar l'important que varen ser i són les persones que ahí apareixen. Però, degut principalment a les meves limitacions literàries, no he pogut fer que aparegueren tots els que

m'han acompanyat, companys com **Javi M.**, **Miquel**, **Miguel**, **Pau**, **Lorena**, **Joan** i **Neus** que també m'han fet passar bons moments. **Marc** que no calla. Gent com **Jose Ángel** que sempre troben la solució més original o **Anselmo**, que ens explica les coses que no entenem per a que pugam entendre-les. **Diego** que sempre te un bon motiu per a discutir. La gent de la banda, **Ana**, **Majo**, **Adri**, **Vane**, **Ximo** i per supost **Manel** amb les seves dos noves xiques, com hem canviat! També la gent de la piscina que tant ens fan patir però que sempre acabem tornant.

Per suposat, tot açò no hagues començat mai si en la carrera no m'hagues trobat amb gent com **Manu**, **Paco**, **Maria** i per supost **Alberto**. Alguns d'estos amics també estaven en aquelles nits llargues observant estels amb la **AAUV** on **Javi** ens va ensenyar a navegar per les constel·lacions.

També he d'agrair a la gent de JotDown, en especial a **Ángel**, haver-me permés fer coses que de cap altra manera hagués aconseguit.

Per descomptat la resta de la meva família, la meva àvia, les meves tietes i tiots, però sobretot els meus cosins: **Noe** i **Pedro** (que també es cosí), **Paco**, **Jesús**, **Santi**, **Iñaki** i **Asier** i la peque **Marieta** que ja ha deixat de ser "peque". Ha deixat de ser "peque" perquè ara hi ha uns enormes ulls blaus que sempre m'arranquen un somriure, els ulls d'**Aitana**, que junt amb els ulls de **Bego** han aparegut no fa molt a la meva vida però ara no sabria que fer sense ells.

Per últim, gràcies a **Santi** que encara que se'n va anar molt abans d'hora em va ensenyar una de les coses que més he necessitat per a aplegar fins aquí, a lluitar sense guardar-se res, a lluitar pel que vols sense cap por, a lluitar encara que sàpigues que no ho vas a aconseguir.

Gràcies.

Thesis advisor: Juan J. Gómez Cadenas Francesc Monrabal Capilla

Demonstration of electroluminescent TPC technology for neutrinoless double beta searches using the NEXT-DEMO detector

Abstract

Neutrinos have contributed to the evolution of particle physics since they were postulated. In the last years experiments have demonstrated that neutrinos have mass. The results of those experiments, combined with enduring efforts to directly measure neutrino masses, offer a landscape with three neutrino families much lighter than the other fermions. This difference suggests that some "unusual" physics is behind the neutrino mass.

This thesis explains the different physics processes that can allow the neutrinos to have mass. It focusses on the only process that can realistically measure and demonstate the underlying physics, the neutrinoless double beta decay process.

In order to find and measure the neutrinoless double beta decay process, the NEXT Collaboration aims to build a detector of 100kg enriched Xenon in the ^{136}Xe isotope. In order to demonstrate the technology and obtain experience carrying out the experiment, the Valencia group has built a medium size prototype, NEXT-DEMO. This prototype has been operating at IFIC for the last two years and it has evolved to be as close to the final NEXT-100 detector as possible. The work presented in this thesis is focused on the operation and first data analysis of this detector in various configurations.

The text is organized as follows: chapter 1 is an introduction to neutrinos where

only the basic concepts and the current status of the field are described. Chapter 2 describes the two mechanisms to generate the neutrino masses and the possible observables that can help to differenciate them. Chapter 3 describes in detail the theory of the neutrinoless double beta decay process. Chapter (4) is a detailed description of the more relevant experiments in the field and their results are shown. Chapters 5 and 6 are a description of the NEXT dector concept and its implementation on the NEXT-DEMO prototype.

Chapter 7 and 8 show the results of the operation of the NEXT-DEMO prototype, where both the energy resolution and the tracking capabilities are shown. This is the central part of my work, in those papers I was in charge of commisioning the detector, determine the trigger to be used and responsible of the data taking. I was also very involved, together with my supervisor, in the event reconstruction. In that sense I participated in the development of the whole pre-processing algorithms and also in the energy and topology reconstruction algorithms.

Chapter 9 describes the NEW prototype that will be commissioned abd operating at Canfranc Underground Laboratory next year and will contribute to the final NEXT-100 detector.

Contents

Our imagination is stretched to the utmost, not, as in fiction, to imagine things which are not really there, but just to comprehend those things which are there.

Richard P. Feynman

1

A brief history of the tiniest particle

When many of us first fell in love with physics what we really fell in love with were tales of heroes. Heroes whose fortitude gave them courage to follow their own paths beyond what was known and conventional. Through their labours these individuals managed to change the prevailing, contemporary picture of physics.

The history of the neutrino is full of these heroes, physicists who invented a particle as a "desperate remedy" and others, even at the risk of seeming mad, who decided to look for such particle and to find it.

This discovery was just the beginning, a particle so small that it had gone unnoticed. Indeed, the neutrino has participated in discoveries of new particles. it has shaken the standard model that it helped to build and has opened new windows on the universe. Furthermore, the neutrino may be the key to explain why we are here, in

a universe where a tiny asymmetry between matter and anti-matter made it possible that not all matter annihilate with anti-matter as the universe cooled down.

1.1 A desperate remedy

Sometimes physics gives the appearance of being complete. We understand how the world works except for small details. In the early twentieth century one of those details was the spectrum of beta decay, that is a type of radioactive decay in which a proton is transformed into a neutron, or vice versa, inside an atomic nucleus. The total energy of the emitted particles was always observed to vary over a range and give lower values than expected.

The great physicist Wolfgang Pauli decides to solve this situation and declares that the spectrum of beta decay can be explained if an extra particle is emitted. A massless particle (or a very small mass) without electric charge. A particle that barely interacts with matter, almost undetectable, a desperate remedy. A ghost!

1.2 A selection of experiments looking for the mysterious neutrino

Luckily, many physicists are not impressed for something that sounds "almost" impossible, what interests them is the almost. One of the first experiments trying to find this elusive particle, 20 years after being postulated, was the "Cowan-Reines experiment".

1.2.1 Cowan-Reines Experiment

This experiment aimed to detect neutrinos from a nuclear reactor. Neutrinos would interact with protons in the detector generating neutrons and positrons. The positrons on annihilating with the environmental electrons produce two prompt 511keV gammas while the neutrons are captured by the ^{108}Cd nuclei. The excited ^{108}Cd nucleus

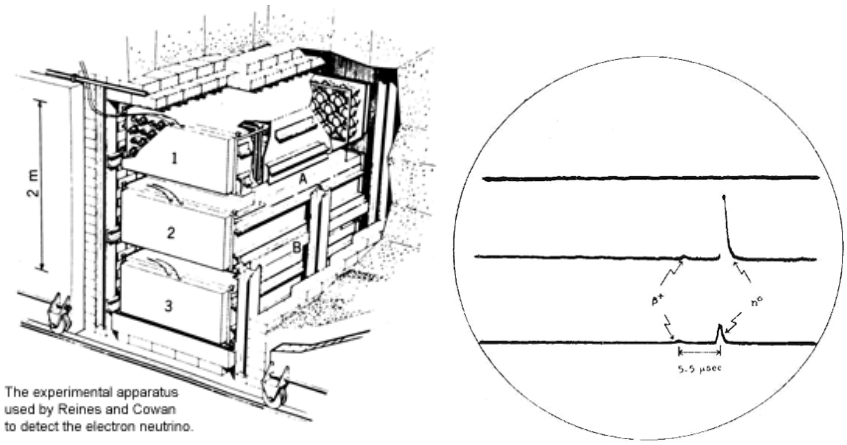

Figure 1.2.1: Schematic of Cowan Reines 1956 experiment (Left). Typical signal in the Cowan-Reines experiment (Right). First seen in coincidence are the 'positron' annihilation gamma-ray pulses in each tank followed in 5.5 μs by the larger 'neutron' pulses. The amplification was chosen in this case to enable measurement of the neutron pulses. A second oscilloscope with higher amplification was operated in parallel to enable measurement of the positron pulses. Images from NuMi-MINOS homepage (left) and from [1] (right).

de-excites by emitting delayed gammas. This characteristic signal allowed significant reduction in background.

1.2.2 Davis at Homestake

Another intense source of neutrinos is the Sun. The Earth is bathed in a sea of nearly 70 billion of solar neutrinos per square centimeter per second. This large flux suggests that those neutrinos can be detected despite this tiny effective cross section. To detect neutrinos Raymond Davis Jr. built a tank of 380 cubic meters, placed it deep inside the Homestake Gold Mine Mine (1500 meters deep) and filled it with cleaning fluid rich in chlorine. When chlorine reacts with a neutrino, argon is produced. Being a noble gas, argon atoms remain in the solution. Every few weeks, all the fluid was filtered to separate and count the atoms of argon produced. Davis managed to find

these argon atoms. In that way Davis was the first to observe and characterise the solar neutrino flux. However, something was still missing.

1.3 Solar neutrino Problem

Comparison of the observed solar fluxes to those predicted by theoretical calculations, many of them by John Bachall (another hero in this story), indicated that there was a three fold deficit between observation and prediction [2].

This discrepancy between the data was not taken as something really serious, at the end of the day the two physicists working on this problem, one claimed to be able to measure a few atoms each month after cleaning a pool inside a mine and the other was calculating some numbers based on the incomplete knowledge of solar processes. Solar models, at that time, were not as precise as those today.

However, these physicists continued to work and publish their results and the discrepancy between theory and experiment increased. The scientific community began to take these results seriously, and as often happens in science, new experiments were designed and built to try to solve this problem. A series of experiments like GALLEX (Italy) [3], SAGE (Soviet Union) [4], Kamiokande (Japan) [5] and SNO (Canada) were built in order to contrast the results of Davis and shed some light on the problem..

The definitive solution to the problem came form SNO. The SNO experiment was a tank of heavy water. The big difference between SNO and Homestake is that SNO was sensitive to both types of neutrino reactions, neutrinos reacting via charged current and also neutrinos reacting via neutral currents. While the charged currents are sensitive only the ν_e component, because neutrinos do not have enough energy to generate muons or taus, neutral currents are sensitive to all neutrino flavours. In addition, the SNO detector was able to distinguish these two interactions and therefore count the absolute number of neutrinos and electron neutrinos to the corresponding fraction of electron neutrinos. SNO results show that the electron neutrino measurements are consistent with the Davis results [7]. Only a third of neutrinos that we ex-

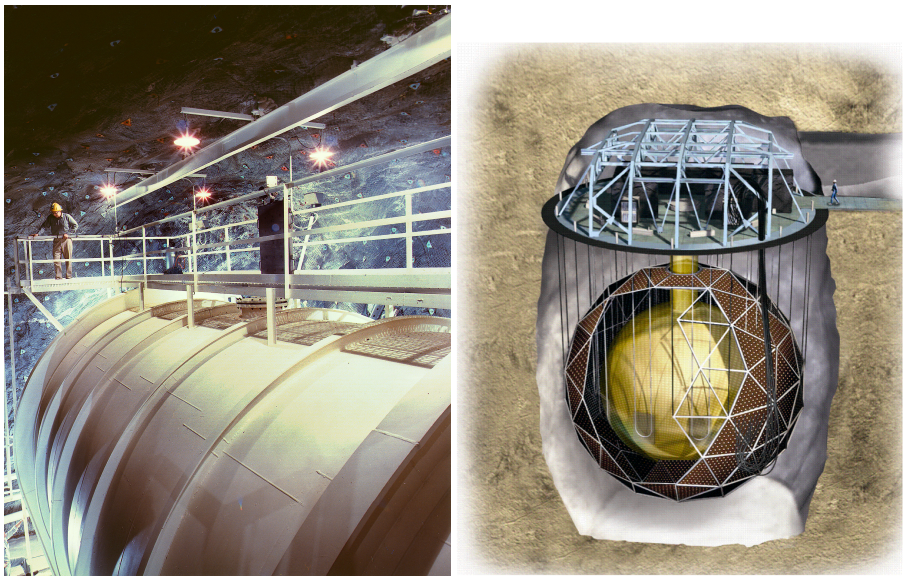

Figure 1.3.1: Picture of R. Davis on top of the detector (Left). Image from Brookhaven National Lab. Schematic of SNO detector (Right). Image from [6]. While Davis could only measure neutrino flavor, SNO was sensitive to all three neutrinos flavours. The results of those experiments were crucial in the understanding of neutrinos properties.

pect from the Sun interact. However, when taking into account all types of neutrino regardless of the flavor, the number of interactions matches the number predicted by J. Bachall. This is the first evidence that neutrino oscillations resolved the solar neutrino problem.

This results, together with the atmospheric results from SuperKamiokande as I will show in section 1.6.3 shows that neutrinos change flavor, the first experimental results of physics beyond the standard model. The simplest explanation to this change is that neutrinos have mass and mix. It is intriguing, since one could say that the measurements already indicated that Davis discovered neutrino mass and therefore the stadard model failed even before it was built! These results opens new questions, as it often happens in science, questions like what is the nature of neutrino mass? why

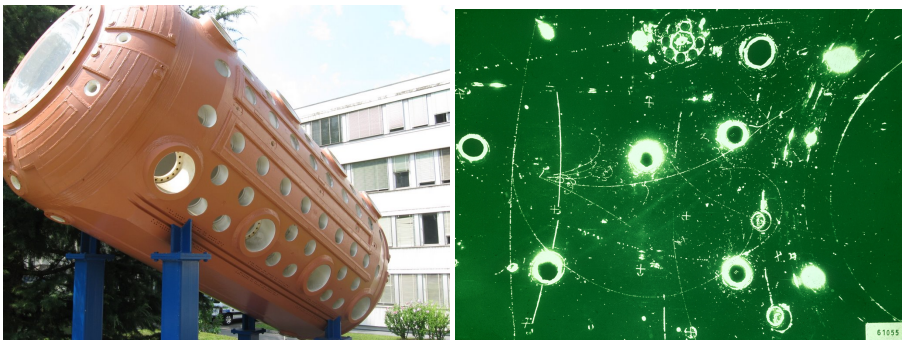

Figure 1.4.1: Gargamelle detector (Left). Image of the neutral currents observed in Gargamelle (Right). Observation of neutral currents in Gargamelle provided the experimental foundation for what we now call the Standard Model. Images from CERN website.

their mass scale is so different with respect to the other fermions? To answer those questions it is necesary to have experiments like NEXT.

1.4 Building the SM

Not only did the neutrino shake up the standard model it has also helped to build it. The neutrino has only weak charge and therefore offers the possibility of studying the weak interaction independently (or almost) to the other interacions. Moreover, the appearance of beams of neutrinos (Nobel prize to J. Steinberger, L. Lederman and M.Schwartz in 1988 "for the neutrino beam method and the demonstration of the doublet structure of the leptons through the discovery of the muon neutrino") led to the discovery of neutral currents in the experiment Gargamelle in 1974 at CERN. The discovery of neutral currents [8] represented a "significant step towards the unification of electromagnetism and the weak force into the electroweak force, and led to the discovery of the W and Z bosons."

Moreover, the decay of Z boson at LEP (ALEPH, DELPHI, L3 and OPAL) showed

that there can be only 3 families of light neutrinos ($m_\nu < M_Z$) providing information on the total number of families existing in nature at low energies.

1.5 Neutrino mixing

Neutrino oscillations occur because the flavor eigenstates of neutrinos (ν_e, ν_μ and ν_τ), i.e. the states that coupled to the $e^-, \mu^- and \tau^-$ leptons are different from the eigenstates of evolution of the particles (or mass eigenstates that are also the eigenstates of the Hamiltonian when neutrinos propagate in vacuum). If we express this mathematically, we say that the flavor eigenstates (weak eigenstates) can be expressed as a unitary rotation of mass eigenstates:

$$|\nu_\alpha\rangle = \sum_i U^*_{ai} |\nu_i\rangle \tag{1.1}$$

In this equation, U is a 3x3 matrix known as neutrino mixing matrix and usually parameterized in terms of three Euler angles (θ_{12} θ_{13} θ_{23}) 3 phases and generically (δ, α_{21}, α_{31}) as:

$$U = \begin{pmatrix} c_{12}c_{13} & s_{12}c_{13} & s_{13}e^{-i\delta_{CP}} \\ -s_{12}c_{23} - c_{12}s_{13}s_{23}e^{i\delta_{CP}} & c_{12}c_{23} - s_{12}s_{13}s_{23}e^{i\delta_{CP}} & c_{13}s_{23} \\ s_{12}s_{23} - c_{12}s_{13}c_{23}e^{i\delta_{CP}} & -c_{12}s_{23} - s_{12}s_{13}c_{23}e^{i\delta_{CP}} & c_{13}c_{23} \end{pmatrix} \tag{1.2}$$

$$\times diag(1, e^{i\frac{\alpha_{21}}{2}}, e^{i\frac{\alpha_{31}}{2}})$$

where $c_{ij} = cos\theta_{ij}, s_{ij} = sin\theta_{ij}$, the angles $\theta_{ij} = [0, \pi/2]$, $\delta = [0, 2\pi]$ is the Dirac CP violation phase and α_{21}, α_{31} are two Majorana CP violation phases (see, for example, [9]).

Ignoring for the moment Majorana phases, which are not observable by oscillations, the mixing matrix may be parameterized by a product of three matrices. Each

of these would be associated with a different rotation angle. This setting is typically used for the different experiments to highlight the angle being measured.

$$U = \begin{pmatrix} 1 & 0 & 0 \\ 0 & c_{23} & s_{23} \\ 0 & -s_{23} & c_{23} \end{pmatrix} \begin{pmatrix} c_{13} & 0 & s_{13}e^{-i\delta} \\ 0 & 1 & 0 \\ -s_{13}e^{i\delta} & 0 & c_{13} \end{pmatrix} \begin{pmatrix} c_{12} & s_{12} & \\ -s_{12} & c_{12} & 0 \\ 0 & 0 & 1 \end{pmatrix} \tag{1.3}$$

In this parametrization, the angle θ_{23} is mostly responsible for flavour transitions observed in solar neutrinos. The angle θ_{12} is responsible for oscillations observed in atmospheric neutrinos and θ_{13} is the angle recently measured in reactor neutrinos.

Moreover, the probability of oscillation depends not only on the angles of the mixing but also the difference in mass squared between the different mass eigenstates, the propagating distance and their energy. The data of ν-oscillations experiments are often analyzed assuming 2-neutrino mixing:

$$|\nu_l\rangle = |\nu_1\rangle cos\theta + |\nu_2\rangle sin\theta, \qquad |\nu_x\rangle = -|\nu_1\rangle sin\theta + |\nu_2\rangle cos\theta, \tag{1.4}$$

where θ is the neutrino mixing angle in vacuum and ν_x is another flavour neutrino $x = l' \neq l$. In this case, we have:

$$\begin{aligned} P^{2\nu}(\nu_l \to \nu_l) &= 1 - \frac{1}{2} sin^2 2\theta \left(1 - cos(2\pi \frac{L}{L^\nu})\right), \\ P^{2\nu}(\nu_l \to \nu_x) &= 1 - P^{2\nu}(\nu_l \to \nu_l) \end{aligned} \tag{1.5}$$

where $L^\nu = 4\pi p/\Delta m^2$, $\Delta m^2 = m_2^2 - m_1^2 > 0$.

These equations were used in the analysis of many experiments to determine compelling evidence for neutrino oscillations. The probability
$P^{2\nu}(\nu_l \to \nu_x)$ depends on three factors: the distance over neutrino energy and the mass square difference that determines the period of the oscillation, and the mix-

ing angle that fixes the amplitude of the oscillation. The difficulty to accurately measure the different parameters relies on the experimental capabilities to maximizes the probability of oscillation. Finding the appropiate distance over neutrino energy is fundamental for the success of the experiment.

1.5.1 Current knowledge of ν oscillation parameters

There is a large amount of data on neutrino oscillations. This has alllowed the community to have precise measurements and understanding of the different neutrino parameters.

The solar mass splitting has been measured to be $\Delta m^2_{sol} \equiv m^2_2 - m^2_1 = (7.45^{+0.19}_{-0.16}) \times 10^{-5}$ eV^2. Atmospheric and accelerator-based experiments have measured a different mass splitting, the so-called *atmospheric mass splitting*, to be: $|\Delta m^2_{atm}| \equiv |m^2_3 - (m^2_1 + m^2_2)/2| = (2.421^{+0.022}_{-0.023}) \times 10^{-3}$ eV$^2 \gg \Delta m^2_{sol}$. These results are compatible with two type of neutrino spectra shown in 1.6.1, either the two most degenerate states are the lightest (normal hierarchy) or the heaviest (inverted hierarchy). In the standard 3-neutrino oscillations paradigm, those are the only two independent mass splittings available. The best-fit values and 1σ ranges quoted were obtained from a recent global 3-neutrino fit [10].

The neutrino mixing matrix components have also been measured in great detail. In the same reference [10] we find that the best-fit values and 1σ ranges in the neutrino mixing parameters measured via neutrino oscillations for the $|U_{\mu 3}|$, $|U_{e2}|$, $|U_{e3}|$ elements (the other matrix elements can be calculated assuming unitarity) are: $sin^2\theta_{12} = 0.306^{+0.012}_{-0.012}$, $sin^2\theta_{23} = 0.437^{+0.061}_{-0.031}$, $sin^2\theta_{13} = 0.0231^{+0.0023}_{-0.0022}$. The value of the Dirac CP-violating phase δ, also potentially observable in neutrino oscillation exeriments, is currently unknown.

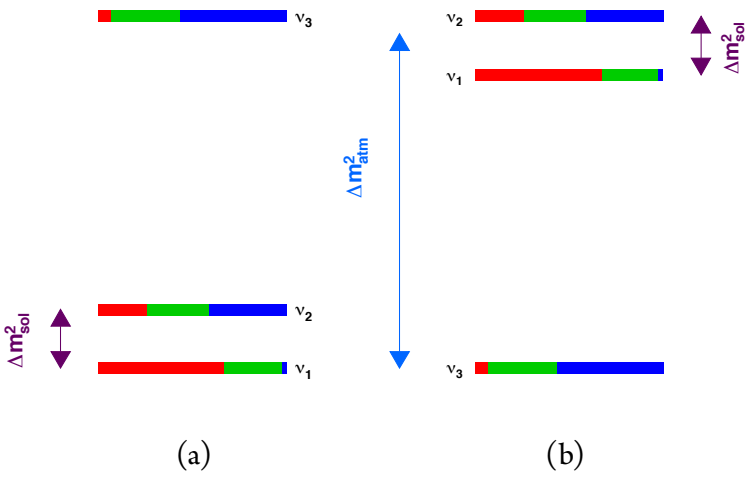

Figure 1.6.1: Knowledge on neutrino masses and mixings from neutrino oscillation experiments. Panels (a) and (b) show the normal and inverted mass orderings, respectively. Neutrino masses increase from bottom to top. The electron, muon and tau flavor content of each neutrino mass eigenstate is shown via the red, green and blue fractions, respectively.

1.6 Measuring the Oscillations

Following the qualitative understanding of the problem of solar neutrinos, a race started to try to better understand neutrino oscillations and measure all the oscillation parameters appering in equations 1.5 and 1.3.

1.6.1 Solar neutrinos

As noted earlier, the different experiments are sensitive to different angles. Thus the disappearance of solar neutrinos (ν_e) has been observed in several experiments, Super- Kamiokande and SNO being the two most important.

Super-Kamiokande (Fig. 1.6.2) is a tank of 50,000 tons of ultrapure water containg over 11,000 photomultipliers to detect the Cerenkov light produced by particles that travel faster than light in water. The neutrinos from the sun interact with

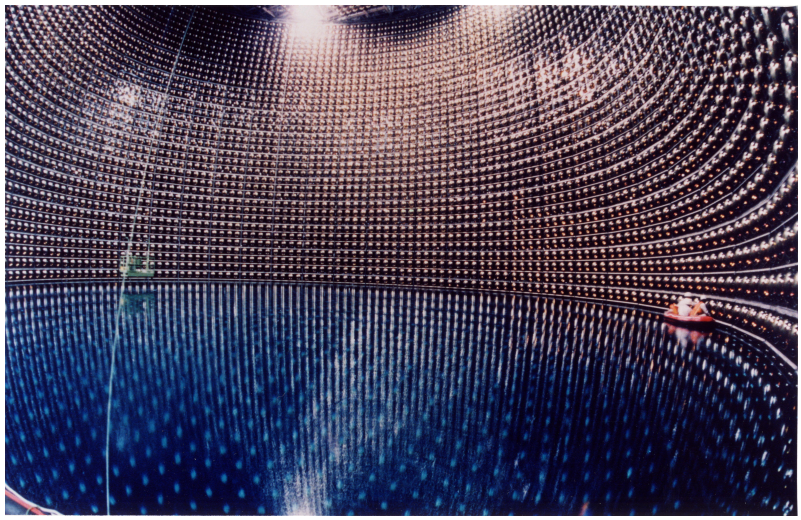

Figure 1.6.2: Image of the internal part of SuperKamiokande. The image shows the technicians doing the maintenance of the detector. SuperKamiokande images can be found at the official website.

the water producing electrons. These particles emit a cone of Cerenkov light. Super -Kamiokande can, in addition to counting the interactions of neutrinos, distinguish among electrons and muons due to the light distribution, that helps in discriminating background. Thus, it was able to confirm the neutrino deficit observed by Davis and it confirmed the solar neutrino oscillation.

1.6.2 Reactor neutrinos

Han contribuido a la solar y la atmosférica gracias a que se ha podido escoger la baseline que tocaba

Meanwhile, reactor antineutrino experiments ($\overline{\nu_e}$) have contributed significantly to the understanding of this particle . Reactor neutrinos were the first to be detected in the experiment of Reines and Cowan. On the other hand, they have proved crucial in demonstrating neutrino oscillations associated with....(KamLAND) and in making precise measurements of mixing parameters (DAYA-BAY).

Kamland demuestra que las flavor transitions del sol estan debidos a mixing/oscilaciones

The KamLAND experiment in Japan was built in a mine surrounded by more than 50 nuclear reactors. KamLAND Consists of an 18 m diameter spherical stainless steel vessel with 1,879 large (50cm diameter) photo -multiplier tubes mounted on the inner surface. A nylon balloon of 13 m diameter is filled with liquid scintillator. Outside the balloon a non-scintillating oil provides highly purified medium for the balloon buoyancy and acts as a shield against external radiation. A 3.2 kiloton cylindrical water Cherenkov detector, that acts as a muon veto counter and provides shielding from cosmic rays and radioactivity, surrounds the vessel. KamLAND measured anti-neutrino disappearance at a confidence level of 99.998% [11]. KamLAND is also able to measure the energy spectrum of neutrinos so not only the distortion in the spectrum is observed, but also the periodic feature of the $\bar{\nu_e}$ survival probability expected from neutrino oscillations is measured.

1.6.3 Atmospheric neutrinos

The oscillation of atmospheric neutrinos produced by the interaction of cosmic rays with the atmosphere, was first measured by the Super-Kamiokande collaboration in 1998 [12]. Super-Kamiokande observed a dependence of muon coming from below with respect to the zenith angle demonstrating a clear deficiency of events compared to the case of non-oscillation.

Figure 1.6.3 shows the dependence of the neutrino zenith angle in different energy ranges. In the same figure, the MC value predicted in the absence of oscillation can be seen. The SK experiment wsa able to show the oscillations of atmospheric neutrinos at a confidence level of 4.9σ.

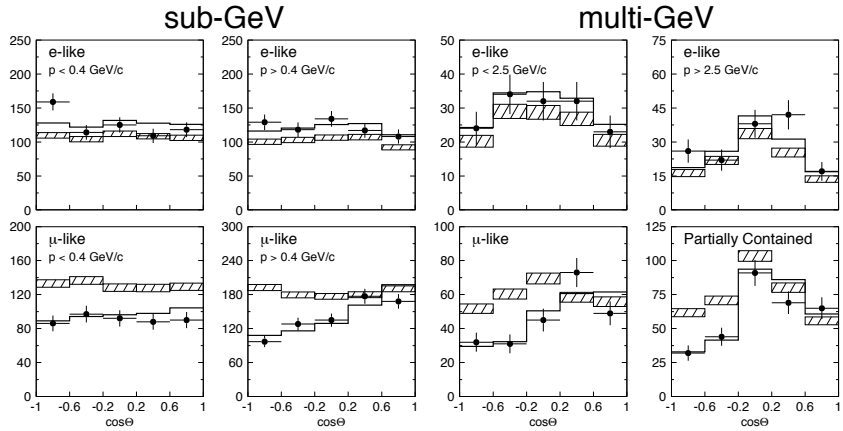

Figure 1.6.3: Zenith angle distributions for μ-like and e-like events for sub-GeV and multi-GeV data sets. The angle is defined in such a way that upward-going partilcles have $\Theta < 0$. The sub-GeV set is shown separately for $p < 400 MeV/c$ and $p > 400 MeV/c$. The multi-GeV the separation is done at $p = 2.5 GeV$. The hatched region shows the Monte Carlo expectation for no oscillations normalized to the data live time with statistical errors. The bold line is the best-fit expectation for $\nu_\mu \rightarrow \nu_\tau$ oscillations with the overall flux normalization fitted as a free parameter. Image taken from [12]

1.6.4 Measuring θ_{13}

With successive measurements of neutrino oscillations a very good knowledge of the neutrino mixing matrix has been achieved. One of the few remaining parameters to be measured was the angle θ_{13}. This angle has recently been measured by various collaborations, two experiments stand out, Daya-Bay by having the first result, as seen above, and T2K for being the first off-axis long baseline neutrino oscillation experiment.

The T2K experiment generates an intense beam of muon neutrinos in the J-PARC synchrotron. This beam travels almost 300 kilometers to Super-Kamiokande which measures the flux of ν_μ and ν_e. This is then compared with measured fluxes by the near detector ND280 located 280 meters from the production point of the beam.

The main feature of T2K is that it is the first off-axis neutrino experiment with two detectors located 2.5 degrees from the center of the beam. The off -axis part of the beam has a narrower range of energies than the on-axis part, that means a larger fraction of neutrinos change flavor by the time they reach Super-K. The most important measurement is the neutrino energy. This measurement is made with high accuracy from events where a neutrino interacts with a neutron to produce a muon and a proton. The off-axis component of the beam has a larger fraction of these events than the on-axis component, which enables T2K to make more precise estimation of neutrino energy. This leads to more accurate measurements of the probability of neutrino oscillations and neutrino mass differences than those from previous experiments.

T2K has recently published [13] the first observation of ν_e appearance in a ν_μ beam with a peak energy of 0.6GeV and a baseline of 295 km. The value obtained for $sin^2 2\theta_{13}$ is $sin^2 2\theta_{13} = 0.140^{+0.038}_{0.032}(0.170^{+0.045}_{0.037})$ with a significance of 7.3σ over the hypothesis of $sin^2 2\theta_{13} = 0$. This result also reduces the possible values of δ_{CP} as some values are disfavored at the 90% CL.

The Daya Bay experiment [14] measured $\overline{\nu_e}$ from the Daya Bay nuclear power complex (six 2.9 GWth reactors) in China with six functionally identical detectors deployed in two near (470 m and 576 m of flux-weighted baselines) and one far (1648 m) underground halls. With live time of 55 days, the ratio of the observed to expected number of $\overline{\nu_e}$ at the far hall is $R = 0.940 \pm 0.011 \pm 0.004$ and the rate-only analysis yielded

$$sin^2\theta_{13} = 0.092 \pm 0.016(stat) \pm 0.005(syst) \tag{1.6}$$

From this result, θ_{13} is non-zero with a significance of 5.2σ

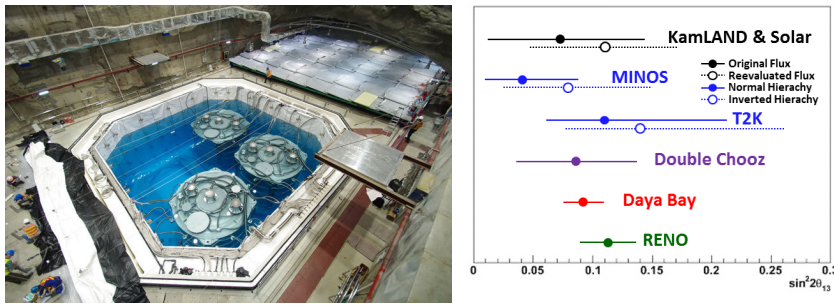

Figure 1.6.4: Left: Daya-Bay experiment. Right: Summary of all non-zero measurements of $sin^2(\theta_{13})$, as of May 2012. Figure adapted from presentation by Y. Nakajima (Daya Bay) [15]

1.7 Measuring neutrino mass

Although the Standard Model assumes that the neutrino masses are zero, the existance of neutrino oscillations prove the contrary. Indeed, the oscillation experiments have managed to measure the differences between neutrino masses, however we can not say anything about its absolute value. To measure the absolute value of the neutrino mass there are three possible options: direct measurement of the mass, double beta experiments and cosmological measurements.

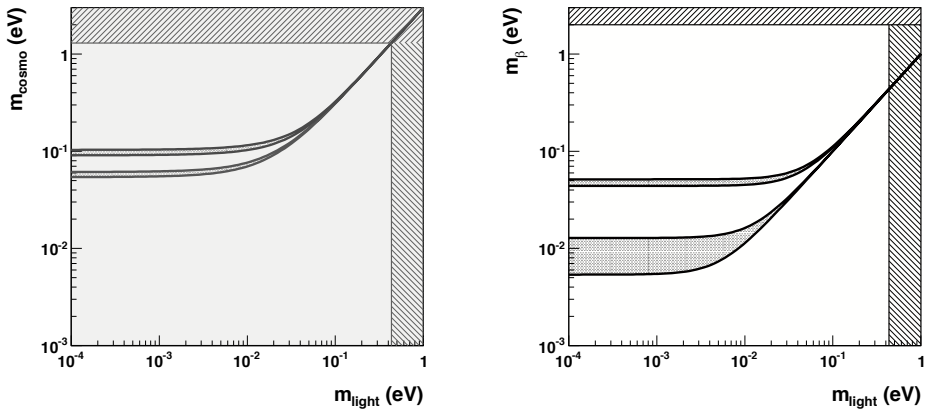

(a) (b)

Figure 1.7.1: Constraints on the lightest neutrino mass m_{light} coming from a) cosmological and b) β decay experiments. The red and green bands correspond to the normal and inverted orderings, respectively. The m_{cosmo} upper bound in panel (a) is from [16], and translates into a m_{light} upper limit shown via the vertical band in the same panel. The cosmological constraint on m_{light} is also shown in panel (b), together with the upper limit on m_β from tritium β decay experiments [9].

1.7.1 Direct mass measurement

The experiments trying to measure the mass directly are spectrometers with excellent energy resolution that attempt to measure the endpoint of the energy spectrum of electrons emitted in beta decay. The difference between this point and the total Q-value of the reaction provides a measurment of the mass of the neutrino. The next generation β-decay experiment is KATRIN [17]. In the presence of flavor mixing, the end-point of the β-decay measures the mass:

$$m_\beta^2 \equiv \sum_{i=1}^{3} |U_{ei}|^2 m_i^2 \tag{1.7}$$

1.7.2 Double beta experiments

Double beta decay is nuclear process where two protons or two neutrons decay simultaneously. The process could have two different modes, with and without neutrinos. The two neutrino mode is allowed as a second order process in the Standard Model. In the other hand, the process without neutrinos (neutrinoless double beta decay) is forbiden in the Standard Model and will imply that neutrinos are Majorana particles. A detailed description of the process is presented in 3.

The rate of the neutrinoless double beta decay process is related to the effective neutrino mass in the process, the so-called majorana mass, and so it is related to the absolute scale of the neutrino mass. Furthermore, experiments would provide information about the mechanism responsible for the neutrino mass (Dirac vs. Majorana). The NEXT experiment, the central theme of this thesis looks for this decay.

1.7.3 Cosmological Limits

Cosmological observations can probe the sum of the three neutrino masses:

$$m_{\text{cosmo}} \equiv \sum_{i=1}^{3} m_i \tag{1.8}$$

Cosmological data is currently compatible with massless neutrinos. Several upper limit values on m_{cosmo} can be found in the literature, depending on the details of the cosmological datasets and of the cosmological model that was used in the analysis. A conservative upper limit on m_{cosmo} of 1.3 eV at 95% confidence level [16] was achieved. Some other authors [18], [19] claim for an absolute measurement of the sum of the neutrino masses using Plank data and comparing the CMB with the lensing data from CFHTLenS. They found a positive result of:

$$\sum m_\nu = (0.320 \pm 0.081) eV \tag{1.9}$$

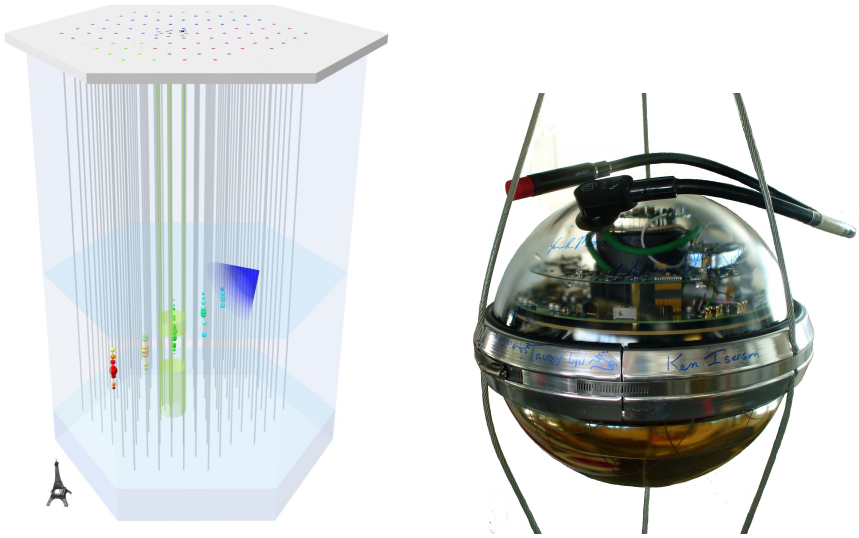

Figure 1.8.1: Scheme of the IceCube detector (left). Detail of one of the optical modules inserted in the antartic ice (right).

1.8 New window on the universe

ICECUBE is an experiment in the South Pole that was built to do astronomy with neutrinos in the ice. The simplest way of thinking about astronomy is that you go out at night, you look at the sky and you see beams of light coming from stars. This is the perfect analogy, IceCube is basically a big eye that looks at the sky and, instead of seeing beams of light, it sees beams of neutrinos.

Why is neutrino astronomy so interesting? Why not use light when it is easier and cheaper? The reason is that we are very likely to see very different things. The main reason is that neutrinos are neutral and very waekly interacting, therefore they point back to the source. In fact the IceCube collaboration have detected the first events of ultra high energy neutrinos and they are trying to figure out what they are seeing. Their first guesses are that they are seeing neutrinos from very powerful cosmic ac-

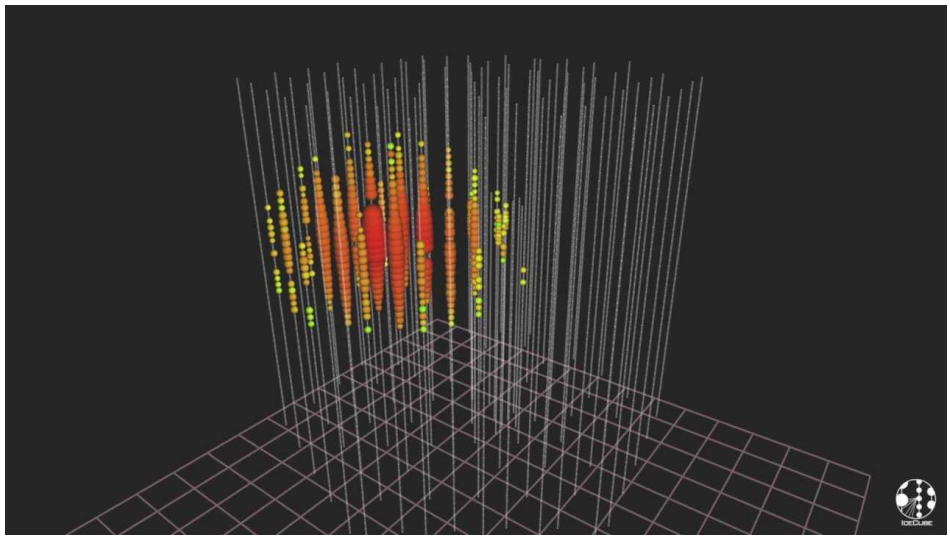

Figure 1.8.2: Visualiztion of "Bert" event in the IceCube detector. Bert has an energy of 1PeV. A few events of similar energies have been detected in the IceCube detector [20]. Those extremely high energy neutrino events help in the understanding the high energy universe.

celerator. Supernova remanents, gamma ray burst, these are the processes that power the very high energy universe..

IceCube is built in ice. The sensors are placed 1.5 to 2.5 kilometers below the surface. The critical number in the design of IceCube is the absorption length of the light in ice. Effectively, IceCube detects the Cerenkov light produced by particles traveling faster than light in ice. To detect that light the distance between sensor should be of the order of the absorption length of the light. One tipically needs to space the light sensors by something that is called the absorption length. In normal water the absorption length is of the order of a few meters, in IceCube, at 2 kilometers deep in the ice the absorption length is more than 100 meters. The ice at South Pole is one of the clearest solids that exist.

IceCube is publishing their first results. Two years ago they were doing an analysis

where they were looking for extremely high energy neutrinos looking for cosmogenic neutrinos. They did not find them, but they found two events (”Bert” and ”Ernie” 1.8.2) of PeV energies, in the lower range of cosmogenic neutrinos.. They started a new analysis optimizing the search for neutrinos in this energy range. Now, ”Bert” and ”Ernie” have other 26 friends. With all those events the collaboration claims they are seeing neutrinos coming from space [21]. The next frontier is to find out where they come from. To solve that question they will need more statistics, At the same time they are working on the next step of the detector, building a even larger detector that will allow for a better understanding of neutrino astronomy.

I'm not strange, weird, off, nor crazy, my reality is just different from yours.

Lewis Carroll, Alice's Adventures in Wonderland.

2

Majorana neutrinos

As shown in chapter 1, neutrino masses are much smaller than the other fermion masses and so it is difficult to accomodate them using the same physics that is used for the others. Moreover, neutrinos are the only chargeless fermions and so the only ones that could be Majorana particles, that is, indistinguishable from their antiparticles. The existence of Majorana neutrinos would have decisive implications in particle physics and cosmology. Majorana neutrinos allow for a simple explanation for their large gap between neutrino masses and the rest of the fermions, at the same time, will prove the existence of physics at a different scale. That is one of the most important open questions in particle physics today due to its implications [22].

Furthermore, the existence of Majorana neutrinos would imply that lepton number is not a conserved quantum number which could be the origin of the matter-antimatter asymmetry observed in the Universe. The new physics related to neutrino

masses could provide a new mechanism to generate the asymmetry, called leptogenesis. Although the predictions are model dependent, two essential ingredients must be confirmed experimentally: 1) the violation of lepton number and 2) CP violation in the lepton sector.

2.1 The origin of neutrino mass: Dirac versus Majorana neutrinos

In the Standard Model, only the negative chirality component Ψ_L of a fermion field $\Psi = \Psi_R + \Psi_L$ is involved in the weak interactions. A negative (positive) chirality field $\Psi_{L(R)}$ is a field that obeys the relations $P_{L(R)}\Psi_{L(R)} = \Psi_{L(R)}$ and $P_{R(L)}\Psi_{L(R)} = 0$, where $P_L = (1 - \gamma_5)/2$ and $P_R = (1 + \gamma_5)/2$ are the positive and negative chiral projection operators.

In the Standard Model neutrinos are massless and only left-handed. For massless neutrinos (see, for example, [22]), only the negative chirality neutrino field ν_L is needed in the theory, regardless of the Dirac/Majorana nature of the neutrino discussed below, since neutrinos only participate in the weak interactions. This field describes *negative helicity* neutrino states $|\nu_L\rangle$ and *positive helicity* antineutrino states[1]. The positive and negative helicity states are eigenstates of the helicity operator $h \equiv \vec{\sigma} \cdot \hat{p}$ with eigenvalues $\pm 1/2$, respectively, where $\vec{\sigma}$ is the neutrino spin and $\hat{p}$ the neutrino momentum direction. The fact that ν_L annihilates particles of negative helicity, and creates antiparticles with positive helicity, is not inconsistent with Lorentz invariance, given that the helicity is the same in any reference frame for a fermion travelling at the speed of light. In the Standard Model with massless neutrinos, positive helicity neutrinos and negative helicity antineutrinos do not exist. As a consequence, and since a negative helicity state transforms into a positive helicity state under the parity transformation, the chiral nature of the weak interaction (differentiating negative

[1] As customarily done, we use the subscript "L" to denote both negative helicity states $|\nu_L\rangle$ and negative chirality fields ν_L, since the terms left-handed helicity states and left-handed chirality fields are also commonly used. Similarly, we denote positive helicity states and positive chirality fields with the subscript "R", as in "right-handed".

from positive chirality) implies that parity is maximally violated in the weak interactions.

For relativistic neutrinos of non-zero mass m, the neutrino field participating in the weak interactions has still negative chirality, ν_L, but there are sub-leading corrections to the particle annihilation/creation rules described above. The state $|\nu_L\rangle$ that is annihilated by the negative chirality field ν_L is now a linear superposition of the $-1/2$ and $+1/2$ helicity states. The $+1/2$ helicity state enters into the superposition with a coefficient $\propto m/E$, where E is the neutrino energy, and is therefore highly suppressed.

Neutrino mass terms can be added to the Standard Model Lagrangian in two ways (see, for example, [23]). The first way is in direct analogy to the Dirac masses of quarks and charged leptons, by adding the positive chirality component ν_R of the Dirac neutrino field, describing predominantly positive helicity neutrino states and predominantly negative helicity antineutrino states that do not participate in the weak interactions: This term that is not $SU(2) \times U(1)$ invariant, but it appears after the spontaneous symmetry breaking of a Yukawa term:

$$-\mathcal{L}_D = m_D(\overline{\nu_L}\nu_R + \overline{\nu_R}\nu_L), \tag{2.1}$$

where $m_D = yv/\sqrt{2} > 0$, y is a dimensionless Yukawa coupling coefficient and $v/\sqrt{2}$ is the vacuum expectation value of the neutral Higgs field after electroweak symmetry breaking. In equation (2.1), ν_L and ν_R are, respectively, the negative and positive chirality components of the neutrino field ν. The chiral spinors ν_L and ν_R have only two independent components each, leading to the four independent components in the Dirac spinor ν. This is different from the case of massless neutrinos, where only the 2-component spinor ν_L was needed.

The second way in which neutrino mass terms can be added to the Standard Model Lagrangian is unique to neutrinos. Majorana first realized [24] that, for neutral particles, one can remove two of the four degrees of freedom in a massive Dirac spinor

by imposing the *Majorana condition*:

$$\nu^c = \nu \tag{2.2}$$

where $\nu^c = C\bar{\nu}^T = C(\gamma^0)^T\nu^*$ is the CP conjugate of the field ν, C is the charge-conjugation operator, and $(\nu_L)^c$ ($(\nu_R)^c$) has positive (negative) chirality. This result can be obtained by decomposing both the left-hand and right-hand sides of eq. (2.2) into their chiral components, yielding:

$$\nu_R = (\nu_L)^c \tag{2.3}$$

and therefore proving that the positive chirality component of the Majorana neutrino field ν_R is not independent of, but obtained from, its negative chirality counterpart ν_L via charge conjugation. By substituting eq. (2.3) into the mass term in eq. (2.1), we obtain a *Majorana mass term*:

$$-\mathcal{L}_L = \frac{1}{2} m_L(\overline{\nu_L}(\nu_L)^c + \overline{(\nu_L)^c}\nu_L) \tag{2.4}$$

where m_L is a free parameter with dimensions of mass.

This Lagrangian mass term also violates $SU(2) \times U(1)$. That term can be generated in many ways, one of the simplest is if there was a higgs triplet that gets a neutral component with a non-vanishing expectation value in vacuum after electroweak symmetry breaking. Equation (2.4) represents a mass term constructed from negative chirality neutrino fields alone, and we therefore call it a *negative chirality Majorana mass term*. If positive chirality fields also exist and are independent of negative chirality ones, this is not the only possibility. In this case, we may also construct a second Majorana mass term, a *positive chirality Majorana mass term*:

$$-\mathcal{L}_R = \frac{1}{2} m_R(\overline{\nu_R}(\nu_R)^c + \overline{(\nu_R)^c}\nu_R) \tag{2.5}$$

In the Standard Model, right-handed fermion fields such as ν_R are weak isosopin

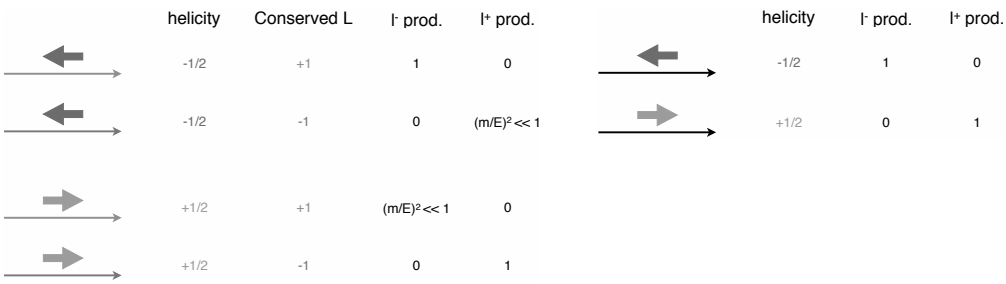

Figure 2.1.1: The difference between Dirac (left) and Majorana (right) massive neutrinos in a scattering experiment. See text for details. Adapted from [25].

singlets. As a consequence, and in contrast with m_D or m_L, the mass parameter m_R is therefore not connected to a Higgs vaccum expectation value, and could be arbitrarily high. All three mass term in eqs. (2.1), (2.4) and (2.5) convert negative chirality states into positive chirality ones [2]. Chirality is therefore not a conserved quantity, regardless of the Dirac/Majorana nature of neutrinos. Furthermore, the Majorana mass terms in eqs. (2.4) and (2.5) convert particles into their own antiparticles. As stated previously, they are therefore forbidden for all electrically charged fermions because of charge conservation. Furthermore, processes involving Majorana mass terms violate the Standard Model total lepton number $L \equiv L_e + L_\mu + L_\tau$ by two units ($|\Delta L| = 2$), which is not a good quantum number anymore.

Which of the mass terms allowed in theory, among $\mathcal{L}_D$, $\mathcal{L}_L$ and $\mathcal{L}_R$ in eqs. (2.1), (2.4) and (2.5) exist in nature? What are the numerical values of the corresponding coupling constants m_D, m_L, m_R? These questions can in principle be answered experimentally. Majorana and Dirac massive neutrinos will in fact have different Standard Model interactions. Let us consider for now an instructive, albeit unrealistic, scattering experiment, see fig. 2.1.1.

In the Dirac case, Standard Model interactions conserve lepton number L, with $L(\nu) = L(l^-) = -L(\bar{\nu}) = -L(l^+) = +1$, where $l^\pm$ indicates charged leptons. Par-

[2] This is because the charge conjugate of a field with a given chirality, such as the ones appearing in eqs. 2.4 and 2.5, always has the opposite chirality.

ticles are then identified as neutrinos or antineutrinos in accordance with the process through which they are produced. Charged-current interactions of Dirac neutrinos (as opposed to antineutrinos) produce only l^- and carry a well-defined lepton number $L = -1$, and viceversa. As shown in fig. 2.1.1, for Dirac neutrinos we would thus have four mass-degenerate states: for each of the two available helicity states[3], two distinct particle/antiparticle states characterized by a different L value would be available. Standard Model interactions of neutrino (as opposed to antineutrino) states of positive helicity would have, however, much weaker l^--producing interactions with matter compared to neutrino states of negative helicity, as indicated by the coefficients in fig. 2.1.1. On the other hand, we have seen that in the Majorana case L is not conserved. We would only have two mass-degenerate states, defined by the two available helicity states, see fig. 2.1.1.

Given these differences between Dirac and Majorana massive neutrinos, can we establish which of the two possibilities is realized in Nature via a scattering experiment? In practice, no. The reason is that l^- production from positive helicity Dirac neutrinos (and l^+ production from negative helicity Dirac antineutrinos) is expected to be highly suppressed in the ultra-relativisitc limit, and cannot be experimentally observed. Experimentally, all we know is that the neutral particle produced in association with a l^+ produces, when interacting, a l^-. In the Dirac case, lepton number conservation is assumed and such neutral particle is identified as the neutrino, with $L = -1$. In the Majorana case, such neutral particle is instead identified as the negative helicity state, interacting differently from its positive helicity counterpart. Both interpretations are viable, and what happens when a neutrino interacts can be understood without invoking a conserved lepton number [26].

[3]As mentioned above, the weak interaction is maximally parity violating, therefore the two helicity states are distinguishable.

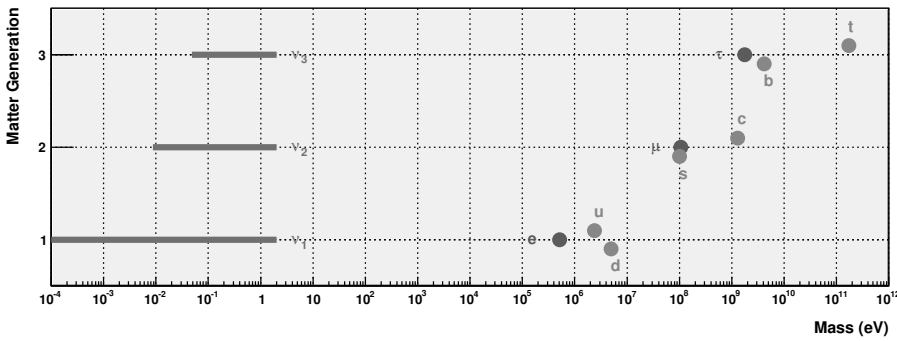

Figure 2.1.2: Hierarchical structure of fermion masses. Only upper bounds for neutrino masses exist. The figure assumes a normal ordering for neutrino masses. Values taken from [9].

2.1.1 The see-saw mechanism

Neutrino masses, although not measured yet, are known to be small, of the order of 1 eV or less, see section 1.7. Such mass values are much smaller than the masses of all other elementary fermions, see fig. 2.1.2. The explanation of neutrino masses via Dirac mass terms alone require neutrino Yukawa couplings of the order of 10^{-12}, about six orders of magnitude smaller than the e^- Yukawa. The current theoretical prejudice is that neutrino Yukawa couplings with $y_\nu \ll 1$ and $y_\nu \ll y_l$ are unnatural, if not unlikely.

The so-called *see-saw mechanism* provides a way to accommodate neutrino masses that is considered more natural. The simplest realization of the see-saw model is to add both a Dirac mass term and a positive chirality mass term to the Lagrangian, as given by eqs. (2.1) and (2.5), respectively, for each of the three neutrino flavors. This is sometimes called the *type I see-saw mechanism*, where we take $m_L = 0$, $m_D \neq 0$,

and $m_R \neq 0$. In this case, the neutrino mass terms can be recast in the matrix form:

$$-\mathcal{L}_{D+R} = \frac{1}{2}\,\overline{(\mathcal{N}_L)^c}\,M\,\mathcal{N}_L + \text{h.c.}\,, \tag{2.6}$$

where the matrix M has the form:

$$M = \begin{pmatrix} 0 & m_D \\ m_D & m_R \end{pmatrix} \tag{2.7}$$

and the negative chirality vector $\mathcal{N}_L$ is:

$$\mathcal{N}_L = \begin{pmatrix} \nu_L \\ (\nu_R)^c \end{pmatrix}\,. \tag{2.8}$$

The chiral fields ν_L and ν_R do not have a definite mass, since they are coupled by the Dirac mass term. In order to find the fields ν_{1L} and N_{1L} with definite masses m_1 and M_1, respectively, it is necessary to diagonalize the mass matrix in equation (2.6). In other words, it is necessary to find a unitary mixing matrix $\mathcal{U}$ such that:

$$\mathcal{U}^T\,M\,\mathcal{U} = \begin{pmatrix} m_1 & 0 \\ 0 & M_1 \end{pmatrix}\,, \tag{2.9}$$

where:

$$\mathcal{N}_L = \mathcal{U}\,n_L\,, \qquad \text{with} \qquad n_L = \begin{pmatrix} \nu_{1L} \\ N_{1L} \end{pmatrix}\,, \tag{2.10}$$

For each neutrino flavor, two fields of definite chirality and definite mass are therefore obtained, and the diagonalized mass terms can be written as:

$$-\mathcal{L}_{D+R} = \frac{1}{2}\left(m_1\,\overline{(\nu_{1L})^c}\,\nu_{1L} + M_1\,\overline{(N_{1L})^c}\,N_{1L}\right) + \text{h.c.}\,, \tag{2.11}$$

Both terms in eq. (2.11) have the same form as the pure negative chirality Majorana mass term in eq. (2.4). In other words, both mass eigenfields ν_{1L} and N_{1L} are

equal to their CP-conjugate fields, and thus both describe Majorana particles. The insertion of a Dirac mass term and a positive chirality Majorana mass term in the Lagrangian for massive neutrinos has resulted in Majorana particles.

Since the positive chirality fields are electroweak singlets in the Standard Model, the Majorana mass of the neutrino described by such field, m_R, may be orders of magnitude larger than the electroweak scale. In the so-called *see-saw limit*, we assume that neutrino Yukawa couplings are of the order of the charged fermion couplings, and that $m_R \gg m_D$ is of the order of some high mass scale where new physics responsible for neutrino masses is supposed to reside. In this approximation, the see-saw mechanism naturally yields a small mass eigenvalue $m_1 \simeq m_D^2/m_R \ll m_D$ for a predominantly negative helicity neutrino mass state, and a large mass eigenvalue $M_1 \simeq m_R$ for a predominantly positive helicity (and therefore sterile) neutrino mass state. A very heavy N_1 corresponds to a very light ν_1 and viceversa, as in a see-saw.

The see-saw mechanism presented above can easily be generalized from the one-family case that we discussed to three neutrino species, yielding the three light neutrinos ν_i we are familiar with, and three heavy neutrinos N_i, with $i = 1, 2, 3$ [23]. In this case, the neutrino mass matrix in equation 2.6 is a 6×6 mass matrix of the form:

$$M = \begin{pmatrix} 0 & (M^D)^T \\ M^D & M^R \end{pmatrix} . \tag{2.12}$$

where M^D and M^R are now 3×3 complex matrices, and the 6-component vector of negative chirality fields has the form:

$$N_L = \begin{pmatrix} \nu_L \\ (\nu_R)^c \end{pmatrix} , \qquad \text{with} \qquad \nu_L = \begin{pmatrix} \nu_{eL} \\ \nu_{\mu L} \\ \nu_{\tau L} \end{pmatrix} \qquad \text{and} \qquad (\nu_R)^c = \begin{pmatrix} (\nu_{s_1 R})^c \\ (\nu_{s_2 R})^c \\ (\nu_{s_3 R})^c \end{pmatrix} , \tag{2.13}$$

In equation 2.13, the subscripts $e,\ \mu,\ \tau$ label the active neutrino flavors, while the subscripts $s_1,\ s_2,\ s_3$ indicate sterile states that do not participate in the weak interactions. The mass matrix is diagonalized via a 6×6 mixing matrix $\mathcal{V}$ analogous to $\mathcal{U}$ in

equation 2.9, where the three negative chirality fields and the three positive chirality fields are now expressed in terms of the negative chirality components of 6 massive neutrino fields $v_{iL},\ i = 1, \ldots, 6$. In the see-saw limit where the eigenvalues of M^R are much larger than those of M^D, the 6×6 mass matrix in equation 2.12 can be written in block-diagonal form $M \simeq \mathrm{diag}(M_{\mathrm{light}}, M_{\mathrm{heavy}})$, where the two 3×3 mass matrices of the light and heavy neutrino sectors are practically decoupled, and given by $M_{\mathrm{light}} \simeq -(M^D)^T (M^R)^{-1} M^D$ and $M_{\mathrm{heavy}} \simeq M^R$, respectively.

For the low-energy phenomenology, it is sufficient to consider only M_{light}, sometimes called the *neutrino mass matrix* m_ν, that is the 3×3 matrix in the flavor basis which is diagonalized by the matrix U:

$$U^T M_{\mathrm{light}} U = \mathrm{diag}(m_1, m_2, m_3) \ , \tag{2.14}$$

where the *neutrino mixing matrix* U appearing in equation 2.14 is the same matrix defined in equation 1.1 up to corrections of $\mathrm{O}(\frac{m_{ligh}}{M_{heavy}})$, and $m_1,\ m_2,\ m_3$ are three light neutrino mass eigenvalues .

An important assumption in the simplest realization of the see-saw mechanism described above is that $m_L = 0$. This assumption is not arbitrary, and directly follows from enforcing the gauge symmetries of the Standard Model, see for example [23]. In models with a left-right symmetric particle content, this type I see-saw mechanism is often generalized to a *type II see-saw*, where an additional direct mass term m_L for the light neutrinos is present, because the scalar sector is extended by Higgs triplet.

2.1.2 Leptogenesis

One of the direct implications of a Majorana mass is the possibility of producing the baryon asymmetry of the universe via the leptogenesis scenario [27]. If neutrinos are Majorana particles, the decays of the heavy Majorana neutrinos into leptons l_a plus Higgs particles φ in the early Universe provides an ideal scenario for leptogenesis. Heavy Majorana neutrinos are their own anti-particles, so they can decay to both $l_a\varphi$ and $\bar{l_a}\bar{\varphi}$ final states. If there is an asymmetry in the two decay rates, a net lepton

asymmetry will be produced. Finally, this lepton asymmetry can be efficiently converted into a baryon asymmetry via the so-called *sphaleron processes* (see [28], [29] for details).

In more detail, for leptogenesis to occur, three conditions must be met. These conditions directly follow from the ingredients that are required to dynamically generate a baryon asymmetry (*Sakharov's conditions* [30]):

1. Presence of lepton number violating processes resulting in baryon number violation;
2. Beyond-SM sources of CP violation [4];
3. Departure from thermal equilibrium.

The decay of heavy Majorana neutrinos can provide all of these conditions, namely

1. Total lepton number is violated in these decays;
2. CP can be violated in these decays, provided that there is more than one heavy Majorana field;
3. Departure from thermal equilibrium is obtained if the decay rate is slower than the expansion rate of the Universe at the time of decoupling, occurring for $T \sim M_1$, where T is the temperature of the Universe's thermal bath, and M_1 is the mass of the lightest among the three heavy neutrinos.

In order to be fully successful, any theory of leptogenesis must be able to explain the magnitude of baryon asymmetry that is inferred from BBN and CMB observations:

$$\eta \equiv \frac{n_B - n_{\bar{B}}}{n_\gamma} = 273.9 \cdot 10^{-10} \Omega_b h^2 = (6.19 \pm 0.15) 10^{-10} \qquad (2.15)$$

where n_B, $n_{\bar{B}}$, n_γ are the number densities of baryons, antibaryons and photons, $\Omega_b = (0.0458 \pm 0.0016)$ is the fraction of the critical energy density carried by

[4] CP violation is allowed by the Standard Model and has been measured; however, the magnitude of such CP-violating effects is far too small to provide the necessary amount of leptogenesis.

baryons, and $h \equiv H_0/100 \text{ km} \cdot \text{s}^{-1} \cdot \text{Mpc}^{-1} = (0.742 \pm 0.036)$ is the Hubble parameter, where H_0 is the Hubble constant today.

Leptogenesis via heavy Majorana neutrino decays is in principle able to do this. In this case, the asymmetry in lepton flavour a produced in the decay of N_1, defined as:

$$\varepsilon_{aa} \equiv \frac{\Gamma(N_1 \to \varphi l_a) - \Gamma(N_1 \to \bar{\varphi}\bar{l}_a)}{\Gamma(N_1 \to \varphi l) + \Gamma(N_1 \to \bar{\varphi}\bar{l})} \tag{2.16}$$

should be of order $|\varepsilon_{aa}| > 10^{-7}$ [29], where the factors Γ in eq. (2.16) stand for the decay rates into the corresponding N_1 decay final states. It is at present unclear whether there is a direct connection between the high-energy CP-violating processes responsible for the asymmetry in the early Universe of eq. (2.16), and the low-energy CP-violating processes that may potentially affect laboratory-based experiments. In most models ther is no direct connection. Nonetheless, the discovery of CP violation in the lepton sector via neutrino oscillations on the one hand, and the discovery of the Majorana nature of neutrinos via neutrinoless double beta decay on the other, would undoubtedly strengthen the case for leptogenesis as a source of the baryon asymmetry of the Universe.

2.2 Lepton number violating processes

We have seen that Majorana mass terms induce lepton number violating processes of the type $|\Delta L| = 2$. The heavy neutrino decay needed for leptogenesis, discussed in section 2.1.2, requires Majorana mass terms and is therefore an example of a lepton number violating process. However, heavy neutrino decay is unobservable in a laboratory-based experiment, given the tremendous energies needed for heavy neutrino production. A number of more promising lepton number violating processes have been proposed to probe the Majorana nature of neutrinos. The best known example is $\beta\beta 0\nu$, introduced in chapter 3. We anticipate that $\beta\beta 0\nu$ is considered the most promising probe of the Majorana nature of neutrinos. However, and because of neutrino mixing, the phenomenology associated with $|\Delta L| = 2$ processes is very

rich. The basic process with $|\Delta L| = 2$ is mediated by [31]:

$$W^- W^- \to l_\alpha^- l_\beta^- \tag{2.17}$$

and we can categorize such processes according to the lepton flavors (α, β) involved. Assuming no lepton flavor violating contributions other than light Majorana neutrino exchange, the matrix element for the generic $|\Delta L| = 2$ process in eq. (2.17) is proportional to the element (α, β) of the *neutrino mass matrix*:

$$(m_\nu)_{\alpha\beta} \equiv \left(U^* \mathrm{diag}(m_1, m_2, m_3) U^\dagger\right)_{\alpha\beta} = \sum_{i=1}^{3} U_{\alpha i}^* U_{\beta i}^* m_i \tag{2.18}$$

where $m_\nu = M^{\mathrm{light}}$ is the matrix appearing in equation 2.14, $U_{\alpha i}$ are the elements of the 3×3 neutrino mixing matrix appearing in equation 1.1, and m_i are the three light neutrino masses. In a sense, this effective neutrino mass definition provides a metric to compare the sensitivity of various $|\Delta L| = 2$ processes. The processes with the most competitive constraints on $|\Delta L| = 2$ processes involving the flavors (α, β) are reported in table 2.2.1.

As it is apparent in table 2.2.1, indeed the constraint on the effective Majorana mass m_{ee} coming from $\beta\beta0\nu$ searches outperforms by several orders of magnitude other searches involving a different flavor combination (α, β). The most important reason behind this is of statistical nature. While it is possible to amass macroscopic quantities of a $\beta\beta$ emitter to study $\beta\beta0\nu$ decay (as we will see, even a ton of isotope is in the cards for several experiments), this is not the case for the other experimental techniques listed in table 2.2.1. Nevertheless, it is important to keep exploring lepton flavor violating processes other than $\beta\beta0\nu$İt is in principle possible that phase cancellations are such that $m_{ee} \ll m_{\alpha\beta}$ with $(\alpha, \beta) \neq (e, e)$, making the search for $\beta\beta0\nu$ much less favourable than others because of Nature's choice of neutrino masses and mixings. Furthermore, this effort may possibly lead to the identification of an even more promising experimental probe of lepton flavor violation in the future.

Table 2.2.1: Current bounds on effective neutrino masses from total lepton number violating processes, organized according to the flavors involved. Numbers taken (or derived) from [9, 31].

Flavors	Exp. technique	Exp. bound	Mass bound (eV)
(e,e)	$\beta\beta 0\nu$	$T_{1/2}(^{76}\mathrm{Ge} \to {}^{76}\mathrm{Se} + 2e^-) > 1.9 \times 10^{25}$ yr	$\lvert m_{ee}\rvert < 3.6 \times 10^{-1}$
(e,μ)	$\mu^- \to e^+$ conversion	$\Gamma(\mathrm{Ti} + \mu^- \to e^+ + \mathrm{Ca}_{\mathrm{gs}}) \,/$ $\Gamma(\mathrm{Ti} + \mu^-\mathrm{capture}) < 1.7 \times 10^{-12}$	$\lvert m_{e\mu}\rvert < 1.7 \times 10^{7}$
(e,τ)	Rare τ decays	$\Gamma(\tau^- \to e^+\pi^-\pi^-)/\Gamma_{\mathrm{tot}} < 8.8 \times 10^{-8}$	$\lvert m_{e\tau}\rvert < 2.6 \times 10^{12}$
(μ,μ)	Rare kaon decays	$\Gamma(K^+ \to \pi^-\mu^+\mu^+)/\Gamma_{\mathrm{tot}} < 1.1 \times 10^{-9}$	$\lvert m_{\mu\mu}\rvert < 2.9 \times 10^{8}$
(μ,τ)	Rare τ decays	$\Gamma(\tau^- \to \mu^+\pi^-\pi^-)/\Gamma_{\mathrm{tot}} < 3.7 \times 10^{-8}$	$\lvert m_{e\tau}\rvert < 2.1 \times 10^{12}$
(τ,τ)	none	none	none

Unless you expect the unexpected you will never find it, for it is hard to discover and hard to attain.

Heraclitus

3

Neutrinoless double beta decay

Double beta decay is a rare nuclear transition in which a nucleus with Z protons decays into a nucleus with $Z + 2$ protons and the same mass number A. The decay can occur only if the initial nucleus is less bound than the final nucleus, and both more than the intermediate one, as shown in figure 3.0.1. Such a condition is fulfilled by 35 nuclides in nature because of the nuclear pairing force, ensuring that nuclei with even Z and N are more bound than the odd-odd nuclei with the same $A = Z + N$.

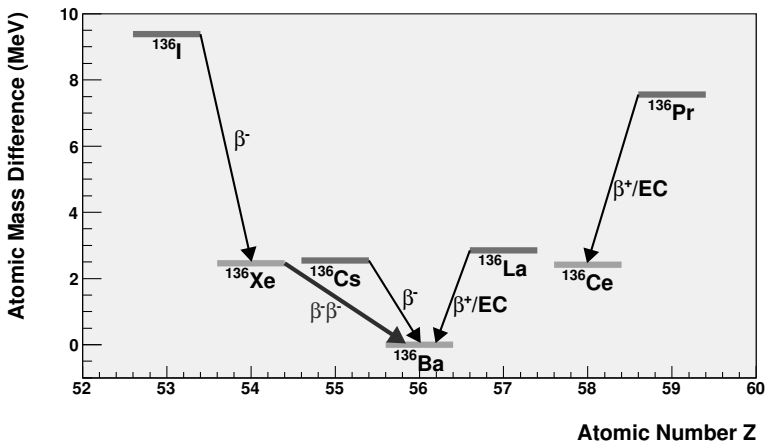

Figure 3.0.1: Atomic masses of $A = 136$ isotopes. Masses are given as differences with respect to the most bound isotope, ^{136}Ba. The red (green) levels indicate odd-odd (even-even) nuclei. The arrows β^-, β^+, $\beta^-\beta^-$ indicate nuclear decays accompanied by electron, positron and double electron emission, respectively. The arrows EC indicate electron capture transitions.

3.1 Double beta decay modes

The standard decay mode ($\beta\beta 2\nu$), consisting in two simultaneous beta decays,

$$(Z, A) \rightarrow (Z + 2, A) + 2\, e^- + 2\, \overline{\nu}_e, \tag{3.1}$$

was first considered by Maria Goeppert-Mayer in 1935 [32]. Total lepton number is conserved in this mode, and the process is allowed in the Standard Model of particle physics. This process was first detected in 1950 using geochemical techniques [33]. The first direct observation of $\beta\beta 2\nu$ events, in ^{82}Se and using a time projection chamber, did not happen until 1987 [34]. Since then, it has been repeatedly observed in several nuclides, such as ^{76}Ge, ^{100}Mo or ^{150}Nd. Typical lifetimes are of the order of 10^{18}–10^{20} years, the longest ever observed among radioactive decay processes. For a list of $\beta\beta 2\nu$ half-lives measured in several isotopes, see table 3.1.1 [35]. The longest

Table 3.1.1: Current best direct measurements of the half-life of $\beta\beta 2\nu$ processes. The values reported are taken from the averaging procedure described in [35].

Isotope	$T^{2\nu}_{1/2}$ (year)	Experiments
^{48}Ca	$(4.4^{+0.6}_{-0.5}) \times 10^{19}$	Irvine TPC [40], TGV [41], NEMO3 [42]
^{76}Ge	$(1.5 \pm 0.1) \times 10^{21}$	PNL-USC-ITEP-YPI [43], IGEX [44], H-M [45]
^{82}Se	$(0.92 \pm 0.07) \times 10^{20}$	NEMO3 [46], Irvine TPC [47], NEMO2 [48]
^{96}Zr	$(2.3 \pm 0.2) \times 10^{19}$	NEMO2 [49], NEMO3 [50]
^{100}Mo	$(7.1 \pm 0.4) \times 10^{18}$	NEMO3 [46], NEMO-2 [51], Irvine TPC [52]
^{116}Cd	$(2.8 \pm 0.2) \times 10^{19}$	NEMO3 [42], ELEGANT [53], Solotvina [54], NEMO2 [55]
^{130}Te	$(6.8^{+1.2}_{-1.1}) \times 10^{20}$	CUORICINO [56], NEMO3 [57]
^{136}Xe	$(2.11 \pm 0.21) \times 10^{21}$	EXO-200 [36]
^{150}Nd	$(8.2 \pm 0.9) \times 10^{18}$	Irvine TPC [52], NEMO3 [58]

half-life in tab. 3.1.1 is the one for ^{136}Xe, which has been measured for the first time only in 2011 [36][1].

[1] The 10% accuracy in the ^{136}Xe $\beta\beta 2\nu$ decay measured half-life in [36] should be contrasted with a spread of more than one order of magnitude in the corresponding theoretical expectations from several nuclear structure calculations [37–39].

The neutrinoless mode ($\beta\beta 0\nu$),

$$(Z, A) \rightarrow (Z + 2, A) + 2\, e^{-}, \tag{3.2}$$

was first proposed by W. H. Furry in 1939 [59] as a method to test Majorana's theory [24] applied to neutrinos. In contrast to the two-neutrino mode, the neutrinoless mode violates total lepton number conservation and is therefore forbidden in the Standard Model. Its existence is linked to that of Majorana neutrinos (see section 3.2). No convincing experimental evidence of the decay exists to date (see section 3.5).

The two modes of the $\beta\beta$ decay have some common and some distinct features [60]. The common features are:

- The leptons carry essentially all the available energy, and the nuclear recoil is negligible;
- the transition involves the 0^+ ground state of the initial nucleus and, in almost all cases, the 0^+ ground state of the final nucleus. For some isotopes, it is energetically possible to have a transition to an excited 0^+ or 2^+ final state[2], even though they are suppressed because of the smaller phase space available;
- both processes are second-order weak processes, *i.e.* their rate is proportional to G_F^4, where G_F is the Fermi constant. They are therefore inherently slow. Phase space considerations alone would give preference to the $\beta\beta 0\nu$ mode which is, however, forbidden by total lepton number conservation.

The distinct features are:

- In the $\beta\beta 2\nu$ mode the two neutrons undergoing the transition are uncorrelated (but decay simultaneously), while in the $\beta\beta 0\nu$ mode the two neutrons are correlated;

[2] The transition to an excited 0^+ final state has been observed for both ^{100}Mo [61–63] and ^{150}Nd [64].

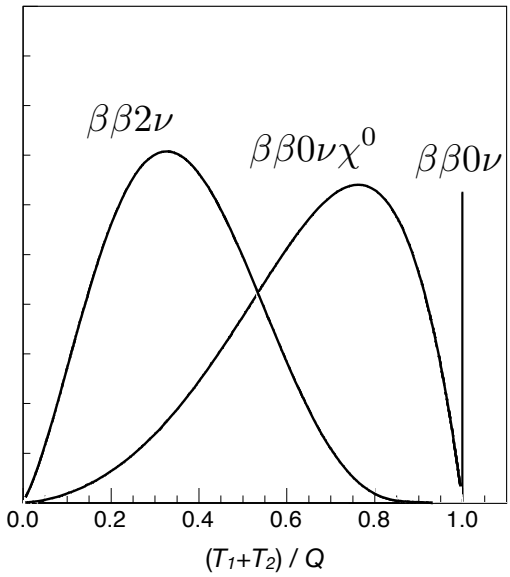

Figure 3.1.1: Spectra for the sum kinetic energy $T_1 + T_2$ of the two electrons, for different $\beta\beta$ modes: $\beta\beta 2\nu$, $\beta\beta 0\nu$, and $\beta\beta$ decay with Majoron emission.

- in the $\beta\beta 2\nu$ mode, the sum electron kinetic energy $T_1 + T_2$ spectrum is continuous and peaked below $Q_{\beta\beta}/2$, where $Q_{\beta\beta}$ is the Q-value of the reaction. In the $\beta\beta 0\nu$ mode, since no light particles other than the electrons are emitted and given that nuclear recoil is negligible, the $T_1 + T_2$ spectrum is a monoenergetic line at $Q_{\beta\beta}$, smeared only by the detector resolution. This is illustrated in fig. 3.1.1.

In addition to the the two basic decay modes described above, several decay modes involving the emission of a light neutral boson, the Majoron (χ^0), have been proposed in extensions of the Standard Model, see section 3.4.

While in the following we will focus on $\beta\beta 0\nu$ as defined in equation 3.2, there are

three closely related lepton number violating processes that can be investigated:

$$\beta^+\beta^+0\nu: \quad (Z,A) \to (Z-2,A) + 2\,e^+ \tag{3.3}$$

$$\beta^+\mathrm{EC}0\nu: \quad e^- + (Z,A) \to (Z-2,A) + e^+ \tag{3.4}$$

$$\mathrm{ECEC}0\nu: \quad 2\,e^- + (Z,A) \to (Z-2,A)^* \tag{3.5}$$

Such processes are called *double positron emission*, *single positron emission plus single electron capture* (EC), and *double electron capture*, respectively. All three involve transitions where the nuclear charge decreases (as opposed to increasing, as in $\beta\beta0\nu$) by two units. From the the theoretical point of view, the physics probed by $\beta^+\beta^+0\nu$, $\beta^+\mathrm{EC}0\nu$ and $\mathrm{ECEC}0\nu$ is identical to the one probed by $\beta\beta0\nu$. From the experimental point of view, however, $\beta^+\beta^+0\nu$ and $\beta^+\mathrm{EC}0\nu$ are less favorable than $\beta\beta0\nu$ because of the smaller phase space available. On the other hand, the process $\mathrm{ECEC}0\nu$ is gaining some attention recently as a promising (but still much less developed) alternative to $\beta\beta0\nu$, since a resonant enhancement of its rate can in principle occur [65].

In the following, the neutrinoless mode $\beta\beta0\nu$ is discussed in more detail, from both the theoretical and experimental point of view.

3.2 The black box theorem

In general, in theories beyond the Standard Model there may be several sources of total lepton number violation which can lead to $\beta\beta0\nu$. Nevertheless, as was first pointed out in reference [66], irrespective of the mechanism, $\beta\beta0\nu$ necessarily implies Majorana neutrinos. This is called the *black box* (or Schechter-Valle) theorem. The reason is that any $\Delta L \neq 0$ diagram contributing to the decay would also contribute to the (e,e) entry of the Majorana neutrino mass matrix, $(m_\nu)_{ee}$. This is shown in fig. 3.2.1, where a $\bar{\nu}_e - \nu_e$ transition, that is a non-zero $(m_\nu)_{ee}$, is induced as a consequence of any $\Delta L \neq 0$ operator responsible for $\beta\beta0\nu$.

From a quantitative point of view, however, the diagram in fig. 3.2.1 corresponds to a tiny mass generated at the four-loop level, and is far too small to explain the neutrino

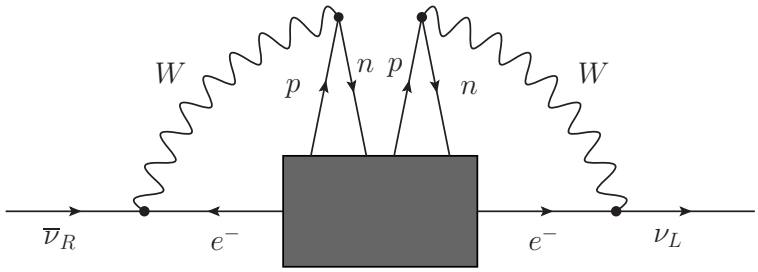

Figure 3.2.1: Diagram showing how any neutrinoless double beta decay process induces a $\bar{\nu}$-to-ν transition, that is, an effective Majorana mass term. This is the so-called *black box theorem* [66].

mass splitting observed in neutrino oscillation experiments [67]. Other, unknown, Majorana and/or Dirac mass contributions must exist. As a consequence, therefore, the black box theorem says nothing about the physics mechanism dominating a $\beta\beta0\nu$ rate that is large enough to be observable. The dominant mechanism leading to $\beta\beta0\nu$ could then either be directly connected to neutrino oscillations phenomenology, or only indirectly connected or not connected at all to it [68]. The former case is realized in the standard $\beta\beta0\nu$ mechanism of light neutrino exchange, discussed in section 3.3. The latter case involves alternative $\beta\beta0\nu$ mechanisms, briefly outlined in section 3.4.

3.3 The standard $\beta\beta0\nu$ mechanism: light Majorana neutrino exchange

Neutrinoless double beta decay can arise from a diagram (figure 3.3.1) in which the parent nucleus emits a pair of virtual W bosons, and then these W exchange a Majorana neutrino to produce the outgoing electrons. The rate is non-zero only for massive, Majorana neutrinos. The reason is that the exchanged neutrino in fig. 3.3.1 can be seen as emitted (in association with an electron) with almost total positive helicity. Only its small, $\mathcal{O}(m/E)$, negative helicity component is absorbed at the other vertex by the Standard Model electroweak current. Considering that the amplitude is

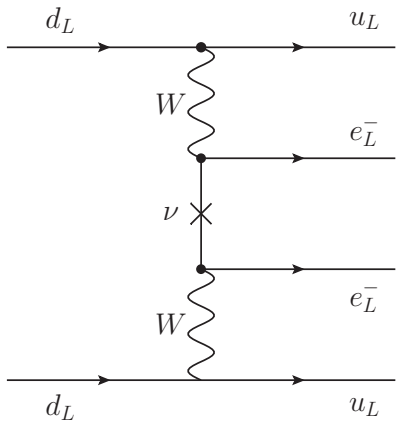

Figure 3.3.1: The standard mechanism for $\beta\beta 0\nu$ decay, based on light Majorana neutrino exchange.

in this case a sum over the contributions of the three light neutrino mass states ν_i, and that is also proportional to U_{ei}^2, we conclude that the modulus of the amplitude for the $\beta\beta 0\nu$ process must be proportional in this case to the *effective neutrino Majorana mass*:

$$m_{\beta\beta} \equiv \left| \sum_{i=1}^{3} m_i U_{ei}^2 \right| \tag{3.6}$$

In other words, the effective neutrino Majorana mass corresponds to the modulus of the (e, e) element of the neutrino mass matrix of equation 2.18, $m_{\beta\beta} \equiv |\,(m_\nu)_{ee}\,|$.

In the case where light Majorana neutrino exchange is the dominant contribution to $\beta\beta 0\nu$, it means that the neutrinos contributing to the process have masses lower than $\sqrt{Q} \sim 100 MeV$ because otherwise the neutrino propagator cannot be approximated by $\frac{m_\nu}{p^2}$. With that consideration, the inverse of the half-life for the process can be written as [69]:

$$\frac{1}{T_{1/2}^{0\nu}} = G^{0\nu}(Q, Z)\, |M^{0\nu}|^2\, m_{\beta\beta}^2, \tag{3.7}$$

where $G_{0\nu}(Q_{\beta\beta}, Z)$ is a phase space factor that depends on the transition Q-value

and on the nuclear charge Z, and $M^{0\nu}$ is the nuclear matrix element (NME). The phase space factor can be calculated analytically, in principle with reasonable accuracy[3]. The NME is evaluated using nuclear models, although with considerable uncertainty. In other words, the value of the effective neutrino Majorana mass $m_{\beta\beta}$ in equation (3.6) can be inferred from a non-zero $\beta\beta0\nu$ rate measurement, albeit with some nuclear physics uncertainties. Conversely, if a given experiment does not observe the $\beta\beta0\nu$ process, the result can be interpreted in terms of an upper bound on $m_{\beta\beta}$.

If light Majorana neutrino exchange is the dominant mechanism for $\beta\beta0\nu$, it is clear from eq. (3.6) that $\beta\beta0\nu$ is in this case directly connected to neutrino oscillations phenomenology, and that it also provides direct information on the absolute neutrino mass scale, as cosmology and β decay experiments do (see section 1.7). The relationship between $m_{\beta\beta}$ and the actual neutrino masses m_i is affected by:

1. the uncertainties in the measured oscillation parameters;
2. the unknown neutrino mass ordering (normal or inverted);
3. the unknown phases in the neutrino mixing matrix (both Dirac and Majorana).
4. extra neutrino physics, for example extra neutrinos states in type I seesaw models.

For example, the relationship between $m_{\beta\beta}$ and the lightest neutrino mass m_{light} (which is equal to m_1 or m_3 in the normal and inverted mass ordering cases, respectively) is illustrated in figure 3.3.2. This graphical representation was first proposed in [70]. The width of the two bands is due to items 1 and 3 above, where the uncertainties in the measured oscillation parameters (item 1) are taken as 3σ ranges from a recent global oscillation fit [71]. Figure 3.3.2 also shows an upper bound on m_{light}

[3] An accurate description of the effect of the nuclear Coulomb field on the decay electron wavefunctions is, however, required.

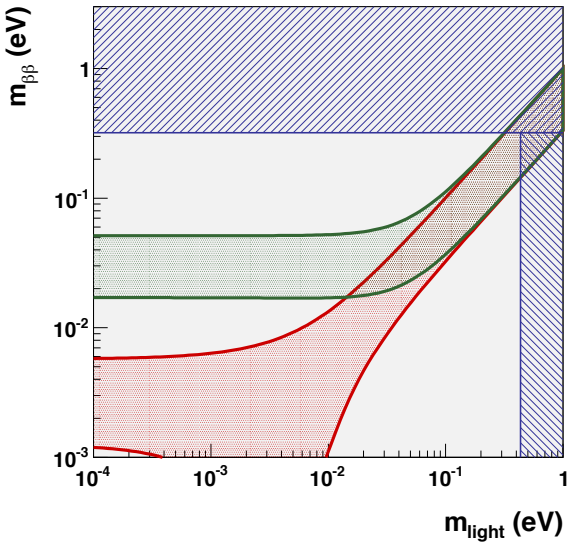

Figure 3.3.2: The effective neutrino Majorana mass $m_{\beta\beta}$ as a function of the lightest neutrino mass, m_{light}. The red (green) band corresponds to the normal (inverted) ordering, respectively, in which case m_{light} is equal to m_1 (m_3). The vertically-excluded region comes from cosmological bounds, the horizontally-excluded one from $\beta\beta0\nu$ constraints.

from cosmology ($m_{\text{light}} < 0.43$ eV), also shown in fig. 1.7.1, and an upper bound on $m_{\beta\beta}$ from current $\beta\beta0\nu$ data ($m_{\beta\beta} < 0.32$ eV), which we will discuss in sec. 3.5. As can be seen from fig. 3.3.2, current $\beta\beta0\nu$ data provide a constraint on the absolute mass scale m_{light} that is almost as competitive as the cosmological one.

In figs. 1.7.1 and 3.3.2, we have shown only upper bounds on various neutrino mass combinations, coming from current data. The detection of positive results for absolute neutrino mass scale observables would open up the possibility to further explore neutrino properties and lepton number violating processes. We give three examples in the following. First, the successful determination of both m_β in eq. (1.7) and $m_{\beta\beta}$ in eq. (3.6) via β and $\beta\beta0\nu$ decay experiments, respectively, can in principle be used to determine or constrain the phases a_i [72]. Second, measurements of m_β or m_{cosmo}

in eq. (1.8) may yield a constraint on m_{light} that is inconsistent with a $m_{\beta\beta}$ upper limit. In this case, the non-observation of $\beta\beta0\nu$ would not imply that neutrinos are Dirac particles. Third, measurements of m_β or m_{cosmo} may yield a constraint on m_{light} that is inconsistent with a measured non-zero $m_{\beta\beta}$. This scenario would demonstrate that additional lepton number violating physics, other than light Majorana neutrino exchange, is at play in the $\beta\beta0\nu$ process. We briefly describe some of these possible $\beta\beta0\nu$ alternative mechanisms in the following.

3.4 Alternative $\beta\beta0\nu$ mechanisms

A number of alternative $\beta\beta0\nu$ mechanisms have been proposed. For an excellent and complete discussion of those, we refer the reader to [68]. The realization of $\beta\beta0\nu$ can differ from the standard mechanism in one or several aspects:

- The Lorentz structure of the currents. Positive chirality currents mediated by a W_R boson can arise, for example, in left-right symmetric theories. A possible diagram involving positive chirality current interactions of heavy Majorana neutrinos N_i is shown in fig. 3.4.1(a).

- The mass scale of the exchanged virtual particles. One example would be the presence of "sterile" (that is, described by positive chirality fields) neutrinos, either light or heavy, in the neutrino propagator of fig. 3.3.1, in addition to the three light, active, neutrinos we are familiar with. Another example would be the exchange of heavy supersymmetric particles, as in fig. 3.4.1(b).

- The number of particles in the final state. A popular example involves decay modes where additional Majorons, that is very light or massless particles which can couple to neutrinos, are produced in association with the two electrons (see fig. 3.4.1(c)).

In non-standard $\beta\beta0\nu$ mechanisms, the scale of the lepton number violating physics is often larger than the momentum transfer, in which case one speaks of *short-range*

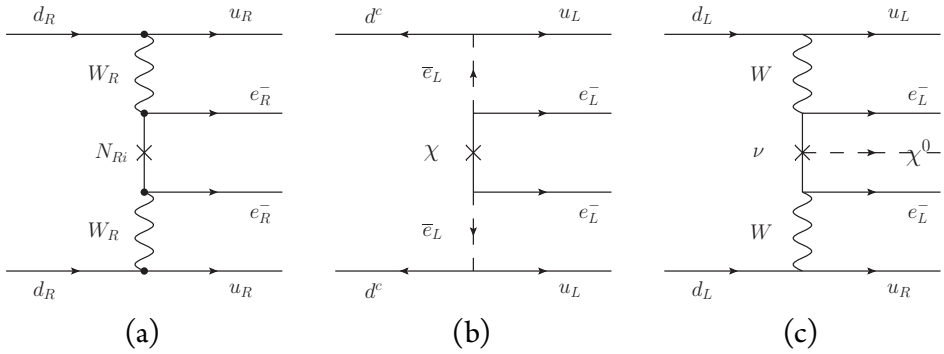

Figure 3.4.1: Examples of non-standard mechanism for $\beta\beta 0\nu$: (a) heavy neutrino exchange with positive chirality currents [73]; (b) neutralino exchange in R-parity violating supersymmetry [74]; (c) Majoron emission [75].

processes. This is in contrast to the standard $\beta\beta 0\nu$ mechanism of light Majorana neutrino exchange, in which case the neutrino is very light compared to the energy scale, resulting in a *long-range* process. Non-standard and long-range $\beta\beta 0\nu$ processes are, however, also possible.

In general, several contributions to the total $\beta\beta 0\nu$ amplitude can add coherently, allowing for interference effects. Neutrinoless double beta decay observables alone may be able to identify the dominant mechanism responsible for $\beta\beta 0\nu$. We give two examples. First, if Majorons are also emitted in association with the two electrons, energy conservation alone requires the electron kinetic energy sum $T_1 + T_2$ to be a continuous spectrum with $Q_{\beta\beta}$ as endpoint. This spectrum is potentially distinguishable from the $\beta\beta 2\nu$ one (see fig. 3.1.1), provided that the Majoron-neutrino coupling constant is large enough. Second, if positive chirality current contributions dominate the $\beta\beta 0\nu$ rate, electrons will be emitted predominantly as positive helicity states. As a consequence, both the energy and angular correlation of the two emitted electrons will be different from the ones of the standard $\beta\beta 0\nu$ mechanism. A detector capable of reconstructing individual electron tracks may therefore be able to distinguish this

Isotope	$T^{0\nu}_{1/2}$ (years)	Experiment
^{48}Ca	$> 5.8 \times 10^{22}$	ELEGANT [77]
^{76}Ge	$> 1.9 \times 10^{25}$	Heidelberg-Moscow [78]
^{82}Se	$> 3.6 \times 10^{23}$	NEMO3 [79]
^{96}Zr	$> 9.2 \times 10^{21}$	NEMO3 [50]
^{100}Mo	$> 1.1 \times 10^{24}$	NEMO3 [79]
^{116}Cd	$> 1.7 \times 10^{23}$	Solotvina [54]
^{130}Te	$> 2.8 \times 10^{24}$	CUORICINO [80]
^{136}Xe	$> 4.4 \times 10^{23}$	GOTTHARD [81]
^{150}Nd	$> 1.8 \times 10^{22}$	NEMO3 [58]

Table 3.5.1: Limits on the half-life of $\beta\beta0\nu$ processes for the most interesting isotopes until 2012. All values are at 90% CL. Results of the most recent experiments are shown in the following chapter.

type of non-standard $\beta\beta0\nu$ mechanism from light Majorana neutrino exchange (see, for example, [76]).

3.5 Existing experimental results

Neutrinoless double beta decay searches have been carried out over more than half a century, exploiting the same experimental techniques used for measuring the two-neutrino mode rate. Several $\beta\beta$ emitting isotopes have been investigated, as shown in table 3.5.1.

The most sensitive limit to date was set by the Heidelberg-Moscow (HM) experiment [78]: $T^{0\nu}_{1/2}(^{76}\mathrm{Ge}) > 1.9 \times 10^{25}$ years (90% CL), corresponding to an effective Majorana mass bound of $m_{\beta\beta} < 0.32$ eV. A subset of this collaboration claimed to observe evidence for a $\beta\beta0\nu$ signal, with a best value for the half-life of 1.5×10^{25} years [82]. The claim is very controversial [83]. Also, a subsequent re-analysis by the same group updated this result to $(2.23^{+0.44}_{-0.31}) \times 10^{25}$ years [84], resulting in an effective Majorana mass of about 0.30 eV. The authors claim a statistical significance for the evidence of 6σ, and do not present any systematic uncertainty analysis. It should be

mentioned that a different germanium detector, IGEX, did not observe any evidence for $\beta\beta 0\nu$, and reported a lower bound on the half-life of: $T^{0\nu}_{1/2}(^{76}\mathrm{Ge}) > 1.57 \times 10^{25}$ years (90% CL) [85].

In the next chapter a description of the current experiments with their respective results is performed.

Take young researchers, put them together in virtual seclusion, give them an unprecedented degree of freedom and turn up the pressure by fostering competitiveness.

James D. Watson

4

Current status of neutrinoless double beta decay experiments

The status of the field was recently reviewed in [86] Among the proposed and ongoing experiments many different experimental techniques are utilized, each with its pros and cons. Germanium calorimeters like GERDA and Majorana emphasize detection efficiency and energy resolution, while bolometers such as CUORE offer the additional possibility of deploying large masses of $\beta\beta$ isotope using natural tellurium. The first new-generation experiments that have produced results are xenon-based: KamLAND-Zen, in which xenon is dissolved in liquid scintillator and EXO-200, a liquid xenon (LXe) TPC. Xenon is an interesting isotope for $\beta\beta 0\nu$ searches for the following reasons: two naturally occurring isotopes of xenon can decay via the $\beta\beta$ process, ^{134}Xe ($Q_{\beta\beta} = 825$ keV) and ^{136}Xe ($Q_{\beta\beta} = 2458$ keV). The latter, having a higher

Q-value, is preferred since the decay rate is proportional to $Q_{\beta\beta}^5$ and the radioactive backgrounds are less abundant at higher energies. Moreover, the $\beta\beta 2\nu$ mode of ^{136}Xe is slow (2.3×10^{21} years) and hence the experimental requirement for good energy resolution is less stringent than for other $\beta\beta$ sources. The process of isotopic enrichment is relatively simple and cheap compared to that of other $\beta\beta$ isotopes and consequently ^{136}Xe is the most obvious candidate for a future multi-ton $\beta\beta$ experiment.

EXO-200 has recently set the most stringent limit in the search for neutrinoless double beta decay [87]. The experiment deploys a total mass of 200 kg of liquid xenon enriched to 85% in ^{136}Xe . About half of this mass is used for self-shielding. The achieved energy resolution is 4% FWHM at $Q_{\beta\beta}$. This is obtained by using the anti-correlation between the ionization and scintillation signals provided by the xenon. The background rate measured in the region of interest (ROI) is excellent, $1.5 \times 10^{-3} counts/(keV \cdot kg \cdot y)$. The total exposure used for the published result is 32.5 kg·year, corresponding to 79.4 kg of ^{136}Xe (98.5 kg of xenon in total in the active volume) and 120.7 days of data. The background model predicts 4 events in the region of 1σ around $Q_{\beta\beta}$ and 7.5 events in the 2σ region. They observe 1 event in the 1σ region of interest (ROI) and 5 events in the 2σ ROI. A limit on the half-life of $\beta\beta 0\nu$ is extracted from this observation: $T_{1/2}^{0\nu}{}^{136}\mathrm{Xe} > 1.6 \times 10^{25}$ years. Notice that this limit is, therefore, considerably better than the expected sensitivity of EXO-200 at this stage, given that less background events than expected are detected. In terms of the effective neutrino mass, the EXO Collaboration quotes a sensitivity ranging between 140 and 380 meV, depending on the NME.

KamLAND-ZEN has also published first results this year [88]. Their effective mass of ^{136}Xe is only 129 kg, with respect to the total mass of 300 kg. This is due, as in the case of EXO, to the required shielding of the fiducial area from backgrounds emanating from the acrylic balloon containing the liquid scintillator-xenon mixture. The measured background rate, 0.01 counts/(keV · kg · y), is significantly higher than that foreseen by the collaboration. As mentioned above, the EXO experimental background model predicts the observed background spectrum to a high degree of accu-

racy. It follows that substantial improvements in the detector are needed to compete with EXO-200.

4.1 GERDA

The Gerda experiment looks for the neutrinoless double beta decay process in ^{76}Ge using semiconductor diodes able to measure energy with very high precission. The Gerda approach is different from the other experiments presented in this chapter. While both EXO and KamLAND-ZEN push to get vary large fidutial masses (100kg) Gerda focusses on obtaining the best possible energy resolution to improve the background suppresion and so the signal to background ratio and sensitivity.

The GERDA experiment consists on two phases: Phase I is designed to collect a total exposure of $> 20 kg \cdot yr$ with a background index of $10^{-2} cts/(keV \cdot kg \cdot yr)$. This exposure will be sufficient to test the positive result in [84]. GERDA Phase II aims to acquire am exposure of $100 kg \cdot yr$ and also to reduce the background by an order of magnitude to $10^{-3} cts/(keV \cdot kg \cdot yr)$. With that exposure, the sensitivity of the detector to the effective neutrino mass will be near 100 meV.

4.1.1 Detector

The main feature of those detectors is to operate bare Ge detectors made out of material enriched in ^{76}Ge (enriched Ge) in LAr.

The core of the GERDA experiment is an array of germanium diodes suspended in strings into a cryostat filled with LAr. The LAr serves both as cooling medium and shield. The cryostat is a steel vessel with a copper lining used primarily to reduce the gamma radiation from the steel vessel. The cryostat is placed in a large water tank, that fulfills the functions of shielding the inner volumes from radiation sources within the hall, such as neutrons, as well as providing a sensitive medium for a muon veto system.

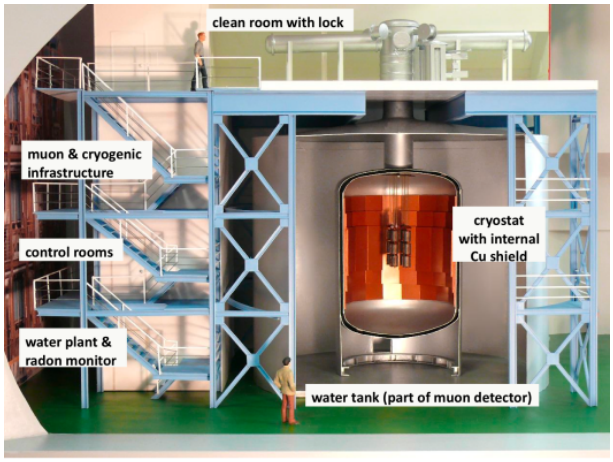

Figure 4.1.1: Model of the GERDA detector.

Germanium Detectors

The detectors used for Phase I were refurbished and redeployed from the HdM and Igex experiments. In Phase I of the experiment eight semi-coaxial and five BEGe type detectors have been deployed. The latter type is used in this field of research for the first time. All detectors are made from material with enriched ^{76}Ge fraction. The isotopic abundance in ^{76}Ge in the enriched detectors is 85% while the abundance in the natural Ge is 7.8%.

Operation of bare HPGe detectors in cryogenic liquids is a non-standard technique. The success of Gerda depends strongly on the long-term stability of the Ge detectors operated in LAr.

The energy resolutions of the Phase I detectors were between 2.5 and 5.1 keV (FWHM) for the 1332 keV spectral line of ^{60}Co . The Phase II, the detectors are of Broad Energy Germanium (BEGe). The energy resolution reached with those detectors is of 1.7 keV FWHM at the 1332 keV ^{60}Co line. When extrapolating to the $Q_{\beta\beta}$ value for ^{76}Ge (2039 keV) the energy resolution becomes 0.15% and 0.10% FWHM respectively.

4.1.2 Background

The Gerda collaboration was using some detectors used in previous experiments, their understanding of the sensors was really good from the beginning. Furthermore, the Gerda collaboration has made an enormous effort measuring all possible sources of background to the detectors and estimating the final background rate in their window of interest. The analysis process including the determination of the background index is as follows:

- Perform an analysis blinding a window of $\Delta E = 40$ keV centered in $Q_{\beta\beta}$ value in order to predict the background index in the region of interest avoiding bias in the event selection criteria.
- Develop the background model and compare its prediction with the energy spectra outside the blinded region.
- After the energy calibration and the background model were finalized, open the window for ± 5 keV around $Q_{\beta\beta}$.
- Develop the pulse-shape analysis algorithms and cuts.
- Finally, unblind the window and find the result.

Predictions for the number of eventes in the blinded region are shown in [89]. It is shown that the expected background is flat in a region of $\sim$ 200 keV around $Q_{\beta\beta}$ and that no significant peak like structures are expected in the blinded region. The background model and an interpolation of a fit to data from a 200 keV energy window into the blinded energy window give compatible results. The background index interpolated into the region are $(1.75^{+0.26}_{-0.24}) \cdot 10^{-2}$ for the coaxial detectors and $(3.6^{+1.3}_{-1.0}) \cdot 10^{-2}$ for the Broad Energy Germanium (BEGe) detectors.

In the other hand, the analysis performed using the Pulse Shape Discrimination (PSD) is presented in [90]. The data for semi-coaxial detectors and for BEGe is analyzed with different methods using in each case the one that gives the best result.

In the case of the semi-coaxial an artificial neural neutwork analysis has shown to reject 45% of the events around $Q_{\beta\beta}$. For the BEGe detectors a selection on A/E and a pulse asymmetry, where A is the maximum of the current pulse and E is the energy of the corresponding event, rejects about 80% of the events in the region. That rejection has a very small cost in efficiency being $0.90^{+0.05}_{-0.09}$ for the semi-coaxial detectors and 0.92 ± 0.02 for the BEGe detectors. Gerda background index (average over all data) is hence reduced from (0.021 ± 0.002) cts/(keV kg yr) to (0.010 ± 0.001) cts/(keV kg yr).

4.1.3 Results

The half-life of the $\beta\beta 2\nu$ decay of ^{76}Ge was derived from the first data from the GERDA experiment in [91]. The analysis has been carried out on the data collected with six ^{enr}Ge detectors (14.6 kg total weight) during 125.9 live days by fitting the energy spectra with a comprehensive model. The best estimate of the half-life of the $\beta\beta 2\nu$ decay is:

$$T^{2\nu}_{1/2} = (1.84^{+0.09}_{-0.08fit}{}^{+0.11}_{-0.06syst}) \times 10^{21} yr = (1.84^{+0.14}_{-0.10}) \times 10^{21} yr, \qquad (4.1)$$

In the other hand, the analysis to $T^{0\nu}_{1/2}$ using the results from the previous background estimations is shown in [92]. The analysis shows that the Gerda data is compatible with no neutrinoless events and so only a lower limit to $T^{0\nu}_{1/2}$ can be determined. This lower limit is determined using both, a frequentist coverage interval and a Bayesian calculation. The frequentist interval was calculated with a profile likelihood fit with a constant term for the background and a Gaussian peak for the signal. This method gives a result of $T^{0\nu}_{1/2} > 2.1 \times 10^{25}$ yr (90% C.L.). The Bayesian method gives a compatible result with a median sensitivity of $T^{0\nu}_{1/2} > 2.0 \times 10^{25}$ yr.

4.2 EXO

EXO-200 has recently set the most stringent limit in the search for neutrinoless double beta decay [87]. The experiment deploys a total mass of 200 kg of liquid xenon enriched to 85% in ^{136}Xe . About half of this mass is used for self-shielding. The achieved energy resolution is 4% FWHM at $Q_{\beta\beta}$. This is obtained by using the anti-correlation between the ionization and scintillation signals provided by the xenon.

4.2.1 EXO detector

EXO-200 uses the xenon as both source and detector in a homogeneous, liquid phase Xenon TPC. The experiment deploys 200kg of Xenon enriched to $80.672 \pm 0.14\%$ in the ^{136}Xe isotope. Of the 200 kg of enriched xenon available, 175 kg are in liquid phase. Of those, 110 kg are in the active volume of the detector. The EXO detector records both the ionization and the scintillation signal. Charge is collected at each end of the TPC by wire planes, held at virtual ground, while the 178 nm-wavelength scintillation light is collected by two arrays of large area avalanche photodiodes (LAAPDs), one behind each of the two charge collection planes ("U" wires). A second wire plane ("V" wires), positioned in front of the charge collection plane and oriented at 60° from it, is biased to ensure full electron transparency and is used to inductively record a second coordinate for each ionization cluster. Three-dimensional position sensitivity is achieved by using the difference in the arrival time between the ionization and scintillation signals to calculate the electron drift time.

Event Reconstruction

In the event reconstruction process, the waveform information is analyzed to extract the relevant information of the events such as energy content, the position and the topology. The reconstruction is subdivided into three stages: Signal finding, signal parameter estimation and clustering or determination of event topology.

Calibration and Corrections

The TPC is calibrated using radioactive sources with gammas at different energies, between 662keV (^{137}Cs) to 2614keV (^{208}Tl from ^{228}Th chain). ^{228}Th is used near the cathode to monitor the electron life-time and to measure the energy response. The other sources are deployed in different places of the TPC for detailed calibration studies.

I will not describe de calibration method in the U and V-wires, but I will focus in the position and time corrections to the energy. The amount of light collected by the APDs depends on the location of the charge deposition inside the TPC. This variation is caused by differences in the solid angle covered by the APDs and by their gain differences. To correct this effect a 3-D correction function is used. The total fiducial volume is subdivided in bins with enough statistics and, at the same time, to ensure an adequate description of the regions with high light collection gradient.

The light map is normalized to have a mean response of 1. A continuous correction function, $f(r, \varphi, z)$, is created with a trilinear interpolation between the centers of the voxels in the light map.

For events with single deposition, the correction function is applied by multiplying the sum of the two APD plane signals by $1/f(r, \varphi, z)$, while for events with multiple depositions, a correction factor is deduced by taking the appropriate charge-cluster energy-weighted sum.

To correct for the electron attachment while drifting in LXe, a simple exponential correction is applied using the value of the electron life time calculated in the calibration runs with the ^{228}Th source.

Rotated energy measurement

To optimize the energy resolution of the detector they take advantage of the microscopic anti-correlation between ionization and scintillation in LXe as discussed in [93]. The best energy resolution is obtained when combining the scintillation and charge signals with the appropiate weights according to:

$$E_R = E_S \cdot sin(\theta^R) + E_I \cdot cos(\theta^R) \tag{4.2}$$

After all different correction, the time-averaged energy resolution for EXO at the $\beta\beta$ Q value is $4.32 \pm 0.07\%$ FWHM for single deposition events (slighly higher for multiple deposition events).

With this energy resolution, an efficiency of $87.4 \pm 2.53\%$ for events inside the fiducial region, EXO obtains a total exposure for the measurement of the two neutrino mode of $23.14\ kg \cdot year$. This gives the best measurement for the half life of the process as shown in Table 4.3.1.

4.2.2 EXO-200 Results

For the estimation of the half life of the neutrinoless process the data published corresponds to an exposure of $32.5 kg \cdot yr$ [87]. The lower limit on $T^{0\nu}_{1/2}$ is obtained by the profile likelihood fit to the entire single and multiple deposition. The fit yields an estimate of 4.1 ± 0.3 background counts in the $\pm 1\sigma$ region, giving an expected background rate of $(1.5 \pm 0.1) \times 10^3 kg^{-1} yr^{-1} keV^{-1}$. The number of events observed in the single deposition spectrum in a region of interest of $\pm 1\sigma$ and $\pm 2\sigma$ are 1 and 5, respectively, with the 5 events in the $\pm 2\sigma$ region accumulating at both edges of the interval. This corresponds to a $T^{0\nu}_{1/2} > 1.6 \times 10^{25}$ yr at 90% C.L. ($T^{0\nu}_{1/2} > 4.6 \times 10^{25}$ yr at 68% C.L.). See Table 4.3.1

4.3 KamLAND-ZEN

The KamLAND-ZEN experiment uses ^{136}Xe as a source for the experiment but it bases its sensitivity on a different approach to EXO or NEXT. KamLAND compromises the energy resolution of the detector in order to be able to use very large masses fo Xenon. Effectively they are able to use a mass of 300kg of ^{136}Xe . On the other hand, the poor resolution has many disadvantages. I will describe the detector and the results they obtain in their first runs.

4.3.1 KamLAND Detector

KamLAND-ZEN is a modification of the existing KamLAND detector and was carried out in the summer of 2011. The $\beta\beta$ source/detector consists in 13 tons of Xe-loaded liquid scintillatior (Xe-LS) contained in a 3 meter diameter spherical inner balloon (IB). The IB is made out of transparent nylon film and is suspended at the center of the KamLAND detector by 12 straps of the same material. The IB is surrounded by 1kton of LS in a 13 meter diameter spherical outer ballon (OB). The outer LS acts as an active shield for external γ's and as a detector for internal radiation from the Xenon (See Fig. 4.3.1).

The event energy (visible energy) is estimated from the number of observed photoelectrons (p.e.) after correcting for PMT gain variation and solid angle, shadowing, and transparency of detector materials. The vertex reconstruction is based on the maximum likelihood fit to the pulse shape of each PMT hit timing after correcting for photon time of flight. The vertex resolution is estimated from radial distributions of radioactive contaminants (see Fig. 3) to be $\sigma \sim 15cm/\sqrt{(E(MeV))}$. The energy response is calibrated with γ's from a ^{228}Th (ThO2W) source, ^{214}Bi ($\beta + \gamma$'s) from ^{222}Rn (τ = 5.5 day) introduced during detector modification, and 2.225 MeV γ's from spallation neutrons captured on protons.

The energy resolution obtained after corrections measured at 2.614 MeV (^{208}Tl γ energy) is found to be $\sigma = (6.6 \pm 0.3)\%/\sqrt{(E(MeV))}$. The value of the energy resolution at $Q_{\beta\beta}$ is σ = 4.21% (FWHM = 9.89%).

Isotope	$T^{2\nu}_{1/2}$ (years)	Experiment
^{76}Ge	$1.84^{+0.14}_{-0.10} \times 10^{21}$	GERDA [91]
^{136}Xe	$2.1720.017(stat)0.060(sys)10^{21}$	EXO [94]
^{136}Xe	$2.32 \pm 0.05(stat) \pm 0.08(syst) \times 10^{21}$	KAMLand-Zen [95]

Table 4.3.1: Current best measurements on the half-life of $\beta\beta$2nu processes for the most interesting isotopes. All values are at 90% CL.

4.3.2 Background Estimation

The backgrounds in KamLAND-ZEN could fall in in three different categories: Background from the impurities in the Xe-LS, background from the IB and spallation backgrounds.

The main contribution to the background rate comes from the impurities in the Xe-LS with a event rate of near 300 $events/(ton \cdot day)$ from the ^{232}Th chain. The background from the IB produced by spallation is in both cases of the order of 1 $event/(ton \cdot day)$

In the other hand, the background in the region of interest near the $Q_{\beta\beta}$ value is 0.22 ± 0.04.

4.3.3 Results

From the fitting result, the measured half-life of the ^{136}Xe $\beta\beta 2\nu$ decay is $T^{2\nu}_{1/2} = 2.38 \pm 0.02(stat) \pm 0.14(syst) \times 10^{21}$ yr, which is consistent with the EXO-200 result (Table 4.3.1), and falls below the lower limit, $> 1.0 \times 10^{22}$ yr, obtained by DAMA. The estimated lower limit of the ^{136}Xe $\beta\beta 0\nu$ decay half-life is $> 1.6 \times 10^{25}$ yr at 90% C.L. (Table 4.3.2).

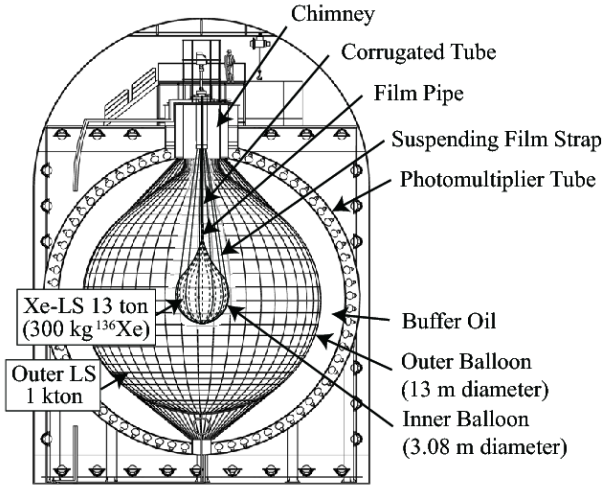

Figure 4.3.1: Schematic diagram of the KamLAND-Zen detector.

Isotope	$T^{0\nu}_{1/2}$ (years)	Experiment
^{76}Ge	$> 2.1 \times 10^{25}$	GERDA [92]
^{136}Xe	$> 1.6 \times 10^{25}$	EXO [87]
^{136}Xe	$> 2.6 \times 10^{25}$	KAMLand-Zen [95]

Table 4.3.2: Current best limits on the half-life of $\beta\beta 0\nu$ processes for the most interesting isotopes. All values are at 90% CL.

4.4 Towards 1 ton detectors

In this chapter we have introduced the latest results of the field. Most of the collaborations with a running experiment have started talking about the next generation of experiments, the so-called 1-ton scale. In this section, we review the weak and strong features of the newly proposed experiments and how they will affect their scalability to the 1-ton detector concepts.

4.4.1 Germanium detectors

The biggest advantage of the germanium detector based experiments is their impressive energy resolution. This results in a very narrow region of interest being the main tool for background discrimination. Their ability to measure energy with extreme precision and their very low energy threshold also allows for a data driven background estimation resulting in a very good understanding of their backgrounds.

Although rejecting events out of the region of interest is the most powerful tool of those detectors for rejecting background, new techniques like the pulse shape analysis in point contact detectors can help in the discrimination of the background event [96]. With that technique, the Majorana collaboration aims to improve the background rate by an order of magnitude to reach $\sim 10^{-3} counts/(kev \cdot kg \cdot year)$ [97].

The scalability of those detectors is based on the replication of a unit module up to the desired mass. That implies that the background scales with the same function as the mass. Furthermore, the enrichment of the crystals in the desired isotope is a complex process and so the required crystals are very expensive.

4.4.2 EXO detector

The main advantage of the EXO technique is the isotope. Effectively, ^{136}Xe is the cheapest isotope to enrich, and so it is very realistic for a single collaboration to get 1 ton of enriched Xenon. On the other hand, EXO uses a lot of its enriched Xenon in self-shielding the fiducial volume against backgrounds. In EXO-200 the fidutial volume is less than 50% of the total Xenon volume, that ratio will depend on the final geometry of the detector as well as the desired level of shielding required.

The tools for background rejection are based on the selection of events with single site depositions of energy in the active volume and, of course, in the energy selection of the events. The EXO detector has a moderate resolution that should be good enough for a good understanding of the backgrounds and to keep the region of interest free of $\beta\beta 2\nu$ events.

As an enriched Xenon based experiment, EXO has a possibility for background

rejection that will confirm event by event if it is a Xenon decay or not. The Barium tagging option will localize and identify the Barium ion produced after the Xenon decay rejecting all other kinsd of background, the result is that the only potential background source will be the two neutrino mode. In case of an experiment with good enough resolution, it will operate a non-background experiment with its sensitivity improving much faster than in the case of experiments with background.

4.4.3 KamLAND-ZEN detector

KamLAND-ZEN is also using the ^{136}Xe isotope. All the benefits described for EXO can be applied here also, with the difference that KamLAND-ZEN is not using enriched Xenon for shielding.

The KamLAND-ZEN approach consist on accumulating the largest ^{136}Xe mass and dissolving it into a liquid scintillator to measure the energy of the event using only the primary light. That method results in a poor energy resolution that implies problems in understanding the background in the region of interest. Their results are based on a fit to a background with big uncertainties and not from a counter measurement in a narrow energy window. It seems hard to imagine a claim for a discovery with that technique, although it might be appropriate to confirm or refute a result.

4.4.4 Summary

Table 4.4.1 summarizes the different approaches of the experiments described in the previous sections. When looking at the different experiments one has the impression that all of them have positive things but also strong limitations. A proper quantification of the 1 ton capabilities of the different techniques will be needed to compare the sensitivity of the 1 ton projects (similar to what was done in [98]) or at least a comparison of the ratio $M/(\Delta E \cdot b)$ where M is the fiducial mass of the isotope, ΔE is the amplitude of the ROI window and b is the background rate in the usual units.

In chapter 9 the sensitivity of NEXT-100 is described, and also the potential of the NEXT technology for extrapolating to the 1 ton scale.

Experiment	Energy Resolution	Scalability	Background rejection	Background estimation
Gerda	⋆⋆⋆⋆⋆	⋆⋆	⋆⋆	⋆⋆⋆⋆
EXO	⋆⋆⋆	⋆⋆⋆⋆	⋆⋆⋆	⋆⋆⋆
KamLand-ZEN	⋆⋆	⋆⋆⋆⋆⋆	⋆⋆	⋆

Table 4.4.1: Summary table with the strong and week points of the experiments presented in this chapter when extrapolating to the ton scale.

It always seems impossible until it's done.

Nelson Mandela

5

NEXT Detector

Next-generation double beta decay experiments have to be sensitive to effective Majorana neutrino masses smaller than 100 meV, and the next-to-next generation must reach 20–25 meV if a discovery is not made previously. Designing a detector capable of identifying efficiently and unambiguously such a rare signal is a major experimental challenge.

Effectively, in order to reach those extreme sensitivities the detector should use as many tools as possible to unambiguous identify the signal and reject background. A perfect knowledge of the signal signature is mandatory. In the case of the neutrinoless double beta, the signal is characterized by emitting the two electrons with always the same energy, therefore an excellent energy resolution is mandatory. Also, the two-electron topology is very characteristic and can be used to distinguish signals from backgrounds.

5.1 The SOFT concept

The NEXT experiment combines excellent energy resolution, a low background rate and the possibility to scale-up the detector to large masses of $\beta\beta$ isotope by using a high-pressure xenon gas (HPXe) electroluminescent time projection chamber (TPC) to search for $\beta\beta 0\nu$ in ^{136}Xe. The combination results in excellent sensitivity to $m_{\beta\beta}$.

A major bonus of the NEXT technology is the topological signature. Neutrinoless double beta decay events leave a distinctive topological signature in gaseous xenon: an ionization track, about 30 cm long at 10 bar, tortuous due to multiple scattering, and with larger energy depositions at both ends (see Figure 5.1.1 and section 5.3 for more details). The Gotthard experiment [99], consisting in a small xenon gas TPC (5.3 kg enriched to 68% in ^{136}Xe) operated at 5 bar, proved the effectiveness of such a signature to discriminate signal from background.

To achieve optimal energy resolution, the ionization signal is amplified in NEXT using the electroluminescence (EL, see section 5.2) of xenon. Also, following ideas introduced in [100] and further developed in our Conceptual Design Report (CDR) [101], the chamber will have separated detection systems for tracking and calorimetry. This is the so-called *SOFT* concept, illustrated in Figure 5.1.2. The detection process is as follows: Particles interacting in the HPXe transfer their energy to the medium through ionization and excitation. The excitation energy is manifested in the prompt emission of VUV ($\sim$ 178 nm) scintillation light. The ionization tracks (positive ions and free electrons) left behind by the particle are prevented from recombination by an electric field (0.3–0.5 kV/cm). The ionization electrons drift toward the TPC anode, entering a region, defined by two highly-transparent meshes, with an even more intense electric field (3 kV/cm/bar). There, further VUV photons are generated isotropically by electroluminescence. Therefore, both scintillation and ionization produce an optical signal, to be detected with a sparse plane of PMTs (the *energy plane*) located behind the cathode. The detection of the primary scintillation light constitutes the start-of-event, whereas the detection of EL light provides an en-

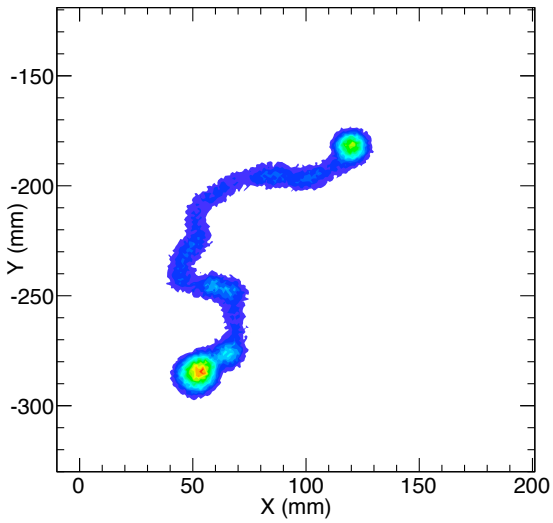

Figure 5.1.1: Monte-Carlo simulation of a ^{136}Xe $\beta\beta 0\nu$ event in xenon gas at 10 bar: the ionization track, about 30 cm long, is tortuous because of multiple scattering, and has larger depositions or *blobs* in both ends.

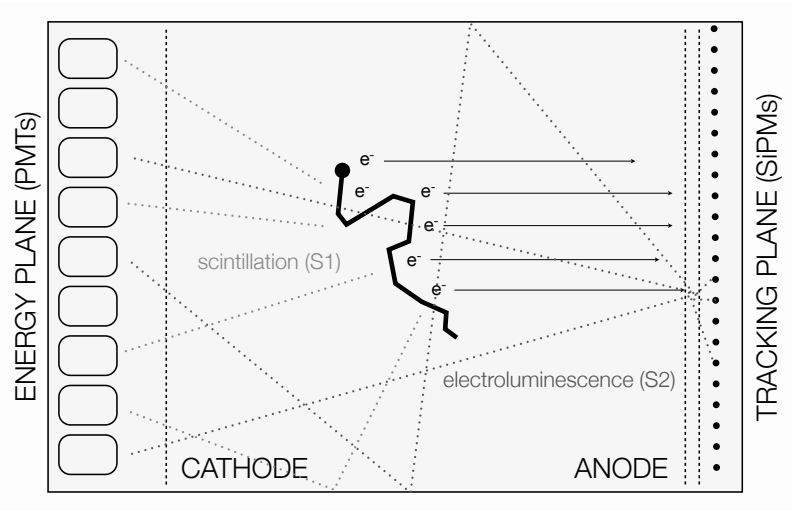

Figure 5.1.2: The *Separate, Optimized Functions* (SOFT) concept in the NEXT experiment: EL light generated at the anode is recorded in the photosensor plane right behind it and used for tracking; it is also recorded in the photosensor plane behind the transparent cathode and used for a precise energy measurement.

ergy measurement. Electroluminescent light provides tracking as well, since it is detected also a few millimetres away from production at the anode plane, via an array of 1-mm² MPPCs, 1-cm spaced (the *tracking plane*).

5.2 Electroluminescence

5.2.1 The Gas Proportional Scintillation Chamber

Figure 5.2.1 (top), illustrates the principle of a Gas Proportional Scintillation Chamber (GPSC) [103, 104]. An x-ray enters through the chamber window and is absorbed in a region of weak electric field (> 0.8 kV cm^{-1} bar^{-1}) known as the drift region. The ionization electrons drift under such a field to a region of moderately high electric field (around $3 - 4$ kV cm^{-1} bar^{-1} range), the so-called scintillation or EL region. In the scintillation region, each electron is accelerated so that it excites, but does not ionize, the gas atoms/molecules. The excited atoms decay, emitting UV

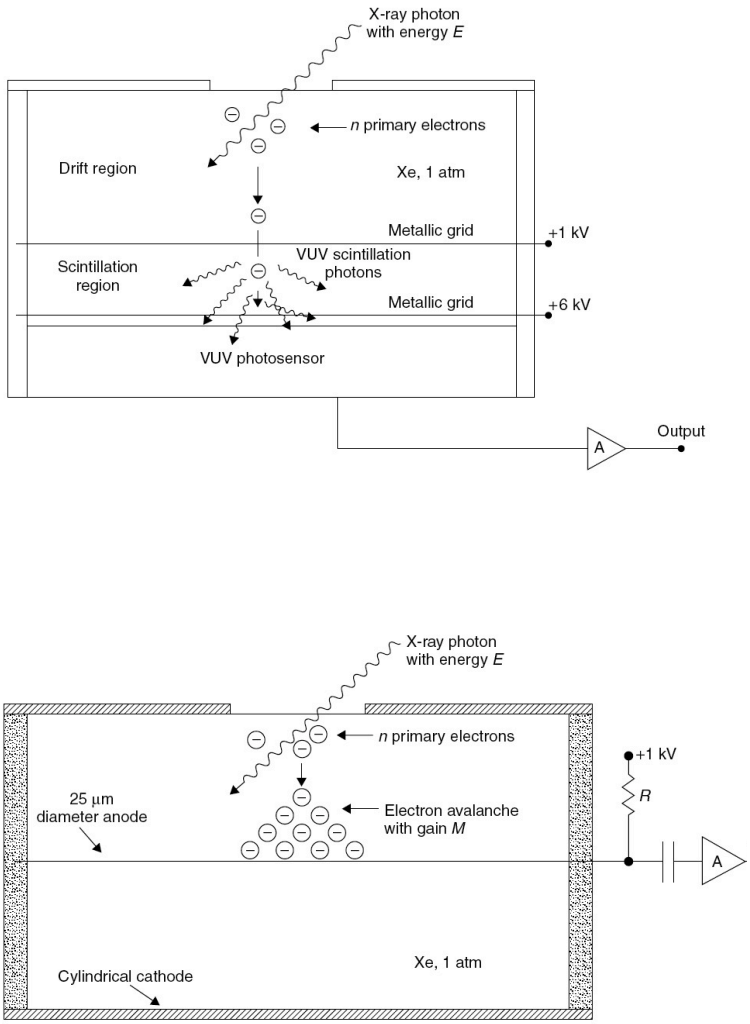

Figure 5.2.1: Top: principle of a Gas Proportional Scintillation Counter. Bottom: principle of a Gas Proportional Counter with avalanche gain (from [102]).

light (the so-called secondary scintillation), which is detected by a photosensor, usually a photomultiplier tube. The intensity of the secondary scintillation light is two or three orders of magnitude stronger than that of the primary scintillation. However, since the secondary scintillation is produced while the electrons drift, its latency is much longer than that for the primary scintillation, and its rise time is much slower (a few μs compared to a few ns). For properly chosen electric field strengths and EL region spatial widths, the number n_{ph} of secondary scintillation photons produced by a single primary electron is nearly constant and can reach values as large as a few thousand photons per electron.

The average total number, N_t, of secondary scintillation photons produced by an X-ray photon is then $N_t = n_{ph} \cdot N_I$, (recall that N_I is the number of primary ionization electrons) so the photosensor signal amplitude is nearly proportional to E, hence the name of gas proportional scintillation counter (GPSC) for this device.

What makes the devices extraordinarily attractive is their improved energy resolution compared with conventional Proportional Chambers (PC) — Figure5.2.1 (bottom). In a PC the primary electrons are made to drift towards a strong electric field region, usually in the vicinity of a small diameter (typically 25 μm) anode wire. In this region, electrons engage in ionizing collisions that lead to an avalanche with an average multiplication gain M of the order of 10^3 to 10^4. If M is not too large, space charge effects can be neglected, and the average number of electrons at the end of the avalanche, $N_a = M \cdot N_I$, is also proportional to the energy E of the absorbed X-ray photon (hence the name proportional (ionization) counter given to this device). However, for PC detectors, there are fluctuations not only in N_I but also in M; for GPSCs, since the gain is achieved through a scintillation process with almost no fluctuations, only fluctuations in N_I and in the photosensor need to be considered. Thus a better energy resolution is achieved in the latter case; typical values for 5.9 keV X-rays are 8% for GPSC and 14% for PC.

The Scintillation Drift Chamber (SDC) was invented in 1978 [105]. An SDC is a TPC with EL readout instead of charge gain by electron avalanche multiplication in gas. A large SDC with 19 PMTs [106] demonstrated excellent energy resolution at

high pressure (9 bar), and for high energy X-rays. However, for mainstream particle physics, EL has had applications primarily in only one technique: two–phase LXe detectors aimed at direct detection of WIMPs [107]. In that very successful application, the enabling asset of EL is not the excellent energy resolution (limited, as we have seen, by the anomalous Fano factor in liquid), but the capability to detect single electrons.

5.2.2 Xenon atomic energy structure

In the EL region the drift electrons are accelerated and collide with the gas atoms. If the electric field is not too large, the electrons collide elastically with the atoms and can also excite but not ionize them. In the case that an excitation collision happens, the atom can stay in one of several excited levels. Since, at high pressures (above few hundreds of torr [108]), the time intervals between collisions of an excited atom with other atoms of the gas are much smaller than the atomic radiative lifetimes [109] the main channel of de-population of these excited atoms is through the formation of excimers–electronically excited molecular states. Excimers, R_2^{**}, are formed through three-body collisions between one excited atom, R^*, and two atoms in the ground state, R:

$$R^* + 2R \rightarrow R_2^{**} + R \tag{5.1}$$

The excimers responsible for the VUV electroluminescence, $0_u^+ \left(^1\Sigma_u^+\right)$, $(v = 0)^1 \Sigma_u^+$ and $(v = 0)^3 \Sigma_u^+$, are formed from $1s_4$ and $1s_5$ atomic levels ($J = 3/2$) [110] or by radiative transitions from higher excited molecular levels which are formed from atoms with an energy higher than $1s_4$ and $1s_5$ [111]. The excimers represented with "$(v = 0)$", R_2^*, are vibrationally relaxed through two-body collisions between the unrelaxed excimers, e.g. $0_u^+ \left(^1\Sigma_u^+\right)$, R_2^{**}, and ground atoms, R:

$$R_2^{**} + R \rightarrow R_2^* + R \tag{5.2}$$

Vibrational unrelaxed excimers can decay to the repulsive ground state, $^1\Sigma_g^+$, emit-

ting a VUV photon:

$$R_2^{**} \rightarrow 2R + h\nu \tag{5.3}$$

as well as vibrational relaxed excimers:

$$R_2^{*} \rightarrow 2R + h\nu \tag{5.4}$$

In the case that the radiative decay is from R_2^{**} the energy of the VUV photon is slightly higher than if the decay is from R_2^{*}. In this way, at low gas pressures, a continuum emission spectrum is observed with two peaks, usually called "first continuum" - at higher frequencies - and "second continuum" - at lower frequencies. The reason why, at high pressures, one usually only observes the "second continuum" is because process (5.2) is preferable to (5.3) due to the increase in the number of atom collisions.

5.2.3 Simulation of EL in NEXT

The NEXT software includes a platform to simulate EL [109], based on Garfield [112] and Magboltz [113, 114]. We have used it to study the expected EL yield and energy resolution.

Primary drift electrons were allowed to drift a distance of $d = 5$ mm under the influence of an uniform electric field created by two infinite parallel planes (except in the edges this arrangement simulates well the large EL grids in the NEXT detector). It was considered that the gas is at a pressure $p = 10$ bar and at a temperature of 293K. A set of $N_e = 10.000$ primary electrons was used for each value of the potential applied between the parallel planes, V.

5.2.4 Electroluminescence yield

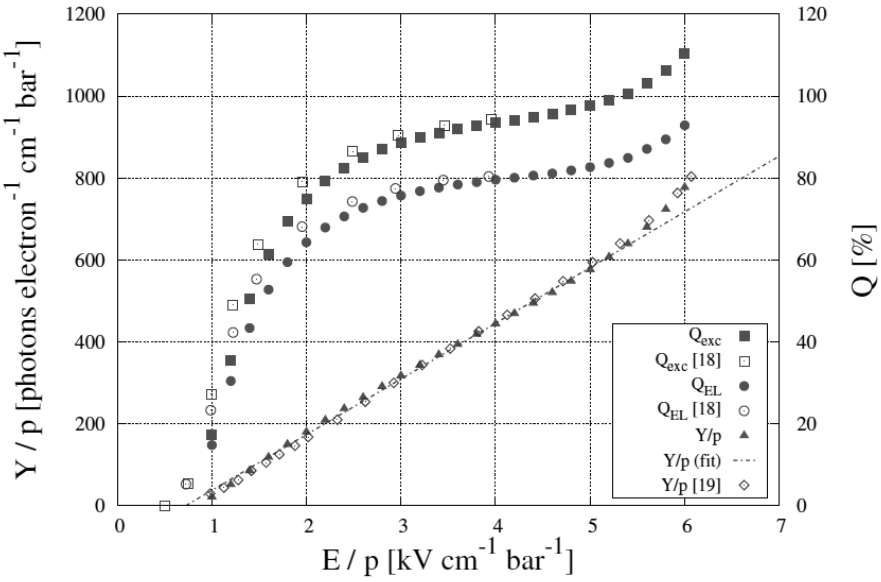

Figure 5.2.2: Reduced electroluminescence yield, $\left(\frac{Y}{p}\right)$, as a function of the reduced electric field (pressure units), $\left(\frac{E}{p}\right)$. Excitation efficiency, Q_{exc}, and electroluminescence efficiency, Q_{EL}, as a function of the reduced electric field are also shown. Full symbols are results of this work. Former Monte Carlo results of Q_{exc} and Q_{EL} [115] as well as experimental measurements of the reduced EL yield [116] are included (open symbols) for comparison.

In Figure 5.2.2 it is shown the reduced electroluminescence yield, $\left(\frac{Y}{p}\right)$, is shown as a function of the reduced electric field, $\left(\frac{E}{p}\right)$. The reduced electroluminescence yield is defined as the number of photons emitted per primary electron and per unit of drift length divided by the number density of the gas, N. The behavior of $\left(\frac{Y}{p}\right)$ with $\left(\frac{E}{p}\right)$ is approximately linear even when the actual ionization threshold is achieved at $\left(\frac{E}{p}\right) \sim 3$ kV cm^{-1}bar^{-1}. In Figure 5.2.3 it can be easily seen that this threshold is achieved since, for higher values of the electric field, the fluctuations in the secondary charge

production, which are bigger than in the electroluminescence, start to dominate. The EL yield keeps its linear behavior while the probability of ionization is low.

Performing a linear fit to the obtained points we obtain the dependence:

$$\left(\frac{Y}{p}\right) = (130 \pm 1)\left(\frac{E}{p}\right) - (80 \pm 3)\left[\text{photons electron}^{-1}\,\text{cm}^{-1}\,\text{bar}^{-1}\right] \quad (5.5)$$

Consider, for example, the number of photons produced in a TPC operating at 15 bar pressure, with a EL region of 5 mm and E/p set to 3.5. One then produces 2800 EL photons per primary electron. Since there are about 10^5 primary electrons in a $\beta\beta0\nu$ event, we end up with $\sim 3 \times 10^8$ EL photons.

Consider now the variance G of the gain:

$$G = 1/Y + (1 + \sigma_{pd}^2)/n_{pe} \quad (5.6)$$

The contributions to the gain resolution G must include fluctuations in:

1. the EL gain Y;
2. n_{pe}, the number of photo-electrons per incident electron;
3. the gain process in the photo-detector per single photo-electron, whose fluctuation we express by σ_{pd}.

The first term in (5.6) is much smaller than the second, since Y is large, while the limited photon detection efficiency results in a smaller number for n_{pe}. Assuming $\sigma_{pd}^2 = 0.5$ (most PMTs will do better than that) and setting G = 0.15 (so that it contributes no more than the Fano factor) one obtains:

$$n_{pe}^{EL} \geq 10 \quad (5.7)$$

Thus, in order to optimize the resolutiona a device capable of detecting at least 10

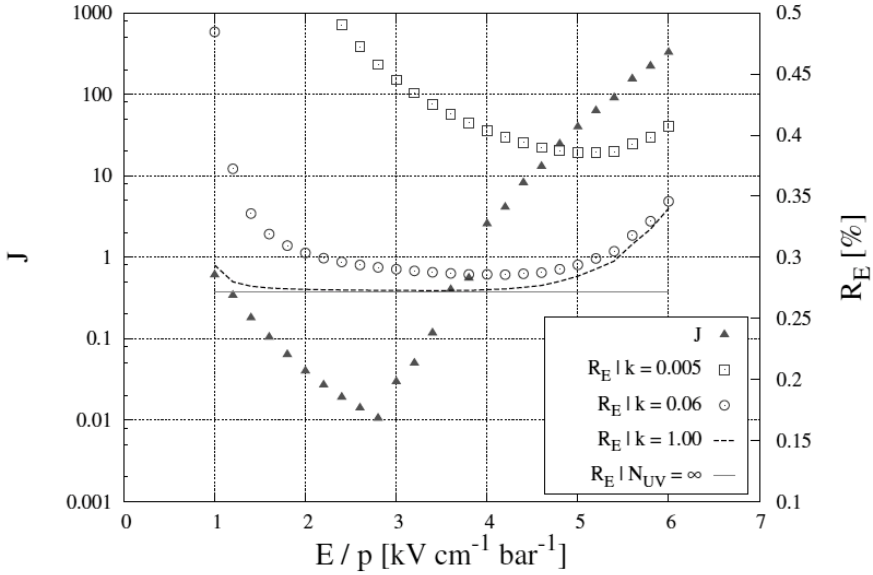

Figure 5.2.3: Relative variance in the number of emitted EL photons as a function of the reduced electric field. Energy resolution, R_E, as a function of the reduced electric field for three different scenarios: a) an ideal detector that detects all EL photons; b) an detector with 50% effective PMT coverage and an effective detection efficiency per PMT of 10% ($k = 0.5 \times 0.1 = 0.05$); and c) a detector with 5% PMT coverage and 10% detection efficiency ($k = 0.005$). The value of R_E if only the fluctuations in the production of primary charge contributed is also shown (red line). Notice that the resolution is always better than 0.5% even in case c).

photoelectrons per primary electron is necessary. We will revisit this condition when discussing the NEXT design.

Using our detailed simulation we can estimate the energy resolution attainable by NEXT for the $\beta\beta 0\nu$ events. Figure 5.2.3 shows energy resolution R_E curves as a function of the reduced electric field for three different scenarios: a) an ideal detector that detects all EL photons; b) an detector with 50% effective PMT coverage and an effective detection efficiency per PMT of 10% ($k = 0.5 \times 0.1 = 0.05$); and c) a detector with 5% PMT coverage and 10% detection efficiency ($k = 0.005$). J is the parameter that describes the fluctuations relative to the electroluminescence production, defined as the relative variance in the number of emitted VUV photons per primary electron, N_{EL}:

$$J = \frac{\sigma^2_{N_{EL}}}{\bar{N}_{EL}} \tag{5.8}$$

To summarize, we have a detailed understanding of the EL process, which is fully simulated within the NEXT software framework. Our predictions for both the EL yield and the EL resolution are consistent with data available in the literature and with our own measurements within the NEXT R&D and confirm the possibility to reach a resolution at $Q_{\beta\beta}$ which can be as low as 0.4%, and in any case, at the level of our target resolution of 1%.

5.3 Electron topology in HPXe gas

A major advantage of the NEXT design is the possibility of reconstructing the topology of an event in the detector. A $\beta\beta 0\nu$ signal event involves 2 electrons, the energies of which sum to $Q_{\beta\beta}$ ($\sim$2.45 MeV). While good energy resolution is enough to separate such events from the more abundant $\beta\beta 2\nu$ events, backgrounds still exist in the form of the compton and photoelectric interactions of high-energy photons emitted after the decay of ^{208}Tl and ^{214}Bi which result in single electrons with energy similar to $Q_{\beta\beta}$. An electron passing through xenon gas at 10 bar will lose energy, generally, in

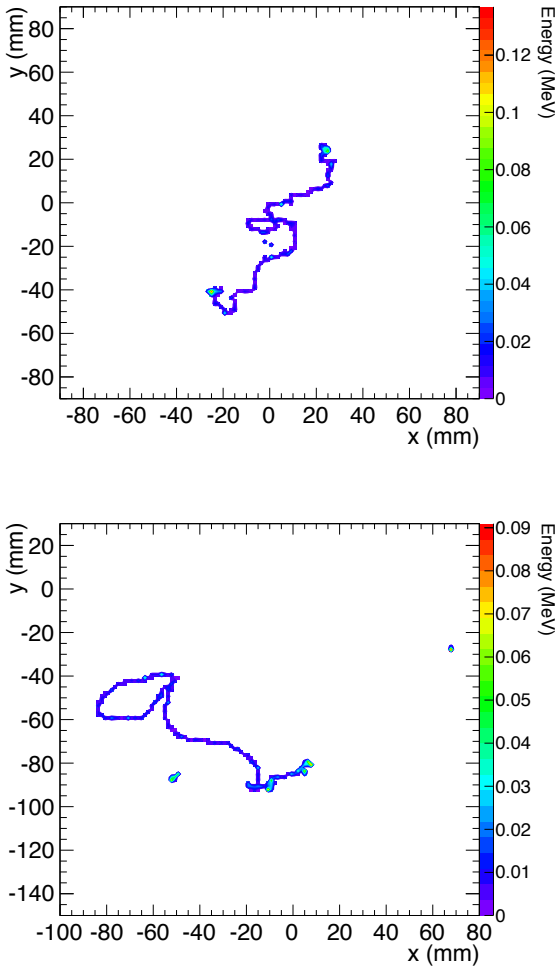

Figure 5.3.1: Topological signatures left by interactions in NEXT. Left: Monte-Carlo simulation of a ^{136}Xe $\beta\beta0\nu$ event in xenon gas at 15 bar. Right: Monte-Carlo simulation of a background event, in this case an electron produced via Compton scattering of a 2.447 MeV photon emitted by ^{214}Bi.

two distinct phases: a MIP-like region with $dE/dx \simeq 70$ keV cm^{-1} and, a region at the end of the track dominated by multiple scattering where $\sim$300 keV is deposited in a short distance (a "blob"). In order to separate a signal event from one induced by the backgrounds described above, a topology of two electrons with a common vertex must be distinguished from a single electron track. This requires the power to resolve the "blob" and MIP regions as well as separate an end-point blob energy deposit from a fluctuation in the dE/dx of the MIP region induced, for example, by bremsstrahlung or delta rays emitted by the electrons. Therefore, in designing the tracking plane a number of physical effects, both inherent to the interaction of electrons in the gas and resulting from the read-out of the signal, must be taken into account. The most important of these are the emission of delta electrons and bremsstrahlung photons, and the diffusion of the electron cloud during drift.

The tracks shown in figure 5.3.1 are those of a simulated signal event and a compton electron liberated by a 2.447 MeV gamma from ^{214}Bi where the energy scale shown is that of the energy deposited by the electron and the effects of drift are not included. In both cases the end-point "blob" regions are clearly visible as high energy deposits at the extremes of the tracks. However, both exhibit additional deposits of energy greater than that predicted by MIP energy loss within the track as well as deposits which are separated from the main trace of the electrons. While sufficient position resolution is required to separate the "blob" and MIP regions and so that regions of increased dE/dx are not added together to the extent that they can mimic the deposit of an additional "blob", very fine grained tracking is of little use since the blurring of the track due to photon and delta electron emission and the subsequent drift of the charge cloud remove any useful information at this level. In pure xenon, the transverse diffusion expected is of order 1 mm cm$^{-\frac{1}{2}}$ and the read-out plane must be positioned a few mm from the EL production region which results in blurring of order 1 cm at read-out. In other hand, the sensor needed should have high stability and be resistant to pressures of 10-15 bar, also the gain should be in the proper range ($\sim 10^5$) so they do not saturate but give enough information to distinguish the MIP region and the "blob". Taking all these effects into account, SiPM are a good technologi-

cal choice since they allow for the use of moderate EL without problems of stability, they have a relatively low cost and, a reasonable position resolution can be achieved without very dense arrays. Detailed simulation studies [101] yielded a pitch of 1 cm as the best compromise to provide a good separation between the two blobs of the signal electron and an acceptable number of channels at 10-15 bar of pure xenon.

The only source of knowledges is experience

Albert Einstein

6

NEXT DEMO Prototype

NEXT-DEMO is a high-pressure xenon TPC contained within a cylindrical stainless-steel pressure vessel of diameter 30 cm and length 60 cm which was designed to withstand up to 15 bar. The TPC itself is defined by three metallic wire grids — called *cathode*, *gate* and *anode* — which define the two active regions: the 30-cm long *drift region*, between cathode and gate with a drift field up to 800 V cm^{-1}; and the 0.5-cm long *EL region*, between gate and anode. The electric field is created by supplying a large negative voltage to the cathode, then degrading it using a series of metallic rings of 30 cm diameter spaced 5 mm and connected via 0.5 GΩ resistors (shown in figure 6.3.1). The gate is at negative voltage so that a moderate electric field — [1.0, 4.0] kV cm^{-1} bar^{-1} — is created between the gate and the anode, which is at ground. A set of six panels made of PTFE (Teflon) coated with tetraphenyl-butadiene (TPB)

are mounted inside the electric-field cage forming a *light tube* of hexagonal cross section with an apothem length of 8 cm.

The main objective of NEXT-DEMO was the validation of the NEXT-100 design. More specifically, the goals of the prototype were the following: (a) to demonstrate good energy resolution in a large active volume; (b) to reconstruct the topological signature of electrons in high-pressure xenon gas (HPXe); (c) to test long drift lengths and high voltages; (d) to understand gas recirculation and purification in a large volume, including operation stability and robustness against leaks; and (e) to understand the collection of light and the use of wavelength shifters (WLS).

6.1 Gas system

The functions of the gas system of NEXT-DEMO are the evacuation of the detector, its pressurization and depressurization with xenon (and argon), and the recirculation of the gas through purification filters. A schematic of the system is shown in figure 6.1.1.

The standard procedure during normal operation of the detector starts with the evacuation of the vessel to vacuum levels around 10^{-5} mbar, followed by an argon purge. A second vacuum step exhausts the argon from the system. The detector is then filled with xenon gas to pressures up to 15 bar. The xenon can be cryogenically recovered to a stainless-steel bottle connected to the gas system by simply immersing this in a dewar filled with liquid nitrogen. The pressure regulator of the bottle is fully opened to allow the xenon gas to flow inside it (due to the temperature difference) and freeze.

The vacuum pumping system consists of a roughing pump (Edwards XDS5 scroll vacuum pump) and a turbo molecular pump (Pfeiffer HiPace 300). Vacuum pressures better than 10^{-7} mbar have been obtained after pumping out the detector for several days. The recirculation loop is powered by an oil-less, single-diaphragm compressor (KNF PJ24999-2400) with a nominal flow of 100 standard liters per minute. This translates to an approximate flow of 10 liters per minute at 10 bar, thus recirculat-

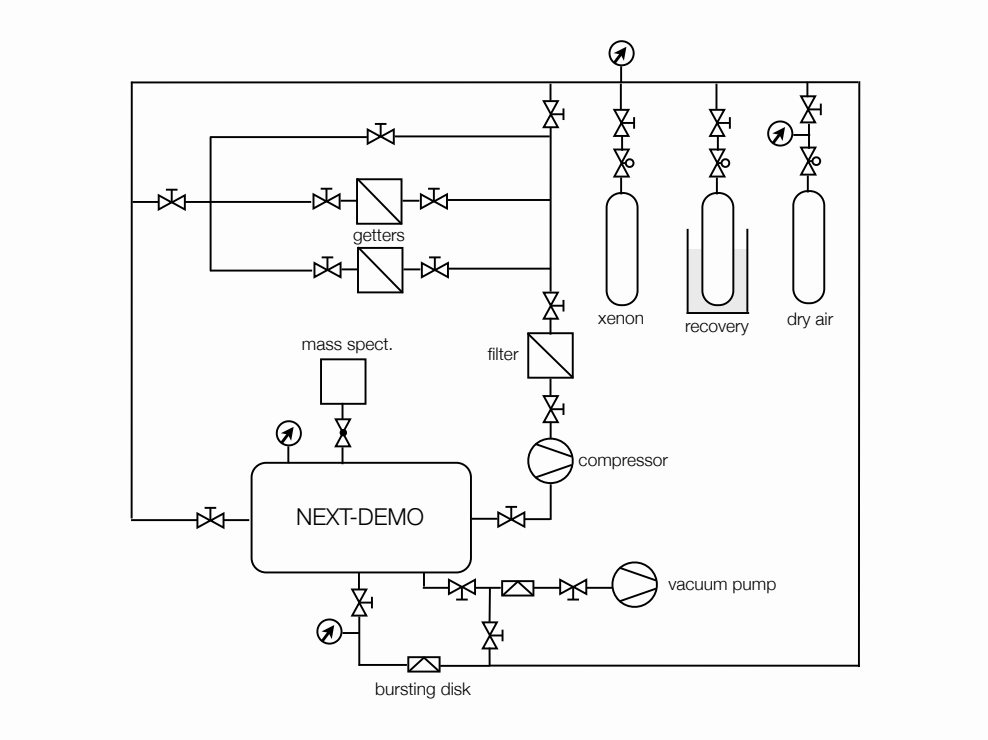

Figure 6.1.1: Simplified schematic of the gas system of NEXT-DEMO.

ing the full volume of NEXT-DEMO ($\sim$ 45 L) in about 5 minutes. The gas system is equipped with both room-temperature (SAES MC50) and heated *getters* (SAES PS4-MT15) that remove electronegative impurities (O_2, H_2O, etc.) from the xenon. All the gas piping, save for the inlet gas hoses and getter fittings, are 1/2 inch diameter with VCR fittings. A set of pressure relief valves (with different settings for the various parts of the system) and a burst disk in the vacuum system protect the equipment and personnel from overpressure hazards.

The operation of the gas system has been, in general, very stable. The detector has run without interruption for long periods of up to 6 weeks with no leaks and continuous purification of the gas. However, one major leak occurred when the diaphragm of the recirculation pump broke, causing the loss of the xenon volume contained in the chamber. This led to the installation of an emergency mechanism that, in the event of pressure drop, automatically closes those valves connecting the pump to the rest of the gas system. Since installation, only one major failure has taken place which the emergency system isolated without loss of gas. Micro-leaks, on the level of 0.005 bar per day, due to bad connections in the gas system have also been detected making it necessary to introduce additional xenon to maintain pressure. The micro-leaks where found and properly repaired allowing for a stable detector operation in the last year.

Several improvements to the initial design of the NEXT-100 gas system have been made thanks to the initial data runs described in this paper. These include the recognition of the importance of reliability of the main pump as well as the decision to use hot getters as the main gas purification stage due to their negligible emission of radon compared to that of room-temperature getters.

6.2 Pressure vessel

The pressure vessel of NEXT-DEMO, shown in figure 6.2.1, is a stainless-steel (grade 304L) cylindrical shell, 3 mm thick, 30 cm diameter and 60 cm length, welded to CF flanges on both ends. The two end-caps are 3-cm thick plates with standard CF knife-edge flanges. Flat copper gaskets are used as sealing. The vessel was certified to 15 bar operational pressure. It was designed at IFIC and built by Trinos Vacuum Systems, a local manufacturer. Additional improvements — including the support structure and a rail system to open and move the end-caps — have been made using the mechanical workshop at IFIC.

The side of the chamber includes 8 CF40 half-nipples. One set of 4 is located in the horizontal plane while the other is displaced towards the underside with respect to the first set by 60°. These contain radioactive source ports used for calibration of the TPC. The ports are made by welding a 0.5 mm blank at the end of a 12 mm liquid feedthrough. On top of the vessel and along the vertical plane there are three additional half-nipples (CF130, CF67 and CF80) used for high-voltage feeding and connection to a mass spectrometer (through a leak valve). On the opposite side, at the bottom, a CF100 port connects the pressure vessel to the vacuum pumping system. A guillotine valve closes this connection when the vessel is under pressure. The end-caps include several CF ports for the connections to the gas recirculation loop and for the feedthroughs (power and signal) of the PMT planes.

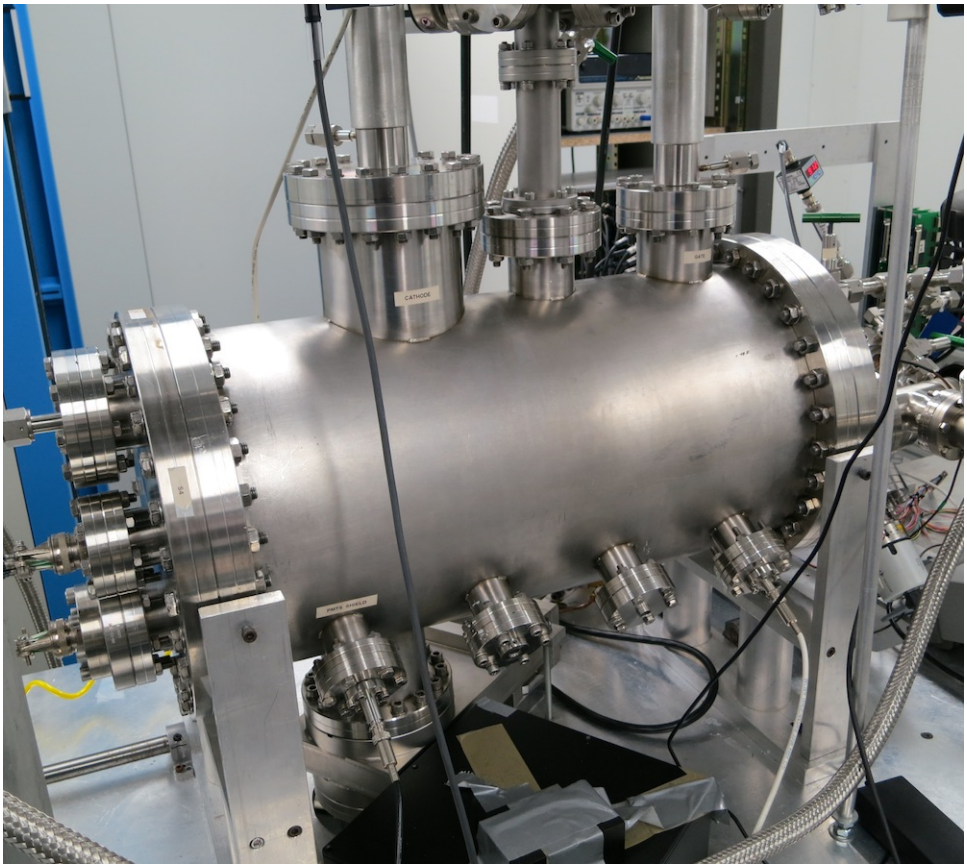

Figure 6.2.1: The pressure vessel of NEXT-DEMO.

6.3 Time projection chamber

Three metallic wire grids — referred to as *cathode*, *gate* and *anode* — define the two active regions of the chamber (see figure 6.3.1): the 30 cm long *drift region*, between cathode and gate; and the 0.5 cm long *EL region*, between gate and anode. Gate and anode were built using stainless-steel meshes with 88% open area (30-μm diameter wires, 50 wires/inch) clamped in a tongue-and-groove circular frame with a tensioning ring that is torqued with set screws to achieve the optimum tension. The cathode was built in a similar fashion by clamping parallel wires 1 cm apart into another circular frame.

The electric field in the TPC is created by supplying a large negative voltage to the cathode then degrading it across the drift region using a series of metallic rings of 30 cm diameter spaced 5 mm apart and connected via 0.5 GΩ resistors. The rings were manufactured by cutting and machining aluminum pipe. The gate is at negative voltage so that a moderate electric field — typically of 2.5 to 3 kV cm^{-1} bar^{-1} — is created between the gate and the anode, which is at ground. A *buffer region* of 10 cm between the cathode and the energy plane protects this from the high-voltage by degrading it safely to ground potential.

The high voltage is supplied to the cathode and the gate through custom-made high-voltage feed-throughs (HVFT), shown in figure 6.3.2, built pressing a stainless-steel rod into a Tefzel (a plastic with high dielectric strength) tube, which is then clamped using plastic ferrules to a CF flange. They have been tested to high vacuum and 100 kV without leaking or sparking.

A set of six panels made of PTFE (Teflon) are mounted inside the electric-field cage forming a *light tube* of hexagonal cross section (see figure 6.3.3) with an apothem length of 8 cm. PTFE is known to be an excellent reflector in a wide range of wavelengths [117], thus improving the light collection efficiency of the detector. In a second stage, the panels were vacuum-evaporated with TPB — which shifts the UV light emitted by xenon to blue ($\sim$ 430 nm) — in order to study the improvement in re-

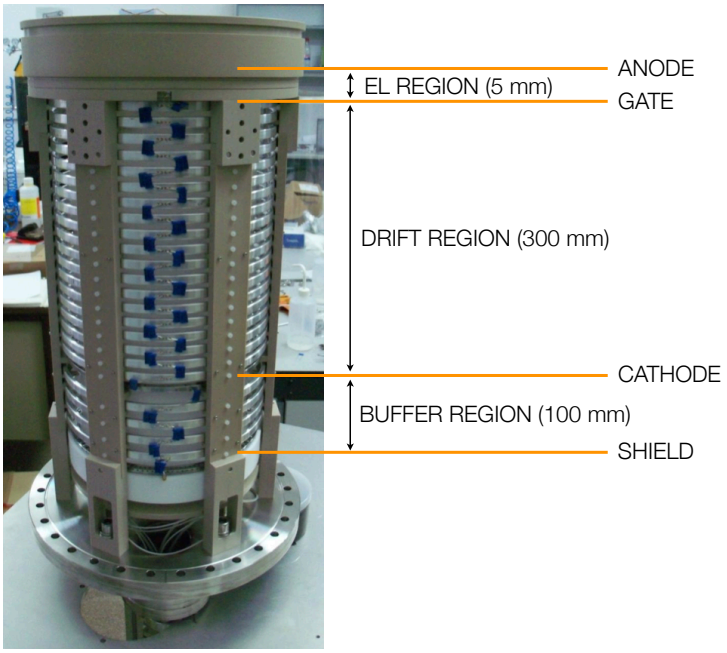

Figure 6.3.1: External view of the time projection chamber mounted on one end-cap. The approximate positions of the different regions of the TPC are indicated.

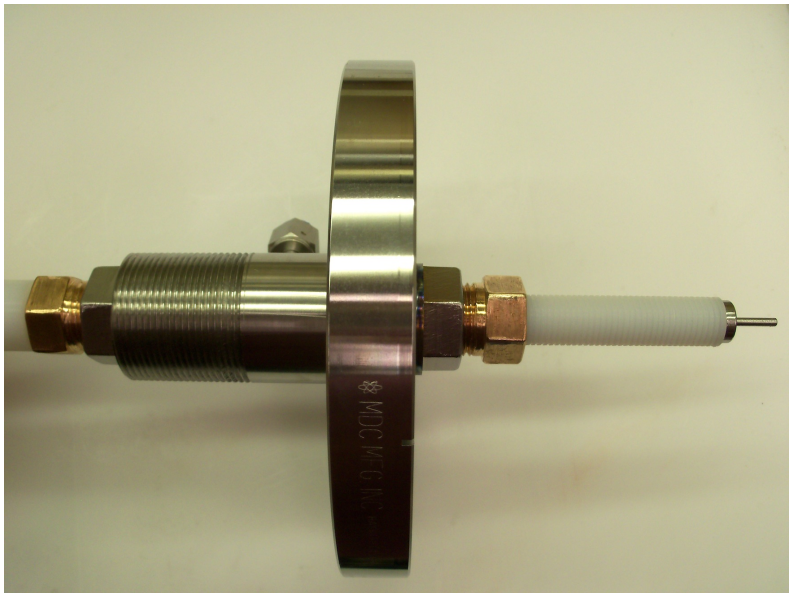

Figure 6.3.2: The NEXT-DEMO high-voltage feed-through, designed and built by Texas A&M.

flectivity and light detection. Figure 6.3.3 (bottom panel) shows the light tube illuminated with a UV lamp after the coating.

Six bars manufactured from PEEK, a low outgassing plastic, hold the electric-field cage and the energy plane together. The whole structure is attached to one of the end-caps using screws, and introduced inside the vessel with the help of a rail system. All the TPC structures and the HVFT were designed and built by Texas A&M.

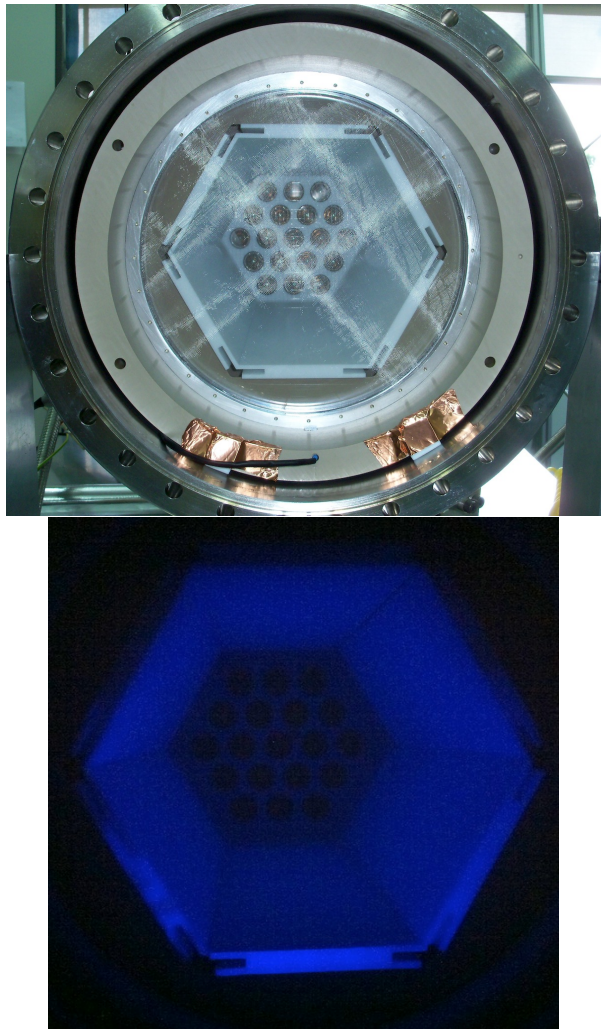

Figure 6.3.3: View of the light tube from the position of the tracking plane. Top: The meshes of the EL region can be seen in the foreground, and in the background, at the end of the light tube, the PMTs of the energy plane are visible. Bottom: The light tube of NEXT-DEMO illuminated with a UV lamp after being coated with TPB.

6.4 Energy Plane

In NEXT-DEMO, the energy plane (see figure 6.4.1) is equipped with 19 Hamamatsu R7378A photomultiplier tubes. These are 1-inch, pressure-resistant (up to 20 bar) PMTs with acceptable quantum efficiency ($\sim$ 15%) in the VUV region. The resulting photocathode coverage of the energy plane is about 39%. The PMTs are inserted into a PTFE holder following a hexagonal pattern. A grid, known as *shield* and similar to the cathode but with the wires spaced 0.5 cm apart, is screwed on top of the holder and set to 500 V. As explained above, this protects the PMTs from the high-voltage set in the cathode, and ensures that the electric field in the 10-cm buffer region is below the EL threshold.

The PMTs are connected to custom-made electrical bases that are used as voltage dividers, and also allow the extraction of the signal induced in the PMTs. This requires a total of 38 cables inside the pressure vessel connected via feed-throughs.

The goals of the PMT plane are first to measure the energy of the events recorded as it is related with total amount of light detected by the PMTs; and second, to detect the primary scintillation signal produced by each event which is fundamental to position the event inside the field cage and can be used also as a trigger signal. More details about the energy measurements performed by the PMT plane are dscribed in chapter 7.

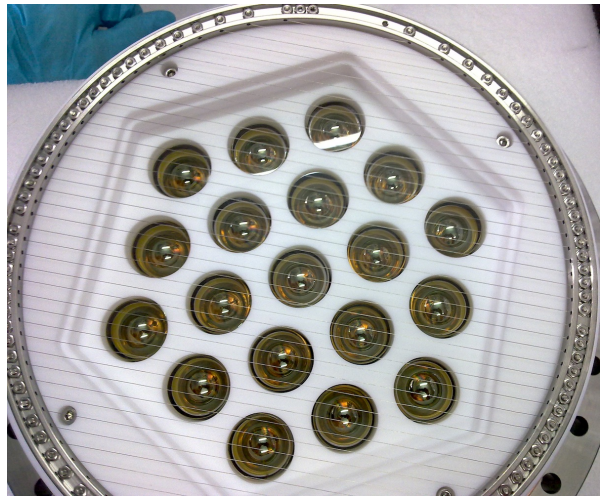

Figure 6.4.1: The energy plane of NEXT-DEMO equipped with 19 Hamamatsu R7378A PMTs. The wires in front of the PMTs are the so called "shield" to fix the voltage in front of the PMTs and protect them from the Cathode Voltage.

6.4.1 Energy Plane Electronics

The two optical signals in the NEXT detector concept have very different scales, and the photomultipliers and their front-end electronics must be ready to handle both. Primary scintillation results in weak (a few photoelectrons per photomultiplier) and fast (the bulk of the signal comes in about 20 ns) signals, whereas the secondary scintillation — that is, the EL-amplified ionization — is intense (hundreds to thousands of photoelectrons per PMT) and slow (several microseconds long).

The gain of the PMTs in the NEXT-DEMO energy plane was adjusted to around 5×10^6 to place the mean amplitude of a single photoelectron pulse well above electronic system noise.

The PMTs produce fast signals (less than 5 ns wide) making the shaping of the detector output necessary so that during the digitization with the 40MHz ADC the signal is sampled well enough to have a good estimation of the charge. This process also performs the important function of eliminating high frequency noise.

The design uses a single amplification stage based on a fully differential amplifier

THS4511, which features low noise ($2\,nV/\sqrt{Hz}$) and provides enough gain to mantain the signal amplitude above the noise level after shaping in the following stage. Amplification is followed by a passive RC filter with a cut frequency of 800 kHz. This filtering obtains the desired effect of stretching the signal to allow the acquisition of many samples per single photo-electron. The front-end circuit for NEXT-DEMO was implemented in 7 channel boards and connected via HDMI cables to 12-bit 40-MHz digitizer cards. These digitizers are read out by the FPGA-based DAQ modules (FEC cards) that buffer, format and send event fragments to the DAQ PCs. As for the FEC card, the 16-channel digitizer add-in card was designed in a joint effort between CERN and the NEXT Collaboration within the RD-51 program [118]. These two cards are edge mounted to form a standard 6U220 mm Eurocard. An additional FEC module with a different plug-in card is used as trigger module. Besides forwarding a common clock and commands to all the DAQ modules, it receives trigger candidates from the DAQ modules, runs a trigger algorithm in the FPGA and distributes a trigger signal. The trigger electronics also accept external triggers for detector calibration purposes.

6.5 Tracking Plane

6.5.1 Tracking Plane with PMTs

As mentioned already, the first tracking plane of the NEXT-DEMO detector also uses 19 Hamamatsu R7378A PMTs, as shown in figure 6.5.1, but operated at lower gain. They are also held by a PTFE honeycomb, mirroring the energy plane. The PMT windows are located 2 mm away from the anode mesh. Position reconstruction is based on energy sharing between the PMTs, being therefore much better than the distance between PMTs (35 mm from center to center).

Position reconstruction with PMTs was used in the first stages of the detector because it allowed for a much simpler commisioning and understanding of the energy plane, trigger and other aspects of the detector with $\sim$ 10 times less number of channels to debug. Of course, reconstruction of the topology in detail with PMTs is not

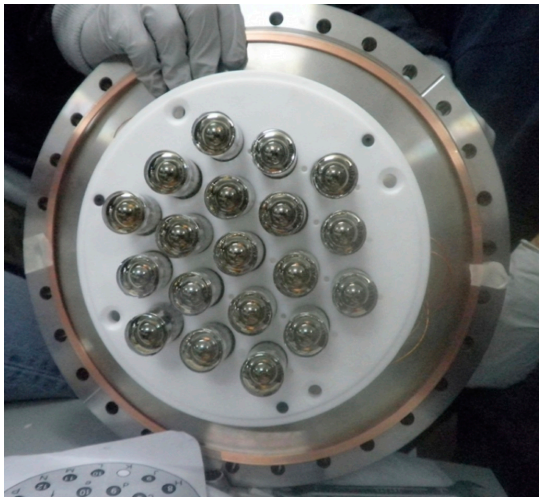

Figure 6.5.1: The tracking plane of NEXT-DEMO in the PMTs configuration, equipped with 19 Hamamatsu R7378A PMTs.

possible but a good average position reconstruction is easily achieved (7.5) and fiducialization of the events is possible.

6.5.2 Tracking plane with SiPMs

The arguments discussed in section 5.3 led to the choice of a tracking plane for NEXT-DEMO instrumented with SiPMs at a sensor pitch of 1 cm. The plane consists of 256 Hamamatsu S10362-11-050P SiPMs distributed between 4 boards, each with 64 sensors (see figure 6.5.2) and is positioned 2 mm behind the EL production region. The active area of a sensor is 1 mm^2 comprised of pixels of side 50 μm. Operating at a bias voltage of 73 V results in a gain of $\sim$ $7.5x10^5$ at room temperature (precise calibration described in section 6.7.2) and dark current at the level of 0.2-0.3 photoelectrons μs^{-1}.

The SiPMs are mounted on multilayer *CuFlon*® PCBs (PTFE substrate with copper layers, gold plated). Each board is supplied with one bias voltage via a FPC (Flat Printed Circuit) kapton cable which also extracts the sensor signals and the readings

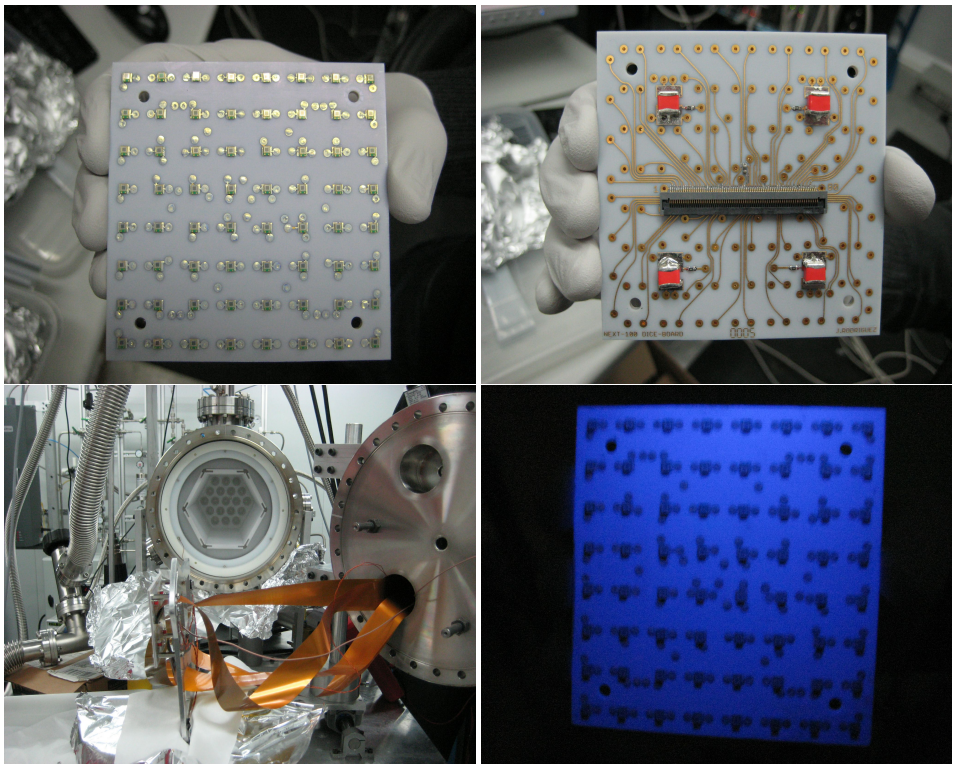

Figure 6.5.2: Details of the *CuFlon*® boards and their mounting in NEXT-DEMO.

of a thermister positioned next to the board. In order to maintain the nominal supply voltage of the sensors and reduce detector dead time, 4 tantalum capacitors are connected to each board and supply the sensors with the required voltage after read-out.

Coating

Since the SiPMs are not directly sensitive at the emission wavelength of Xe (170 nm), it is necessary to use a wavelength shifting coating. TPB has been used since its emission properties match well with the sensitivity of the SiPMs and because it was used to coat the light tube. The SiPM PCBs (DICE boards) were coated to a TPB thickness of 0.1 mg cm^{-2} by evaporation under high vacuum using the techniques described in detail in [119]. The peak of the emission spectrum of TPB (430 nm) matches the region of highest quantum efficiency of the SiPMs well and at the selected TPB thickness the transmittance of the shifted light is $> 96\%$ [119]. While higher transmittance is possible with a thinner coating, the variance of the effective conversion efficiency tends to increase. The thickness chosen is, as such, a good compromise between these two competing considerations.

6.6 Tracking Plane Electronics

6.6.1 PMTs Electronics

The signals in the anode PMTs used for tracking were very different from the signals of the energy plane and consequently the electronics are also different. As the tracking PMTs were not used for energy measurement nor for primary scintillation detection, the signal over background ratio requirements were relaxed. Moreover, the number of photoelectrons in a single PMT could reach much higher levels than in the energy plane.

Those differences allow the simplification of the electronics opening the possibility to use commercial amplifiers. A factor 10 amplification was applied using *Phillips 600023423042* . After the amplification a RC filter with a cut-off frequency of 30MHz is applied to reduce the noise level.

6.6.2 SiPM Electronics

Signal processing, digitization and read-out is performed using an electronics chain comprised of a 16-channel front-end electronics board with 16 analogue paths, a digital processor and a front-end concentrator (FEC) which was developed by CERN and the NEXT Collaboration under the auspices of the RD51 read-out systems R&D collaboration [118]. Signals from the tracking plane first pass through a 3-stage analogue preprocessing before being digitized. In the first stage, the signals are subject to pre-amplification and filtering in order to adapt them to the correct line impedance. At this stage, offset control can be used to optimize the dynamic range of the system. Signals are then passed through a gated integrator with a variable integration time. An integration interval of 1 μs was chosen for the data presented to limit the possibility of either saturating the ADC — a saturation level of greater than 200 pe μs^{-1} is achieved — or exceeding the maximum data-uplink rate. This interval results in a z position resolution of approximately 1 mm — considering a nominal drift velocity of 1 mm μs^{-1}. The final analogue stage inverts the signal to match the ADC dynamic range.

Digitization of the signals is controlled via a small, low-power Xilinx Spartan-3 FPGA charged with the operation of the gated integrators, the building of a digitized frame via a 12-bit 1 MHz ADC and the transfer of these frames to the upstream read-out stage (the FEC). The SiPM front-end boards and the FEC are connected by means of a high-speed full duplex link consisting of two LVDS pairs in each direction over a standard CAT-6 network cable. The FEC sends a master clock to the front-end board FPGA over one of the LVDS pairs, thus providing system-level synchronization. A second downstream pair is used to send trigger and configuration commands to the front-end board. Data are sent to the DAQ PC via gigabit Ethernet link.

6.7 Sensors Calibration

In order to achieve a reliable, stable measurement of the energy resolution of the detector, the photo-detectors must be calibrated so that the number of photo-electrons detected by each sensor can be accurately calculated from the digitized response. This calibration must then be monitored during run time as the calibration constants can be sensitive to external effects including the temperature and pressure as well as to degradation of the sensors due to age or the occasional sparks present in the TPC. A number of complementary methods are used in NEXT-DEMO in order to achieve a reliable calibration.

6.7.1 Energy Plane Calibration

The PMTs of the energy plane are calibrated using their single photon response. This is performed in situ using a 400 nm LED mounted in the centre of the tracking plane. The PMTs are illuminated at a LED intensity adjusted to limit the probability of the detection of more than 1 photoelectron resulting in a spectrum of the form shown in figure 6.7.1. The distribution for each PMT is then fitted using 3 Gaussian distributions representing the system noise, single photon and two photon response of the PMT. The single photon centroid in ADC counts represents the conversion factor between photoelectrons and ADC counts with the two photon centroid giving an indication of the robustness of the measurement by its relative position. The calibration was repeated regularly during data taking both in dedicated LED runs and taking advantage of the low rate of the radioactive sources under study to take small groups of LED triggered events every few hundred source triggers. In this way the stability of the calibration could be monitored and any change in conditions isolated to within a small set of events in the analyses. The spectra were also fitted with a function which restricted the relative values of the Gaussian parameters according to Poisson statistics with consistent results. The calibration of the PMTs has been found to be stable over the course of data taking.

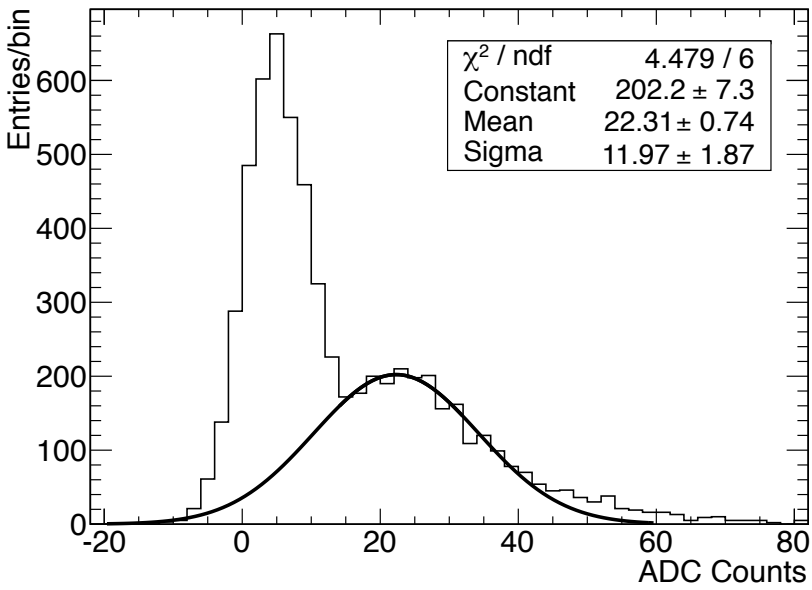

Figure 6.7.1: Typical single photo-electron spectrum of one of the energy plane PMTs. The single photon response is deconvoluted from pedestal and the two-photon response.

6.7.2 Tracking Plane Calibration

The sensitivity of SiPMs to atmospheric conditions is well documented (see, for example, [120]). For this reason and due to the method of bias of the sensors (see section 6.5.2) it was necessary to perform a pre-calibration of the sensors before mounting in the TPC. The absolute gain of each sensor was measured using its single photon response to illumination using a 400 nm LED as explained in [121, 122]. This allowed for the determination of the appropriate distribution of voltage among the individual sensors of a DICE and resulted in a gain spread of less than 4% after these adjustments.

However, the read-out chain of the sensors once mounted in the detector differs significantly from that of the external set-up. As such, an independent calibration is required to give a true representation of the relation between photoelectrons (pe) and ADC counts. A measurement of the dark current of the SiPM channels can give a direct indication of the conversion factor, however, the noise in the system means that the peaks of the dark current distribution are not always obvious. For this reason two independent techniques are used to perform an equalisation of the channels. The response of the channels to the X-ray peak present in source data and a photon transfer curve (PTC) [123] technique using a blue (400 nm) LED are presented here.

Gammas entering in the detector can interact with electrons in the K, L shells of the xenon atoms. These interactions produce electrons of $\sim$30 keV which, since they will travel only $\sim$0.6 mm in Xe at 10 bar [124], can be considered point-like events in the gas. Since the energy of these events is well defined they can be used to equalize the SiPM response.

The equalization is performed by considering, for each source event, only the SiPM with the largest observed charge. This results in spectra of the form shown in figure 6.7.2 after pe calculation using the externally determined constants. The x-ray peak is obvious at low energy and the contribution, in this energy region, from non-x-ray events is limited since only the maximum charge sensor is considered.

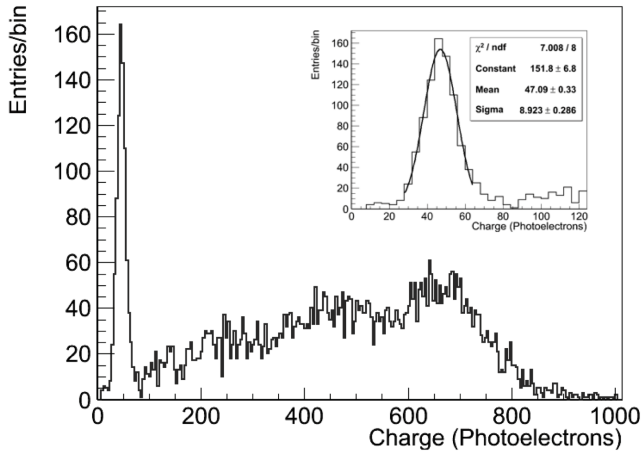

Figure 6.7.2: "Low energy" spectrum obtained with a ^{22}Na calibration source illuminating the detector. The x-ray peak and a gaussian fit for one of the SiPMs of the tracking plane are shown in the inset. The fit is performed for each SiPM in the plane.

While the x-ray method can be used over the course of a run with a radioactive source to monitor the equalization of the gains, it is not possible to measure the actual gain values using this method. As an additional method of absolute determination of the gain in the absence of the dark current method, the PTC [123] method using a blue LED has been proposed. Recording multiple LED pulses at increasing intensities, it can be demonstrated that there should exist a linear region of a plot of variance versus mean intensity where the shot noise of the arriving photons dominates over the other noise sources and hence the gradient is equivalent to the channel conversion gain:

$$S_{ADC} = G n_{pe}\,,\ \sigma^2_{ADC} = (G\sigma_{pe})^2 \tag{6.1}$$

$$\text{when photon stat. dominant } \sigma_{pe} = \sqrt{n_{pe}} \tag{6.2}$$

$$\therefore \sigma^2_{ADC} = G S_{ADC} \tag{6.3}$$

where S_{ADC} is the digitized response, n_{pe} is the number of photoelectrons, G is the

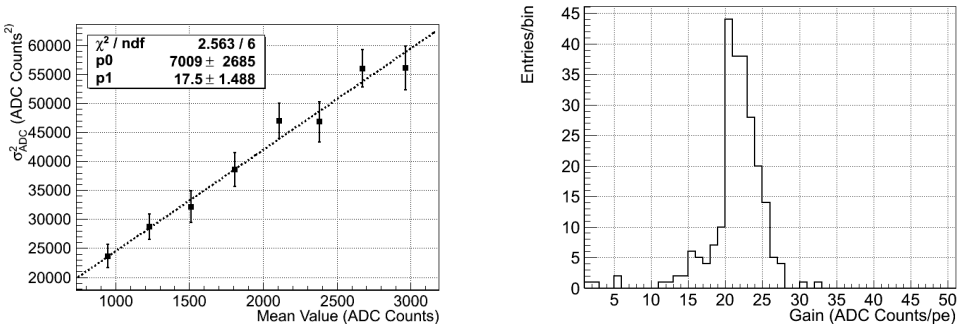

Figure 6.7.3: Extraction of conversion gain using the PTC method. Example linear fit (left) and the gains for all channels (right).

conversion gain and, σ_{ADC} and σ_{pe} are the standard deviations of the digitized signal and photoelectrons respectively. Care must be taken not to exceed the linear region of the SiPMs which is limited by the finite number of pixels. At the light levels used $<$40% of each channel's pixels are excited in general [122]. In this region of operation the SiPM response is linear. If a channel reaches light levels greater than this (equivalent to $\sim$3000 ADC) the points above this level are ignored in the fit both to avoid nonlinearity effects and the saturation of the ADC. Performing this measurement for each SiPM channel individually, the conversion gains can be determined. As can be seen in figure 6.7.3-*right panel* the gains, while being dispersed to a greater extent than those measured outside the chamber, are concentrated at values of $\sim$20. The few channels with G below 10 correspond to those which have been identified as being faulty and are excluded from further analysis. For the channels where dark current measurement is possible the gain measurements are found to be consistent.

6.8 Digital Trigger

6.8.1 Trigger Requirements

In NEXT type detectors, secondary scintillation light provides topological information. This topological information implies a large diversity of pulse structures when reading the secondary light. Therefore, the capability to trigger the detector using different characteristics of the pulses (height, time width, charge,...) is fundamental for an efficient event selection. On the other hand, the primary signal is mandatory to position the event inside the fiducial volume. Therefore, when triggering in S2, a long time window pre-trigger should be sent to look for the small S1 off-line. Trigger on S1 will decrease the data size per event since this window is not necessary. Also, significant time reduction of data processing off-line is observed when triggering in S1. The trigger system should be flexible enough to allow triggering in such different signals as S1 and S2. At the same time, the trigger efficiency has to be valued, the capability of selecting different channels to trigger in coincidence is mandatory. Finally, in order to maximize the flexibility of the system, combinations of different triggers (S1+S2; Figure 6.8.1), within a long time window will result in an extra-handle when looking for rare events.

The Trigger System is distributed among different modules and implemented on FPGA (see figure 6.8.2). DAQ modules also generate trigger candidates, based on the early energy estimation of the events received from the PMT plane and different pulse characteristics.

The Trigger module processes all the trigger candidates received and generates a trigger accept signal. Upon arrival of a trigger accept signal, buffered data in the DAQ modules are formatted and sent to the PC farm for off-line analysis.

The total trigger latency is about 4 μs. Half of this time is due to the transmission of the trigger candidates and the trigger accept, and the rest due to the processing

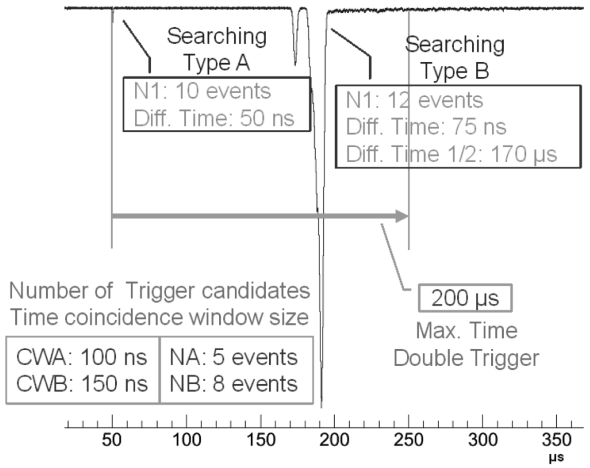

Figure 6.8.1: Example of the double trigger function. A number of PMTs are selected to send a trigger signal looking for an S1-like pulse (trigger type A). Once the trigger card reaches a trigger from the first group of PMTs it opens a 200μs window waiting for a second signal from a different group of PMTs. The trigger in that second group has been defined in order to detect a S2-pulse.

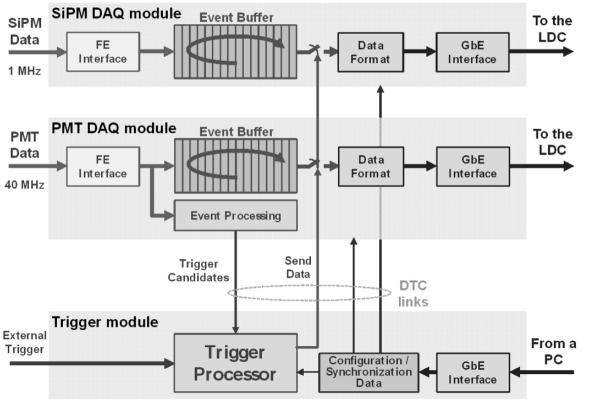

Figure 6.8.2: Trigger scheme for NEXT-DEMO. The PMTs FEC are recording the data in a circular buffer. At the same time, some of them have been defined as *trigger channels*. Every time one of those channels gets a trigger signal it sends a flag to the trigger FEC with information about the trigger. The trigger FEC collects all the trigger signals and looks for coincidence among channels if necessary. If all trigger conditions have been fulfilled, a send-data signal is sent to all FECs in the system.

itself. This latency does not affect the system due to the large buffer provided and the possibility to send a configurable number of pre-trigger data.

6.8.2 Trigger Event Processing

PMT channels in each DAQ module can be configured to generate trigger candidates. Channels are marked either as type A or B. This facility allows configuring the trigger to detect two different type of events.

Trigger candidates are generated for each PMT channel (Event Processing unit) by means of configurable thresholds on maximum amplitude, maximum and minimum energy, baseline deviation and maximum time of the event, combined with the energy estimation of the events (figure 5). Energy estimation is based on a self-calculated (moving average filter applied to the input signal) or a configurable fixed baseline. This allows an efficient rejection of background and non-interesting events.

6.8.3 Trigger Processor

The Trigger module implements a reconfigurable hardware algorithm (Trigger Processor). It is also able to accept an external trigger source, besides internal trigger candidates defined as Type A and B in the DAQ modules. This allows different trigger modes of operation:

- Single trigger (external trigger or internal trigger type A).
- Double trigger (a combination of type A and B). In this mode, when trigger type A is detected, the trigger system waits a maximum pre- configured time for a trigger type B. In case this second trigger happens, the trigger module sends a trigger accept to the system. In this case, data stored in the DAQ modules are sent to the PC farm. In the other case, the system looks for another trigger of type A, starting the trigger accept searching process.

Two more levels of discrimination are available since it is possible to select the minimum number of channels per trigger candidate type in a configurable time window to produce a trigger accept.

Figure 6.8.1 shows an example of Double Trigger Mode configuration. Trigger accepts are generated if at least 5 trigger candidates of type A in a time window of 100ns are received, and then, in a maximum time of 200μs, at least 8 trigger candidates of type B in 150ns are also received.

That was the thing about the world: it wasn't that things were harder than you thought they were going to be, it was that they were hard in ways that you didn't expect.

Lev Grossman, *The Magician King*

7

NEXT-DEMO PMT Results

One major objective for NEXT-DEMO was to demonstrate the energy resolution capabilities of the technology used (SOFT+EL). In this chapter we will focus on the analysis and results with the two first configurations of the detector. In those two configurations the fiducialization of the events was performed using a plane of 19 PMTs behind the EL region. (*see section 6.5*). The size of the NEXT-DEMO detector limits the energy of the gammas used in the detector for its calibration due to the extended size of the gammas in gas. In that case, gammas with energies in the range of 500-600 keV (^{22}Na and ^{137}Cs) have been used to perform the study.

The following sections describe with detail the sources used and the analysis chain used to reach the final energy resolution. The results where published in [125].

7.1 Analysis of ^{22}Na gamma-ray data

The response of the NEXT-DEMO detector was studied using a 1-μCi ^{22}Na calibration source placed at the port near the TPC cathode. Sodium-22 is a long-lived β^+ radioactive isotope, and the annihilation of the positron emitted in its decay, which rarely travels more than 1 mm, results in two back-to-back 511-keV gammas. The coincident detection of the forward gamma in the TPC and of the backward gamma in an external NaI scintillator coupled to a photomultiplier (see figure 7.1.1) was used to trigger the detector read-out. This arrangement optimized the acquisition of useful calibration data.

Two data sets are studied — one for the *ultraviolet configuration* (UVC), taken during February 2012, and another for the *blue configuration* (BC), taken during April 2012. The detector was constantly operated throughout both periods at a pressure of 10 bar. The TPC cathode was held at -32 kV and the gate at -12 kV, resulting in a drift field of 667 V $\cdot$ cm^{-1} and an EL field of 2.4 kV $\cdot$ cm^{-1} $\cdot$ bar^{-1}. The detector was, in general, operated without interruption with sparks in the EL region no more frequent than one per day. The frequency of these sparks reduced with improved gas quality reducing to a level where distortion of the data was minimal.

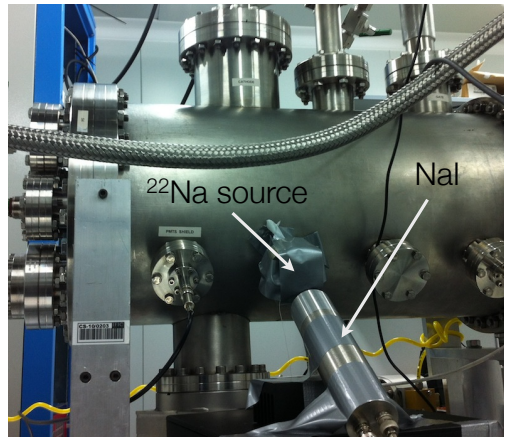

Figure 7.1.1: A view of NEXT-DEMO with the ^{22}Na calibration source installed in the port closest to the TPC cathode with the NaI scintillator used for event tagging visible in the foreground.

7.2 Trigger

During the UVC period, the S1 signals (primary scintillation) were not sufficiently intense to be used as an efficient trigger. Instead, the detector was triggered on the delayed coincidence between a signal in the NaI and an S2 signal (secondary scintillation) in the central PMT of the energy plane up to 400 μs later (a complete drift length plus a margin). Additionally, the NaI signal was required to have a charge greater than 5 photoelectrons, and S2 signal to have an integrated charge greater than 150 photoelectrons and a durations of between 0.5 μs and 10 μs to ensure that they corresponded to the detection of the 511-keV gammas and not to the abundant high energy signals from atmospheric muons. The trigger rate with this particular set of conditions was 1.5 Hz, consistent with the rate expected from the (weak) calibration source according to the detector simulation. Triggering on the S2 signal demanded that a long (450 μs) pre-trigger section of the PMT waveforms (buffered by the front-end electronics) be saved to allow the location of the S1 signals (which always precede the S2) during the offline data analysis.

The higher intensity of the S1 signals under the BC and several improvements in

the *firmware* of the front-end electronics made it possible to trigger the detector during the second period on the coincidence (within 25 ns) of a NaI signal and an S1 in the energy plane. The integrated charge of the S1 was required to be in the range of 1 to 20 photoelectrons. Under these conditions the trigger rate rose to 2.5 Hz. However, the data size shrank by a factor of 2, since the long pre-trigger was no longer required.

7.3 Waveform processing and event selection

The recorded raw data — that is, the individual PMT *waveforms* in ADC counts — were processed in a series of steps. First, ADC pedestals were subtracted for all individual waveforms. The pedestal level was computed for each channel and each event using the first 10 000 samples in a waveform that were not considered statistical outliers. Second, using the (channel-dependent) gain calibration constants obtained with the methods described in the previous section, the pedestal-subtracted waveforms were converted from ADC counts to photoelectrons (pes). In order to limit the effect of statistical fluctuations and uncorrelated noise the signal of all PMTs is added and averaged. The resulting waveforms is then re-binned and used for identifying the different pulses. The re-binning factor used is different when looking for S1 or S2 pulses since its time duration are very different but the resulting bin width should allow sampling the pulses properly in both cases. For S1 pulses, as they are very short ($\sim 1\mu s$), the signal is re-bin to a 10 MHz sample rate (25% of the electronics sample rate). For S2 pulses, ($\sim 10\mu s$) the relevant information is the total charge of the pulse, being important to properly find the start and end points of it. In that case, the re-binning is increased up to 1MHz, having samples of $1\mu s$. Event selection was performed using a peak-finding algorithm which groups collections of consecutive samples rising above the baseline, and classifies these groups as S1-like or S2-like according to their width and total integrated charge. Peaks were considered S1-like (figure 7.3.1, bottom left) if their width was less than 3 μs and their total charge was

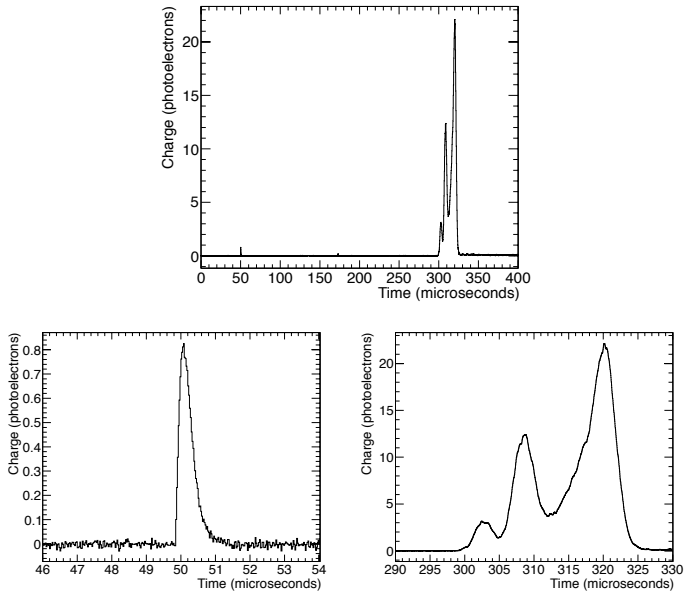

Figure 7.3.1: Top: Typical waveform of a 511-keV gamma-ray event obtained by summing the pedestal-subtracted, gain-corrected signals of the energy plane (and dividing by the number of PMTs, 19). Bottom: Close-up of the S1 (left) and S2 (right) pulses in the above waveform. The time difference between the leading edges of these pulses indicates the drift time, and hence the longitudinal coordinate of the event. S1 pulses are typically shorter than 3 μs (this width mostly due to the shaping of the front-end electronics) and have an average charge of at least 0.5 pe/PMT, whereas S2 peaks are longer than 3 μs and their integrated charge is at least 10 pe/PMT.

at least 0.5 pe/PMT, whereas peaks classified as S2-like (figure 7.3.1, bottom right) were at least 3 μs wide and had a minimum integrated charge of 10 pe/PMT.

Events without an S1-like peak or with more than one were discarded at this stage. Events were also rejected if the S1 was not synchronized within a 50 μs wide window with the NaI signal. For the BC data this check was redundant because the detector had been triggered on that coincidence, but it was kept nonetheless so that both data sets were processed with the same offline algorithms.

7.4 Primary signals in NEXT-DEMO

Charged particles interacting with the xenon gas lose their energy through two different atomic processes: *excitation* and *ionization*. Atomic de-excitations and the recombination of ionization pairs lead to the emission of (primary) scintillation light with a wavelength spectrum that peaks in the vacuum ultraviolet, around 172 nm. Several measurements of the average energy spent in the creation of one primary scintillation photon, W_{sci}, have been reported for xenon gas: 72 ± 6 eV [126], 111 ± 16 eV [127] and 76 ± 12 eV [128]. Their error-weighted mean is $W_{\text{sci}} = 77 \pm 5$ eV. These measurements were made using drift fields of approximately 0.5 kV/cm and gas pressures in the range of 1–20 bar. W_{sci} is correlated with the average energy spent in the creation of an ionization pair, measured as $W_{\text{ion}} = 22.0$ eV [129]. These two empirical values allow the calculation of the expected average ionization and scintillation yields for an electron of energy $E = 511$ keV at $N_{\text{sci}} = E/W_{\text{sci}} = (6640 \pm 430)$ scintillation photons and $N_{\text{ion}} = 23\,227$ ionization pairs. Only a small fraction of the scintillation photons is detected in practice due to the finite photocathode coverage of any detector and the inefficiencies in the collection of light.

The statistical fluctuations of the number of ionization pairs are smaller than those expected from a Poisson distribution, as described by Fano's theory [130]. Specifically, the variance of N_{ion} can be expressed as

$$\sigma^2_{\text{ion}} = F N_{\text{ion}} \,, \tag{7.1}$$

where $F = 0.15$ [100] is the so-called *Fano factor* of xenon gas. Therefore, the lowest achievable energy resolution for the measurement of the ionization of xenon is

$$\delta E/E = 2.35 \sqrt{F W_{\text{ion}}/E} \,. \tag{7.2}$$

Under the influence of the electric field applied to the detector, ionization electrons drift towards the anode at a velocity of approximately 1 mm/μs [131], while positive ions drift towards the cathode. Electrons are absorbed by electronegative

impurities in the gas at a rate described by:

$$N(t_D) = N_o \cdot \exp(-t_D/\tau)\,, \tag{7.3}$$

where t_D is the drift time and τ is the mean *electron lifetime* in the gas. During drift the electons also diffuse in 3 dimensions which results in a physical limit on the position resolution dependent on the drift field.

Once the primary electrons reach the EL region, they are accelerated between two parallel meshes giving rise to secondary scintillation (or electroluminescence). As explained in 5.2 the number of photons emitted per primary electron and per unit of drift length and pressure, the so-called *reduced electroluminescence yield*, is linearly proportional to the reduced electric field E/p above a threshold of about 0.83 kV cm^{-1} bar^{-1} and up to $\sim$ 6 kV cm^{-1} bar^{-1} [132]:

$$\frac{Y}{p} = 140\,\frac{E}{p} - 116 \ \left[\text{photons electron}^{-1}\,\text{cm}^{-1}\,\text{bar}^{-1}\right] \tag{7.4}$$

The fluctuations associated with the electroluminescence production are much smaller than the Fano factor and, hence, the energy resolution of the detector is proportional to the fluctuations in ionization and in the response of the photodetection system [100, 133].

In NEXT-DEMO the width of the EL region (delimited by the gate and anode meshes) is 0.5 cm, and for both the UVC and BC periods the operating pressure was 10 bar and the voltage across the grids was 12 kV. These parameters correspond to a reduced electric field of 2.4 kV cm^{-1} bar^{-1}, or equivalently, according to equation (7.4), 1 100 photons per primary electron emitted across the 0.5 cm of the EL region of NEXT-DEMO.

As mentioned in section 6.4, the energy plane of NEXT-DEMO detects a fraction of the secondary scintillation to provide a precise measurement of the total energy deposited in the chamber. More precisely, the energy of an event is defined as the

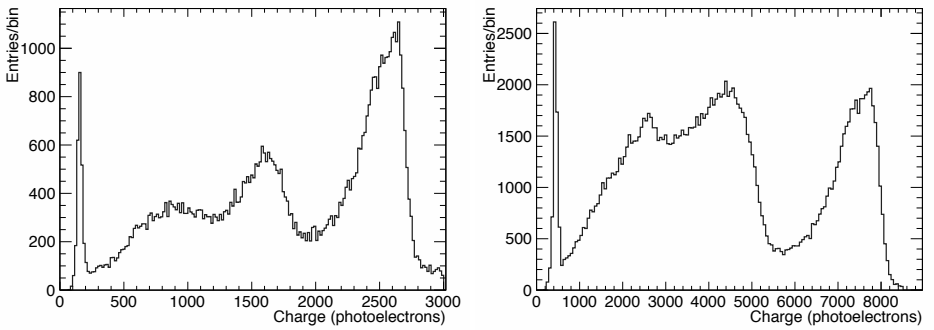

Figure 7.4.1: Raw energy spectrum — defined as the total integrated secondary-scintillation (S2) charge measured by the energy plane divided by the number of PMTs — recorded in NEXT-DEMO for the *ultraviolet* (top panel) and *blue* (bottom panel) configurations. From left to right in the spectra, the xenon x-ray peak, the Compton edge and the full energy peak are clearly visible in spite of the mediocre energy resolution before corrections. The discrepancy between the two spectra in the relative size of the Compton edge and the photoelectric peak is due to the different configuration of the detector trigger for the two periods.

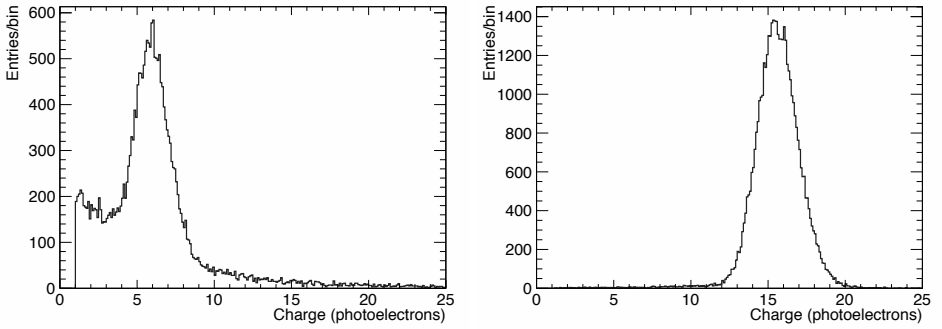

Figure 7.4.2: Intensity of the primary scintillation (S1) signal — i.e., integrated charge of the S1 peak of the energy-plane summed waveform — per PMT for photoelectric (full-energy) events. Top, for the *ultraviolet* configuration; bottom, for the *blue* configuration.

total integrated charge of all the S2 peaks normalized to the number of PMTs in the energy plane. Figure 7.4.1 shows the raw energy spectrum recorded in the chamber for both configurations. The xenon x-ray peak at low energy is clearly visible, as well as the Compton spectrum and the full-energy photoelectric peak. The TPB-coated light tube improves the light collection by a factor of 3 both at the photopeak and for the S1 signal (see 7.4.2). This improvement was attributed to the increased quantum efficiency at the emission peak of the TPB ($\sim$ 430 nm) and the near-perfect reflectivity of PTFE at this wavelength.

Figure 7.4.3 shows the correlation between the S1 and S2 signals (after spatial corrections; see section 7.5) for both the UVC and BC. Notice that the island of full-energy (photoelectric) events shows no indication of correlated fluctuations between S1 and S2, like those observed with alpha particles [131] or in liquid xenon [93].

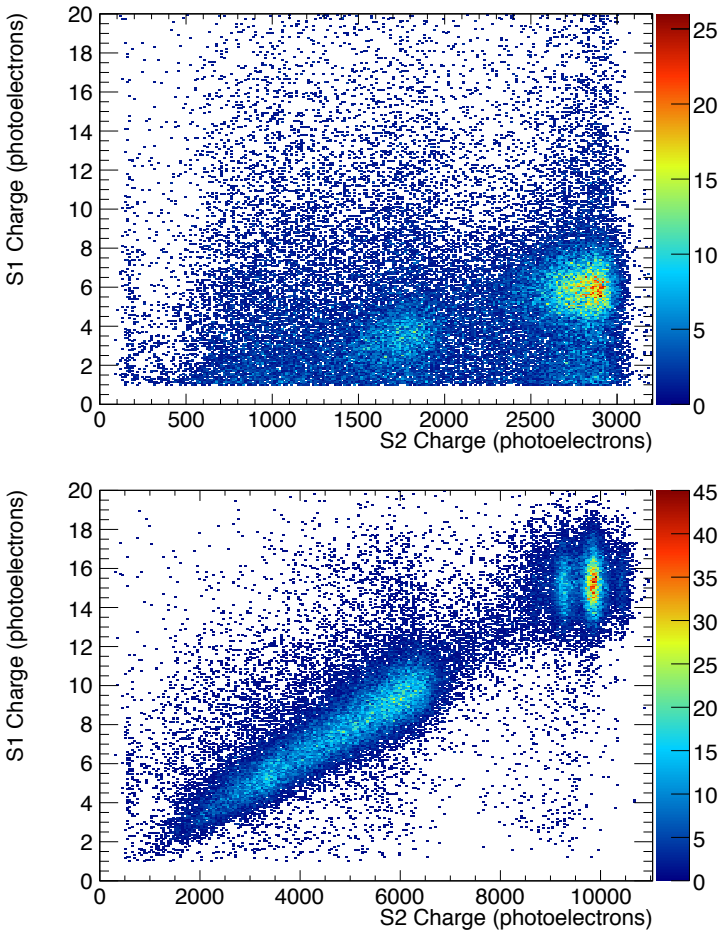

Figure 7.4.3: Correlation between the total integrated charge (per PMT) of the S1 and the S2 signals (after spatial corrections) for the full spectrum of interactions resultant from the ^{22}Na source. Top, for the *ultraviolet* configuration; bottom, for the *blue* configuration. The island of full-energy events shows no indication of correlated fluctuations between S1 and S2.

7.5 Energy resolution analysis

The data of the raw energy spectrum shown in figure 7.4.1 are affected by several factors that contribute to degrade the intrinsic energy resolution of gaseous xenon. An important factor is the position-dependent response of the detector. In order to compensate for this effect the energy recorded is corrected for according to the reconstructed position in the detector. The reconstructed energy, E_{rec}, can be parameterized as the product of the measured energy E_{obs} and a certain *detector response function* η:

$$E_{\text{rec}} = E_{\text{obs}}(x, y, z) \cdot \eta(x, y, z). \tag{7.5}$$

However, the position of an event is always reconstructed with some finite resolution. The longitudinal position z' can be reconstructed with high precision using the time between S1 and S2 signals and the *drift velocity*, measured to be $\sim 1\,\text{mm}/\mu\text{s}$ [131]. The x' and y' coordinates are reconstructed using the *barycentre* of the tracking-plane PMTs with recorded signal:

$$x' = \frac{\sum_i A_i\, x_i}{\sum_i A_i}\,, \quad y' = \frac{\sum_i A_i\, y_i}{\sum_i A_i} \quad \text{and} \quad R' = \sqrt{x'^2 + y'^2}\,, \tag{7.6}$$

where A_i is the integrated charge of the S2 measured by PMT i, which is positioned at $x_i y_i$. Since the events considered in this analysis have, in general, an extent in the detector of only a few mm — the average effective extent, considering multiple scattering, of an electron of 511 keV being about 20 mm — they are considered point-like for the purposes of energy correction. More energetic (and thus longer) tracks would have to be segmented and a different correction applied to the resulting sections.

The reduced position resolution afforded by the limited number of PMTs in the tracking plane and their large surface area means that the barycentre tends to be reconstructed with a bias towards the centres of the PMTs and detector, as seen in figure 7.5.1. For this reason, the energy correction is calculated using events reconstructed in the volume defined by the cylinder centred on the central PMT with

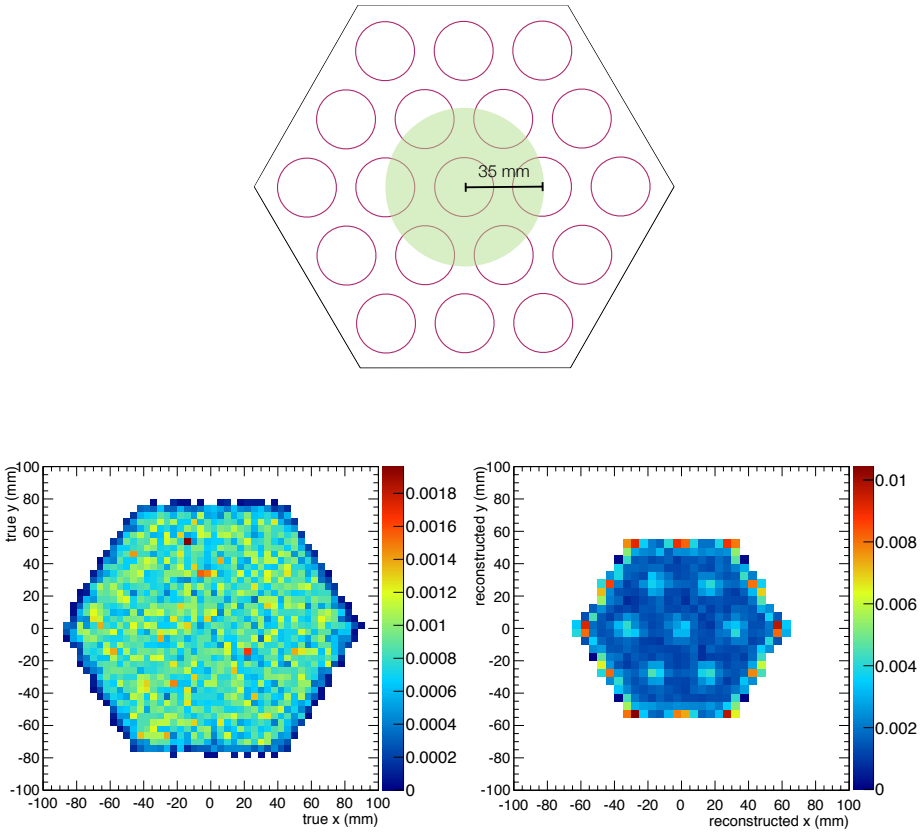

Figure 7.5.1: Top: Sketch of the NEXT-DEMO tracking plane showing the position of the photomultipliers (magenta circumferences) and the defined fiducial volume (green circle). Bottom: True average position (left panel; see text for definition) of simulated events compared to the reconstructed position (right panel) using the barycenter of the tracking plane. The original uniform distribution of events gets distorted, with events accumulating at the centre of the PMTs and in a region intermediate between the first and second rings of sensors.

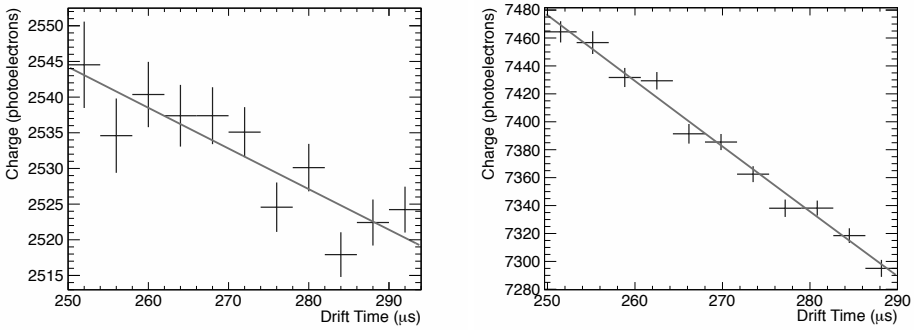

Figure 7.5.2: Dependence of the total integrated charge (energy) on drift time for photoelectric events. Left, for the *ultraviolet* configuration (UVC); right, for the *blue* configuration (BC). An exponential fit (red line) to the data determines the electron lifetime in the gas, obtaining 4.0 ms for the UVC and 1.7 ms for the BC.

cross-section radius $R' < 35$ mm (approximately 13% of the hexagonal cross section instrumented region). In this way the bias has a limited effect on the reconstruction.

The detector response function can be expressed as the product of three terms:

$$\eta(x, y, z) = Z(z') \cdot \rho(R') \cdot \Phi(\varphi') \,, \tag{7.7}$$

where $Z(z')$ is a function that depends only on the reconstructed longitudinal coordinate, $\rho(R')$ is a function that depends only on the reconstructed radius R', and $\Phi(\varphi')$ is a function that depends only on the reconstructed azimuthal coordinate $\varphi' = \tan^{-1}(y'/x')$ with possible factorization of these terms dependent on the amount of correlation between corrections.

Figure 7.5.2 shows the dependence of the total integrated charge on the longitudinal coordinate (expressed, in this case, as drift time) for full-energy (photoelectric) events in the interval $[250, 290]$ μs. This cut was chosen to limit the influence of edge effects at the cathode and the limited statistics that were available for events with drift time less than 250 μs (due to the source port position). Fitting a negative expo-

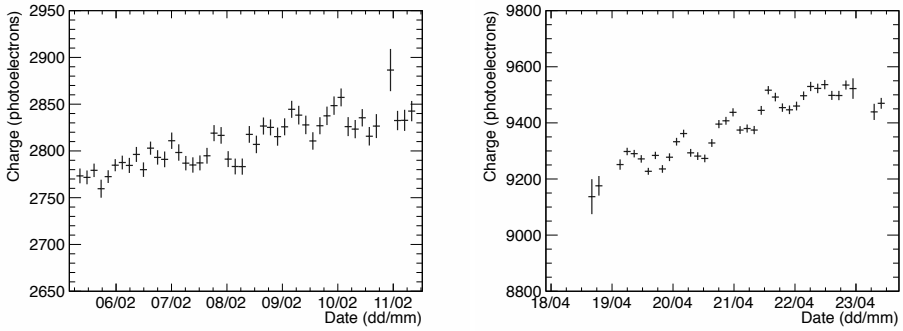

Figure 7.5.3: Evolution of the average S2 charge of the photoelectric peak during the data-taking period for both the UVC (left) and the BC (right).

nential to a set of data allows the determination of the electron lifetime in the gas as demonstrated by equation 7.3. Knowledge of this term enables the calculation of the correction term $Z(z')$ since it is dominated by electron attachment. The data yield τ: 4.0 ± 0.4 ms for the UVC and 1.7 ± 0.4 ms for the BC. As mentioned in section 6.1, new xenon (not clean) had to be added periodically to the detector during the BC runs due to a micro-leak, and hence the quality of the gas was generally worse than that in the UVC, and a greater amount of attachment was expected.

The radial correction — that is, the term $\rho(R')$ in equation (7.7) — was computed numerically by fitting a spline function to the profile histogram (figure 7.5.4, top left panel) of the recorded energy with the reconstructed radius for photoelectric events and normalizing to the value for $R = 0$. The correction was then applied event by event. The result can be seen in the top right panel of figure 7.5.4. The azimuthal correction, $\Phi(\varphi')$, was calculated the same way using the $\rho(R')$-corrected data — see the bottom panels of figure 7.5.4.

Figure 7.5.5 shows the photoelectric peak region of the corrected energy spectrum of 511-keV gamma rays from ^{22}Na in the fiducial volume of NEXT-DEMO for the two studied configurations. A gaussian fit to the peak yields an energy resolution of 2.89% FWHM for the UVC and 1.75% FWHM for the BC. Improved energy resolution for

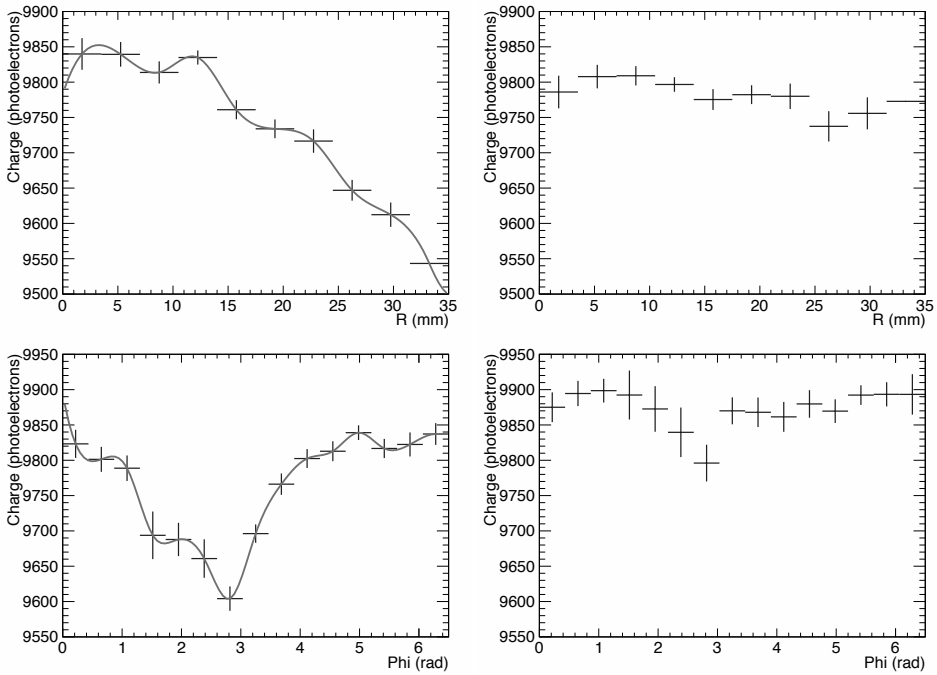

Figure 7.5.4: Radial (top panels) and azimuthal (bottom panels) corrections to the signal recorded by the NEXT-DEMO energy plane under the *blue* configuration. The correction is described by a spline fitted to the data (left panels), and then applied to the data event by event (right panels).

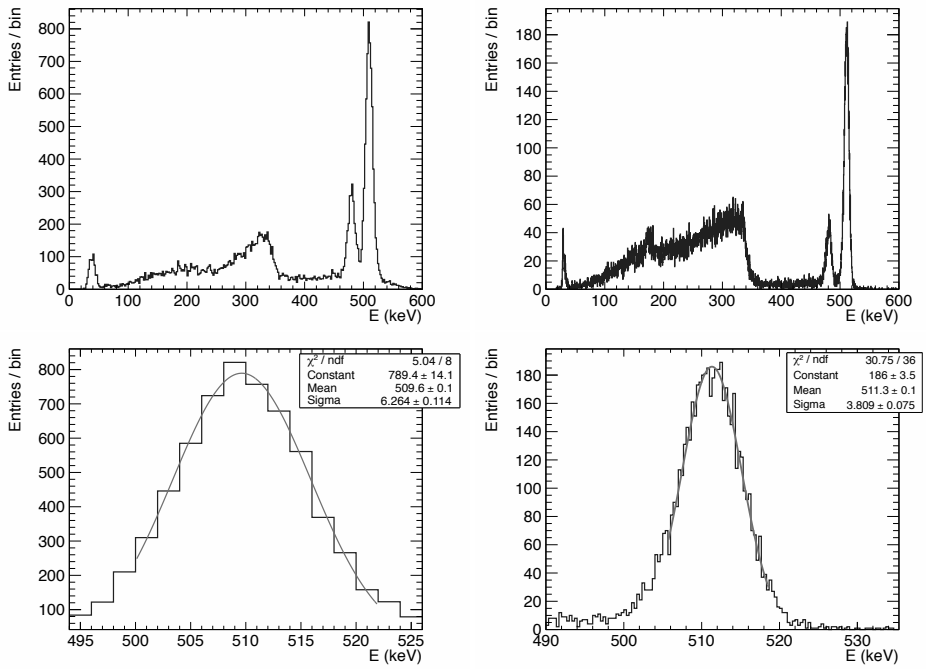

Figure 7.5.5: Top: Energy spectra for ^{22}Na gamma-ray events within the fiducial volume of NEXT-DEMO after spatial corrections. Left for the *ultraviolet* configuration (UVC); right for the *blue* configuration (BC). Bottom: Gaussian fits to the photoelectric peaks of the above energy spectra, indicating an energy resolution at 511 keV of 2.89% FWHM for the UVC and 1.75% FWHM for the BC.

the BC period data is explained by the improved photoelectron statistics, which is a factor of three larger than in the UVC. Extrapolating using the BC result to the Q value of ^{136}Xe (2458 keV) assuming a $E^{-1/2}$ dependence predicts a resolution of 0.8% FWHM. This result improves on the NEXT target resolution of 1% FWHM at $Q_{\beta\beta}$.

The real voyage of discovery consists not in seeking new lands but seeing with new eyes.

'La Prisonnière'; Marcel Proust

8

NEXT-DEMO SiPM Results

One of the major advantages of the NEXT technology is its capability for a topology identification of the particles inside the detector. That results in an increased background rejection factor. The topology function is performed usign a SiPM array near the EL region (section 6.5). The NEXT-DEMO prototype has been operating with an array of 256 SiPMs in order to explore in detail the capabilities of such technology. This chapter offers a detailed explanation of the data processing and analysis. Also the event topology is explained and the requisites for a tracking plane that operates in HGXe extracted from there. The results where published in [134].

8.1 Data Sample

The behavior of the NEXT-DEMO detector with the SiPM configuration has been studied using ^{22}Na and ^{137}Cs sources. The source is placed in the central lateral port (Fig. 8.1.1). When taking data with ^{22}Na a *NaI* scintillator was placed behind the radioactive source to be used as a trigger channel if needed.

The detector has been operating at a pressure of 10 bar and with an electric field in the drift region of 500 V/cm, conditions very similar to the ones used in the previous configurations. On the other hand, the DICE Boards where the SiPMs are soldered have been coated with TPB (*see* 6.5.2). The coating increases the light reflected by the tracking plane and the percentage of photons that reach the energy plane allowing the operation with smaller fields in the EL region increasing the detector stability against sparks. The voltage in the gate to the amplification region (EL) is set to 10kV giving a field of 2.0 kV $\cdot$ cm^{-1} $\cdot$ bar^{-1}. The voltages have been monitored with a LabView © program that is ready for an emergency shut down of the voltage.

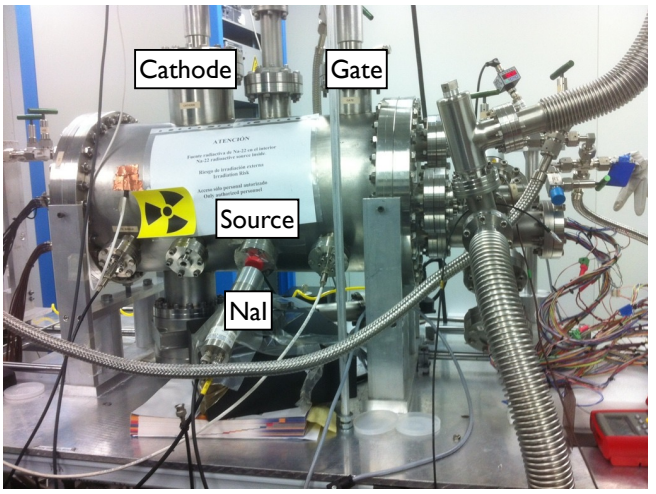

Figure 8.1.1: View of the NEXT-DEMO detector with the source (^{22}Na) placed in port in the center of the drift region. Cathode and Gate HHV are also labeled.

8.2 Trigger

Two distinct online triggers were used for the initial selection of the data presented in this chapter. They used parameters based on the duration and amplitude of the scintillation (S1) signal and, for the first, coincidence between S1 and a signal in an NaI scintillator placed outside the source port. An S1 signal was defined as a pulse with between 1 and 20 photoelectrons per PMT with a duration shorter than 1 μs. The read-out was triggered in the first dataset when an S1 signal was detected within 25 ns of a pulse in the NaI scintillator. This trigger combination, possible with ^{22}Na due to the back-to-back photons produced in positron annihilation, ensures a pure source triggered dataset for analysis. In the second dataset, coincidence of S1-like signals was, instead, required between 3 of 4 central PMTs. The conditions for a positive trigger in each PMT were slightly more restrictive in order to ensure a trigger on the S1 signal. This trigger configuration also has the possibility to be used under different data conditions where the external trigger would not be possible, for example with a ^{137}Cs gamma source. Example spectra of S1 and S2 signals are shown in figure 8.2.1.

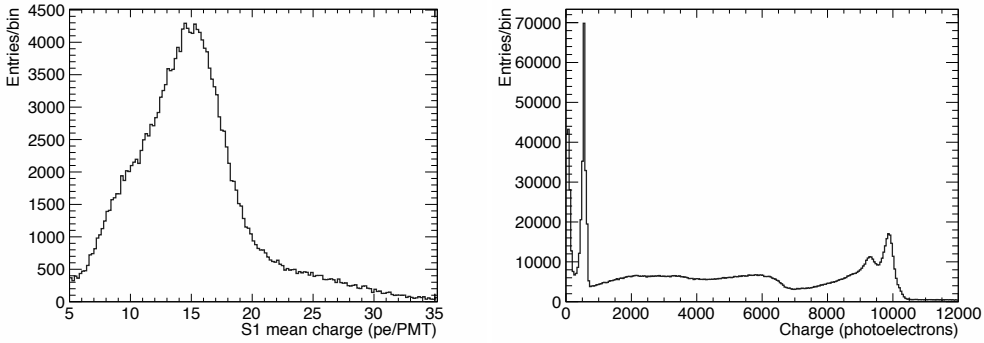

Figure 8.2.1: Top: Primary scintillation spectrum (S1). Bottom: The energy spectrum before any event selection (S2).

8.3 Data Selection

An offline pre-selection of events is performed to further improve data quality prior to analysis. Events containing more than one S1-like pulse are rejected so that the event drift time and, hence, z position in the detector, can be calculated unambiguously. While any number of S2-like signals are allowed per event, a minimum total S2 charge is required to eliminate low energy backgrounds and pulses generated in the cathode wires. The minimum charge is equivalent to 20 photoelectrons per PMT. Additionally, since light distribution in an event produced by a pulse in the cathode wires is non-uniform across the read-out plane, these events are rejected by demanding that the response of the individual PMTs not vary by more than 20%.

8.4 Position reconstruction and fiducial region

While the z position of the events in the chamber is unambiguously defined by the relative position in time of S1 and S2 signals and the drift velocity of the electrons in the gas, a number of possible methods can be used to reconstruct the xy position of a charge deposit. For the data presented the barycentre method is used. Monte Carlo studies of the detector geometry indicate that this method is optimal using the

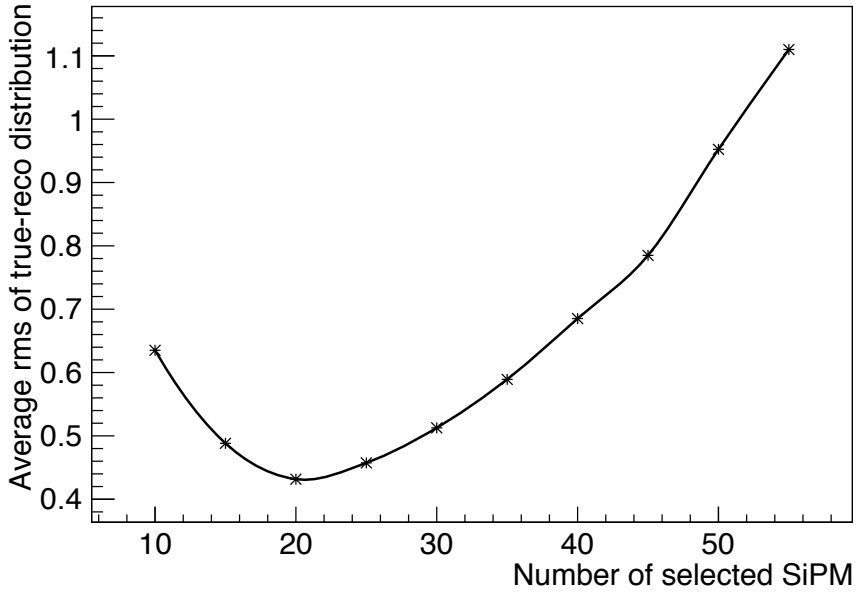

Figure 8.4.1: Averaged difference in true and reconstructed x position as a function of number of channels considered in the reconstruction for MC events.

signals from only the ∼20 SiPMs with greatest charge (figure 8.4.1). The analyses presented here make use of this observation.

In order to eliminate events that are not fully contained in the field cage and those expected to be reconstructed with greater error, a fiducial volume based on the reconstructed *xy* position must be defined. ^{22}Na gamma induced electrons can travel between a few hundred microns and a few cm, however, due to multiple scattering the most probable extent of the higher energy events is a few mm. Thus, events reconstructed within a few mm of the outer edge of the tracking plane can be expected to have high probability to have lost some of their charge to the outer walls of the detector. These observations inspired the definition of a fiducial cut which excludes those events with a reconstructed mean $|x|$ ($|y|$) position greater than that of the sensors in the penultimate column (row) of the plane. This cut defines a fiducial region that covers 77% of the total tracking plane active area. Moreover, to avoid events very close to the cathode which could lose charge and to exclude the region with low statistics due to the position of the source port, an additional requirement that events be reconstructed with $100 \leq z \leq 240$ mm was implemented. As a result the fiducial volume used in the analyses presented is a cuboid of volume $120 \times 120 \times 140$ mm^3 which corresponds to 36% of the active region of the TPC, 3.7 times larger than that used in the previous analysis [135]. A similar definition would result in a fiducial volume corresponding to 88% of the active region of a TPC of the size of NEXT-100.

8.5 Event topology

Using the event timing and the barycentre calculated using the total integrated signal in each SiPM, it is possible to obtain an estimation of the position of the energy deposit associated to the interaction of a particle. This definition is a good approximation when the particle behaviour is point-like, as is the case for x-rays. However, the electrons produced by the interactions of the 511 keV photons emanating from the ^{22}Na calibration source are not necessarily point-like. They have finite probability to travel several centimetres in the gas. As can be seen in figure 8.5.1-*top panel*,

the majority of the charge in ^{22}Na events tends to be concentrated within 4 μs either side of the time sample (μs width slice) with maximum charge. Defining this region as the "blob" and calculating the position of this deposit compared to that calculated from the full integrated charge of the event, it can be seen (figure 8.5.1-*bottom panel*) that the global position is still a good estimator of the position of the energy deposit.

A more involved reconstruction is required to understand the actual topology of individual events. A first approximation of the event topology can be made by subdividing, to a minimum width of one time sample, the charge in time. This allows for a deeper understanding of an event's z structure and is the starting point for track reconstruction. For the analysis presented here, slices of 4 μs width were used, on the grounds that this width is comparable to the width of the blob, as defined above, and the time an electron needs to cross the EL region ($\sim$3 μs). In addition, the charge collected in a 4 μs width window is sufficient to achieve a reliable xy reconstruction. Each time slice, while having a single z coordinate, can be comprised of multiple x, y points. In this preliminary analysis a single xy point is reconstruced per slice and those events exhibiting slices with more than one isolated charge deposit in the tracking plane are excluded from analysis until a more sophisticated clustering algorithm is developed. The xy position of a slice is reconstructed using its barycentre. This position then has the energy recorded in the cathode for the same time interval associated with it so that the event dE/dz can be studied. The energy and position information are then used to calculate a cubic spline between the individual points in order to obtain a finer description of the path.

Figure 8.5.2 illustrates the method applied to the reconstruction of a ^{137}Cs photoelectric event. The reconstructed electron trajectory presents all the features found in the Monte Carlo: a tortuous path due to multiple scattering, a "wire" region of MIP deposition and a blob of high energy deposit towards its end. In figure 8.5.3 examples of three different tracks are shown with the same scale. As expected the ^{22}Na track

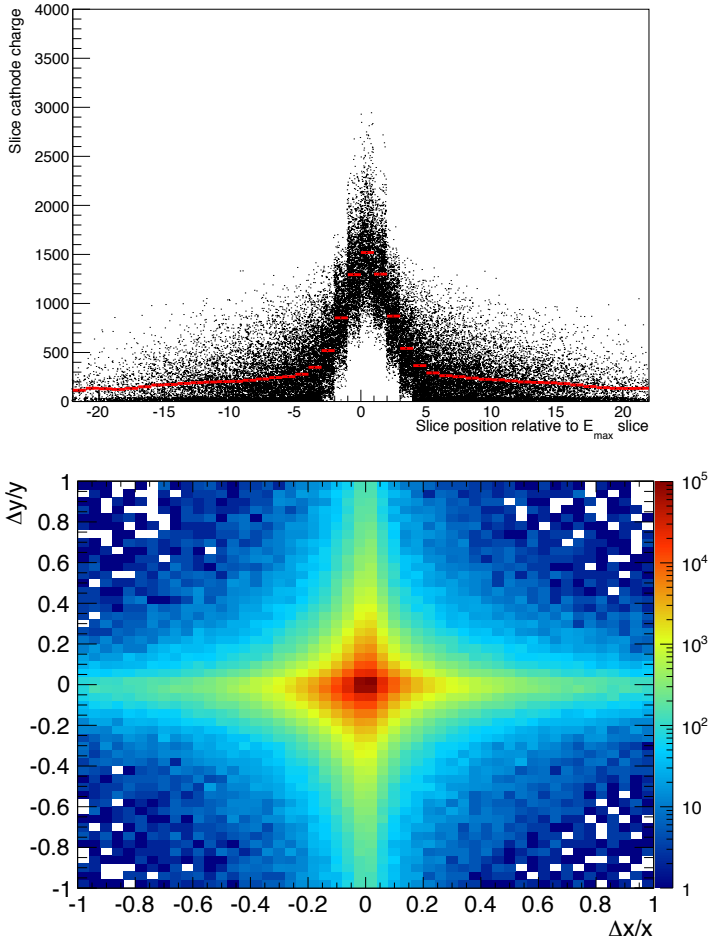

Figure 8.5.1: Slice position relative to the maximum (top) and the pull on the "blob" position compared to the barycentre of the event as a whole ($\Delta y/y$ ($\Delta x/x$) being the difference normalised to the total charge position) (bottom).

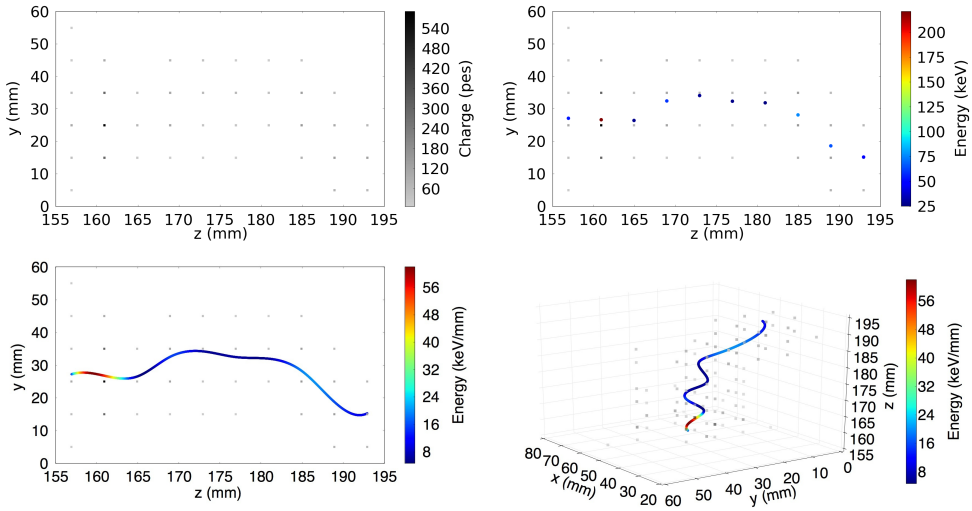

Figure 8.5.2: Example of ^{137}Cs track reconstruction: The charge of the different SiPMs is split into slices of 4 mm width in z (top left). One point is calculated for each slice using the barycentre method and the energy of the points is then associated with the measurement made in the cathode (top right). A cubic spline is used to interconect the different points; YZ projection (bottom left) 3D (bottom right).

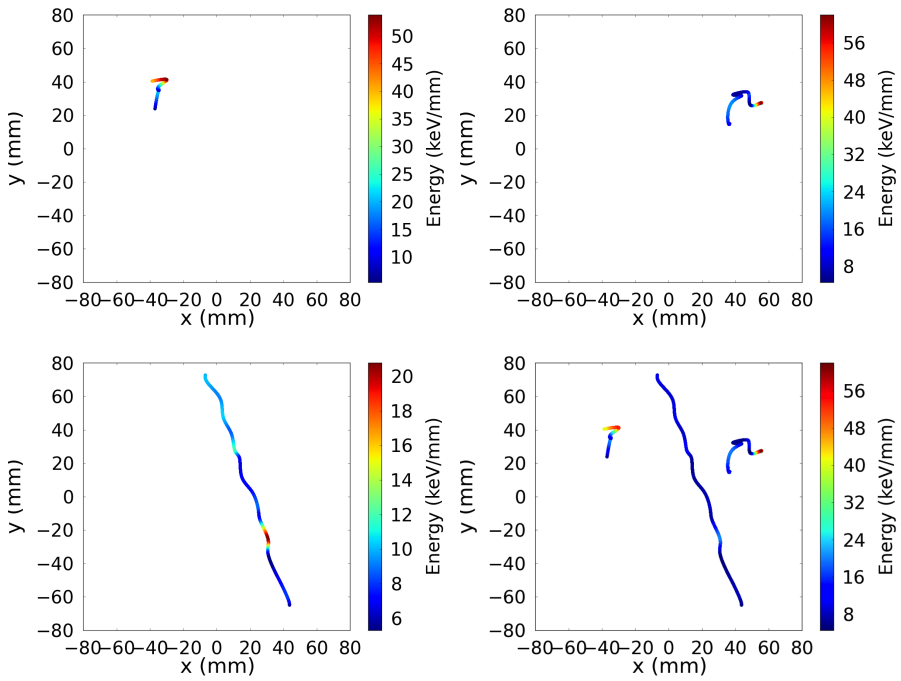

Figure 8.5.3: Examples of ^{22}Na (top left), ^{137}Cs (top right) and muon (bottom) track xy plane projections. Figure bottom right shows the three tracks with the same energy scale. The different topologies are easily appreciated. Tracks reconstructed from NEXT-DEMO data.

is smaller than the track from ^{137}Cs. It is also notable that in the electron tracks the end-point is clearly visible but this is not the case for the muon.

8.6 Energy Resolution

NEXT-DEMO must prove that energy reconstruction can be performed with a resolution compatible with extrapolation to 1% FWHM at $Q_{\beta\beta}$ (the target value in the NEXT-100 TDR) or better over a large fiducial volume. The most important factors affecting the energy resolution of the NEXT-DEMO detector are geometrical inho-

mogeneities in response and any time variation of the detector gain, both in terms of EL yield and sensor calibration [135].

8.6.1 Charge time dependence

As described in section 6.7 the calibration constants of the photodetectors were constantly monitored over the course of data taking so that any variation could be taken into account. Additionally, the temperature and pressure in the TPC have been monitored allowing for the study of the correlation between these physical factors and the detector response. A correlation between the measured pressure and charge is observed in the data as can be seen in figure 8.6.1-*left panel*. The temperature of the vessel has a significantly smaller effect on the PMT charge. Both temperature and pressure oscillate at the level of $\sim$0.2% every 10 minutes due to the cycle of the hot getter which purifies the gas and by up to 3% due to air conditioning and activity in the laboratory over a timescale of 24 hours. Other possible sources of time dependent variation are the occurrence of sparks in the TPC and variation of the gas purity. As explained before, the increased light yield due to the TPB-coated tracking plane enabled the use of lower EL fields compared to previous analyses, and improved gas isolation and recirculation reduced the probability of sparking and of electron attachment due to impurities. By monitoring these variables, the data can be gain corrected to improve consistency and, in the case of any major changes in conditions, affected data could be removed from the analysis.

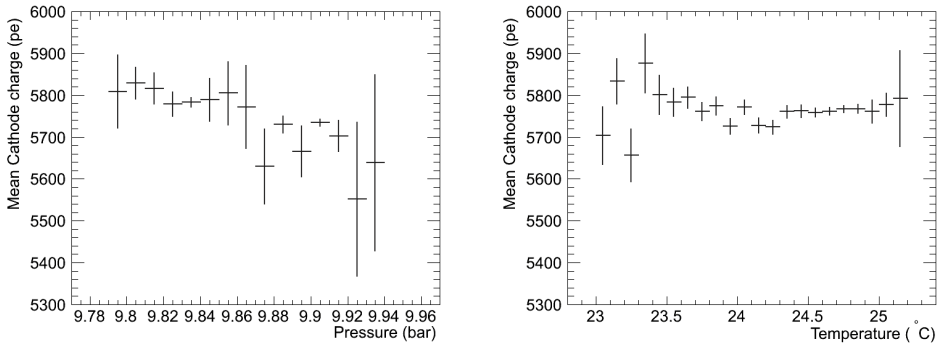

Figure 8.6.1: Relation of observed cathode charge with ambient conditions: Vessel pressure (left) and vessel temperature (right).

8.6.2 Geometrical correction

The geometrical dependence of the observed event charge has a number of physical origins. Among these are: losses along the drift due to electron attachment; losses at the edge of the fiducial region due to inhomogeneities in the electric field; losses due to absorption of light in the meshes and imperfect reflection and rotational symmetry of the light tube. The first effects demand the continuous recirculation and filtering of the gas to minimize attatchment while the latter require the correction of the observed charge.

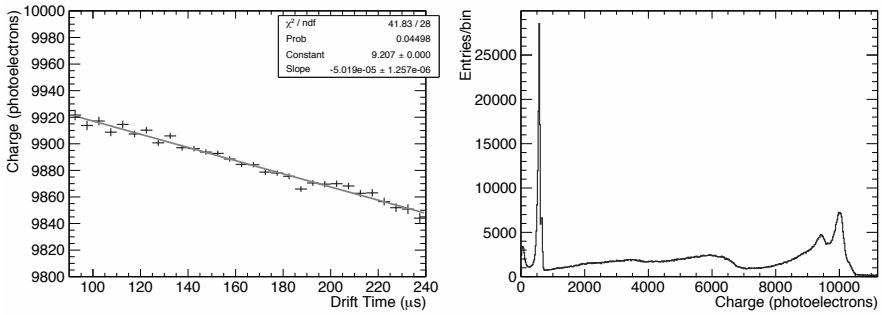

Figure 8.6.2: Energy dependence with drift time due to electron attachment in the gas (left) and the energy spectrum after correction (right).

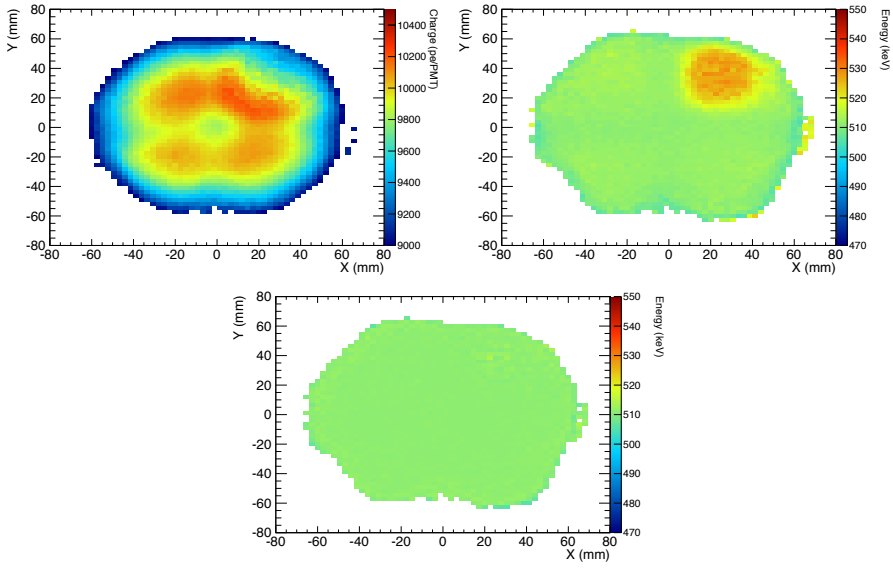

Figure 8.6.3: Top Left: Profile before *xy* corrections. Top Right: Profile after first correction. Bottom: Profile once convergence is achieved.

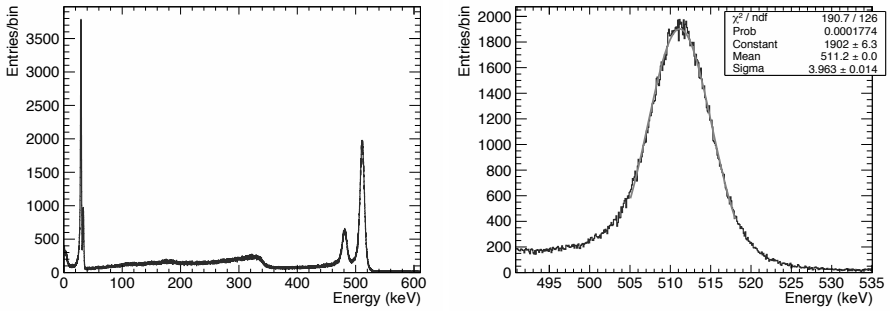

Figure 8.6.4: Energy spectrum after spatial corrections (left) and detail of the photoelectric peak with fit values (right).

The dependence of the observed energy on deposit position can be described by a geometric factor parametrized as:

$$\eta(x, y, z) = Z(z') \cdot F(x, y) \tag{8.1}$$

The z dependence $(Z(z'))$, due to attachment of the electrons in the gas, is expected to be uncorrelated with other factors and can be treated independently. However, the dependence on x and y position are sufficiently correlated that they should be considered simultaneously.

Z correction

The charge dependence on z is well described by an exponential decay scaling with the electron lifetime in the gas. The high quality of the gas in these data runs results in a mean electron lifetime of greater than 10 ms, implying a charge loss due to attachment of less than 3%. Figure 8.6.2 shows the charge dependence with z and how the effect is corrected.

XY correction

After the z correction, correction for transverse inhomogeneities in the detector response was performed using a 2 dimensional profile of the reconstructed charge in the photoelectric peak as a function of reconstructed xy position. Correction factors were computed for all positions using Delaunay interpolation among separate bins (bins correspond to a region with surface area of approximately 1.6×1.6 cm^2) and normalizing to the value for the bin at $R = 0$. This method was applied iteratively until convergence which was generally achieved using 4 iterations. Figure 8.6.3 shows the profile after z without xy correction, the profile after the first iteration and after asymptotic stability is reached.

After the corrections described, the resolution reaches 1.82% FWHM in the photoelectric peak at 511 keV (figure 8.6.4). This extrapolates to an energy resolution of 0.83% FWHM at $Q_{\beta\beta}$.

8.6.3 Energy Resolution Scalability

The values for the energy resolution at $Q_{\beta\beta}$ are computed from the energy resolution measured at lower energies and under the reasonable assumption that the energy resolution in the detector scales as $1/\sqrt{E}$. In order to verify this assumption a measurment of the energy resolution at different energies is necessary. Due to the size of NEXT-DEMO detector electrons with energies near the $Q_{\beta\beta}$ region can not be contained in the detector. The appropiate energy range for that study is such that provides electrons with enough energy to produce a track inside the gas volume but with the track not too long to escape to escape the volume and produce energy losses. A source of ^{137}Cs with a gamma at 662 keV was selected to perform the study.

Trigger and data selection were adapted to the new energy range. The data was then processed usign the same analysis algorithms than for the ^{22}Na source data. The result is a resolution in the ^{137}Cs photoelectric peak of 1.56%FWHM which extrapolates to an energy resolution of 0.83% FWHM at $Q_{\beta\beta}$ (Fig. 8.6.5). That result is

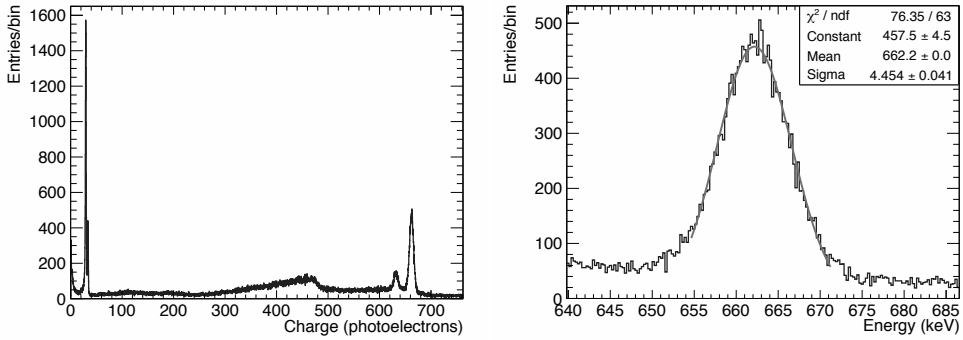

Figure 8.6.5: Energy spectrum after spatial corrections for ^{137}Cs (left) and detail of the photoelectric peak with fit values (right). The resolution at 662 keV is 1.58% FWHM. That result extrapolates to 0.82% FWHM at the $Q_{\beta\beta}$ end-point energy.

compatible with the one measured for the ^{22}Na photoelectric peak and demonstrates the energy resolution scalability.

The distinction between the past, present and future is only a stubbornly persistent illusion.

Albert Einstein

9

Towards NEXT-100

The NEXT collaboration has been operating with medium scale prototypes for the last 3 years. The prototypes, have fully demonstrated the capabilities of the SOFT concept and NEXT technology. Specifically, as explained in the previous chapters, the NEXT-DEMO detector has achieved an energy resolution that is better than expected. Moreover, NEXT-DEMO is the first large scale prototype operating with HPGXe successfully using SiPMs for tracking reconstruction.

The NEXT Collaboration aims to build a detector sensitive to the current limit for the half life of the neutrinoless double beta decay and the corresponding neutrino mass. A detector holding 100 kg of enriched Xenon has been designed and it is being build. The detector implements the NEXT technology concept that has been tested in the NEXT-DEMO detector. The so called NEXT-100 detector is a radiopure detector that will start operation in Laboratorio Subterráneo de Canfranc (LSC) in the

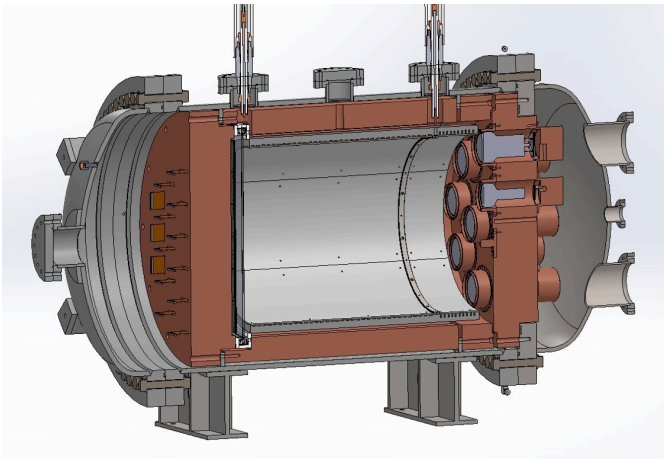

Figure 9.0.1: A 3D drawing of the NEW detector.

following years. The first stage of the NEXT experiment is the NEW detector, figure 9.0.1

The primary goal of NEW is to provide an intermediate step in the construction of the NEXT-100 detector that would allow the validation of the technological solutions proposed in the TDR. In addition, NEW would permit a measurement of the energy resolution at high energy, and the characterisation of the 2-electron topological signature, by measuring the $\beta\beta 2\nu$ mode. Finally, NEW will permit a realistic assessment of the NEXT background model before the construction of the NEXT-100 detector.

9.1 The NEW detector

The NEW pressure vessel (NPV) and field cage (NFC) dimensions are roughly 1:2 with respect to those of NEXT-100. It deploys 20 % of the NEXT-100 sensors and the xenon mass is about 10 kg at 15 bar.

9.1.1 Pressure Vessel

The NPV has been manufactured by the company TRINOS vacuum system, with the same steel alloy selected for the NEXT-100 detector. The fabrication of the NPV was made possible, at zero cost for the NEXT collaboration, thanks to a CEDETI grant. Figure 9.1.1 top shows the pressure vessel and one of the torispherical heads.

With an internal diameter of 64 cm and a length of 950 cm, the dimensions of the NPV are intermediate between NEXT-DEMO and NEXT-100. The NPV can hold pressures of up to 50 bar.

Figure 9.1.1 bottom shows the NPV sitting on a support platform. The platform will be first tested at IFIC, then moved to the LSC. The drawing illustrates the access to the detector. Each head has one of the photosensor detection systems attached (energy plane and tracking plane).

Figure 9.1.1: The NEW Pressure Vessel (NPV). Top: Pictures of the pressure vessel already manufactured. Bottom: Drawing of the final assembly of the NEW detector with the support table.

9.1.2 Field Cage design

Figure 9.1.2 shows the NEW field cage. The design is based on a high density polyethylene (HDP) cylindrical shell, 25 mm thick, which isolates the copper shield from the voltage in the copper rings and the cathode. The rings are placed inside grooves and connected by a resistor chain. The field cage has an outer diameter (OD) of 500 mm and a length of 500 mm. Thus, both the longitudinal and radial dimensions are roughly half of those of NEXT-100.

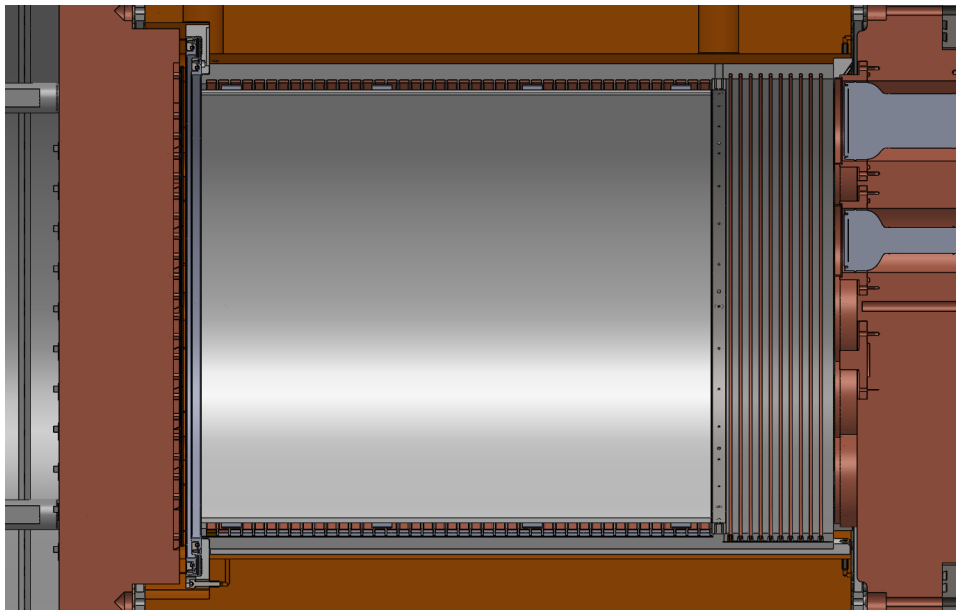

Figure 9.1.2: The NEW field cage (NFC).

The field cage is terminated by a transparent cathode grid, placed at 100 mm from the PMTs and a pair of grids in the anode, whose role is to provide the EL amplification system. The field is degraded to ground in the buffer region between cathode and PMTs by means of additional rings, closely spaced.

The electric field in the two regions have different aims and properties. The fol-

lowing sections describe in detail the characteristics of the electric fields in the corresponding regions.

The nominal drift field for NEW will vary between 0.3 and 0.6 kV/cm, thus a maximum drift voltage of 30 kV (for a drift of 500 mm) is foreseen. The EL voltage between gate and anode will be, at most 3 kV/cm/bar, resulting, for a EL region of 5 mm in 22.5 kV at 15 bar. The field cage is designed to hold a maximum HV at the cathode of 55 kV and a maximum voltage at the grid of 25 kV allowing for some extra safety factors and flexibility in the electric field. The field cage design has to allow for such flexibility of the detector and allow for a correct operation at different pressures and fields in the drift region.

Drift Region

The drift region in a High Pressure Gas Xenon needs of a moderate electric field (300-600 V/cm). This electric field is enough to avoid electron recombination in gas and drift the charges towards the anode. On the other hand, the field in the drift region should be highly uniform and homogeneous trying to avoid any radial component of the field. Those field characteristics are mandatory to ensure no charge losses in the walls during the drifting process. In 9.1.3 we show a detailed study of the field in different regions of the drifting volume.

The rings in the drift region are made out of electrolytic copper and their shape is a rounded rectangle of $10 \times 3mm$ and radius 0.5mm on the edges. The rings are inserted in grooves inside the high density polyethylene body of the field cage which is 20 mm thick. The grooves are 4 mm in depth allowing some space between the surface of the ring and the wall of the field cage that is necessary to support the light tube inside the field cage. The rings are separated 12 mm center to center, which gives 2mm separation between rings that is enough to both hold the voltage and support the rings. Figure 9.1.3 shows the dimensions of the drift rings and their position in the polyethylene tube.

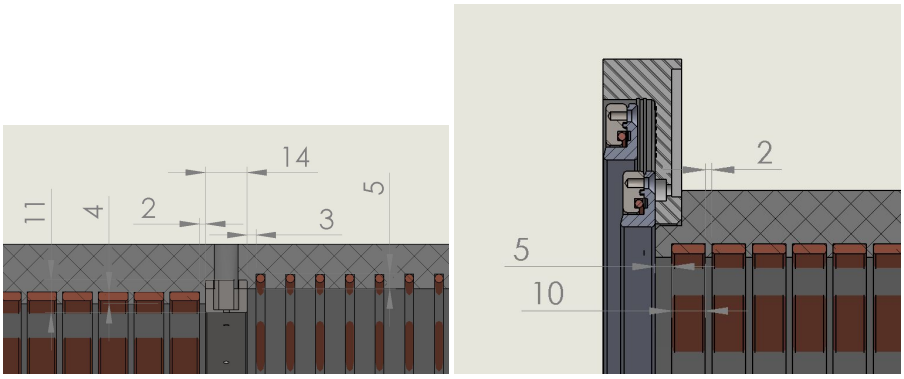

Figure 9.1.3: Detail of drift and buffer region rings and their relative position to the cathode and to the gate mashes.

Buffer Region

The buffer zone is necessary to degrade the electric potential from the cathode to near zero volts at the PMT window surface. In that region of the TPC we do not demand the electric field to be highly uniform and then different degrading options are possible (linear, exponential,...). The possibility to degrade the voltage without using rings or only a few is being explored. Independently of the chosen configuration the difficulty in this region is to avoid electric fields regions with electric field near the breakdown. In this region the electric field is near 5kV/cm.

The polyethylene in the buffer region is slightly thinner than in the drift region to give enough space to introduce the cathode inside the field cage. The thickness for this region is 15 mm. The first option considered to degrade the voltage in the electric fields is based on a cirlex printed circuit where the contiguous rings are in different faces of the kapton layer (See Fig. 9.1.4). The copper lines are 3 mm in width and the separation between rings is 10 mm. The resistors are soldered in a third dimension and potted inside vacuum epoxy. The epoxy has grooves to hinder the charges from travel on its surface (See Fig. 9.1.5). Figure 9.1.6 shows the schematics of the buffer design.

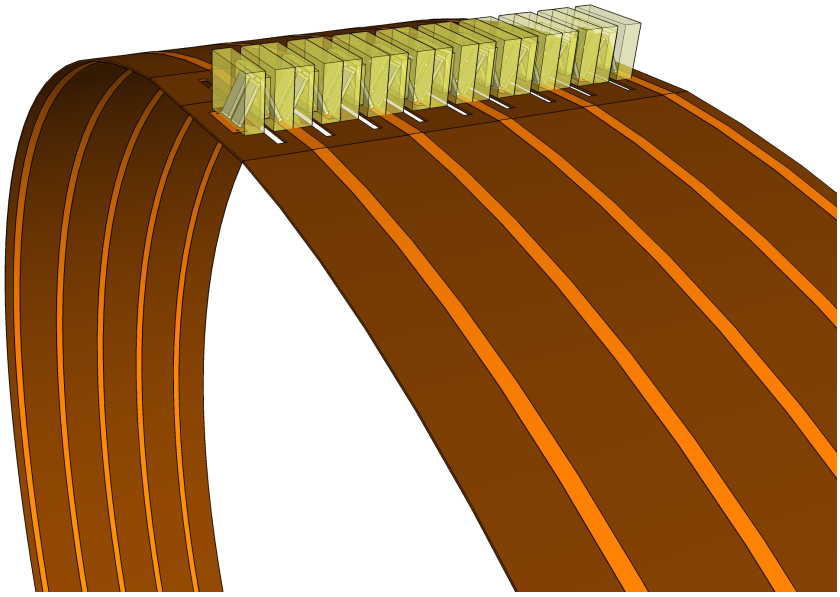

Figure 9.1.4: The figure shows a design for the buffer concept. The material used is cirlex with copper lines in both sides of the kapton. Every line (ring) is in a different kapton face from its closest neighbors.

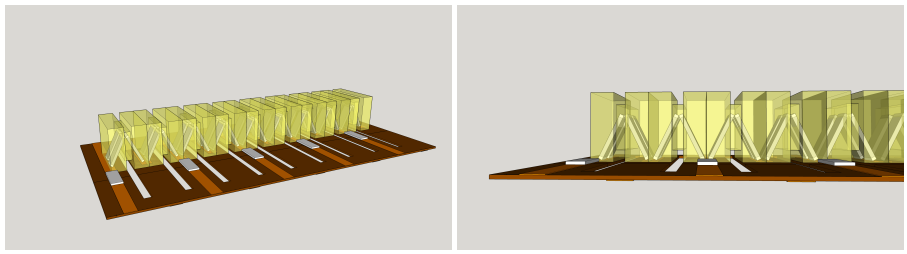

Figure 9.1.5: Detail of the resistor chain inside the vacuum epoxy. As two resistors are needed to hold the potential among rings they are soldered in a inverted "V" shape to fit in the space between rings.

The design counts also with holes of 60 mm length and 2 mm width in the kapton between rings to reduce movement of the charges.

The second option being studied for the buffer region is to use a minimal number of rings allowing them to be well spaced. In that case resistors will fit easily between

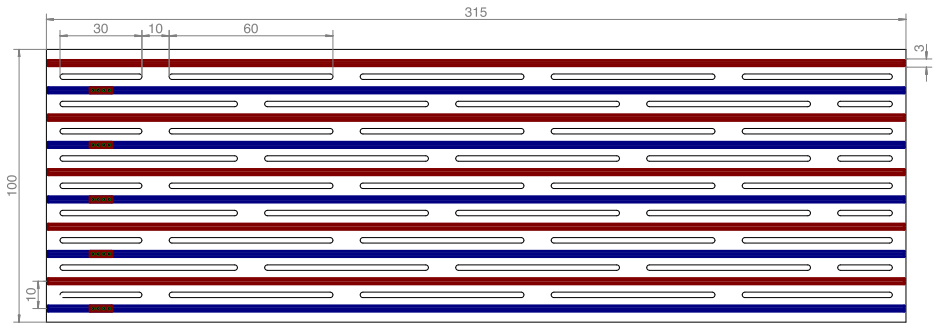

Figure 9.1.6: Schematics of buffer design.

rings and no risk of voltage breakdown or excessive surface charge movement. The extreme solution is to avoid completely the use of rings in the buffer regions. In those cases, the geometry of the grooves needs to be well studied and tested to work with the high electric field needed. Figure 9.1.7 shows the first ongoing studies in that direction.

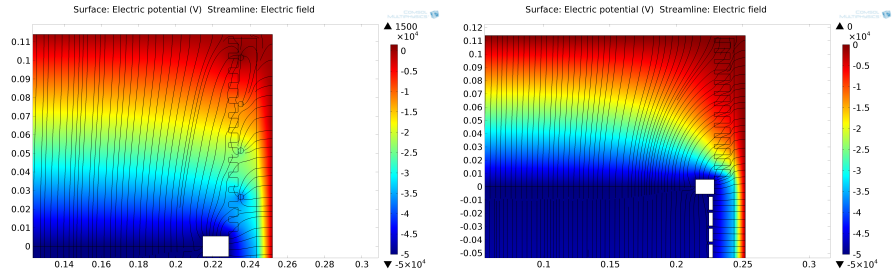

Figure 9.1.7: Electric field simulation of the buffer region with only four rings degrading the voltage (left) and with no rings (right). Those designs produce components of the electric field perpendicular to the walls, therefore they need to be studied carefully.

Resistor Chain

The resistor chain has two purposes: to hold together the two sides of the different rings, and to connect the rings by resistors, so the potential is uniformly degraded.

The NEW resistor chain (Fig. 9.1.8) will be mounted on a kapton board with two parallel resistors connecting every ring to the next one and also the cathode and the gate to their closest rings. The resistors need to hold high voltage and their tolerance needs to be minimum to guarantee homogeneity in the electric field. The resistors chosen for the chain are HVCG3512FDD10Go, which are 10GΩ resistor rated to operate at 3.5kV with 1% tolerance from Stackpole Electronics. In the drift region only one resistor is needed in between rings while in the buffer region we need two resistors in series to hold the voltage drop between rings. In both cases an identical chain is added in parallel to safeguard a possible resistor failure.

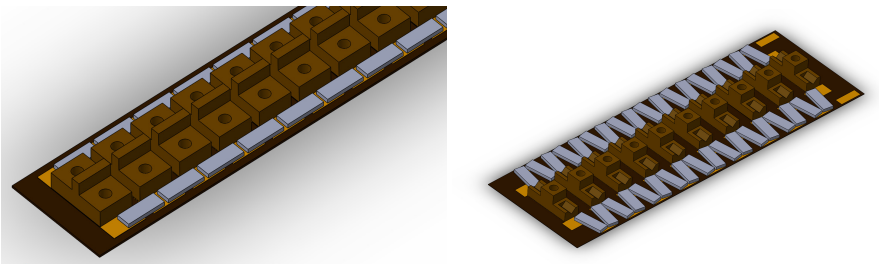

Figure 9.1.8: Resistor chain in the drift region for NEW field cage.

Cathode

The cathode design will be the same as for NEXT-100. It includes one copper ring where parallel wire grids with precise pitch are attached. Model of the cathode and simulation of the stresses of the wire grids is provided by Clement Sofka.

The details on the cathode design are fundamental to understand the assembly protocol. Furthermore, the field cage will need a few stoppers to protect the cathode from the light tube when mounting the detector.

EL Region

The mesh for the gate is 48 cm in diameter. Preliminary COMSOL simulations suggests that it can be built with steel mesh using higher tension to avoid bending. They are more challenging that NEXT-DEMO but no new technology is needed.

The design should allow for a close positioning of the tracking plane (SiPMs) to the anode permitting a full coverage of the active volume.

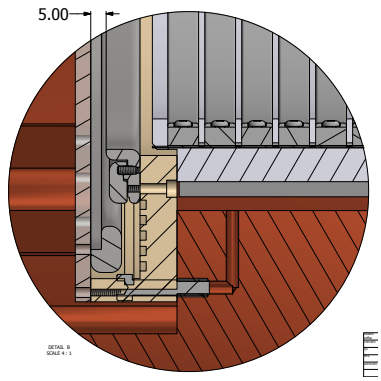

Figure 9.1.9: Detail of the design of the EL region using a quartz plate coated with TPB. The design is much simpler and robust than the one with two meshes. The picture shows a detail of the gard ring needed to save electric field concentrations at the end of the RPB region.

The solution for the EL region is to use a mixture between a mesh for the gate and a solid quartz plate coated with Indium-Tin Oxide (ITO). This coating results in a 90% transparency conductive layer that allows to fix a voltage in the surface of the quartz plate and then creates a homogeneous field in the EL region. The quartz plate has to be coated with TPB to shift the VUV light of the Xenon electroluminescence to blue

to be detected by the tracking plane. A guard ring is needed to prevent concentration of electric field lines in the border of the TPB coated region (Fig. 9.1.9).

The quartz plate solution has multiple advantages. First, it protects the SiPMs from sparking and then nthere is no need for small windows in front of the DICEs any more. Second, it removes the necessity for tension and strength at one side of the mesh, only a small ring surrounding the edge of the ITO coating is needed to prevent sharp edges of the conductive layer. This solution not only greatly simplifies the construction of the gate but also gives some extra space in the EL region to fit it resulting in a simpler assembly protocol. Last but no least, the production of the quartz plate is simpler and cheaper than the mesh.

Feedthroughs

The voltages needed for NEW operation are similar to the NEXT-DEMO requirements. The design has been slightly modified for a better connexion with the cathode and gate of the NEW detector. The gate feedthrough is very similar to the one used in NEXT-DEMO. On the other hand, the cathode feedthough has been completely redesigned to ensure that it holds easily the 50kV considered as the maximum requirement for normal operation. The design is based on an original idea by H. Wang presented in the "High Voltage in Noble Liquids for High Energy Physics" workshop held at Fermilab [136].

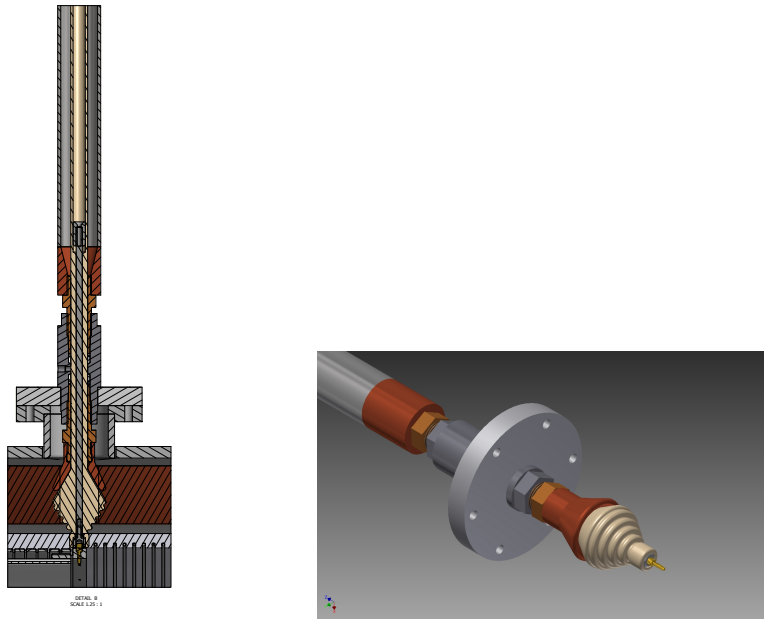

Figure 9.1.10: Cathode feedthrough. The conic shape prevents concentration of electric field lines at the edges of the feedthrough allowing for a higher voltage limit.

9.1.3 Electric Field Simulation

The electric field of the field cage has been simulated with finite elements algorithms using COMSOL Multiphysics. As a first approach to the behavior of the field cage a 2-D axisymmetric model of it has been developed. The simulation has used different mesh sizes in order to optimize computation time without losing precision, figures 9.1.11 and 9.1.12 top left shows a detail of the mesh in different objects of the simulation.

The electric field has been computed in the whole field cage (Fig. 9.1.11). In order to see the variations of the electric field across the field cage a detailed study of the critical regions of the field cage has been performed. In the regions near the cathode and the gate different cutlines in radial and axial directions allow us to examine the

evolution of the different components of the electric field along the field cage. Figure 9.1.13 shows the different lines used to study the electric field.

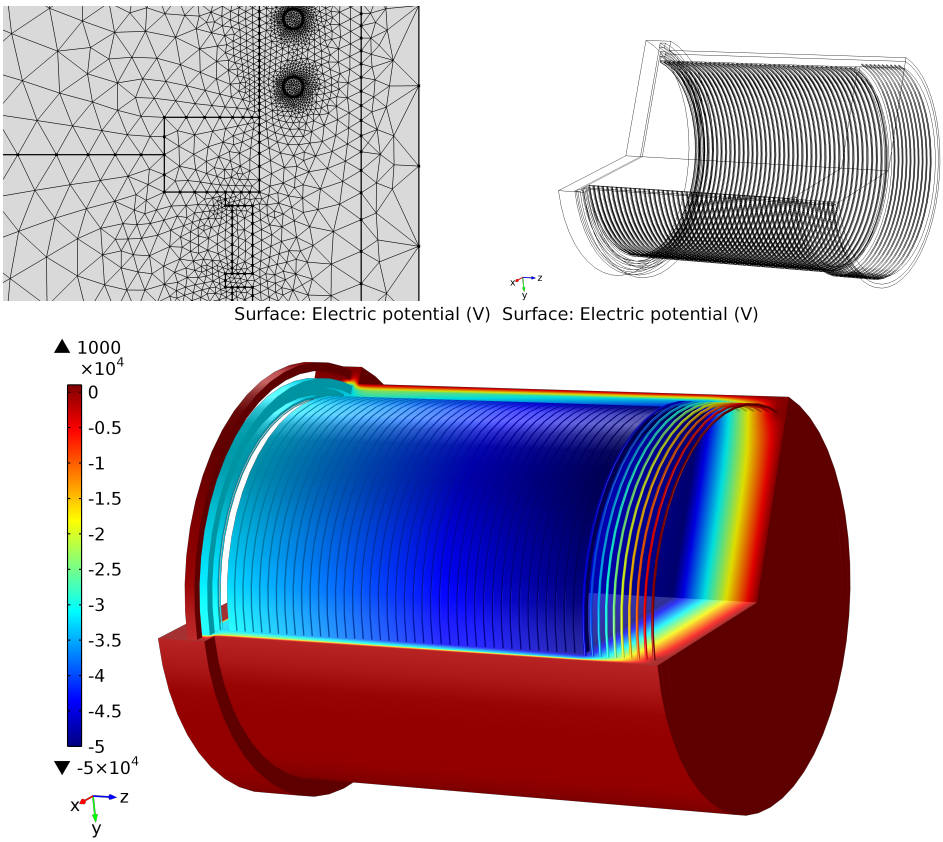

Figure 9.1.11: The NEW field cage electric field is being simulated using finite elements software (COMSOL). Thanks to that program, a detailed study of the electric field in the drift, EL and buffer regions can be performed and optimized for NEW necessities. The geometry simulated (top left). Detail of different mesh sizes depending of the objectes in the field cage (top right). Solution of the simulation in 3D (bottom).

Figures 9.1.14 and 9.1.15 show the radial and z-components of the electric field across the cutlines shown before. The region near the cathode looks very stable and

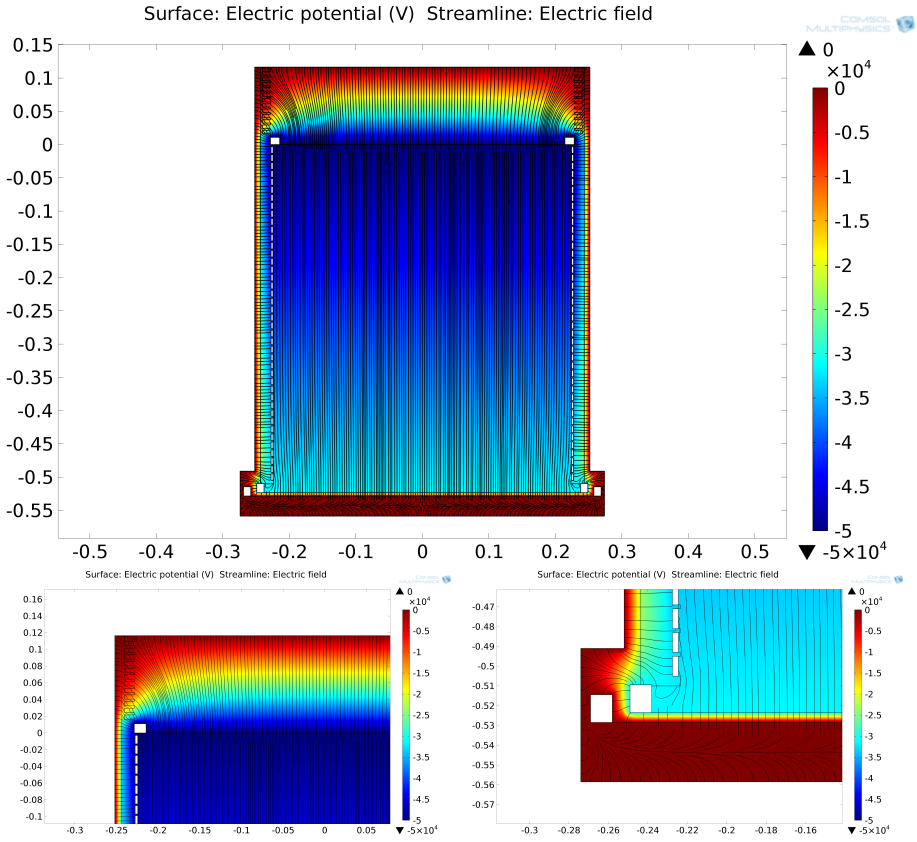

Figure 9.1.12: Results of the electric field in the field cage. The color shows the absolute value of the electric potential while the lines show the direction of the electric field. Bottom figures are a detail of the Cathode (left) and Gate (right) regions.

uniform. On the other hand, the gate regions has more variations in the electric field. This is due to the geometry of the field cage, limitations in the machining of the polyethylene force the distance between the gate and the last ring of the drift region to be much longer than the separation between drift rings. The field variations due to such discontinuity have been minimized for a predefined configuration of the voltages in the cathode and anode modifying accordingly the last step in the resistor

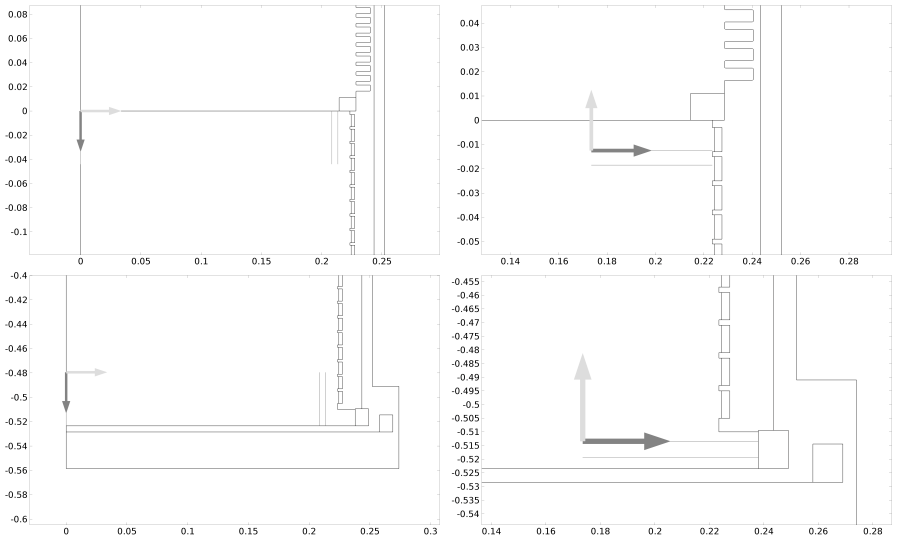

Figure 9.1.13: Positions of the cut lines for a detailed analysis of the electric field inside the field cage. The two top images show the regions near the cathode with cut lines in both axial and radial directions. The two bottom images show the corresponding regions near the Gate. The lines along the z-axis (left images) are useful to compare the electric field in the center of the chamber and near the walls of the field cage and of the light tube. The radial lines (right images) give information about the depth of the perturbations inside the field cage.

chain. The electric field simulation is fundamental to define the right values of those parameters.

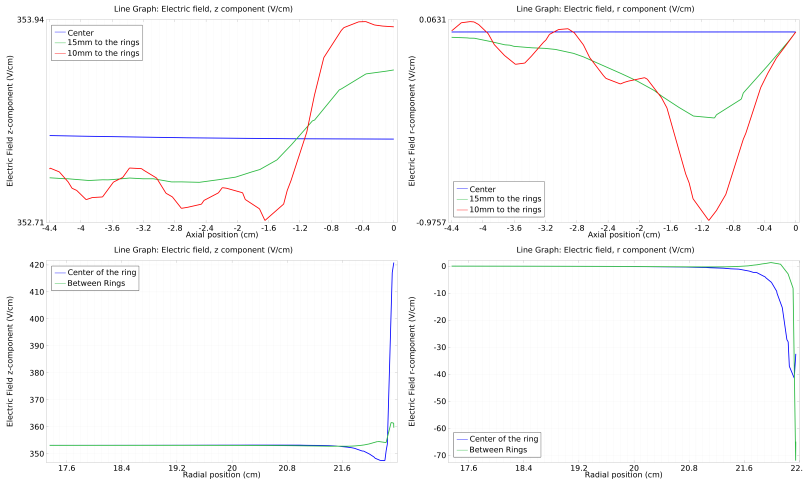

Figure 9.1.14: Electric field in the NEW Field Cage in the cathode region. Top figures show components along the axial cut, bottom images along the radial cut. Left images correspond to the z component while the right corresponds to the radial component of the field. There are small variations of the field near the borders of the field cage that converge rapidly to a stable field in the active region of the detector.

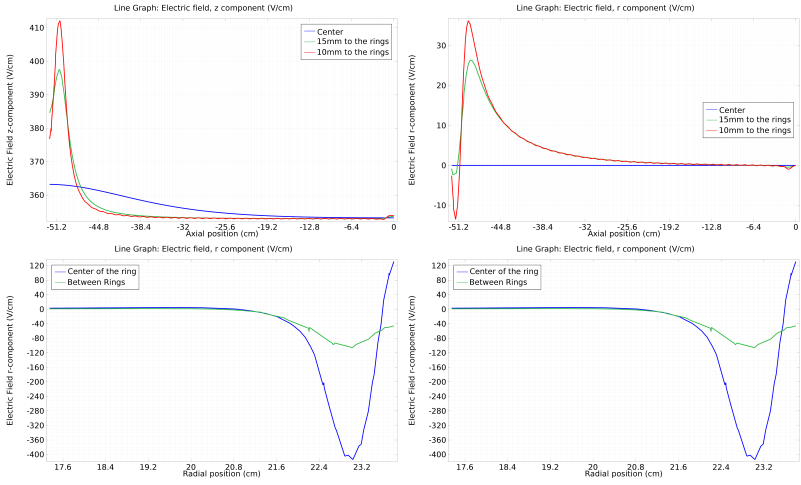

Figure 9.1.15: Electric field in the NEW Field Cage in the gate region. The image distribution is the same as in the previous figure. The variations of the electric field are larger than in the cathode region but they have been minimized using different values of the resistors.

9.1.4 Assembly Protocol

A fundamental part in the design of the field cage is to understand how the different pieces of the field cage need to be assembled to ensure that the different pieces can be in their place.

The following sections describe the assembly and mounting protocol of the different regions of the field cage.

Drift Region

First, the resistor chain must be placed in the groove designed for it in the polyethylene (Fig. 9.1.16). Then, the rings are introduced in their cavities and connected to the copper piece of the resistor chain. The rings are fixed to the resistor chain using normal 3mm screws.

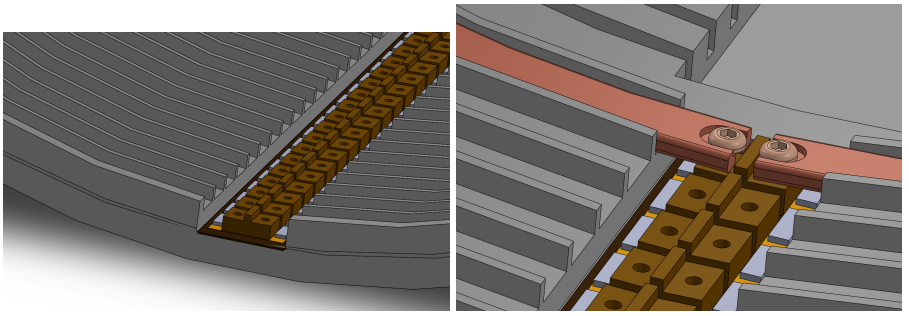

Figure 9.1.16: Resistor chain already mounted in the polyethylene (left). Detail of the assembly of one ring to the resistor chain in the drift region (right).

Buffer Region

With the new design of the buffer the assembly has been simplified. If the cirlex option is chosen, the mounting of resistors and potting of the epoxy will be performed out of the field cage and then it will be sliped into the field cage.

In the case of building the buffer with only a minimum number of rings they can be attached using a similar system to the one used in the drift region. Of course, the simplest solution will be the one without rings, then no assembly is needed.

Cathode

The cathode will need to be introduced from the buffer side and be supported for a small ledge after the last ring of the drift side. Once the cathode is in place, it will be attached to the polyethylene using a few plastic screws.

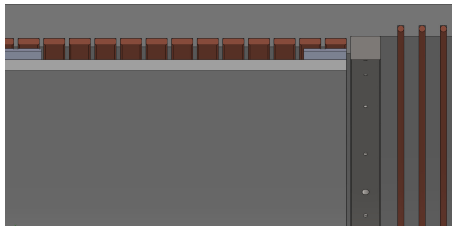

Figure 9.1.17: Detail of the cathode support in the field cage. The support is used also to prevent the light tube from touching the cathode.

9.1.5 Light Tube

The light tube consists of a single teflon piece bent to fit inside the field cage. The teflon is a porous material, that absorbs Xenon getting inflated and soft. In order to prevent any deformation of the light tube it has been designed with a tab that allows for some expansion of the teflon (Fig. 9.1.18).

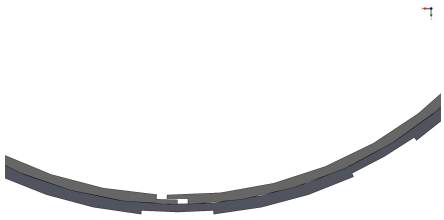

Figure 9.1.18: Light tube tab to prevent deformation of the tube.

The light tube will need plastic supports to slide it through the inner wall of the

field cage up to its position (Fig. 9.1.19). Near the cathode there is a small support that prevents it from touching the cathode wires. The light tube doesn't need any fixing to the field cage, it will be supported by friction to it.

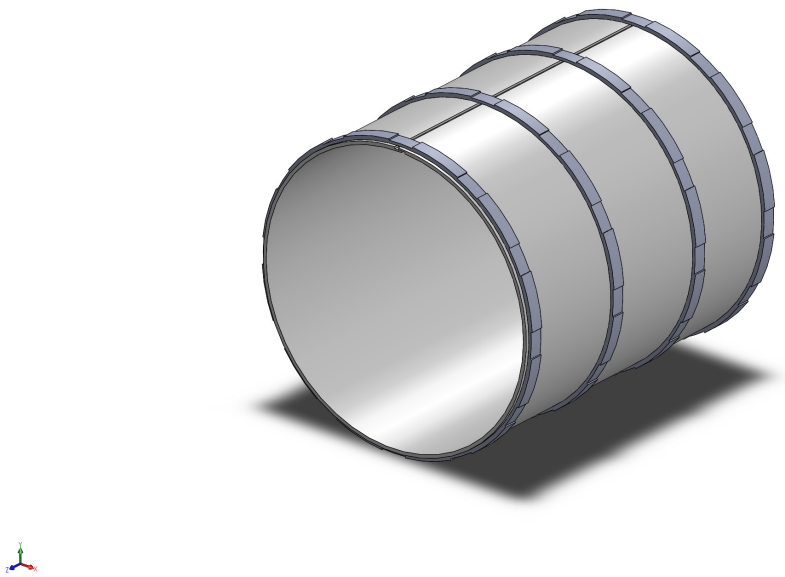

Figure 9.1.19: Light tube guides to support the teflon to the field cage.

Assembly of the field cage to the vessel

Once the field cage is assembled with all its internal components (including the light tube), it is introduced in the vessel trough the tracking plane side. It will slip over polyethylene guides mounted on the shielding. The field cage will reach a support in the energy plane side. It will need to be aligned and then fixed to them using plastic screws. Finally, the EL mesh is fixed in place.

Electroluminescent region

The EL region is the last element to be mounted. The Gate mesh will be mounted directly on the field cage. In its side, the anode will be attached to the tracking plane copper using spring loaded screws that allow for a precise positioning and alignment of the EL region when closing the detector.

9.1.6 Energy Plane

The NEW energy plane (NEP) will use 12 R11410–10 PMTs from Hamamatsu. The PMTs will operate in vacuum, inside the NPV. A thick copper plate separates the PMT-vacuum region from the high pressure region in the chamber, and acts also as a radiation shield. Sapphire windows coated with TPB protect each PMT. Lateral and front views of the NEP are shown in figure 9.1.20. Figure 9.1.21 illustrates a detail, showing the PMT windows, the PMT cans and the thick back copper plugs acting as shields of radiation.

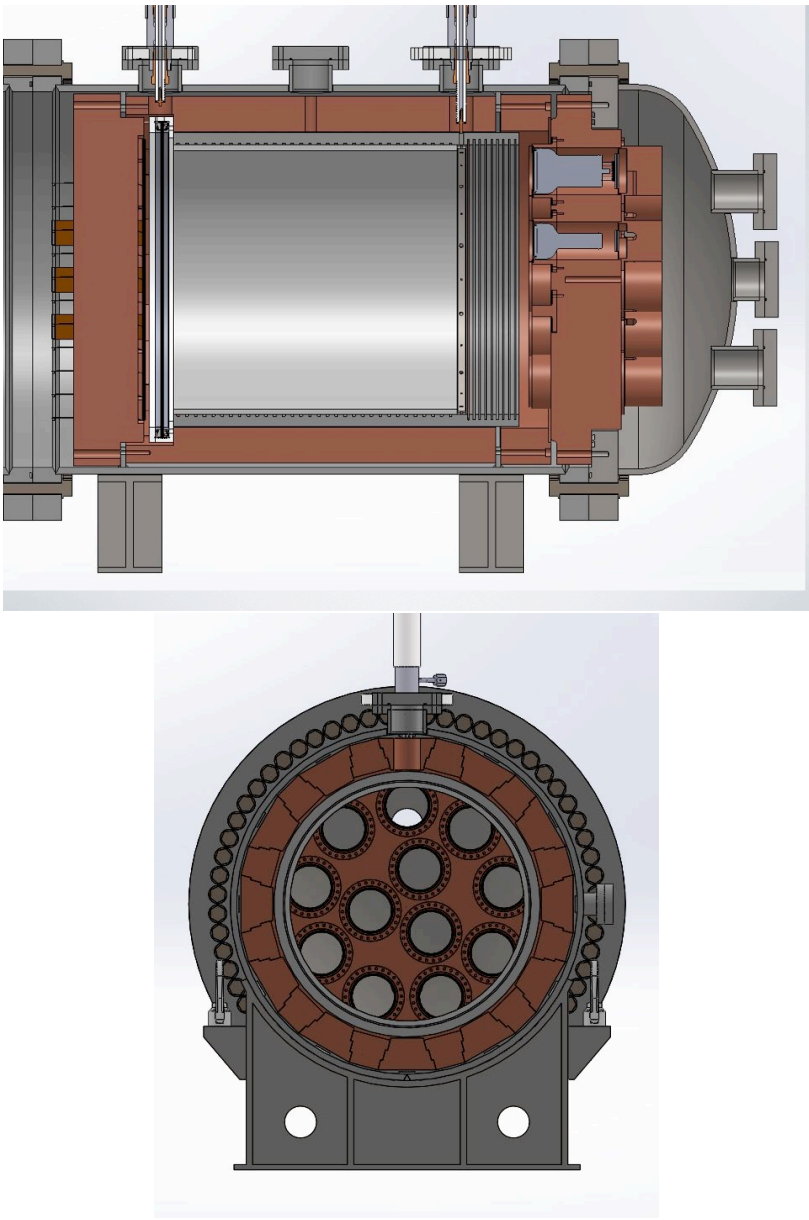

Figure 9.1.20: The NEW energy plane (NEP) deploying 12 PMTs operating in vacuum and viewed by sapphire windows coated with TPB. Top: lateral view. Bottom: front view

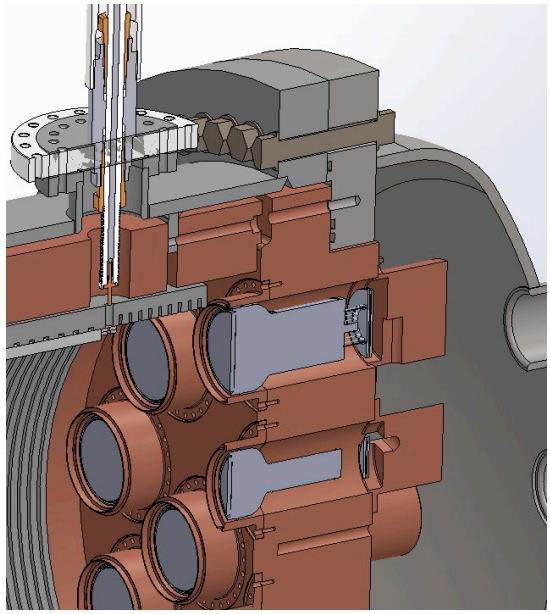

Figure 9.1.21: Detail of the NEP showing the sapphire windows and the PMT enclosures (aka cans) terminated in thick copper caps for radiation shielding.

9.1.7 Tracking Plane

The NEW tracking plane (NTP) is made of 28 kapton dice boards (KDB) as can be seen in 9.1.22. Notice that the KDBs over-cover the fiducial region, ensuring that there are no dead regions.

Figure 9.1.23 shows the evolution from the dice boards (DB) built for NEXT-DEMO and the kapton dice boards (KDB) built for NEW. The DBs were made of multi-layer cuflon, and their radioactivity budget was moderately high, due to the adhesive needed to glue the layers. Two additional problems with the DBs were the need to solder SiPMs by hand (since cuflon does not tolerate the temperatures of an oven) and the need to use connectors (all of which are known to be non radiopure).

The new KDBs manufactured for NEW solve all the above issues. The material is

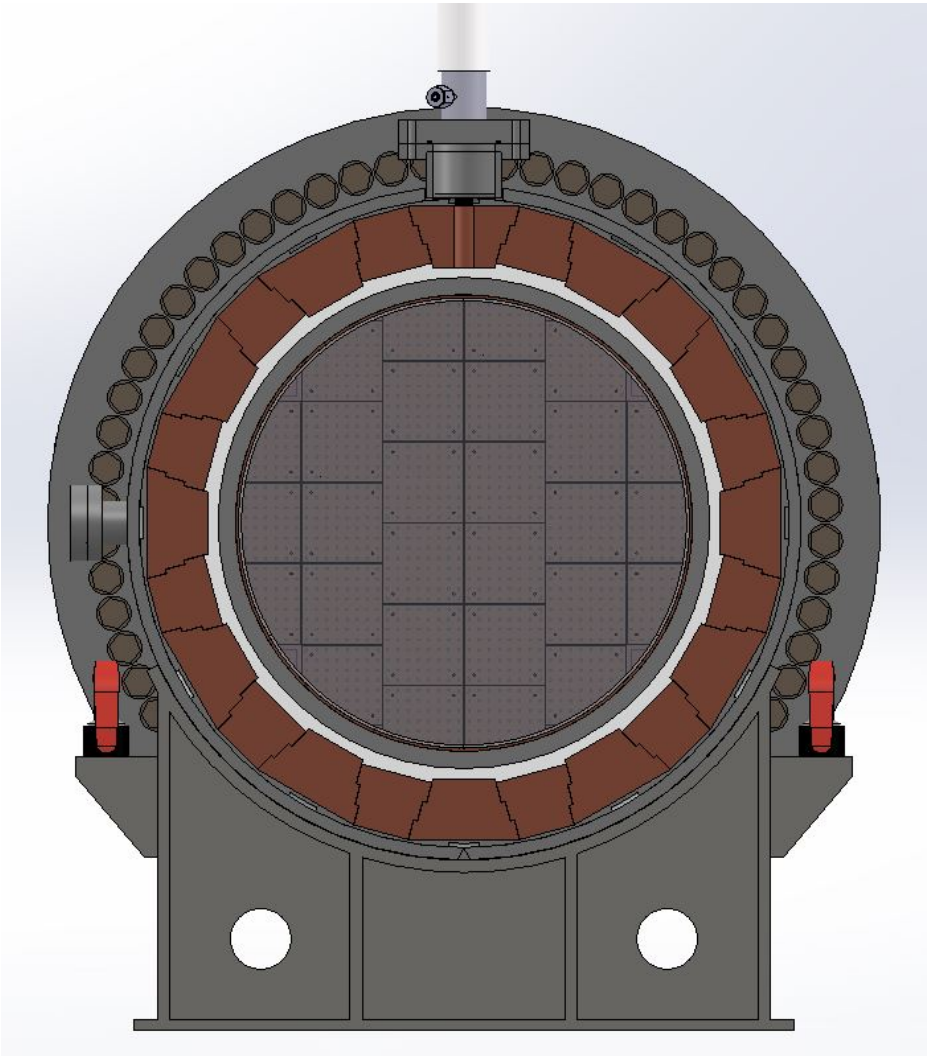

Figure 9.1.22: Drawing of the NEW tracking plane (NTP).

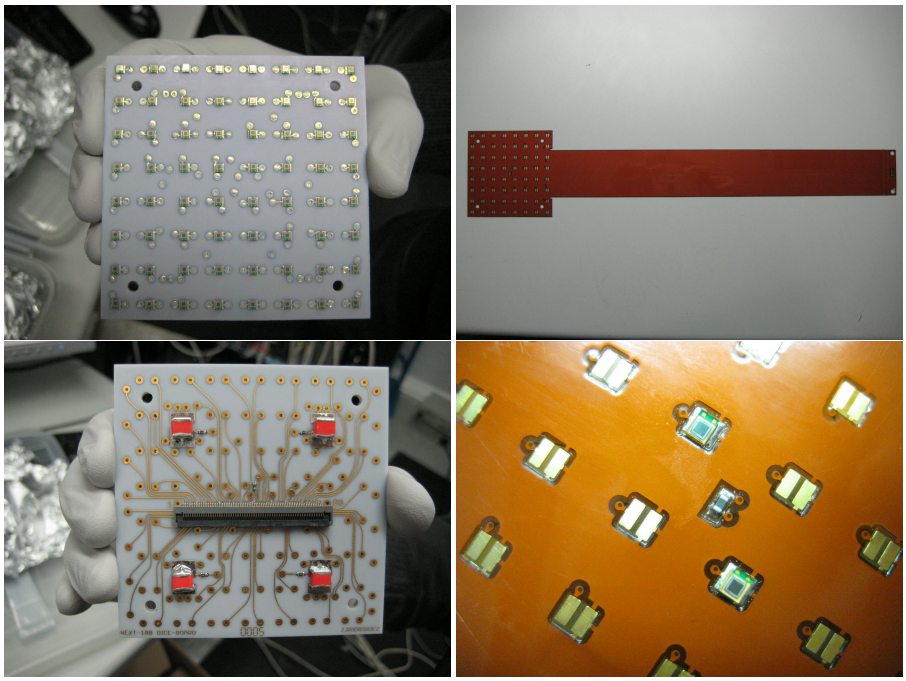

Figure 9.1.23: The evolution of the dice boards. DEMO Boards (right) were made with multilayered cuflon® . On the left side, the NEW Kapton DICE Boards (KDB) that allow for a better soldering of SiPMs. The first stage of the cable is now part of the KDB and the connector can be placed behind the copper shield.

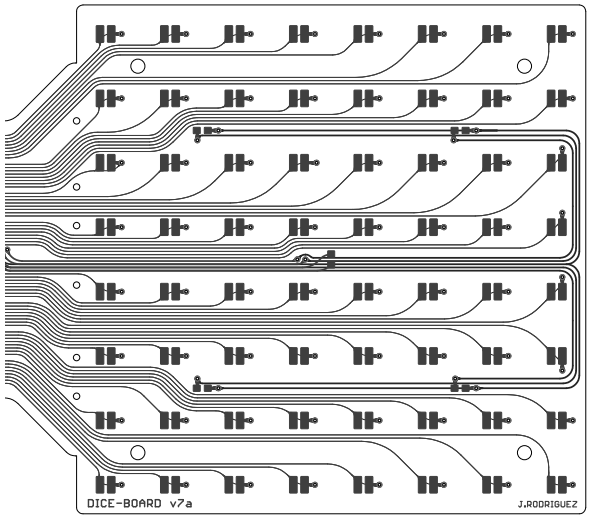

Figure 9.1.24: Schematic of the NEW DICE boards.

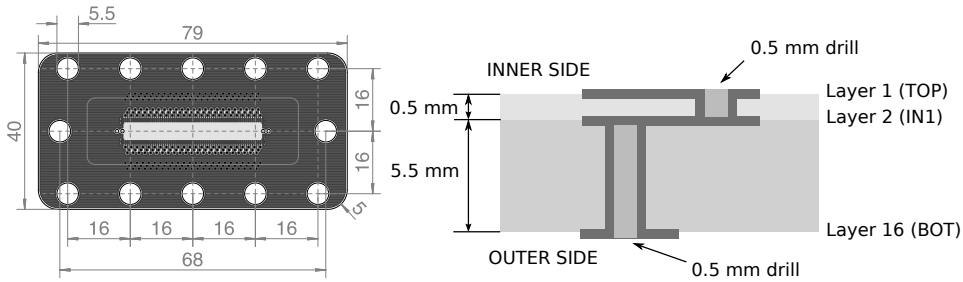

Figure 9.1.25: Drawing of a possible commercial feedthrough made with fiberglass, the same material used in common electronic boards. This design simplifies the cabling and it results in a very cheap solution. Some tests are ongoing to check performance of the solution when operating for a very long time. Right picture shows the internal structure of the feedthrough, three layers of PCB are glued together blocking the internal holes but allowing electrical connections between both sides of the board.

kapton, and the measured radioactivity budget (only upper limits) indicate that they are one order of magnitude cleaner than the old DBs. The SiPMs can be soldered in an oven and the circuit comes with its own piggy tail. The connector is located at the end of the long tail, and is screened from the gas by a thick copper layer.

In addition, TPB was coated directly on top of the DEMO DBs. Instead, the design of the electroluminiscent region with the quartz plate allows for a direct coating of the plate instead of the individual DICEs (or individual plates in front of each one as was also considered).

Finally, the last version of the DICE counts with a symmetric design (Fig. 9.1.24) that allows for a better subtraction of the noise when doing the difference of the voltages in the signal and bias lines. Such design has been tested in a realistic set-up with 4 meter long cables, an operatinal DICE and a front-end and it has proven to be able to separate single photoelectrons. That will allow a direct calibration of the SiPMs.

After the shielding, the KDBs are connected to kapton cables and those are extracted through a feedthrough to the outside. The current solution is based on a commercial model using a multilayer electronic board made with FR4. Figure 9.1.25 shows the internal design of the feedthrough.

9.1.8 The front-end electronics and DAQ

The NEW data-acquisition system (DAQ) has a design similar to the one used in NEXT-DEMO. It follows a modular architecture named the Scalable Readout System (SRS), already described in our CDR [101]. At the top of the hierarchy, a PC farm running the DAQ software, DATE, receives event data from the DAQ modules via Gigabit Ethernet (GbE) links. The DATE PCs (Local Data Concentrators, LDCs) assemble incoming fragments into sub-events, which are sent to one or more additional PCs (Global Data Concentrators, GDC). The GDCs build complete events and store them to disk for offline analysis.

The DAQ modules used are Front-End Concentrator (FEC) cards, which serve as the generic interface between the DAQ system and application-specific front-end modules. The FEC module can interface different kinds of front-end electronics by

using the appropriate plug-in card. The FEC card and the overall SRS concept have been developed within the framework of the CERN RD-51 collaboration. Three different FEC plug-in cards are used in NEXT-100.

Electronics for the energy plane

The front-end (FE) electronics for the PMTs in NEW will be very similar to the system developed for the NEXT-DEMO. In the NEW detector the PMTs signal will be transmitted using a differential configuration. The differential signal allows for very low noise transmission using 4-5 meters length cables, that is fundamental for NEXT-100 where the signals not only have to be extracted from the detector itself, but also go out of the lead castle used for shielding. The differential signal needs an extra circuit in order to supply the voltage to the PMT, decouple the continuous level of the voltage from the signal, and separate the signal to send it to the FEE (Fig. 9.1.26).

The first step in the chain is to shape and filter the fast signals produced by the PMTs (less than 5 ns wide) to match the digitizer and eliminate the high frequency noise.

Our design uses a single amplification stage based on the fully differential amplifier THS4511, which features low noise ($2\ \mathrm{nV}/\sqrt{\mathrm{Hz}}$) and provides enough gain to compensate for the attenuation in the following stage, based on a passive RC filter with a cut frequency of 800 kHz. This filtering produces enough signal stretching to allow acquiring many samples per single photo-electron at 40 MHz.

Electronics for the tracking plane

The tracking plane will have $\sim$ 1800 channels. Our design consists of a very simple, 64 channel Front-End Board (FEB, Figure 9.1.27). Each channel of the FEB provides the bias voltage and reads the differential signal transmitted via low-crosstalk kapton flat cables. The FE includes the analog stages, ADC converters, voltage regulators and an FPGA that handles, formats, buffers and transmits data to the DAQ. LVDS clock and trigger inputs are also needed. A total of 28 FEBs are required.

The design of the electronics is a collaboration between UPV and LBNL. It will be

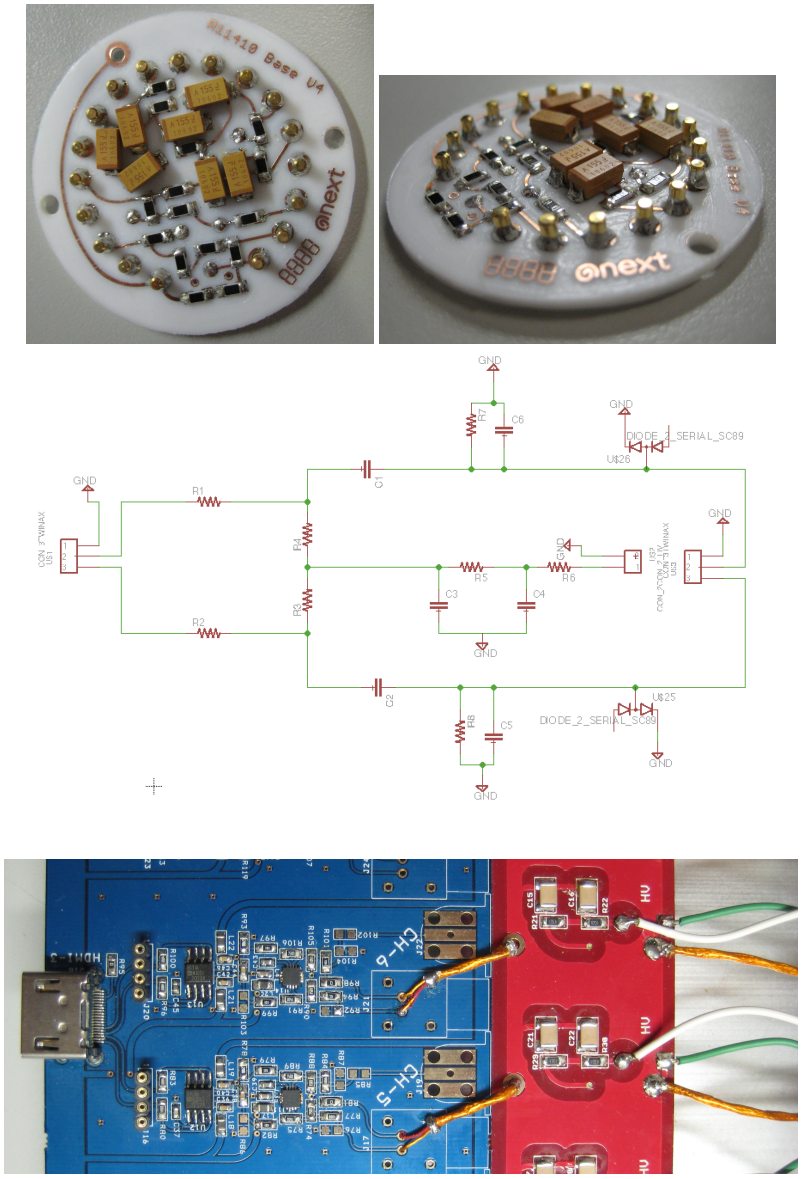

Figure 9.1.26: Detail of the cuflon PMT base for test in the top pictures. The break-out circuit decouples the signal from the voltage supplied to the PMTs. Center image shows the design of the circuit and bottom picture the first prototype used for testing and calibration of the PMTs.

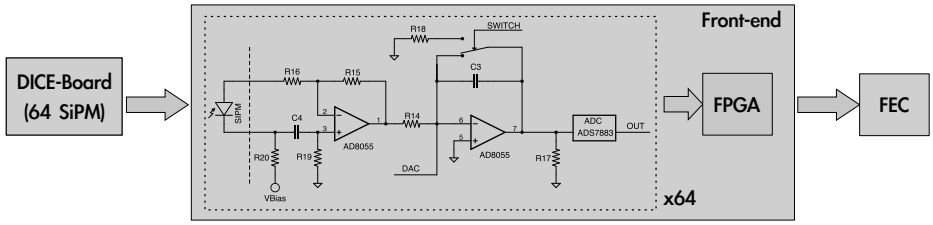

Figure 9.1.27: Functional blocks in the NEW FEB card.

an evolution of the electronics currently operational at NEXT-DEMO. The DAQ is responsibility of UPV, and it will also be an improved version of the DEMO DAQ.

9.2 NEXT 100

9.2.1 The apparatus

Figure 9.2.1 shows a drawing of the NEXT-100 detector, indicating all the major subsystems. These are:

- The pressure vessel, built in stainless steel and designed to withstand a pressure of 15 bar, described in Subsection 9.2.2. A copper layer on the inside shields the sensitive volume from the radiation originated in the vessel material.
- The field cage, electrode grids, HV penetrators and light tube, described in Subsection 9.2.3.
- The energy plane made of PMTs housed in copper enclosures, described in Subsection 9.2.4.
- The tracking plane made of MPPCs arranged into dice boards (DB), described in Subsection 9.2.5.
- The front end electronics, placed outside the chamber, described in Subsection 9.2.8.

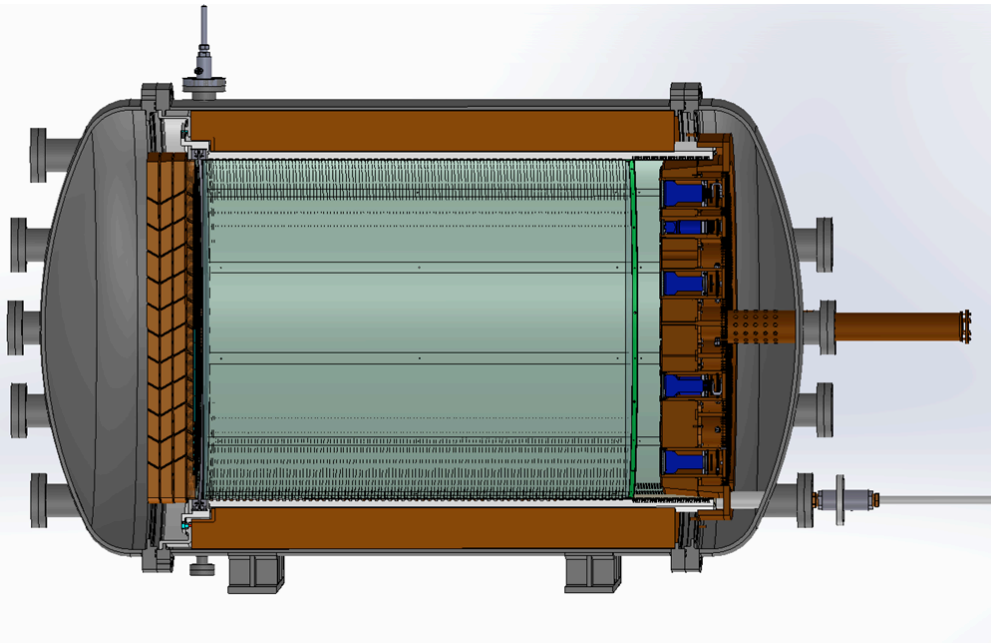

Figure 9.2.1: A 3D drawing of the NEXT100 detector, showing the pressure vessel (gray), the internal copper shield (brown) and the field cage (green). The PMTs of the energy plane are shown in blue.

- The gas system, capable of pressurizing, circulating and purifying the gas, described in Subsection 9.2.6.
- Shielding and other infrastructures, described in Subsection 9.2.9.

The NEXT TDR [137] gives the details of the design and components of the detector, which we summarise briefly here.

9.2.2 The pressure vessel

The pressure vessel (PV) consists of a barrel central section with two identical torispheric heads on each end, their main flanges bolted together. The construction material is stainless steel, specifically the low-activity 316Ti alloy. After screening samples, we have secured batches of material in excess of one ton to build the PV. Mea-

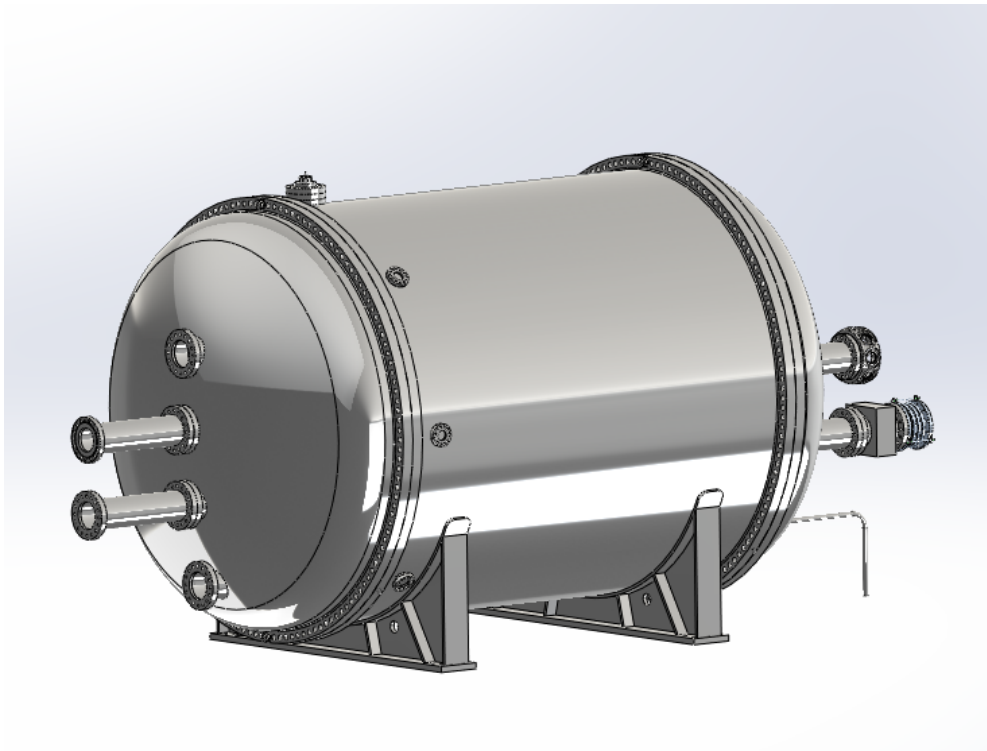

Figure 9.2.2: A 3D drawing of the pressure vessel.

surements of 316Ti show very low level of activity (0.2 mBq/kg for the thorium series and 1.3 mBq/kg for the uranium series) [138]. The mass of the PV is 1 200 kg, resulting in a total activity of about 1.6 Bq for the uranium series. To shield this activity we introduce an *inner copper shield* (ICS) 12 cm thick and made of radiopure copper, with an activity of about 5–10 μBq/kg. The ICS will attenuate the radiation coming from the external detector (including the PV and the external lead shield) by a factor of 100. After the ICS the residual activity due to the PV is about 0.02 Bq. One needs to add the residual activity of the ICS itself which is, taking into account self-shielding, of the order of 0.03 Bq. Thus, the resulting activity of the whole system is $\sim$ 0.05 Bq.

The vessel has been built strictly to *ASME Pressure Vessel Design Code, Section VIII*.

Figure 9.2.3: Exterior of NEXT-100 pressure vessel in the final stages of the construction (left). Detail of one of the gaskets used to hold the vacuum and pressure need in NEXT (right).

It has been designed almost entirely by the collaboration, under the leadership of LBNL and IFIC. The tender for fabrication was awarded to the Madrid-based company MOVESA and the fabrication is already finished, figure 9.2.3 shows a view of the NEXT-100 PV and a detail of the flange. IFIC has been in charge of supervision of fabrication, testing, certification and transport to LSC. The PV is already at the LSC.

9.2.3 The field cage

The main body of the field cage (Figure 9.2.4) will be a high-density polyethylene (HDPE) cylindrical shell, 2.5 cm thick, that will provide electric insulation from the vessel. Two wire meshes and a quartz plate — cathode, gate and anode — generate the two electric field regions of the detector. The drift region, between cathode and gate, is a cylinder of 107 cm diameter and 130 cm length. Copper strips attached to the HDPE and connected with low background resistors grade the high voltage. The EL region, between gate and anode, is 5mm.

All the components of the field cage have been prototyped with the NEW detector (see section 9.1). The NEXT-100 field cage and ancillary systems will be built by our USA collaborators.

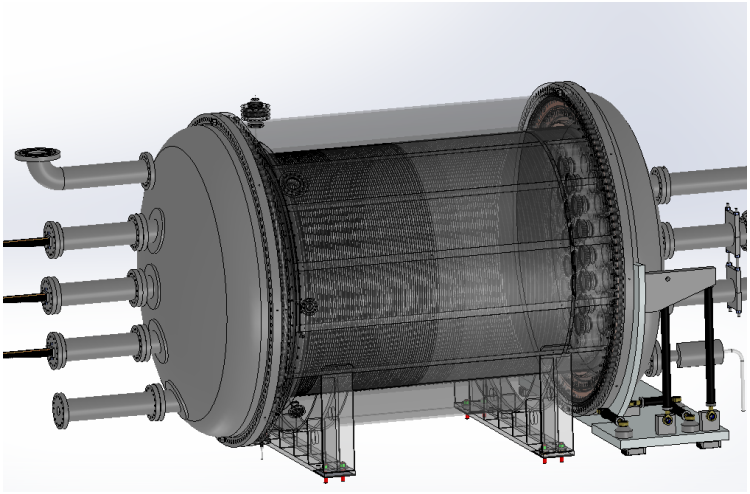

Figure 9.2.4: A 3D drawing of the detector showing the field cage inside.

9.2.4 The energy plane

The energy measurement in NEXT is provided by the detection of the electroluminescence light by an array of photomultipliers, the *energy plane*, located behind the transparent cathode (Figure 9.2.5). These PMTs will also record the scintillation light that indicates the start of the event.

A total of 60 Hamamatsu R11410-10 photomultipliers (Figure 9.2.5 bottom) covering 32.5% of the cathode area constitute the energy plane. This phototube model has been specially developed for radiopure, xenon-based detectors. The manufacturer quoted radioactivity per PMT is 3.3 mBq for the uranium series and 2.3 mBq for the thorium series, although independent measurements show even lower activities. The quantum efficiency of the R11410-10 model is around 35% in the VUV and 30% in the blue region of the spectrum, and the dark count rate is 2–3 kHz (0.3 photoelectron threshold) at room temperature [139].

Pressure-resistance tests run by the manufacturer showed that the R11410-10 cannot withstand pressures above 6 atmospheres. Therefore, in NEXT-100 they need to be protected from the main volume. The method is the one already developed for NEW, use a thick copper plate to separate the vacuum regions where the PMTs are placed from the high pressure of the active volume. The PMTs look to the main volume through sapphire windows. The window, 5 mm thick, is brassed to copper corona that are then screwed to the copper plate. It seals against leakages using helicoflex gaskets. The sapphire windows are not transparent to the VUV light produced by the Xenon, they are also coated with tetraphenil butadiene (*TPB*) to maximize the number of photons in the PMTs. The PMT is optically coupled to the window using silicone optical pads of <2 mm thickness. On the back side of the PMT a thick copper plug provides an extra shielding against radiation and is also used to hold a spring that pushes the PMT agains the window and the optical pad. In order to maximize the light transmission through the sapphire windows they are also coated with tetraphenil butadiene (*TPB*).

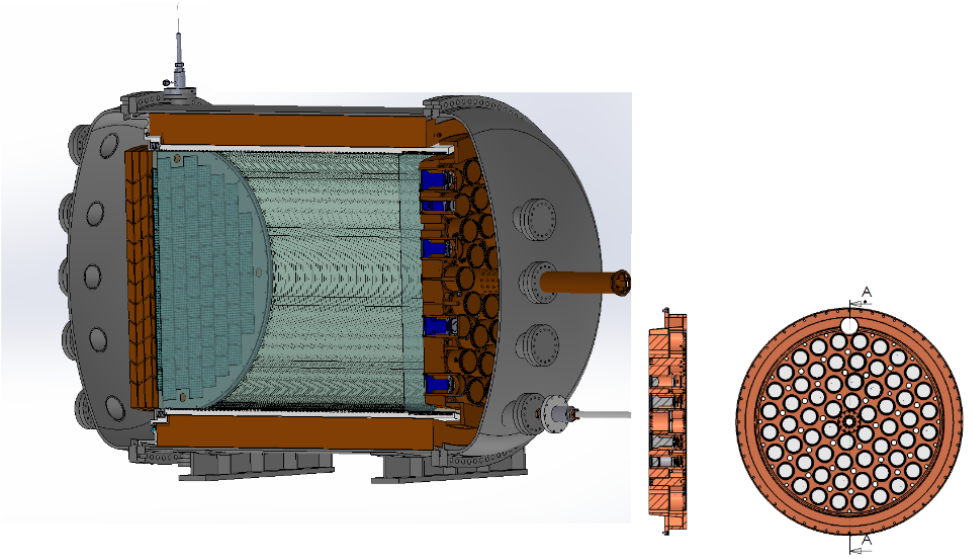

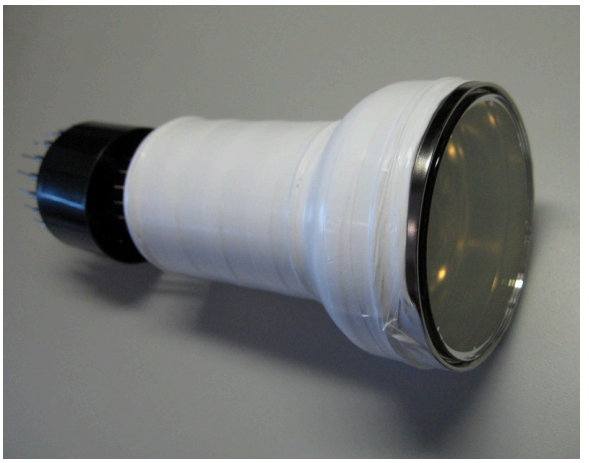

Figure 9.2.5: A drawing of the detector showing the energy plane inside the PV (top). The Hamamatsu R11410-10, a 3-inches photomultiplier with high quantum efficiency ($> 30\%$) at the xenon scintillation wavelengths and low radioactivity (bottom).

The vacuum side is maintained at vacuum well below the Paschen minimum, avoiding sparks and glow discharge across PMT pins. The cables are connected to a vacuum high voltage feedthrough.

The design of the energy plane has been shared between IFIC, UPV (Universidad Politécnica de Valencia) and LBNL groups. The PMTs have already been purchased and tested, and are currently being screened for radioactivity at the LSC.

9.2.5 The tracking plane

The tracking function in NEXT-100 will be provided by a plane of multi-pixel photon counters (MPPCs) operating as sensor pixels and located behind the transparent EL gap. The chosen MPPC is the one used in NEXT-DEMO (S10362-11-050P model by Hamamatsu). This device has an active area of 1 mm^2, 400 sensitive cells (50 μm size) and high photon detection efficiency in the blue region (about $\sim$ 50% at 440 nm). MPPCs are very cost-effective and their radioactivity is very low, given its composition (mostly silicon) and very small mass.

The MPPCs will be mounted in Dice Boards (DB) identical in size to the ones operating in NEXT-DEMO (see Chapter 6) but with an improved design that will simplify the signal extraction from the vessel on one hand, and will allow soldering the SiPMs inside the oven allowing for a faster and more robust assembly of the components. The new DICE boards are produced usign kapton that allows also for a design with the first stage of the cable to be part of the DICE (see Fig. 9.2.6). In the new design, the ground layers of the DICE have been removed resulting in a thinner DICE with improved radiopurity rate.

The electronics for the MPPCs will also be an improved version of the electronics for the DEMO detector. Also, like in NEXT-DEMO and NEW, all the electronics will be outside the chamber. The large number of channels in NEXT-100, on the other hand, requires the use of a multi-pin feedthroughs used and tested in NEW (See 9.1.7).

The $\sim$8 000 MPPCs needed for the tracking plane have already been purchased.

Figure 9.2.6: Picture of the DICE board to be used in the NEXT-100 detector. The material used is cirlex© that allows for an improved soldering protocol and gives more flexibility in the design. The DICE and the first stage of the cable are now part of the same unit resulting in a better signal transmission.

9.2.6 The gas system

The gas system must be capable of pressurizing, circulating, purifying, and depressurizing the NEXT-100 detector with xenon, argon and possibly other gases with less than 10 grams of Xenon loss per year and without damage to the detector. In particular, the probability of any substantial loss of the very expensive enriched xenon (EXe) must be minimized. A list of requirements, in approximate decreasing order of importance, considered during the design is given below:

1. Pressurize vessel, from vacuum to 15 bar (absolute).

2. Depressurize vessel to closed reclamation system, 15 bar to 1 bar (absolute), on fault, in 10 seconds maximum.

3. Depressurize vessel to closed reclamation system, 15 bar to 1 bar (absolute), in normal operation, in 1 hour maximum.

4. Relieve pressure (vent to closed reclamation system) for fire or other emergency condition.

5. Allow a maximum leakage of EXe through seals (total combined) of 100 g/year.

6. Allow a maximum loss of EXe to atmosphere of 10 g/year.

7. Accommodate a range of gases, including Ar and N_2.

8. Circulate all gases through the detector at a maximum rate of 200 standard liters per minute (slpm) in axial flow pattern.

9. Purify EXe continuously. Purity requirements: $<$ 1 ppb O_2, CO_2, N_2, CH_4.

The most vulnerable component of the gas system is the re-circulation compressor, that must have sufficient redundancy to minimize the probability of failure and

leakage. The collaboration has chosen a compressor manufactured by SERA COMPRESS GMBH. The gas is moved through the system by a triple stainless steel diaphragm. Between each of the diaphragms there is a sniffer port to monitor for gas leakages. In the event of a leakage, automatic emergency shutdown can be initiated.

MICROTORR model MC4500-902FV from SAES has been chosen as the purification filter for PS4-MT15 from SAES will be needed (since they result in a longer electron lifetime and do not emit radon) for the enriched xenon run.

An automatic recovery system of the expensive EXe will also be needed to evacuate the chamber in case of an emergency condition. A 19-m^3 expansion tank will be placed inside the laboratory to quickly reduce the gas pressure in the system.

The gas system has been designed as a collaboration between IFIC and University of Zaragoza (UNIZAR), taking advantage of the experience gained with our prototypes. The basic gas system needed for the initial operation of the NEXT-100 apparatus has already been purchased and shipped to the LSC, but the system must be upgraded during 2014 for the enriched xenon run in 2015.

9.2.7 Slow Control

When the detector is operating it needs to be monitored to guarantee the data quality and to start the different emergency protocols if needed. The detector control is performed using different custom made LabView© programs. The programmes monitor all the different components of the detector: PMTs voltage, HHV, gas system pressure, temperature and electronics power supply voltage. They are able to react agains different emergency situations and interact with the corresponding shifter (alarms, e-mails,...) and even stop the detector automatically depending on the situation observed. The different programmes comunicate among themselves through a general one allowing an independent response of the different subsystems monitored but also a general reaction of the whole system if needed.

A fundamental piece of the slow control is the multi-channel RGA that will allow for continuous checks of leaks in the most delicate parts of the detector which are PMT enclosures and the different flanges. The RGA will be autonomous and

controlled by a specific software programme that, connected with the general slow control programme, will allow for a emergency stop of the full detector.

9.2.8 Electronics

The electronics is a critical part of the detector. The electronics for NEXT-100 will be fully tested in the NEW detector. It is already described in 9.1.8. Testing it in the Canfranc Underground Lab is an important step in the process to the final design. There are some aspects of the electronics that need to be understood when the detector operates underground. First, the operation of the electronics with radiopure materials. Second, the noise spectrum needs to be understood and operating the detector is the best way to integrate all the effects that noise can have in the signal: long cables, capacitive coupling, etc. The operation of NEXT-100 will be modified if needed to improve the signals.

9.2.9 Shielding and other infrastructures

To shield NEXT-100 from the external flux of high-energy gamma rays a relatively simple lead castle, shown in Figure 9.2.7, has been chosen, mostly due to its simplicity and cost-effectiveness. The lead wall has a thickness of 20 cm and is made of layers of staggered lead bricks held with a steel structure. The lead bricks have standard dimensions ($200 \times 100 \times 50$ mm^3), and, by requirement, an activity in uranium and thorium lower than 0.4 mBq/kg.

The lead castle is made of two halves mounted on a system of wheels that move on rails with the help of electric motors. The movable castle has an open and a closed position. The former is used for the installation and service of the pressure vessel; the latter position is used in normal operation. A lock system fixes the castle to the floor in any of the two configurations to avoid accidental displacements.

The design of the lead castle has been led by the University of Girona (UdG), in collaboration with UPV and IFIC. The design is completed and the shield is ready to be built pending the availability of funds.

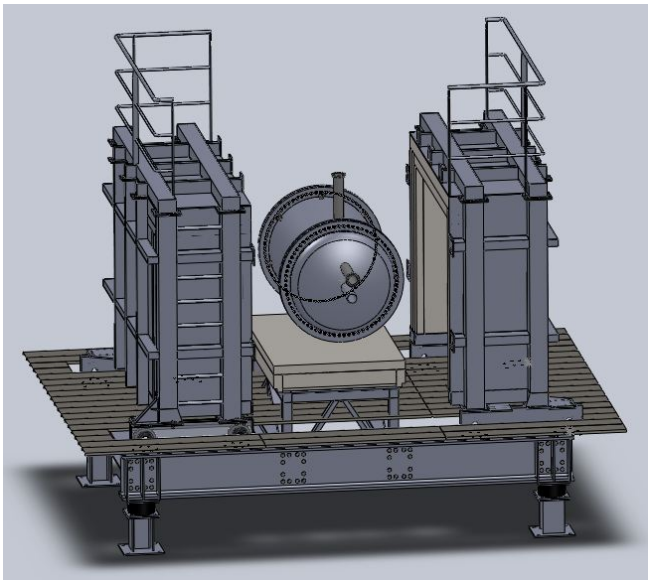

Figure 9.2.7: Drawing of the NEXT-100 lead castle shield in its open configuration.

The construction of the infrastructures needed for the NEXT-100 experiment (working platform, seismic pedestal) is currently underway. They will be fully installed at the LSC by the end of 2013.

Figure 9.2.8 shows an image of Hall A, future location of NEXT-100. The pool-like structure is intended to be a catchment reservoir to hold xenon or argon (a liquid-argon experiment, ArDM, will be neighbouring NEXT-100 in Hall A) gas in the event of a catastrophic leak. Therefore, for reasons of safety all experiments must preclude any personnel working below the level of the top of the catchment reservoir.

An elevated working platform will be built prior to the installation of NEXT-100. It is designed to stand a uniform load of 1500 kg/m² and a concentrated load of 200 kg/m². It is anchored to the hall ground and walls. The platform floor tiles are made of galvanized steel and have standard dimension to minimize cost.

Due to the mild seismic activity of the part of the Pyrenees where the LSC is located, a comprehensive seismic study has been conducted as part of the project risk

Figure 9.2.8: View of Hall A of the Laboratorio Subterráneo de Canfranc prior to any equipment installation (left). Hall A with the working platform already installed (right). Installation of the seismic infrastucture will be ready in 2014.

analysis. As a result, an anti-seismic structure that will hold both pressure vessel and shielding has been designed. This structure will be anchored directly to the ground and independent of the working platform to allow seismic displacements in the event of an earthquake.

Figure 9.2.9 shows the placement of NEXT-100 and components on the platform as well as the dimensions.

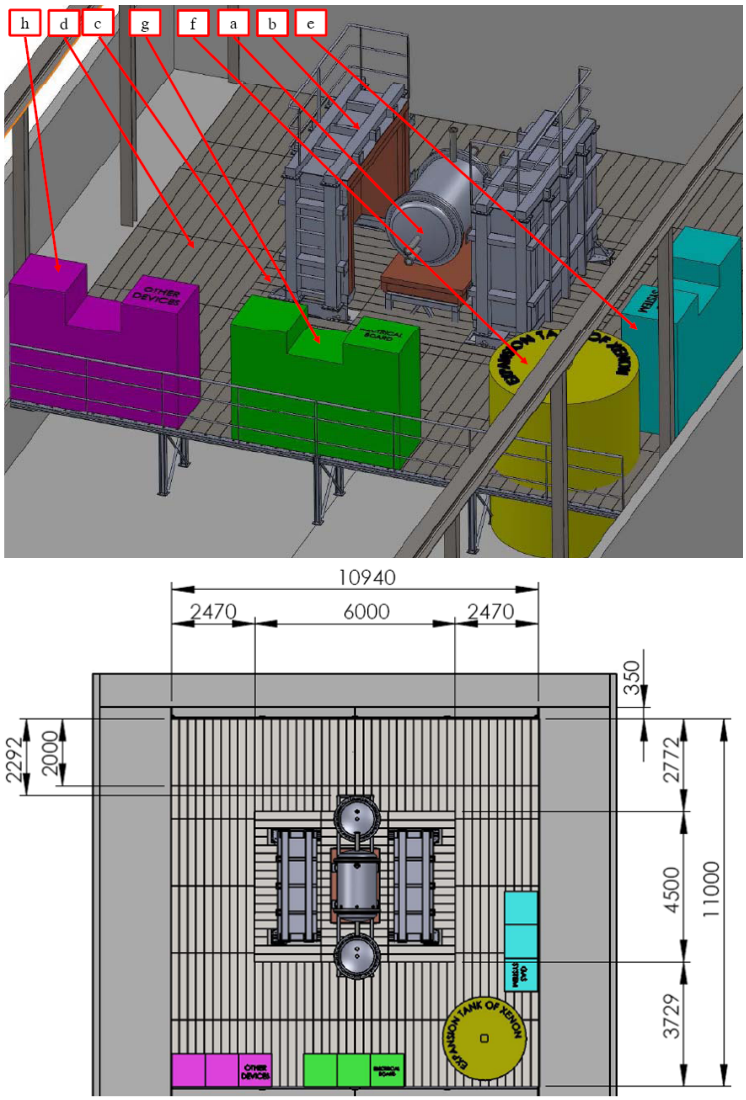

Figure 9.2.9: Top: Intended location of the components and subsystems for the operation of NEXT-100 on the working platform: (a) NEXT-100; (b) the lead castle shield in its open configuration; (c) seismic platform; (d) working platform; (e) gas purification system; (f) emergency gas vent tank; (g) data acquisition system; (h) other systems. Bottom: Top view showing the dimensions of the working platform.

9.3 NEXT background model

Every $\beta\beta 0\nu$ experiment must have a model that describes the sources of radioactive contaminants and their activity, as well as a detailed simulation that allows to predict the fraction of background events that are misidentified as signal. The ensemble of data and calculations is called the experiment background model.

9.3.1 Sources of background

Radioactive contaminants in detector materials

After the decay of ^{214}Bi, the daughter isotope, ^{214}Po, emits a number of de-excitation gammas with energies above 2.3 MeV. The gamma line at 2447 keV, of intensity 1.57%, is very close to the Q-value of ^{136}Xe. The gamma lines above $Q_{\beta\beta}$ have low intensity and their contribution is negligible.

The daughter of ^{208}Tl, ^{208}Pb, emits a de-excitation photon of 2614 keV with a 100% intensity. The Compton edge of this gamma is at 2382 keV, well below $Q_{\beta\beta}$. However, the scattered gamma can interact and produce other electron tracks close enough to the initial Compton electron so they are reconstructed as a single object falling in the energy region of interest (ROI). Photoelectric electrons are produced above the ROI but can lose energy via bremsstrahlung and populate the window, in case the emitted photons escape out of the detector. Pair-creation events are not able to produce single-track events in the ROI.

Radon

Radon constitutes a dangerous source of background due to the radioactive isotopes ^{222}Rn (half-life of 3.8 d) from the ^{238}U chain and ^{220}Rn (half-life of 55 s) from the ^{232}Th chain. As a gas, when produced in the detector materials can end up mixed in the main volume of the detector. ^{214}Bi is a decay product of ^{222}Rn, and ^{208}Tl a decay product of ^{220}Rn. In both cases, radon undergoes an alpha decay into polonium, producing a negative ion which is drifted towards the anode by the electric field of the TPC. As a consequence, ^{214}Bi and ^{208}Tl contaminations can be assumed to be de-

posited on the anode surface. Radon may be eliminated from the TPC gas mixture by recirculation through appropriate filters. There are also ways to suppress radon in the volume defined by the shielding. Radon control is a major task for a $\beta\beta 0\nu$ experiment, and will be of uppermost importance for NEXT-100.

Cosmic rays and laboratory rock backgrounds

Cosmic particles can also affect our experiment by producing high energy photons or activating materials. This is the reason why double beta decay experiments are conducted deep underground. At these depths, muons are the only surviving cosmic ray particles, but their interactions with the rock produce neutrons and electromagnetic showers. Furthermore, the rock of the laboratory itself is a rather intense source of ^{208}Tl and ^{214}Bi backgrounds as well as neutrons.

The flux of photons emanating from the LSC walls is (see our TDR and references therein):

- $0.71 \pm 0.12\ \gamma/\mathrm{cm}^2/\mathrm{s}$ from the ^{238}U chain.
- $0.85 \pm 0.07\ \gamma/\mathrm{cm}^2/\mathrm{s}$ from the ^{232}Th chain.

These measurements include all the emissions in each chain. The flux corresponding to the ^{208}Tl line at 2614.5 keV and the flux corresponding to the ^{214}Bi line at 1764.5 keV were also measured (from the latter it is possible to deduce the flux corresponding to the 2448 keV line). The results are:

- $0.13 \pm 0.01\ \gamma/\mathrm{cm}^2/\mathrm{s}$ from the ^{208}Tl line.
- $0.006 \pm 0.001\ \gamma/\mathrm{cm}^2/\mathrm{s}$ from the ^{214}Bi line at 2448 keV.

The above backgrounds are considerably reduced by the shielding. In addition, given the topological capabilities of NEXT, the residual muon and neutron background do not appear to be significant for our experiment.

9.3.2 Radioactive budget of NEXT-100

Information on radiopurity of the materials expected to be used in the construction of NEXT100 has been compiled, performing specific measurements and also examining data from the literature for materials not yet screened. A detailed description is presented in [138]. A brief summary of the results presented there is shown in Table 9.3.1.

Material	Subsystem	^{238}U	^{232}Th
Lead Shield		0.37	0.07
Copper	ICS	< 0.012	< 0.004
Steel (316Ti)	PV	< 1.9	< 1
Inconel 718	PV	< 5.6	< 13.8
Inconel 625	PV	< 2.4	< 6.0
Peek	FC/EP/TP	36	11.7
Capacitors (Tantalum)	FC/EP/TP	320	1.23×10^3
SMD Resistors, Finechem (per pc)	FC	0.022	0.048
Polyethylene	FC	0.23	<0.14
TTX	LT	12.4	1.6
TPB	LT/EP/TP	1.63	0.47
PTFE (Teflon)	EP/TP/DB	0.025	0.031
PMT (R11410-MOD per pc)	EP	< 2.5	< 2.5
PMT (R11410-MOD per pc)	EP	< 0.4	< 0.3
Sapphire window	EP	0.31	0.12
CUFLON	TP	0.36	0.28
Kapton cable	TP/EP	14	39

Table 9.3.1: Activity (in mBq/kg) of the most relevant materials used in NEXT.

9.3.3 Expected background rate

As already remarked, NEXT has two powerful handles to distinguish signal from background:

- *Energy resolution*: Signal events have all the same energy. Selecting only the events in the energy region around $Q_{\beta\beta}$ defined by the resolution eliminates most of the spurious activity in the detector.

- *Event topology*: Signal events appear uniformly distributed in the source (i.e., the enriched xenon) and have a distinctive topology (a twisted track with blobs in both ends, see Figure 5.3.1). Requiring signal events to be strictly contained in the active volume of the chamber eliminates essentially all charged backgrounds entering the detector. Confined tracks generated by neutral particles, like high-energy, gammas can be suppressed by pattern recognition.

As explained above, the only relevant backgrounds for NEXT are the photons emitted by the ^{208}Tl line (2614.5 keV) and the ^{214}Bi line (2448 keV). These sit very near $Q_{\beta\beta}$ and the interaction of the photons in the gas can fake the $\beta\beta0\nu$ signal. NEXT-100 has the structure of a Matryoshka (a Russian nesting doll). The flux of gammas emanating from the LSC walls is drastically attenuated by the lead castle (LC), and the residual flux, together with that emitted by the lead castle itself and the materials of the pressure vessel is further attenuated by the inner copper shielding (ICS). The ICS also attenuates the flux emitted by the tracking plane FE electronics (FEE), which sit behind it. One then needs to add the contributions of the "inner elements" in NEXT: field cage (FC), energy plane (EP), and the elements of the tracking plane (TP) not shielded by the ICS.

A detailed Geant4 simulation of the NEXT-100 detector was written in order to compute the background rejection factor achievable with the detector. Simulated events, after reconstruction, were accepted as a $\beta\beta0\nu$ candidate if

(a) they were reconstructed as a single track confined within the active volume;

Table 9.3.2: Acceptance of the selection cuts for signal and backgrounds.

	Fraction of events		
Selection cut	$\beta\beta0\nu$	^{214}Bi	^{208}Tl
Confined, single track	0.48	6.0×10^{-5}	2.4×10^{-3}
Energy ROI	0.33	2.2×10^{-6}	1.9×10^{-6}
Topology $\beta\beta0\nu$	0.25	1.9×10^{-7}	1.8×10^{-7}

(b) their energy fell in the region of interest, defined as ± 0.5 FWHM around $Q_{\beta\beta}$;

(c) the spatial pattern of energy deposition corresponded to that of a $\beta\beta0\nu$ track (*blobs* in both ends).

The achieved background rejection factor together with the selection efficiency for the signal are shown in Table 9.3.2. As can be seen, the cuts suppress the radioactive background by more than 7 orders of magnitude. This results in an estimated background rate of about 5×10^{-4} counts/(keV $\cdot$ kg $\cdot$ y).

9.4 Discovery Potential

Using the background expected rate shown in last section and with the fiducial mass of the detector we can calculate the sensitiviy of the detector as a function of time and then evaluate its potential for a discovery.

Using the method described in [98] for the experimental sensitivity determination, the sensitivity of NEXT-100 detector to the $m_{\beta\beta}$ is as low as 100meV. When comparing this value with the sensitivity calculated using the same method for the other two Xenon experiments (EXO and KamLAND-ZEN) it reaches the best sensitivity (Figure 9.4.1).

Even more important than the absolute value of the sensitivity is to compare that value with the current landscape of the neutrino mass. On one hand, the current

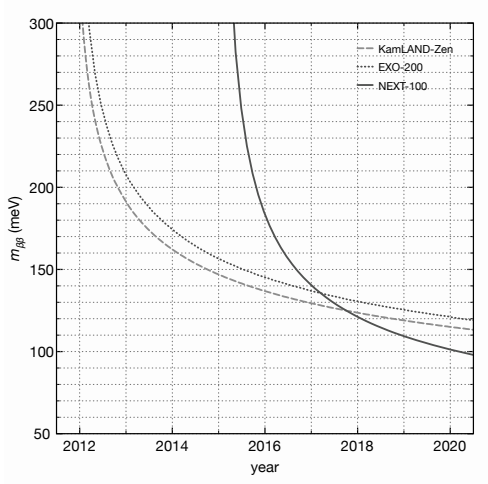

Figure 9.4.1: Sensitivity to $m_{\beta\beta}$ of the three Xenon detectors in the market. NEXT-100 reaches the best value after a few years of operation thanks to its great background rejection potential.

limit to the double beta mass is at the level of 250meV (Figure 9.4.2). In the other, recent publications ([18], [19]) suggest that cosmological observations show a sum of neutrino masses at the level of 320 meV ($\sum_{i=1}^{3} = 0.32 \pm 0.11$eV).

When we draw the possible values of the neutrino mass sum in a plot $m_{\beta\beta}$ vs $\sum_m$ we can see that NEXT-100 may contribute with a new measurement in the region (Fig. 9.4.3), and may also discover the neutrinoless double beta decay process.

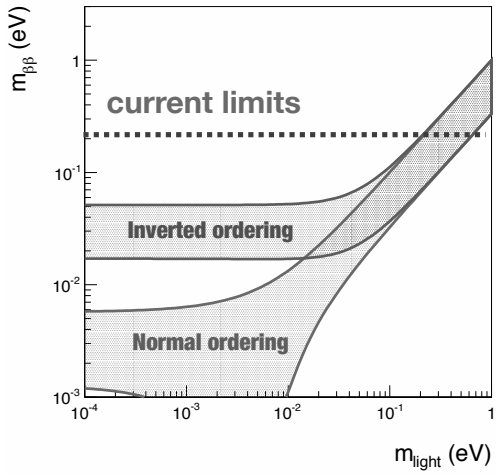

Figure 9.4.2: Current limit to $m_{\beta\beta}$. Most of the experiments reach a limit of the order of 250 meV, NEXT-100 will go to 100 meV.

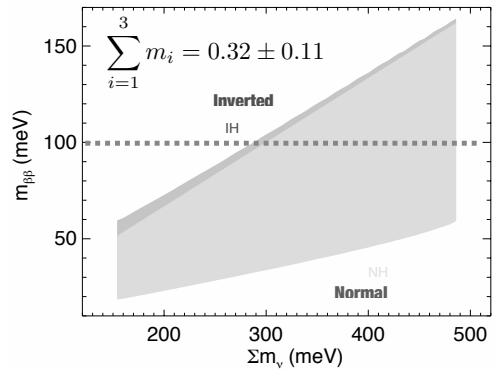

Figure 9.4.3: Sensitivity of NEXT-100 over the cosmological results. NEXT-100 will cover a large fraction of the region of interest.

Some part of our being knows this is where we came from. We long to return. And we can. Because the cosmos is also within us. We're made of star-stuff. We are a way for the cosmos to know itself.

Carls Sagan

10

Trencant la simetria

El ser humà sempre ha tingut la necessitat de entendre la seva propia existencia i la del món que ens envolta. No només l'existència sino també el nostre paper a l'univers, com es aquest univers, com funciona, i un fum mès de preguntes que han sigut fonamentals al llarg de la historia per a aconseguir el nivell de la ciencia actual i el món tecnologic en el que vivim. En el camí per a respondre aquestes preguntes ens em trobat amb altres noves i, clar, algunes respostes. De la mateixa manera, l'atracció per la bellessa ha estat sempre present en el nostre desenvolupament fins al punt de trovar multiples conexions entre algunes de les preguntes que en principi semblaven estar relacionades amb la ciencia però que també tenen a veure amb la bellesa. El ser humà s'en ha adonat de que hi ha estructures, formes que són belles per a una gran diversitat d'observadors, semblen estard dotades d'una bellessa intrínseca, objectiva. Per tant, ens hem preguntat si hi ha magnituds quantificables (medibles) que puguen

servir per a evaluar d'una forma o altra la bellesa. No vaig a clavar-me a explicar amb detall tots els estudis relacionats amb la ciencia de la bellesa, tan sols nombraré dos: La simetria i les proporcions.

A la natura ens trobem amb simetries per tot arreu i al mateix temps tractem de reproduïr-les, quasi-totes les estructures humanes les fan servir en un lloc o altre. Que passa quan el que volem no es observar la natura o alterar-la, sino explicar-la? Estem acostumats a viure entre simetries, sabem que poden simplificar un problema complexe reduïnt-lo a transformacions sobre objectes simples. A mès a mès, com em comentat abans, la simetria està directament relacionada amb la bellesa, podria ser que aquesta relació vingues donada desde un nivell bàsic? Quan ens enfrontem al repte de tractar de descriure el món tractem de buscar relacions entre els seus components fonamentals, els més simples, a fi de explicar com es combinen entre ells per construïr el món complex en el que vivim. Podriem fer-ho mitjançant simetries que ens relacionen els diferents nivells de complexitat? Aquesta idea es la que es troba darrere del Model Estandard de la Física de Partícules.

D'altra banda, les simetries no poden contar la historia sencera. Al igual que un edifici construït simétricament necesita portes i finestres per a que la gent i la llum puguen entrar i utilitzar-lo, per a plenar-lo. Aquestes portes i finestres trenquen la simetria a canvi d'obrir-lo i il·luminar-lo. Efectivament, quan una simetria es trenca sempre ve acompanyada d'una historia, es ben conegut que contant els anells d'un tronc d'arbre podem saber la seva edat. Però al mateix temps, aquells anells que no descriuen un cercle perfecte, que tenen "imperfeccions", son els que ens poden contar mès coses de la vida d'aquell arbre si els observem amb detall. Podem coneixer si va sofrir cap incendi prop seu, si va estar malalt, etc. En el cas de les particules fonamentals, si no trenquem les simetries del model la realitat que aquest descriuria seria molt distinta del que en realitat observem. D'una banda les partícules no tindrien massa, es el *famós* mecanisme Higgs i el seu *trencament espontani de la simetria* el que li confereix massa a les partícules. D'altra, si la relació materia/anti-materia fos perfecta (totalment simètrica) deuria d'existir un univers igual que el nostre tot fet d'anti-materia, o (i més probable) la materia i l'anti-materia s'haurien aniquilat

totalment en els primers instants de l'univers i tan sols quedaria llum, nosaltres no estariem aquí per plantejar-nos estes coses. Si no s'hagues trencat la simetria no hi hauria cap historia que contar, no existiriem. Però existim, i per tant sabem que aquesta simetria també es trenca, el que no entenem es com. S'han observat diferencies en les partícules que formen protons i neutrons però no es suficient, hi ha d'haver diferencies mès grans. Aquestes diferencies podrien trobar-se en els neutrins [1], i es això el que tractem de trobar amb el detector NEXT. NEXT tracta d'entendre i explicar les histories responsbles del trencament de la simetria materia/anti-materia.

10.1 Un troç de realitat.

Començarem parlant una mica sobre els neutrins, aquestes partícules diminutes que ho plenen tot, ens travessen el cos constantment a mil·lions però mai les sentim. Els neutrins son partícules neutres (sense carrega eléctrica) i per tant no senten els camps electromagnetics; no tenen practicament massa sent molt difícil observar el efecte dels potencials gravitatoris sobre aquests; per últim, tampoc tenen color (cárrega de les interaccións fortes). Els neutrins tan sols son sensibles a les interaccions febles. El resultat es una partícula capaç d'atravessar un any llum de plom sense interactuar amb ell, com si fos transparent. Aleshores, perquè ens interessa aquest *diminut tros de la realitat*? Perquè hi ha tantes persones dedicant el seu esforç i les seves vides a estudiar i coneixer les propietats d'un component tan minuscul del nostre món? La resposta a estes preguntes es que aquesta peça pot ser la clau per a entendre com es trenquen les simetries en el Model Estandard.

Com em dit abans, el neutri tan sols sent la interacció febla, una de les característiques mès rellevants d'aquesta interacció es que viola 100% la simetria de paritat. Al aplicar aquesta simetria a una partícula o conjunt de partícules obtenim la seva reflexió especular. La interacció febla també viola totalment la simetria de conjugació de càrrega, simetria que transforma tots els números quantics d'una partícula per els

[1] Els neutrins son els companys dels electrons en l'interacció febla. igual que en el l'electromagnetisme existeixen carregues positives i negatives, els electrons i els neutrins tenen carregues "febles" que els fan sensibles a la interacció febla.

de la seva corresponent antipartícula. D'altra banda, la interacció febla si respecta la combinació de les dues simetries. El que la violació d'aquestes simetries implica es que si la interacció febla ens crea una partícula amb el braç esquerre aixecat, quan la ficarem davant d'un mirall no hi veuriem res reflexat ja que no podría existir una partícula amb el braç dret aixecat. De la mateixa manera, si en lloc de reflexar-la en un mirall la intentem transformar en la seva anti-partícula tampoc ho aconseguirem, ja que no pot haver-hi anti-particules amb el braç esquerre aixecat. No obstant això, si que pot existir la combinació de totes dues transformacions, una anti-particula amb el braç dret en l'aire (Figura 10.1.1). Aquesta partícula creada per la interacció febla es el neutrí, així en la natura sols trobem neutríns levogirs i anti-neutrins dextrógirs [2] [3], però mai neutríns dextrogirs o anti-neutrins levogirs. D'altra banda, com que els neutrins son neutres, podem interpretar aquest fet d'una altra forma. Podem dir que en realitat, la reflexió especular del neutrí levogir si que existeix, però es tracta de l'anti-neutrí. Es a dir, el neutrí i l'anti-neutrí son la mateixa partícula i tan sols es diferencien en el braç que han aixecat (si son levogirs o dextrogirs). Aquesta forma de descriure la natura dels neutrins es el que es coneix com *descripció Majorana dels neutrins* i ens obrí una porta per entendre la asimetria materia/anti-materia, si tenim particules que son al mateix temps anti-partícules, particules en el paper d'agents dobles jugant a dos bandes, segur que ens ajuden a entendre perque l'univers està ple de materia i no s'ha aniquilat amb l'anti-materia.

Com hem vist, introduïr un neutrí de Majorana a la teoría ens ajudaria a entendre el nostre univers. Però, per a anyadir una peça nova o diferent a la teoría hem de tenir proves (estem fent ciencia!) per tant, el primer que hem de buscar es la forma de demostrar que efectivament el neutrí i el anti-neutrí son la mateixa anti-partícula. Per fer-ho, l'única manera realista es medir processos ón dos neutrins es destrueixen

[2]La definició de levogir i dextrogir està relacionat amb l'helicitat de la partícula, es a dir l'orientació de l'espí d'aquesta respecte al seu sentit del moviment. En el cas dextrogir, els dos tenen el mateix sentit, en el cas levogir sentit opossat.

[3]En realitat la interacció febla selecciona les partícules per quiralitat que es una altra de les propietats de les partícules. Per al cas de partícules sense massa no hi existeix diferencia amb l'helicitat.

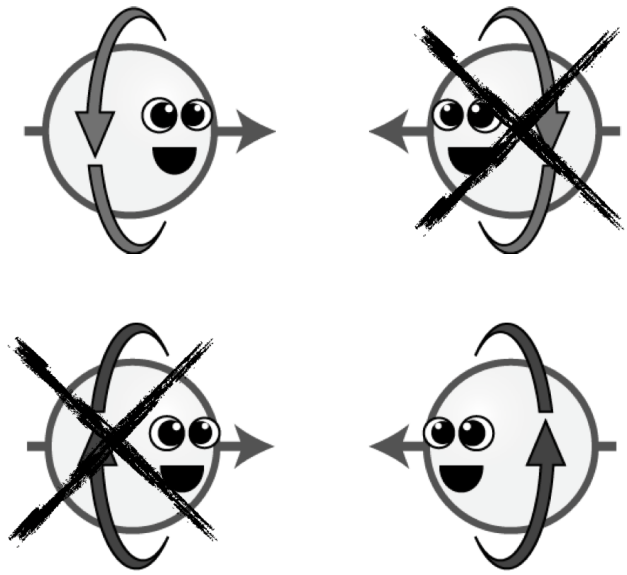

Figure 10.1.1: La interaccó febla ens crea una partícula que gira sobre ella mateixa en una determinada direcció (línea superior). Aquesta mateixa partícula no pot reflexar-se en un mirall per a canviar el seu sentit de la marxa però seguir girant en la mateixa direcciò. El mateix ocorre quan s'intenta canviar la particula per la seva anti-particula (línea inferior). L'única solucó posible es la de canviar partiícula per anti-partícula i fer la reflexió especular al mateix temps per a obtindre un estat real (cantó inferior dret).

mutuament. Per desgracia, aquesta aniquilació no s'ha observat encara ja que, com hem dit, els neutrins pràcticament no interactuen aixi que dificilment van a trobar-se entre ells i destruir-se. No obstant, la natura sempre troba la forma de fer-nos seguir endavant. Existeixen uns experiments, anomenats **Experiments de desintegració doble-beta sense neutrins** que busquen processos on dos neutrins s'aniquilen mutuament.

10.2 Experiments doble beta

En una desintegració beta simple un neutró es desintegra a un protó, un electró i un anti-neutrí. En una emissió doble-beta, per tant, s'emeten dos protons, dos electrons i dos neutrins (Figura 10.2.1). Aquestes desintegracions son conegudes i encaixen perfectament dintre de l'actual model de la física de partícules però tan sols son posibles a l'interior de nuclis atomics, per a que les dos desintegracións es produeixin simultàneament. Per açó, només uns pocs nuclis atómics poden produïr aquesta desintegració ja que sols es posible en aquells on la desintegració beta simple està prohibida energèticament degut principalment a efectes en la forma dels nuclis. Aquesta desintegrció doble beta amb la emissió de dos neutrins es ben coneguda i ha estat mesurada en un extens grup d'isotops. D'altra banda, en el cas les desintegració doble beta sense neutrins continuen sent un misteri. Cap experiment ha estat capaç de trobar un senyal que confirme la seva existencia, tot i aixo, els físics continuen buscant-la perfeccionant les técniques de mesura i construïnt detectors mès grans. Un resultat positiu en aquest tipus d'experiments implicaria necessariament que el neutrí es una partícla Majorana amb totes les repercusions que aixo tindría, com hem explicat abans.

Les desintegracions doble beta sense neutrins son successos extraordinariament rars, a dia de hui la vida mitga [4] sabem que es superior a 10^{25}anys, si comparem aquest

[4]La vida mitga d'un element radiactiu es defineix com el temps necessari per a que un conjunt d'atoms de l'anomenat element es desintegren la meitat dels atoms. Per tant es un indicador del temps que ú deuria esperar per a observar una desintegració en un sol àtom.

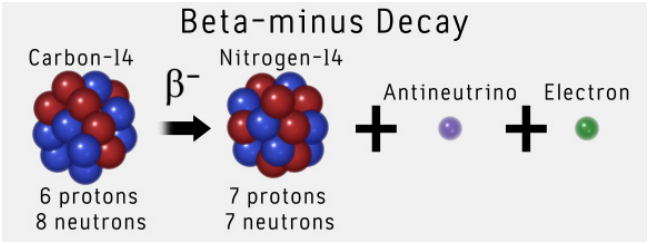

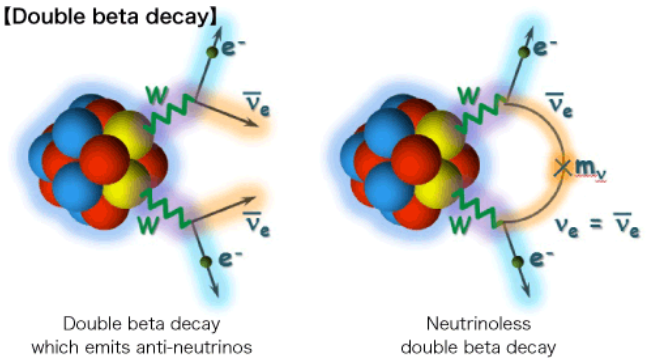

Figure 10.2.1: La desintegració beta simple (imatge superior) es produeix degut a la interacció febla. En aquest cas, un neutró es desintegra emetent un protò, un electrò i un neutrí. La desintegració beta doble (imatge inferior esquerra), no es més que dos desintegracions beta simultànees amb els seus corresponents electrons i neutrins. Per la seva banda, a la desintegració doble beta sense neutrins (inferior dreta), el procés tan sols emet dos electrons, ja que els neutrins han estat aniquilats mutuament durant el process.

número amb l'edat de l'univers (10^{10} anys) ens podem fer una idea de la magnitud del problema que representa trobar aquesta desintegració. Necessitariem un altre univers per cada minut de vida del nostre a fi de que un átom en concret es desintegrés. Com podem fer doncs per a medir aquesta desintegració en un sol univers i sense tenir que esperar milers de vides per fer-ho? Com hem dit abans, sempre hi ha un camí per a seguir avançant, en aquest cas el que fem es en lloc d'observar un sol nucli durant moltisim temps, observar un nombre enorme de nuclis durant un temps mes raonable (uns pocs anys). Efectivament, reunir este nombre enorme d'atoms no es tan dificil ja que al ser tan menuts podem reunir grans quantitats amb relativa facilitat. Els experiments actuals ja son capaços de reunir $\sim 10^{26}$ atoms en un únic experiment. Este nombre representa de l'ordre d'un centenar de quilos. Amb aquestes quantitats de material ja tenim alguna possibilitat (esperança) de detectar unes poques desintegracions cada any.

D'altra banda, per trobar la desintegració sense neutrins no hi ha prou amb ser capaços de reunir un gran nombre d'atoms. Com hem vist, reunir cent quilos de material ens permetria observar unes poques desintegracions, el problema es que l'univers està continuament bombardejan't-nos amb partícules i radiació de tot tipus que ens donarien molts més senyals en el nostre detector que les desintegracions doble beta. Per a poder observar aquest parell de successos per any, em de protegir el nostre detector de la radiació. Per fer-ho ens refugiem en coves, cavernes i mines abandonades. Tornem a les cavernes per entendre l'univers. Instalem el detector en laboratoris subterranis de forma que la terra que tenim per sobre ens protegeisca de totes les partícules que ens arriven. A pesar de tot, amagar-se no es suficient. El nostre món es radiactiu, ho son les roques que formen el laboratori, ho son tots els materials que emprem per a construir el detector i ho som nosaltres[5]. Per esta raó, es necessari fer una extensiva selecció de materials a fi d'escollir aquells mes nets (amb menys radiac-

[5]En el terra hi ha del ordre de decenes de desintegracions per segons de diferents nuclis. L'aigua dels oceans unes poques menys, passa a les poques desintegracions per segon. El nostre cos oscila entre 1 desintegració d'un atom d'urani per segon fins a les milers provenent del Potasi. En el nostre detector aspirem a tenir de l'ordre d'una desintegració per segón.

tivitat) per a construir el detector i al mateix temps aïllar-lo de qualsevol radiactivitat exterior.

Per sort, la senyal d'una desintegració doble beta sense neutrins te dues propietats molt característiques que ens permeten diferenciar-la de la resta de radiació. D'una banda, l'energia dels electrons emessos en la desintegració es sempre la mateixa e igual a la differencia de masses entre el nucli inicial i el nucli final més la massa dels dos electrons. D'altra banda, el fet de tenir dos electrons que parteixen d'un mateix punt ens pot ajudar a distinguir events veridics d'altres produïts per la radioactivitat natural. Per fer-ho em de ser capaços de veure el senyal, distinguir els dos electrons, saber que surten d'un sol punt,... Necessitem que el nostre detector tinga ulls per vore els events i decidir si es o no un event interessant. La major part dels experiments doble beta s'han centrat sempre en medir l'energia del que passava en el detector amb molta precissió, aixo ha donat molts bons resultats, entre ells les medides de la desintegració doble beta amb neutrins. Altres detectors han estat disenyats per a poder observar l'emissió simultànea dels dos electrons en la desintegració. Malgrat els bons resultats d'aquest experiments, no ha sigut fins fa uns pocs anys que ha aparegut l'unic experiment amb una gran capacitat per a medir l'energia i al mateix temps ulls per a distingir els electrons. Aquest experiment es NEXT.

10.3 Construïnt el detector NEXT

El detector NEXT es una TPC (*Càmera de Projecció Temporal* en les seves sigles en angles) que treballa amb Xenon enriquit en el isotop ^{136}Xe que es en el que tractem d'observar la desintegració doble beta sense neutrins. El funcionament bàsic d'una TPC ens permet la reconstrucció tridimensional d'events fent ús d'un pla de medida en dos dimensions. Per a aconseguir-ho prenim una successió de *fotografies* del que ocorre dins del detector per a després juntar-les i tenir la reconstrucció en tres dimensions del event. La idea bàsica es semblant a la que hi ha darrere dels TACs o escanner que s'utilitza en física mèdica. En estos procediments es prenen diverses imatges que

representen un tall o una secció de la zona a estudiar, a continuació aquestes imatges es poden combinar per a obtindre una imatge tridimensional amb gran precisió.

Un de les principals característiques de NEXT es la forma en la que amplifica el senyal dels electrons. Tots els detectors necessiten amplificar les senyals primaries a fi de poder medir-les, però la majoria de detectors treballen amb amplificacions molt grans amb la finalitat d'assegurar-se la lectura de la senyal. Amplificar per grans factors no es gratuït i sol estar relacionat amb grans fluctuacions sent utils per a contar events però perdent precissió i resolució. En NEXT, l'amplificació de la senyal primaria es produeix mitjançant un mecanisme conegut com Electroluminiscencia. Bàsicament consisteix en excitar el gas sense aplegar a ionitzar-lo de forma que el gas emet llum però sempre de manera controlada i sense grans fluctuacions en el nombre de fotons. Aquestos fotons es propagen en totes les direccions dins la càmera i detectan't-los en diferents llocs podem medir diferents propietats del event que els ha produït. D'una banda, els fotons que apleguen a la part de darrere son detectats per uns tubs fotomultiplicadors (PMT), aquest tubs son molt sensibles als fotons sent capaços de contar un sol fotó. El nombre de fotons detectat ens dona una mesura de l'energia del event amb gran precissió. D'altra banda, molt prop de la zona d'amplificació, i per tant de la producció de llum, es troba un pla de sensors distribuïts en una matriu cuadrada que son els responsables de *vore* els senyals dins del detector. Efectvament, aquestos detectors anomenats SiPMs, o fotomultiplicadors de Silici, també mesuren fotons i sense ser tan sensibles com els tubs fotomultiplicadors tenen l'avantatge de ser molt mès petits i barats. Cadascún dels SiPMs es com un *pixel* d'una càmera de fotografiar, amb la matriu de NEXT-100 tindrem una càmera d'uns 7000 pixels que ens permetrà pendre fotografies de tot el que passe dins del detector.

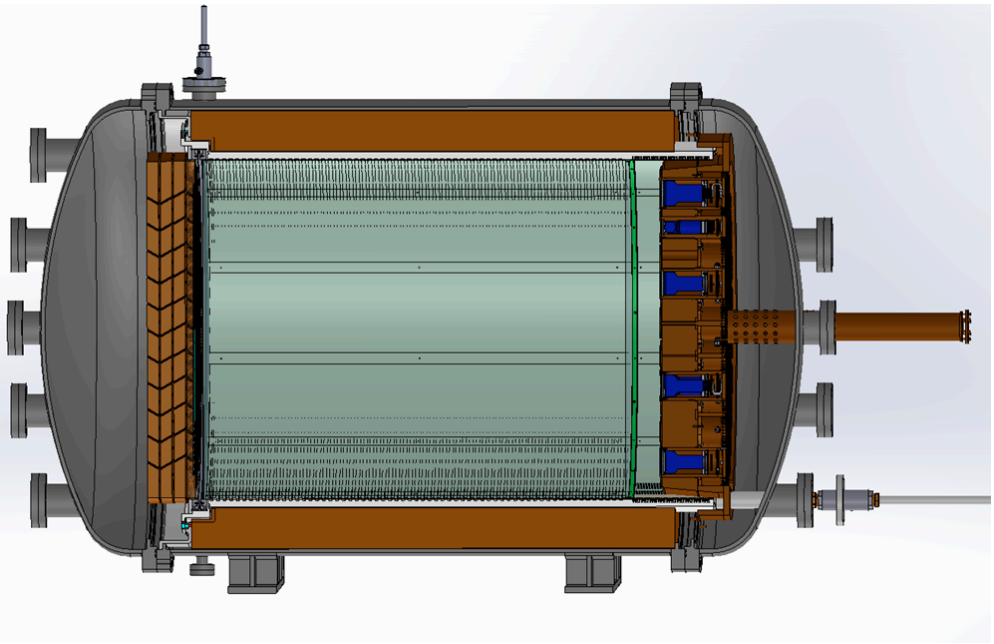

Figure 10.3.1: Un dibuix en 3D del detector NEXT-100 on es mostra l'atuell a pressió (gris), les barres de coure que serviran d'escut contra la radiactivitat ambiental i milloraran la radiopuressa (verd) i els PMTs en blau.

Figure 10.3.2: L'exterior del detector NEXT-100 en les fases finals de la construcció (esquerra). Detall d'una de les juntes que serviran per a mantindre el gas Xenon a pressió sense perdues en el detector (dreta).

10.3.1 NEXT-DEMO.

Els sistema de detecció de NEXT es totalment nou i revolucionari, no hi ha cap altre detector al món emprant la mateixa tecnologia. Este fet, que representa una finestra d'oportunitat en un negoci amb tanta competencia com es el dels experiments doble beta, també representa una aposta molt forta ja que em d'apendre a construïr i operar una TPC amb 100 kg de gas i uns 2.5 m^3 en poc temps. Per aconseguir-ho es necessari donar unes poques passes abans i construir detectors mes menuts, manejables i que factorizen (separen) alguns problemes com la radiopuressa dels materials o els requeriments per a l'estabilitat del sistema. Amb aquesta idea es varen construir alguns prototius dins de la col·laboració sent NEXT-DEMO el que va estar operant en el IFIC i del que s'han obtés resultats mès significatius.

El detector NEXT-DEMO (Imatge 10.3.3) ha passat per diverses configuracions que han permés un coneixement en profunditat de la tecnologia emprada descobrint els seus punts forts així com les seves limitacions i com reduïr-les al mínim. En una primera fase, el detector va estar treballant amb dos planols cadascú amb 19 tubs fotomultiplicadors, un planol servia per a mesurar l'energia com en el detector final i un altre per a posicionar els events dins del volum fiducial[6] del detector. Els resultats d'aquesta primera fase varen demostrar les capacitats que la tecnologia d'amplificació amb electroluminiscencia oferia pel que feia a la resolució energètica. Així, el detector va obtenir una resolució de 1.92% FWHM per a l'energia de la font radiactiva emprada, ^{22}Na buscant el fotó de 511keV. D'altra banda, com esperavem, es va observar una dependencia radial en la quantitat de llum llegida per els fotomultiplicadors del cátode relacionada principalment amb les variacions d'angle solid i de les diferents absorpcions de la llum al propagar-se per el detector en funció de la posició. Aquesta dependencia radial va ser corregida normalitzant les diferents regions a un mateix valor. M'algrat aquesta correció, encara s'observa una petita dependencia de la resolució energética a medida que el tamany del volum fiducial augmenta degut prin-

[6] El volum fiducial es aquell on busquem senyals al nostre detector, es el volúm *util* del detecor i ve definit per les característiques d'aquest.

Figure 10.3.3: Vista del detector NEXT-DEMO amb tots els seus components operant en el IFIC (Valencia).

cipalment a efectes del tamany limitat del detector. Tot i aquest residu, la resolució calculada per al detector NEXT-100 a partir dels resultats mesurats es notablement millor del que la col·laboració tenia com a requisit.

En una segona fase, el planol de PMTs que s'utilitzava per a posicionar els events es substituït per la matriu de 256 SiPMs amb el corresponent increment en la complexitat del sistema que multiplica per 14 el nombre de sensor a tenir en compte tant per a processar els senyals com per a analitzar-les. El augment complexitat ha estat acompanyat per notables beneficis com l'augment de la zona fiducial on la reconstrucció de la posició dels events es correcta a tot el volum del detector així com una correcció dels efectes de la posició mes detallada que ha permés millorar encara mès la resolució energética. Tot i aquestes millores, el que ha estat realment revolucionari ha sigut la capacitat per reconstruir les trajectories dels electrons en el gas del detector fent ús dels SiPMs. NEXT-DEMO ha estat el primer detector del món a fer-ho i ha demon-

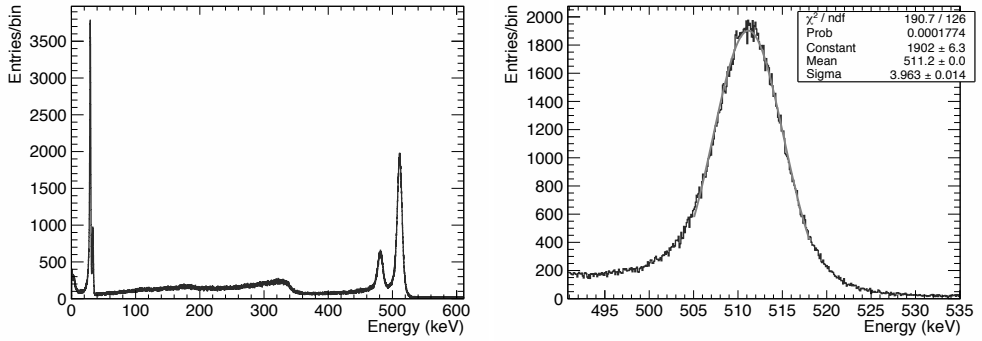

Figure 10.3.4: Espectre d'energia després d'aplicar les corresponents correccions espacials (esquerra). Detall del pic fotoelectric amb els valors de l'adjust (dreta)

strat la capacitat d'aquestos sensors tant per la reconstrucció de la trajectoria com per a diferenciar el punt final de l'eelctró, característica fonamental per a diferenciar la senyal en el detector NEXT-100.

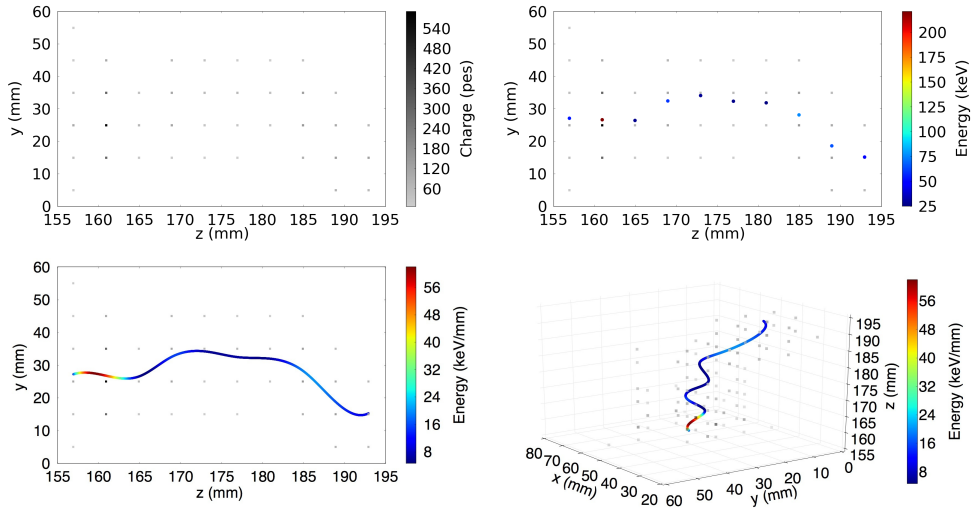

Figure 10.3.5: Example de la reconstrucció d'una traça de ^{137}CsL'a càrrega dels diferents SiPMs es separa en talls d'uns 4mm d'amplada seguint el eix z (dalt esquerra). Per a cada una de les seccions del pols es calcula un punt mitjançant el mètode del baricentre i l'energia d'este punt es l'associada amb la medida pressa en el càtode (dalt dreta). Finalment, els punts s'interconecten entre ells amb una spline cúbica; projecció YZ (baix esquerra) 3D (baix dreta).

10.4 Futur

El camí d'un descobriment es llarg i en el cas de la desintegració doble beta sense neutrins no sembla que el seu final siga prop. La generació actual d'experiments estan publicant els seus primers resultats en els que no troven cap indicació de un senyal positiu. A més a més, les mesures d'altres experiments que ens podríen aportar indicis sobre l'escala necessaria per a fer el descobriment fan pensar que no serà aquesta generació l'encarregada de demostrar la naturalessa Majorana dels neutrins (si es que son Majorana).

Pel que fa a NEXT, la seva construcció i posterior engegada es cada cop més a prop. La part exterior del detector que contindrà el gas ja està construïda i els detalls del diseny de la part interior seràn testejats amb el nou detector NEW que s'instalarà al llarg de 2014 en el Laboratori Subterrani de Canfranc (LSC). Aquest detector, a mès a mès, permetra fer mesures de la radiactivitat de fons en el laboratori i medir la desintegració doble beta en el mode amb dos neutrins.

L'escenari en els pròxims anys passa per un conjunt d'experiments aproximant-se al limit de la seva sensibilitat [7], un experiment amb una tecnologia diferent donant els seus primers resultats de medides físiques i una discussió oberta sobre com seguir endavant, quines passes donar i en quina direcció. En el cas més probable en el que es decideixca donar un pas endavant i construir detectors de nova generació caldrá pendre decicions sobre quin diseny es la que ofereix mès garanties de funcionar a una escala major [8]. En qualsevol cas una cosa es segura, serà necessari desenvolupar noves tecnologies que permeten construïr detectors mès radiopurs, treballar amb diferents presions i camps electrics o pendre i processar dades a majors velocitats.

Sembla que la simetria es resisteix a trencar-se una volta més, que no vol que trovem les seves portes i finestres per a poder accedir a d'ella. Com fer-ho, com aplegar als llocs on la natura ens torne a sorprendre es l'objecitu d'aques projecte i del treball

[7] La sensibilitat d'un experiment està relacionada amb el valor màxim (mínim) que aquest experiment es capaç de mesurar.

[8] Pasariem a tenir uns 10 cops més massa

de tesis. Crear noves ferramentes i apendre a gastar-les a fi de trobar les preguntes adequades per a les respostes que la natura ens pot oferir.

Per altra banda, la ciencia sempre ens sorpren i no podem descartar que les noves tecnologies i materials que han anat sortit en els ultims anys s'intergen dins del camp dels experiments doble beta produïnt una revolució que permetria construir detectors amb formes i tamanys que a dia de hui tan sols podem somiar. En aquest sentit, podem destacar materials com el grafè [9] amb propietas que semblen tretes d'un llibre de ciencia ficció.

En qualsevol cas una cosa es segura, la historia encara no s'acavat d'escriure.

[9]Wikipedia Grafè

References

[1] F. Reines and C. L. Cowan, "The neutrino," *Nature* **178** (1956) 446–449.

[2] J. N. Bahcall, J. Davis, Raymond, and L. Wolfenstein, "Solar Neutrinos: A Field in Transition," *Nature* **334** (1988) 487–493.

[3] **GALLEX** Collaboration, P. Anselmann *et al.*, "GALLEX solar neutrino observations: Complete results for GALLEX II," *Phys.Lett.* **B357** (1995) 237–247.

[4] **SAGE** Collaboration, J. Abdurashitov *et al.*, "Solar neutrino flux measurements by the Soviet-American Gallium Experiment (SAGE) for half the 22 year solar cycle," *J.Exp.Theor.Phys.* **95** (2002) 181–193, arXiv:astro-ph/0204245 [astro-ph].

[5] **Kamiokande** Collaboration, K. S. Hirata *et al.*, "Constraints on neutrino oscillation parameters from the kamiokande-ii solar neutrino data," *Phys. Rev. Lett.* **65** (1990) 1301–1304.

[6] D. D'Angelo, "Low Energy Neutrino Measurements," *Pramana* **79** (2012) 757–780, arXiv:1211.5359 [hep-ex].

[7] **SNO** Collaboration, Q. R. Ahmad *et al.*, "Direct evidence for neutrino flavor transformation from neutral-current interactions in the sudbury neutrino observatory," *Phys. Rev. Lett.* **89** (2002) 011301, arXiv:nucl-ex/0204008.

[8] **Gargamelle Neutrino** Collaboration, F. Hasert *et al.*, "Observation of Neutrino Like Interactions without Muon or Electron in the Gargamelle Neutrino Experiment," *Nucl.Phys.* **B73** (1974) 1–22.

[9] **Particle Data Group** Collaboration, K. Nakamura *et al.*, "Review of particle physics," *J. Phys.* **G37** (2010) 075021.

[10] M. Gonzalez-Garcia, M. Maltoni, J. Salvado, and T. Schwetz, "Global fit to three neutrino mixing: critical look at present precision," *JHEP* **1212** (2012) 123, arXiv:1209.3023 [hep-ph].

[11] **KamLAND** Collaboration, T. Araki *et al.*, "Measurement of neutrino oscillation with KamLAND: Evidence of spectral distortion," *Phys.Rev.Lett.* **94** (2005) 081801, arXiv:hep-ex/0406035 [hep-ex].

[12] **Super-Kamiokande** Collaboration, Y. Fukuda *et al.*, "Evidence for oscillation of atmospheric neutrinos," *Phys.Rev.Lett.* **81** (1998) 1562–1567, arXiv:hep-ex/9807003 [hep-ex].

[13] **T2K** Collaboration, K. Abe *et al.*, "Observation of Electron Neutrino Appearance in a Muon Neutrino Beam," *Phys.Rev.Lett.* **112** (2014) 061802, arXiv:1311.4750 [hep-ex].

[14] **DAYA-BAY** Collaboration, F. An *et al.*, "Observation of electron-antineutrino disappearance at Daya Bay," *Phys.Rev.Lett.* **108** (2012) 171803, arXiv:1203.1669 [hep-ex].

[15] R. Litchfield, "(Direct) Measurement of θ_{13}," arXiv:1209.3884 [hep-ex].

[16] **WMAP** Collaboration, E. Komatsu *et al.*, "Seven-Year Wilkinson Microwave Anisotropy Probe (WMAP) Observations: Cosmological Interpretation," *Astrophys. J. Suppl.* **192** (2011) 18, arXiv:1001.4538 [astro-ph.CO].

[17] **KATRIN** Collaboration, M. Sturm, "KATRIN, an experiment for determination of the ν-mass: status and outlook," *PoS* **DSU2012** (2012) 037.

[18] R. A. Battye and A. Moss, "Evidence for massive neutrinos from CMB and lensing observations," *Phys.Rev.Lett.* **112** (2014) 051303, arXiv:1308.5870 [astro-ph.CO].

[19] M. Wyman, D. H. Rudd, R. A. Vanderveld, and W. Hu, "$\nu\Lambda$CDM: Neutrinos help reconcile Planck with the Local Universe," *Phys.Rev.Lett.* **112** (2014) 051302, arXiv:1307.7715 [astro-ph.CO].

[20] **IceCube** Collaboration, M. Aartsen *et al.*, "First observation of PeV-energy neutrinos with IceCube," *Phys.Rev.Lett.* **111** (2013) 021103, arXiv:1304.5356 [astro-ph.HE].

[21] **IceCube** Collaboration, M. Aartsen *et al.*, "Evidence for High-Energy Extraterrestrial Neutrinos at the IceCube Detector," *Science* **342** no. 6161, (2013) 1242856, arXiv:1311.5238 [astro-ph.HE].

[22] P. Hernández, "Neutrino physics," arXiv:1010.4131 [hep-ph].

[23] C. Giunti and M. Laveder, "Neutrino mixing," arXiv:hep-ph/0310238.

[24] E. Majorana, "Theory of the Symmetry of Electrons and Positrons," *Nuovo Cim.* **14** (1937) 171–184.

[25] S. J. Parke, "Neutrino physics today, important issues and the future,". Presented at 24th International Conference On Neutrino Physics And Astrophysics (Neutrino 2010), Athens, Greece, 14-19 Jun 2010.

[26] B. Kayser, "Neutrino mass, mixing, and flavor change," arXiv:hep-ph/0211134.

[27] M. Fukugita and T. Yanagida, "Baryogenesis Without Grand Unification," *Phys. Lett.* **B174** (1986) 45.

[28] M.-C. Chen, "TASI 2006 Lectures on Leptogenesis," arXiv:hep-ph/0703087.

[29] S. Davidson, E. Nardi, and Y. Nir, "Leptogenesis," *Phys. Rept.* **466** (2008) 105–177, arXiv:0802.2962 [hep-ph].

[30] A. D. Sakharov, "Violation of CP Invariance, c Asymmetry, and Baryon Asymmetry of the Universe," *Pisma Zh. Eksp. Teor. Fiz.* **5** (1967) 32–35.

[31] A. Atre, V. Barger, and T. Han, "Upper bounds on lepton-number violating processes," *Phys. Rev.* **D71** (2005) 113014, hep-ph/0502163.

[32] M. Goeppert-Mayer, "Double beta-disintegration," *Phys. Rev.* **48** (1935) 512–516.

[33] M. G. Inghram and J. H. Reynolds, "Double beta-decay of Te-130," *Phys. Rev.* **78** (1950) 822–823.

[34] S. R. Elliott, A. A. Hahn, and M. K. Moe, "Direct evidence for two-neutrino double-beta decay in Se- 82," *Phys. Rev. Lett.* **59** (1987) 2020–2023.

[35] A. S. Barabash, "Precise half-life values for two neutrino double beta decay," *Phys. Rev.* **C81** (2010) 035501, arXiv:1003.1005 [nucl-ex].

[36] **EXO** Collaboration, N. Ackerman *et al.*, "Observation of Two-Neutrino Double-Beta Decay in ^{136}Xe with EXO-200," *Phys. Rev. Lett.* **107** (2011) 212501, arXiv:1108.4193 [nucl-ex].

[37] A. Staudt, K. Muto, and H. Klapdor-Kleingrothaus, "Calculation of two neutrino and zero neutrino double beta decay rates," *Europhys.Lett.* **13** (1990) 31–36.

[38] J. Engel, P. Vogel, and M. R. Zirnbauer, "Nuclear Structure Effects in Double beta Decay," *Phys. Rev.* **C37** (1988) 731–746.

[39] E. Caurier, F. Nowacki, A. Poves, and J. Retamosa, "Shell Model Studies of the Double Beta Decays of Ge-76, Se-82, and Xe-136," *Phys. Rev. Lett.* **77** (1996) 1954–1957.

[40] A. Balysh *et al.*, "Double beta decay of ^{48}Ca," *Phys. Rev. Lett.* **77** (1996) 5186–5189, nucl-ex/9608001.

[41] V. B. Brudanin *et al.*, "Search for double beta decay of Ca-48 in the TGV experiment," *Phys. Lett.* **B495** (2000) 63–68.

[42] **NEMO-3** Collaboration, R. L. Flack, "Results from NEMO 3," *J. Phys. Conf. Ser.* **136** (2008) 022032, arXiv:0810.5497 [hep-ex].

[43] F. T. Avignone, "Double-beta decay: Some recent results and developments," *Prog. Part. Nucl. Phys.* **32** (1994) 223–245.

[44] A. Morales, "Review on double beta decay experiments and comparison with theory," *Nucl. Phys. Proc. Suppl.* **77** (1999) 335–345, arXiv:hep-ph/9809540.

[45] C. Dorr and H. V. Klapdor-Kleingrothaus, "New Monte-Carlo simulation of the HEIDELBERG-MOSCOW double beta decay experiment," *Nucl. Instrum. Meth.* **A513** (2003) 596–621.

[46] **NEMO** Collaboration, R. Arnold *et al.*, "First results of the search of neutrinoless double beta decay with the NEMO 3 detector," *Phys. Rev. Lett.* **95** (2005) 182302, arXiv:hep-ex/0507083.

[47] S. R. Elliott, A. A. Hahn, M. K. Moe, M. A. Nelson, and M. A. Vient, "Double beta decay of Se-82," *Phys. Rev.* **C46** (1992) 1535–1537.

[48] **NEMO** Collaboration, R. Arnold *et al.*, "Double beta decay of Se-82," *Nucl. Phys.* **A636** (1998) 209–223.

[49] R. Arnold *et al.*, "Double beta decay of Zr-96," *Nucl. Phys.* **A658** (1999) 299–312.

[50] **NEMO-3** Collaboration, J. Argyriades *et al.*, "Measurement of the two neutrino double beta decay half- life of Zr-96 with the NEMO-3 detector," *Nucl. Phys.* **A847** (2010) 168–179, arXiv:0906.2694 [nucl-ex].

[51] **NEMO** Collaboration, D. Dassie *et al.*, "Two neutrino double beta decay measurement of Mo-100," *Phys. Rev.* **D51** (1995) 2090–2100.

[52] A. S. De Silva, M. K. Moe, M. A. Nelson, and M. A. Vient, "Double beta decays of Mo-100 and Nd-150," *Phys. Rev.* **C56** (1997) 2451–2467, arXiv:nucl-ex/9706005.

[53] H. Ejiri *et al.*, "Double beta decays of Cd-116," *J. Phys. Soc. Jap.* **64** (1995) 339–343.

[54] F. A. Danevich *et al.*, "Search for 2 beta decay of cadmium and tungsten isotopes: Final results of the Solotvina experiment," *Phys. Rev.* **C68** (2003) 035501.

[55] **NEMO** Collaboration, R. Arnold *et al.*, "Double-beta decay of Cd-116," *Z. Phys.* **C72** (1996) 239–247.

[56] C. Arnaboldi, C. Brofferio, C. Bucci, S. Capelli, O. Cremonesi, *et al.*, "A Calorimetric search on double beta decay of Te-130," *Phys. Lett.* **B557** (2003) 167–175, hep-ex/0211071.

[57] **NEMO3** Collaboration, V. I. Tretyak, "Recent results of the NEMO 3 experiment," *AIP Conf. Proc.* **1180** (2009) 135–139.

[58] **NEMO** Collaboration, J. Argyriades *et al.*, "Measurement of the Double Beta Decay Half-life of 150-Nd and Search for Neutrinoless Decay Modes with the NEMO-3 Detector," *Phys. Rev.* **C80** (2009) 032501, arXiv:0810.0248 [hep-ex].

[59] W. H. Furry, "On transition probabilities in double beta- disintegration," *Phys. Rev.* **56** (1939) 1184–1193.

[60] P. Vogel, "Nuclear physics aspects of double beta decay," arXiv:0807.2457 [hep-ph].

[61] A. S. Barabash *et al.*, "Two neutrino double beta decay of Mo-100 to the first excited 0+ state in Ru-100," *Phys. Lett.* **B345** (1995) 408–413.

[62] **NEMO** Collaboration, R. Arnold *et al.*, "Measurement of double beta decay of Mo-100 to excited states in the NEMO 3 experiment," *Nucl. Phys.* **A781** (2007) 209–226, arXiv:hep-ex/0609058.

[63] M. F. Kidd, J. H. Esterline, W. Tornow, A. S. Barabash, and V. I. Umatov, "New Results for Double-Beta Decay of Mo-100 to Excited Final States of Ru-100 Using the TUNL-ITEP Apparatus," *Nucl. Phys.* **A821** (2009) 251–261, arXiv:0902.4418 [nucl-ex].

[64] A. S. Barabash, P. Hubert, A. Nachab, and V. I. Umatov, "Investigation of $\beta\beta$ decay in ^{150}Nd and ^{148}Nd to the excited states of daughter nuclei," *Phys. Rev.* **C79** (2009) 045501, arXiv:0904.1924 [nucl-ex].

[65] S. Eliseev *et al.*, "Resonant Enhancement of Neutrinoless Double-Electron Capture in Gd-152," *Phys. Rev. Lett.* **106** (2011) 052504.

[66] J. Schechter and J. W. F. Valle, "Neutrinoless double-beta decay in SU(2) $\times$ U(1) theories," *Phys. Rev.* **D25** (1982) 2951.

[67] M. Duerr, M. Lindner, and A. Merle, "On the Quantitative Impact of the Schechter-Valle Theorem," *JHEP* **06** (2011) 091, arXiv:1105.0901 [hep-ph].

[68] W. Rodejohann, "Neutrino-less Double Beta Decay and Particle Physics," *Int.J.Mod.Phys.* **E20** (2011) 1833–1930, arXiv:1106.1334 [hep-ph].

[69] M. Doi, T. Kotani, and E. Takasugi, "Double beta Decay and Majorana Neutrino," *Prog. Theor. Phys. Suppl.* **83** (1985) 1.

[70] F. Vissani, "Signal of neutrinoless double beta decay, neutrino spectrum and oscillation scenarios," *JHEP* **9906** (1999) 022, arXiv:hep-ph/9906525 [hep-ph].

[71] G. L. Fogli, E. Lisi, A. Marrone, A. Palazzo, and A. M. Rotunno, "Evidence of theta(13)>0 from global neutrino data analysis," arXiv:1106.6028 [hep-ph].

[72] F. T. Avignone, III, S. R. Elliott, and J. Engel, "Double Beta Decay, Majorana Neutrinos, and Neutrino Mass," *Rev. Mod. Phys.* **80** (2008) 481–516, arXiv:0708.1033 [nucl-ex].

[73] R. N. Mohapatra, "LIMITS ON THE MASS OF THE RIGHT-HANDED MAJORANA NEUTRINO," *Phys.Rev.* **D34** (1986) 909.

[74] R. Mohapatra, "New Contributions to Neutrinoless Double beta Decay in Supersymmetric Theories," *Phys.Rev.* **D34** (1986) 3457–3461.

[75] H. M. Georgi, S. L. Glashow, and S. Nussinov, "Unconventional Model of Neutrino Masses," *Nucl.Phys.* **B193** (1981) 297.

[76] **SuperNEMO** Collaboration, R. Arnold *et al.*, "Probing New Physics Models of Neutrinoless Double Beta Decay with SuperNEMO," *Eur.Phys.J.* **C70** (2010) 927–943, arXiv:1005.1241 [hep-ex].

[77] S. Umehara *et al.*, "Neutrino-less Double Beta Decay of ^{48}Ca studied by CaF$_2$(Eu) Scintillators," *Phys. Rev.* **C78** (2008) 058501, arXiv:0810.4746 [nucl-ex].

[78] H. Klapdor-Kleingrothaus, A. Dietz, L. Baudis, G. Heusser, I. Krivosheina, *et al.*, "Latest results from the Heidelberg-Moscow double beta decay experiment," *Eur. Phys. J. A* **12** (2001) 147–154, arXiv:hep-ph/0103062 [hep-ph].

[79] A. S. Barabash, V. B. Brudanin, and t. N. Collaboration, "Investigation of double beta decay with the NEMO-3 detector," *Phys. Atom. Nucl.* **74** (2011) 312–317, arXiv:1002.2862 [nucl-ex].

[80] E. Andreotti, C. Arnaboldi, I. Avignone, F.T., M. Balata, I. Bandac, *et al.*, "130Te Neutrinoless Double-Beta Decay with CUORICINO," *Astropart. Phys.* **34** (2011) 822–831, arXiv:1012.3266 [nucl-ex].

[81] R. L. et al., "Search for ββ decay in 136xe: new results from the gotthard experiment," *Physics Letters B* **434** no. 3–4, (1998) 407 – 414. http://www.sciencedirect.com/science/article/pii/S037026939800906X.

[82] H. Klapdor-Kleingrothaus, A. Dietz, H. Harney, and I. Krivosheina, "Evidence for neutrinoless double beta decay," *Mod. Phys. Lett. A* **16** (2001) 2409–2420, arXiv:hep-ph/0201231 [hep-ph].

[83] C. E. Aalseth *et al.*, "Comment on 'Evidence for Neutrinoless Double Beta Decay'," *Mod. Phys. Lett.* **A17** (2002) 1475–1478, hep-ex/0202018.

[84] H. V. Klapdor-Kleingrothaus and I. V. Krivosheina, "The evidence for the observation of onu beta beta decay: The identification of onu beta beta events from the full spectra," *Mod. Phys. Lett.* **A21** (2006) 1547–1566.

[85] **IGEX** Collaboration, C. E. Aalseth *et al.*, "The IGEX Ge-76 Neutrinoless Double-Beta Decay Experiment: Prospects for Next Generation Experiments," *Phys. Rev.* **D65** (2002) 092007, hep-ex/0202026.

[86] J. J. Gómez-Cadenas, J. Martin-Albo, M. Mezzetto, F. Monrabal, and M. Sorel, "The search for neutrinoless double beta decay," *Riv. Nuovo Cim.* **35** (2012) 29–98, arXiv:1109.5515 [hep-ex].

[87] **EXO** Collaboration, M. Auger *et al.*, "Search for Neutrinoless Double-Beta Decay in ^{136}Xe with EXO-200," *Phys.Rev.Lett.* **109** (2012) 032505, arXiv:1205.5608 [hep-ex].

[88] **KamLAND-Zen** Collaboration, A. Gando *et al.*, "First result from KamLAND-Zen: Double beta decay with ^{136}Xe," arXiv:1205.6130 [hep-ex].

[89] **GERDA Collaboration** Collaboration, M. Agostini *et al.*, "The background in the $0\nu\beta\beta$ experiment GERDA," *Eur.Phys.J.* **C74** (2014) 2764, arXiv:1306.5084 [physics.ins-det].

[90] M. Agostini, M. Allardt, E. Andreotti, A. Bakalyarov, M. Balata, *et al.*, "Pulse shape discrimination for GERDA Phase I data," *Eur.Phys.J.* **C73** (2013) 2583, arXiv:1307.2610 [physics.ins-det].

[91] **GERDA** Collaboration, M. Agostini *et al.*, "Measurement of the half-life of the two-neutrino double beta decay of ge-76 with the gerda experiment," *J.Phys.* **G40** (2013) 035110, arXiv:1212.3210 [nucl-ex].

[92] **GERDA Collaboration** Collaboration, M. Agostini *et al.*, "Results on Neutrinoless Double-β Decay of ^{76}Ge from Phase I of the GERDA Experiment," *Phys.Rev.Lett.* **111** no. 12, (2013) 122503, arXiv:1307.4720 [nucl-ex].

[93] **EXO** Collaboration, E. Conti *et al.*, "Correlated fluctuations between luminescence and ionization in liquid xenon," *Phys. Rev. B* **68** (2003) 054201, arXiv:hep-ex/0303008 [hep-ex].

[94] **EXO-200** Collaboration, J. Albert *et al.*, "An improved measurement of the $2\nu\beta\beta$ half-life of ^{136}Xe with EXO-200," (2013) , arXiv:1306.6106 [nucl-ex].

[95] **The KamLAND-Zen** Collaboration, "Results from KamLAND-Zen," (2014) , arXiv:1409.0077 [physics.ins-det].

[96] R. Cooper, D. Radford, K. Lagergren, J. F. Colaresi, L. Darken, R. Henning, M. Marino, and K. M. Yocum, "A pulse shape analysis technique for the {MAJORANA} experiment," *Nuclear Instruments and Methods in Physics Research Section A: Accelerators, Spectrometers, Detectors and Associated Equipment* **629** no. 1, (2011) 303 – 310. http://www.sciencedirect.com/science/article/pii/S0168900210024915.

[97] I. Phillips, D.G., E. Aguayo, I. Avignone, F.T., H. Back, A. Barabash, *et al.*, "The Majorana experiment: an ultra-low background search for neutrinoless double-beta decay," *J.Phys.Conf.Ser.* **381** (2012) 012044, arXiv:1111.5578 [nucl-ex].

[98] J. J. Gomez-Cadenas, J. Martin-Albo, M. Sorel, P. Ferrario, F. Monrabal, *et al.*, "Sense and sensitivity of double beta decay experiments," *JCAP* **1106** (2011) 007, arXiv:1010.5112 [hep-ex].

[99] **Caltech-Neuchâtel-PSI** Collaboration, R. Luscher *et al.*, "Search for $\beta\beta$ decay in Xe-136: New results from the Gotthard experiment," *Phys. Lett. B* **434** (1998) 407–414.

[100] D. Nygren, "High-pressure xenon gas electroluminescent TPC for onu beta beta-decay search," *Nucl.Instrum.Meth.* **A603** (2009) 337–348.

[101] **NEXT** Collaboration, V. Alvarez *et al.*, "The NEXT-100 experiment for neutrinoless double beta decay searches (Conceptual Design Report)," arXiv:1106.3630 [physics.ins-det].

[102] C. A. N. Conde, *Gas Proportional Scintillation Counters for x-ray spectrometry*. John Wiley & sons, 2004. Chapter 4.2 in *X-ray Spectrometry: Recent Technical Advances*, K. Tsuji, J. Injuk and R. van Greiken, eds.

[103] C. A. N. Conde and A. J. P. L. Policarpo *Nucl. Instr. Meth.* **53** (1967) 7–12.

[104] G. Charpak, S. Majewski, and F. Sauli, "The scintillating drift chamber: A new tool for high accuracy, very high rate particle localization," *Nucl. Instr. Meth.* **126** (1975) 381.

[105] H. N. Charpak, G. Ngoc and J. P. L. Policarpo, "Neutral radiation detection and localization," 1981. US Patent 4,286,158, August 25, 1981.

[106] A. Bolozdynya *et al.*, "A high pressure xenon self-triggered scintillation drift chamber with 3D sensitivity in the range of 20-140 keV deposited energy," *Nuc. Inst. Meth.* **A385** (1997) 225.

[107] E. Aprile, A. I. Bolotnikov, A. I. Bolozdynya, and T. Doke, *Noble gas detectors*. Wiley-VCN, 2006.

[108] A. S. Tanaka, Y. Jursa and F. J. LeBlanc, "Continuous Emission Spectra of Rare Gases in the Vacuum Ultraviolet Region II: Neon and Helium," *Journal of the Optical Society of America* **48** (1958) 304–308.

[109] C. A. B. Oliveira *et al.*, "Electroluminescence of Neon, Argon, Krypton and Xenon produced in uniform field: yield and fluctuations," *submitted to Phys. Letters B* .

[110] R. S. Mulliken, "Potential Curves of Diatomic Rare-Gas Molecules and Their Ions with Particular Reference to Xe_2^*," *JThe Journal of Chemical Physics* **52** (1970) 5170–5180.

[111] H. A. Koehler *et al.*, "Vacuum-ultraviolet emission from high-pressure xenon and argon excited by high-current relativistic electron beams," *Phys. Rev. A* **9** (1974) 768–780.

[112] `http://garfield.web.cern.ch/garfield/`.

[113] S. F. Biagi, "Monte Carlo simulation of electron drift and diffusion in counting gases under the influence of electric and magnetic fields," *Nucl. Inst. Meth. A* **421** (1999) 234–240.

[114] `http://consult.cern.ch/writeup/magboltz/`.

[115] T. H. V. T. Dias and others., "Three-dimensional Monte Carlo calculation of the VUV electroluminescence and other electron transport parameters in xenon," *Journal of Physics D* **27** (1994) 42–48.

[116] C. M. B. Monteiro and others., "Secondary scintillation yield in pure xenon," *Journal of Instrumentation* **2** (2007) P05001.

[117] C. Silva, J. Pinto da Cunha, A. Pereira, V. Chepel, M. Lopes, *et al.*, "Reflectance of Polytetrafluoroethylene (PTFE) for Xenon Scintillation Light," `arXiv:0910.1056 [physics.ins-det]`.

[118] S. Martoiu, H. Muller, and J. Toledo, "Front-end electronics for the Scalable Readout System of RD51," in *Nuclear Science Symposium and Medical Imaging Conference (NSS/MIC), IEEE*, pp. 2036–2038. 2011.

[119] V. Alvarez, J. Agramunt, M. Ball, M. Batalle, J. Bayarri, *et al.*, "SiPMs coated with TPB : coating protocol and characterization for NEXT," *JINST* **7** (2012) P02010, `arXiv:1201.2018 [physics.ins-det]`.

[120] N. Dinu, C. Bazin, V. Chaumat, C. Cheikali, A. Para, V. Puill, C. Sylvia, and J. F. Vagnucci, "Temperature and bias voltage dependence of the MPPC detectors," in *Nuclear Science Symposium Conference Record (NSS/MIC), 2010 IEEE*, pp. 215–219. 2010.

[121] J. Rodríguez, M. Querol, J. Díaz, J.J. Gómez-Cadenas, D. Lorca, V. Álvarez, A. Gil, "Mass production automated test system for the NEXT SiPM tracking plane," in *2012 IEEE NSS-MI Conference Record*. 2012.

[122] **NEXT** Collaboration, V. Alvarez *et al.*, "Design and characterization of the SiPM tracking system of NEXT-DEMO, a demonstrator prototype of the NEXT-100 experiment," *JINST* **8** (2013) T05002, arXiv:1206.6199. http://stacks.iop.org/1748-0221/8/i=05/a=T05002.

[123] J. Janesick, *Scientific Charge Coupled Devices*. SPIE Press, 2001.

[124] M. Berger, J. Coursey, M. Zucker, , and J. Chang, "(2005) ESTAR, PSTAR, and ASTAR: Computer Programs for Calculating Stopping-Power and Range Tables for Electrons, Protons, and Helium Ions (version 1.2.3)." Originally published as: Berger, M.J., NISTIR 4999, National Institute of Standards and Technology, Gaithersburg, MD (1993)., February, 2013. URL: http://physics.nist.gov/Star.

[125] **NEXT** Collaboration, V. Álvarez *et al.*, "Initial results of NEXT-DEMO, a large-scale prototype of the NEXT-100 experiment," arXiv:1211.4838 [physics.ins-det].

[126] L. Fernandes *et al.*, "Primary and secondary scintillation measurements in a xenon Gas Proportional Scintillation Counter," *JINST* **5** (2010) P09006, arXiv:1009.2719 [astro-ph.IM].

[127] S. J. C. do Carmo, F. I. G. M. Borges, F. P. Santos, T. H. V. T. Dias, and C. A. N. Conde, "Absolute primary scintillation yield of gaseous xenon under low drift electric fields for 5.9 kev x-rays," *JINST* **3** (2008) P07004,.

[128] A. Parsons, T. Edberg, B. Sadoulet, S. Weiss, J. F. Wilkerson, *et al.*, "High pressure gas scintillation drift chambers with wave shifter fiber readout," *IEEE Trans. Nucl. Sci.* **37** (1990) 541–546.

[129] S. P. Ahlen, "Theoretical and experimental aspects of the energy loss of relativistic heavily ionizing particles," *Rev. Mod. Phys.* **52** (1980) 121–173.

[130] U. Fano, "Ionization Yield of Radiations. 2. The Fluctuations of the Number of Ions," *Phys. Rev.* **72** (1947) 26–29.

[131] **NEXT** Collaboration, V. Álvarez *et al.*, "Ionization and scintillation response of high-pressure xenon gas to alpha particles," arXiv:1211.4508 [physics.ins-det].

[132] C. Monteiro *et al.*, "Secondary Scintillation Yield in Pure Xenon," *JINST* **2** (2007) P05001, arXiv:physics/0702142 [physics.ins-det].

[133] C. A. B. Oliveira, M. Sorel, J. Martín-Albo, J. J. Gómez-Cadenas, A. L. Ferreira, *et al.*, "Energy resolution studies for NEXT," *JINST* **6** (2011) P05007, arXiv:1105.2954 [physics.ins-det].

[134] **NEXT** Collaboration, V. Álvarez *et al.*, "Operation and first results of the NEXT-DEMO prototype using a silicon photomultiplier tracking array," *JINST* **8** (2013) P09011, arXiv:1306.0471 [physics.ins-det].

[135] **NEXT** Collaboration, V. Alvarez *et al.*, "Initial results of NEXT-DEMO, a large-scale prototype of the NEXT-100 experiment," *JINST* **8** (2013) P04002, arXiv:1211.4838 [physics.ins-det].

[136] E. b. B. Rebel, C. H. w. c. f. E. Bernard, C. Faham, T. Ito, B. Lundberg, *et al.*, "High Voltage in Noble Liquids for High Energy Physics," arXiv:1403.3613 [physics.ins-det].

[137] **NEXT** Collaboration, V. Alvarez *et al.*, "NEXT-100 Technical Design Report (TDR): Executive Summary," *JINST* **7** (2012) T06001, arXiv:1202.0721 [physics.ins-det].

[138] V. Alvarez *et al.*, "Radiopurity control in the NEXT-100 double beta decay experiment: procedures and initial measurements," arXiv:1211.3961 [physics.ins-det].

[139] K. Lung, K. Arisaka, A. Bargetzi, P. Beltrame, A. Cahill, T. Genma, C. Ghag, D. Gordon, J. Sainz, A. Teymourian, and Y. Yoshizawa, "Characterization of the Hamamatsu R11410-10 3-in. photomultiplier tube for liquid xenon dark

matter direct detection experiments," *Nuclear Instruments and Methods in Physics Research A* **696** (Dec., 2012) 32–39, arXiv:1202.2628 [physics.ins-det].